Durham E-Theses

The Evolution of Massive Star-forming Galaxies: Energetics and the Interstellar Medium

DANIELSON, ALICE,LOWRY,RUTH

The Evolution of Massive Star-forming Galaxies: Energetics and the Interstellar Medium

Alice Lowry Ruth Danielson

Abstract

Over the last ~20 years, the importance of dusty star-forming galaxies in contributing approximately half the energy density of the Universe has been realised. Much research in this field has focussed on the subset of submillimetre bright galaxies (SMGs). Submillimetre Astronomy has recently seen major advances due largely to huge developments in the available instrumentation. In this thesis I present the first spectroscopic redshift distribution of unambiguously-identified SMGs, targeted with ALMA. The redshift distribution is shown to peak at $z \sim 2.4$. The next step to understanding the SMG population is to use their redshifts to facilitate high-resolution follow-up observations, probing the conditions and physical structure within the interstellar medium (ISM) of these systems. I present the detailed observations of the ISM within the gravitationally lensed SMG, SMM J2135. In particular, the spectral line energy distributions of ^{12}CO, ^{13}CO and C^{18}O are measured and used to infer the temperature, densities and chemical abundances within this intrinsically representative SMG, with strong variation found between the multiple kinematic components in the galaxy. Furthermore, an unusually high abundance of C^{18}O is measured, implying the presence of preferentially massive stars, perhaps highlighting some differences between star formation locally and at high-redshift. The cosmic star-formation rate density has rapidly declined since $z \sim 2$ and there is much evidence to suggest that massive star-forming galaxies at $z \sim 2$ may evolve into massive passive elliptical galaxies at $z = 0$. I investigate the potential influence of active galactic nuclei (AGN) on the suppression of star formation within massive elliptical galaxies over $z = 0.1 - 1.2$. I determine that the hot gas within these evolved systems does not cool as rapidly as expected and demonstrate that heating due to mechanical feedback from radio AGN is more than sufficient to balance the X-ray cooling of hot gas, thus suppressing further star formation.

The Evolution of Massive Star-forming Galaxies: Energetics and the Interstellar Medium

Alice Lowry Ruth Danielson

A Thesis presented for the degree of
Doctor of Philosophy

Durham University

Extragalactic Astronomy
Department of Physics
University of Durham
England

September 2014

Contents

List of Figures

List of Tables

Declaration

The work in this thesis is based on research carried out at the Extragalactic Astronomy group, the Department of Physics, Durham University, England. No part of this thesis has been submitted elsewhere for any other degree or qualification and it is all my own work unless referenced to the contrary in the text. Portions of this work have appeared in the following lead author papers:

1. **"The properties of the interstellar medium within a star-forming galaxy at $z = 2.3$"** Danielson, A. L. R., Swinbank, A. M., Smail, Ian, Cox, P., Edge, A. C., Weiss, A., Harris, A. I., Baker, A. J., De Breuck, C., Geach, J. E., Ivison, R. J., Krips, M., Lundgren, A., Longmore, S., Neri, R., Flaquer, B. Ocana, 2011, Monthly Notices of the Royal Astronomical Society, Volume 410, Issue 3, pp. 1687-1702

2. **"The cosmic history of hot gas cooling and radio active galactic nucleus activity in massive early-type galaxies"** Danielson, A. L. R., Lehmer, B. D., Alexander, D. M., Brandt, W. N., Luo, B., Miller, N., Xue, Y. Q., Stott, J. P., 2012, Monthly Notices of the Royal Astronomical Society, Volume 422, Issue 1, pp. 494-509.

3. **"^{13}CO and C^{18}O emission from a dense gas disc at $z = 2.3$: abundance variations, cosmic rays and the initial conditions for star formation"** Danielson, A. L. R., Swinbank, A. M., Smail, Ian, Bayet, E., van der Werf, Paul P., Cox, P., Edge, A. C., Henkel, C., Ivison, R. J., 2013, Monthly Notices of the Royal Astronomical Society, Volume 436, Issue 3, p.2793-2809

The author has also worked on, or been involved in the following publications:

1. Ivison, R. J.; Swinbank, A. M.; Swinyard, B.; Smail, I.; Pearson, C. P.; Rigopoulou, D.; Polehampton, E.; Baluteau, J.-P.; Barlow, M. J.; Blain, A. W.; Bock, J.; Clements, D. L.; Coppin, K.; Cooray, A.; **Danielson, A.** and 20 other co-authors, "Herschel and SCUBA-2 imaging and spectroscopy of a bright, lensed submillimetre galaxy at $z = 2.3$", 2010, A&A, 518, L35

2. Wardlow, J. L.; Smail, Ian; Coppin, K. E. K.; Alexander, D. M.; Brandt, W. N.; **Danielson, A. L. R.** and 20 other co-authors, "The LABOCA survey of the Extended Chandra Deep Field South: A photometric redshift survey of submillimetre galaxies", 2011, MNRAS, 415, 1479

3. Magnelli, B.; Lutz, D.; Santini, P.; Saintonge, A.; Berta, S.; Albrecht, M.; Altieri, B.; Andreani, P.; Aussel, H.; Bertoldi, F.; Bethermin, M.; Bongiovanni, A.; Capak, P.; Chapman, S.; Cepa, J.; Cimatti, A.; Cooray, A.; Daddi, E.; **Danielson, A. L. R.** and 32 other co-authors, "A Herschel view of the far-infrared properties of submillimetre galaxies", 2012, A&A, 539, 155

4. Hickox, Ryan C.; Wardlow, J. L.; Smail, Ian; Myers, A. D.; Alexander, D. M.; Swinbank, A. M.; **Danielson, A. L. R.** and 8 other co-authors, "The LABOCA survey of the Extended Chandra Deep Field-South: clustering of submillimetre galaxies" 2012, MNRAS, 421, 284

5. Simpson, J. M.; Smail, Ian; Swinbank, A. M.; Alexander, D. M.; Auld, R.; Baes, M.; Bonfield, D. G.; Clements, D. L.; Cooray, A.; Coppin, K. E. K.; **Danielson, A. L. R.** and 15 other co-authors, "The evolutionary connection between QSOs and SMGs: molecular gas in far-infrared luminous QSOs at $z \sim 2.5$", 2012, MNRAS, 426, 3201

6. K. E. K. Coppin, **A. L. R. Danielson**, and 23 other co-authors, "Herschel-PACS observations of [OI]63μm towards submillimetre galaxies at z~1", 2012, MNRAS, 427, 520

Notes:

§2: Chapter 2 is based on data from observing proposals led by Ian Smail and C. M. Casey. The author has carried out all of the data reduction and analysis in this Chapter with the following exceptions: The VIMOS and GNIRS data were reduced by A. M. Swinbank who also provided spectral energy distributions, fit using the

new redshifts determined by the author; the DEIMOS and MOSFIRE data were reduced by C. M. Casey; the XSHOOTER data were reduced by J. M. Simpson who also provided spectral energy distributions fit using the new redshifts determined by the author; the spectral energy distributions fit using MAGPHYS were provided by Elisabete da Cunha.

§3: Chapter 3 is based on data from observing proposals led by A. M. Swinbank in Directors Discretionary Time. The data was all reduced by the author. The large velocity gradient modelling was carried out by Axel Weiss.

§4: Chapter 4 is based on data from proposals led by Paul P. van der Werf and A. M. Swinbank with contributions from the author. All data was reduced by the author, aside from the JVLA data which was reduced by Paul P. van der Werf. Large velocity gradient models were provided by Estelle Bayet.

§5: Chapter 5 is based on published data from various sources.

All of the text has been written by the author.

Acknowledgements

My parents, Ruth and Ethan, instilled in me a thirst for knowledge and a sense of wonder which led me to study Astronomy. They gave me a huge amount of time growing up, which I will never forget and have been an incredible and constant support to me. I remember fondly, stargazing with Dad and Poppa as a child and will never forget us seeing Saturn with my first telescope - beats the VLT any day! I also want to acknowledge the role that my Year 8 teacher, Phil Creasey, had in inspiring me to really love science.

During my PhD I have worked with a wonderful team and I particularly want to thank Ian Smail, Mark Swinbank, Alastair Edge, John Stott, Jim Mullaney, Dave Alexander and James Simpson for their guidance, knowledge and encouragement. Mark, in particular has borne the brunt of my questioning (and occasional ranting!) and has given up a lot of his time for me, which I am truly grateful for.

I have been very lucky to share an office with some great characters these past years, namely Stephen, Rachael, Helen and Tim, but I particularly want to mention Chris Harrison, whose careful approach to science has been inspiring and whose friendship I have truly valued. I was also very privileged to live with the most lovely housemates, Anna Marchant and Tom Billam, during part of my PhD, who were a joy to share a home with and who have been great friends to me ever since.

As part of my time at Durham I worked as an Ogden Scientist in Schools at Bishop Barrington School. There I met some gifted and enthusiastic teachers and made some very good friends, thinking especially of Sarah, Paul and Susan. I am very grateful to the Ogden Trust for funding me to do this and to Pete Edwards, Lorraine Coghill, Linda Campbell and Paula Martin for giving me the opportunity,

Dedicated to

My Dad, Ethan, who first encouraged me to look skywards

and my Mum, Ruth, who kept my feet on the ground

"test everything; hold fast to what is good" 1 Thessalonians 5:21

Chapter 1

Introduction

1.1 Overview

The relatively recent advent of far-infrared and submillimetre (sub-mm) surveys has revealed a huge population of galaxies which were previously hidden due to their heavy dust-obscuration. Such observations have led to the significant conclusion that dusty star-forming galaxies have contributed approximately half the total energy density of the Universe throughout cosmic history. This thesis investigates the properties and evolution of some of the most massive, dusty, rapidly star-forming galaxies in the Universe, with a particular focus on submillimetre galaxies (SMGs), the best-studied population of dusty star-forming galaxies and potentially the progenitors of local massive elliptical galaxies. Three main questions are investigated:

- In what epoch were SMGs most common?

- How do SMGs form stars so rapidly?

- What limits the star formation in local elliptical galaxies?

The properties of the overall SMG population are discussed, followed by detailed observations of the gravitationally lensed SMG, SMM J2135, 'The Cosmic Eyelash', providing a unique insight into the conditions within the interstellar medium of an SMG. Finally, the dramatic fall in the star formation rate of SMGs in the last $\sim$10

billion years is explored, discussing the processes which prevent further formation of stars in local passive elliptical galaxies.

This chapter provides a broad overview of galaxy formation and evolution with a focus on the general properties of SMGs, molecular emission from galaxies and the impact of active galactic nuclei (AGN) on their environment. Detailed introductory material relevant to each section of work can be found at the start of each science chapter.

1.2   Island universes

It is difficult to imagine a time when not only did the general populace believe that the Earth was flat but also that it was at the centre of the Universe. Aristotle helped to establish the view that the Earth was spherical in 330 BC but it would take a further 1900 years before the Copernican revolution was instigated and finally the heliocentric model of the Universe began to be established (Copernicus 1543). The invention of the telescope in the 1600s opened a new window on the Universe but also triggered many disputes as to the nature of the various 'nebulae' that could now be observed. Indeed, less than a century ago a battle was still raging between Haber Curtis and Harlow Shapley concerning whether 'spiral nebulae' (first observed by William Parsons, the third Earl of Rosse in 1845) were simply gas clouds within the Milky Way or in fact galaxies in their own right. The idea of other galaxies had first been suggested by Thomas Wright of Durham, however, the phrase 'Island Universes' was first coined by Immanuel Kant in 1755 in his philosophical speculations on the existence of other galaxies. It was not until Hubble observed Cepheid variable stars in the Andromeda galaxy and utilised the strong correlation between their period and luminosity (discovered in 1912 by Henrietta Swan Leavitt) to measure the distance to Andromeda (Hubble, 1929), that the debate began to be resolved. Hubble proved that the distance of the Andromeda galaxy was even greater than Shapley's proposed extent of our Milky Way galaxy- believed to be the extent of the whole Universe. Shapley did not realise that with his argument he was to
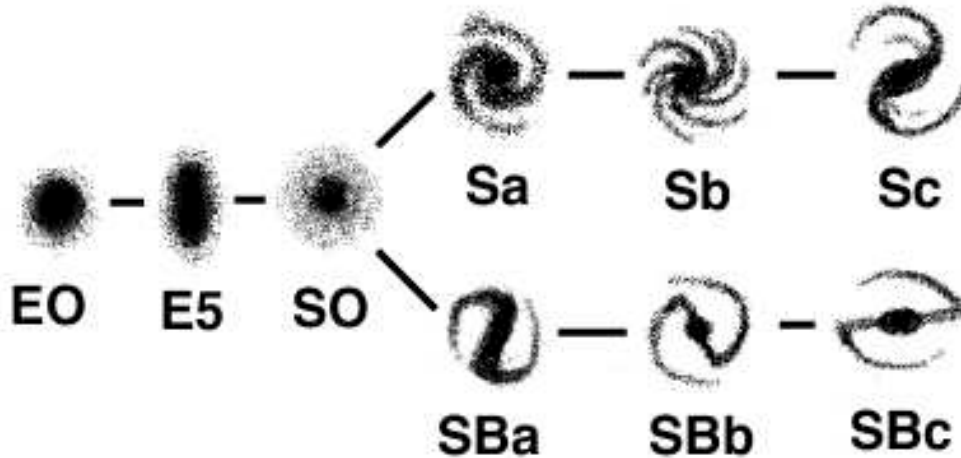
Figure 1.1: The Hubble 'tuning fork' diagram representing the galaxy morphological classification scheme developed by Edwin Hubble in 1926.

underestimate the size of the known Universe by ~300,000 times. The discovery that Andromeda was a galaxy in its own right radically changed our view of the Universe which we now know to contain over 100 billion galaxies, each containing over 100 billion stars.

By 1926 Hubble had established a classification scheme for galaxies which is still used today. The 'Hubble tuning fork' diagram (see Fig. 1.1) is used to visually classify galaxies into three main categories of spirals, ellipticals and irregulars. It was also initially incorrectly believed to describe an evolutionary sequence such that galaxies transitioned from ellipticals (so-called 'early-type' galaxies) through to spirals ('late-type' galaxies). This scheme is very useful for classifying local galaxies, however, if we wish to observe galaxies at the epoch in which they formed most of their stars, the Hubble sequence was not yet in place and galaxies were very different to those we see locally.

Vast improvements in technology have revolutionised Astronomy in the last century but fundamental questions still remain unanswered, in particular with regard to the formation and evolution of galaxies. In this thesis I investigate galaxies at the peak of cosmic star formation history and attempt to understand the conditions and mechanisms driving their rapid star formation, their evolution into passive galaxies today and the processes preventing stars from forming in these passive galaxies.

1.3 The evolution of star formation

The term 'galaxy' covers a wide range of masses, morphologies and luminosities, though most typically galaxies are a gravitationally bound system of $\sim 10^5$ to 10^{13} stars and interstellar medium (ISM) of dust and gas, embedded in a massive halo of dark matter. Although the first galaxies are thought to have formed at $z \gtrsim 10$ (e.g. Greif et al. 2008), just $\sim 0.5\,\mathrm{Gyr}$ after the Big Bang (13.8 billion years ago), the most active epoch of galaxy formation was between $1 < z < 2$. It is therefore fascinating to study the progenitors of the spiral and elliptical galaxies we see today at the time that they were forming most of their stars.

The average star formation rate density of the Universe peaked about 3.5 Gyr after the Big Bang ($z \sim 1.9$; Madau & Dickinson 2014) and has been rapidly declining towards the present day. Until relatively recently, results from optical and ultraviolet (UV) surveys had implied that the peak of star formation in the Universe occurred at $z \sim 1$ (Lilly et al. 1996; Madau et al. 1996). However, since the recent developments in infrared and sub-mm Astronomy, it has been discovered that more than half of the total energy production from star formation or AGN over the history of the Universe came from obscured energy sources (see Fig. 1.2, Lagache et al. 2005; Blain et al. 2002; Casey et al. 2014). Since this radiation comes predominantly from thermal emission from dust, UV/optical surveys miss the population. Fig. 1.3 gives an example of sub-mm observations revealing the UV/optical obscured emission within a local star-forming galaxy. If this infrared and sub-mm energy production is mostly from star formation, then this implies that half of all stars were born in highly obscured systems. Thus, in order to understand the Universe at the peak of its star-formation history we must use mid-infrared, far-infrared and sub-mm surveys to reveal it. Based on these longer wavelength observations, the peak of star formation in the Universe was found to occur at $z \sim 1.9$ (demonstrated in Fig. 1.4; see Madau & Dickinson 2014 for a review), nearly 2.5 Gyr more recent than originally determined from UV and optical surveys alone.

Chapters 2, 3 and 4 of this thesis focus on SMGs, an important population
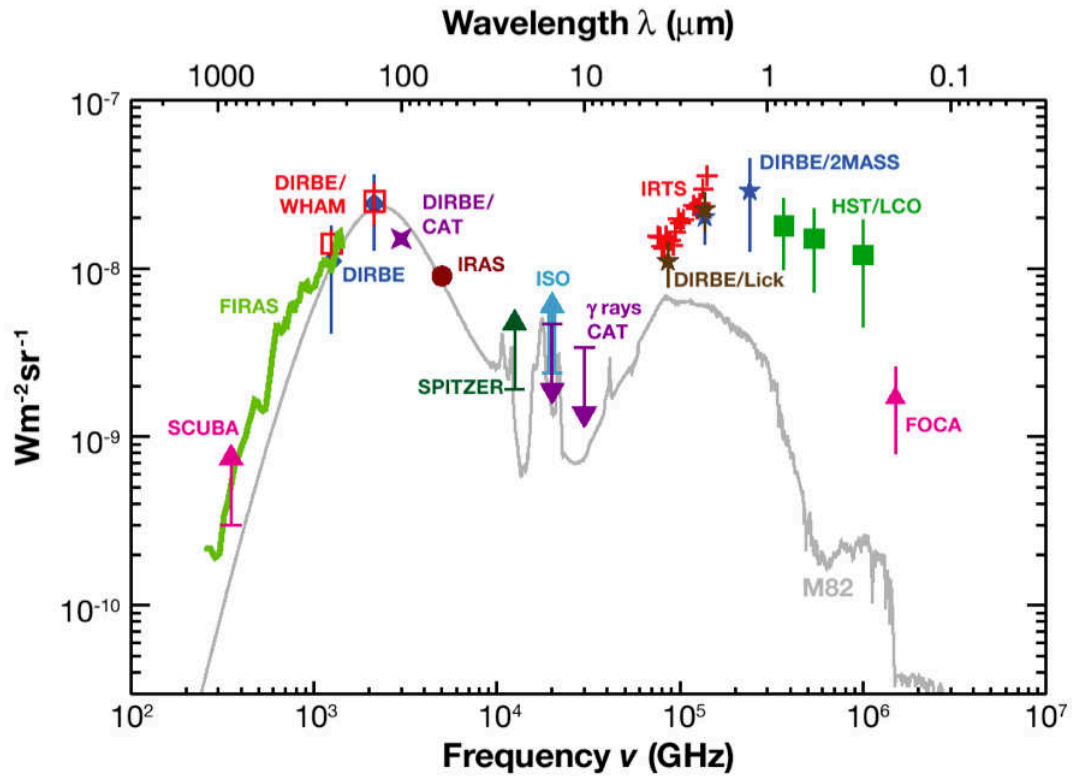
Figure 1.2: The extragalactic background from UV to millimetre wavelengths. The SED for the local starburst galaxy M 82 is shown in grey, normalised to the peak of the cosmic infrared background at 140μm. This demonstrates that the power in the infrared region is comparable to that in the optical region, thus much UV emission from stars is obscured by dust which scatters or absorbs the light and re-emits it at infrared wavelengths. This figure is taken from Lagache et al. (2005) in which the references for each data point are given.

Figure 1.3: This composite image of the Antennae galaxies, a starburst galaxy triggered by a merger of NGC 4038 and 4039, comprises a *Hubble Space Telescope* (*HST*) image with an ALMA image overlaid. The ALMA image has been created from combined images observed in ALMA bands 3 and 7 (tracing carbon monoxide emission) and was taken with only 12 antennas as ALMA test observations. The young massive stars are shown in blue in the *HST* image, whereas ALMA shows the dense cold regions (in red and yellow) of gas where new stars are forming, which are not visible in the optical image. Credit: ALMA (ESO/NAOJ/NRAO). Visible light image: the NASA/ESA *HST*.
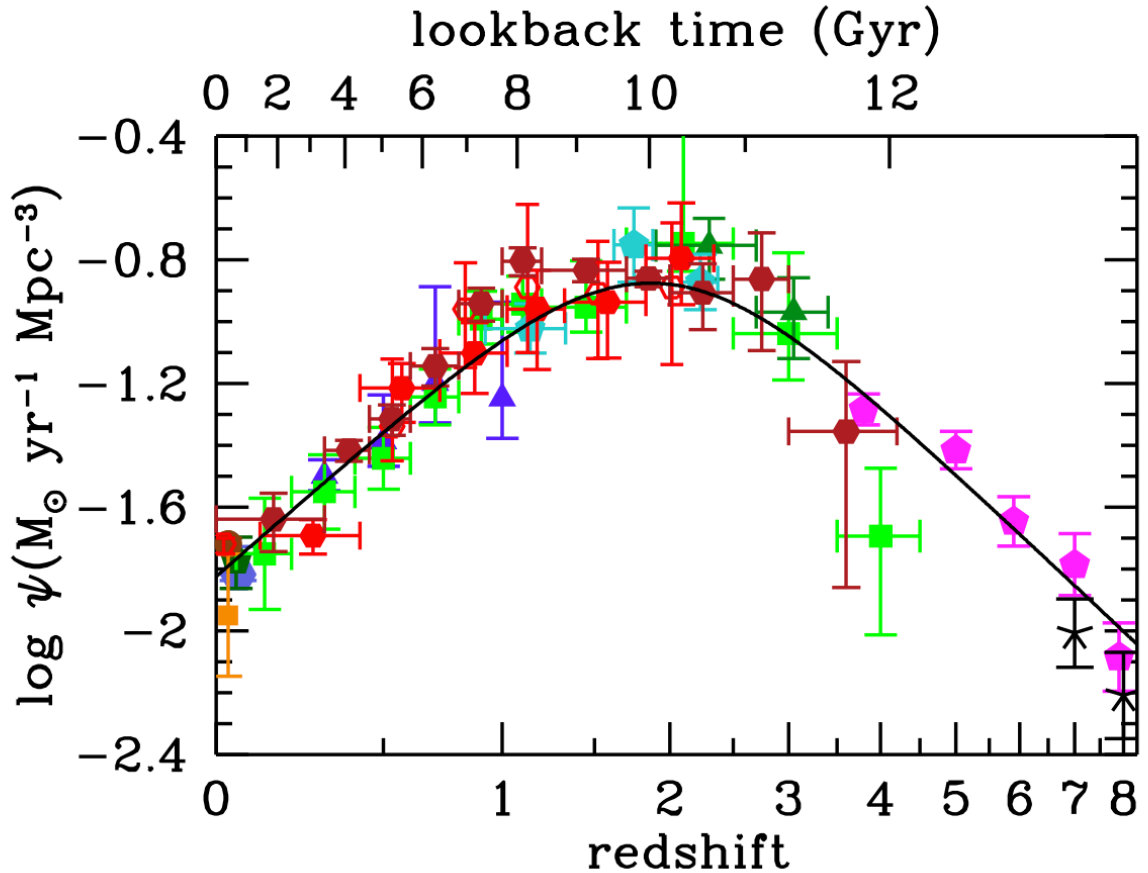
Figure 1.4: This shows the evolution in the star formation rate density of the Universe produced from a combination of UV/optical and infrared observations in state-of-the-art surveys. This clearly demonstrates the peak in cosmic star formation density at $z \sim 1.9$ when the Universe was $\sim 3.5\,\text{Gyr}$ old. This figure is taken from Madau & Dickinson (2014). The UV and infrared luminosities are taken from various sources (see Madau & Dickinson 2014). The conversion factors to convert UV and far-infrared luminosities into instantaneous star formation rates are $\kappa_{\text{FUV}} = 1.15 \times 10^{-28}$ and $\kappa_{\text{FIR}} = 4.5 \times 10^{-44}$ respectively (where far-infrared luminosities are defined over 8–1000μm) for a Salpeter IMF. These conversion factors are dependent on the IMF, metallicity and assumed star formation history. For the far-infrared SFR, the infrared is assumed to be exclusively due to recent star formation. The solid curve shows the best-fit star formation rate density function fit to the data.

of galaxies contributing strongly at infrared and sub-mm wavelengths, in particular around the peak of cosmic star formation history. Here we provide basic background on their discovery and typical properties.

1.4 Submillimetre galaxies

1.4.1 Discovery and surveys

SMGs are a population of distant, rapidly star-forming, dust-obscured galaxies which previous spectroscopic and photometric redshifts surveys have concluded to be most prevalent around $10\,\mathrm{Gyr}$ ago; $z \sim 2.3$ (Chapman et al. 2005; Simpson et al. 2014). Due to heavy dust obscuration in these sources, they emit predominantly in the mid-to-far-infrared and their important role in the evolution of galaxies was therefore only realised with the relatively recent onset of surveys at these higher wavelengths. In 1983, the Infrared Astronomical Satellite (IRAS) All Sky Survey mapped 96% of the sky at mid-to-far infrared wavelengths and catalogued $\sim$20,000 galaxies, most of which had never previously been detected (Neugebauer et al. 1984; Soifer & Neugebauer 1991), providing the first census of the infrared emission from low-redshift galaxies. In 1996, the cosmic infrared background (CIB) was discovered in data from the Far Infrared Absolute Spectrophotometer (FIRAS) on the *Cosmic Background Explorer satellite* (*COBE*) and was later constrained using the Diffuse Infrared Background Experiment (DIRBE) (see e.g. Hauser & Dwek 2001). This discovery revealed that about half of the energy from extragalactic sources is in the CIB, i.e. the power in the infrared part of the cosmic background is comparable to that in the optical (see Fig. 1.2). It also revealed that in higher-redshift galaxies the contribution from infrared emission is more important than in local galaxies, for which their typical infrared output is only a third of the optical output. After this discovery, it then became a priority to resolve and classify the discrete sources contributing to the CIB, to understand how galaxies evolve.

Sub-mm Astronomy has been a relatively recent development, mainly due to

the difficulty of the observations. Sub-mm wavelengths are heavily absorbed by atmospheric water vapour, therefore observations must be carried out either in space or at the optimum high and dry ground-based sites, in particular wavelength windows. Furthermore, it was only recently that sufficiently sensitive sub-mm detectors were developed. The first extragalactic sub-mm and millimetre (mm) surveys to begin to describe this population were carried out with the Submillimetre Common-User Bolometer Array (SCUBA- operating at 450μm and 850μm) on the James Clerk Maxwell Telescope (JCMT), and the Max-Planck Millimetre Bolometer Array (MAMBO- operating at 1.2 mm) on the Institut de Radio Millimétrique (IRAM) 30-m telescope. The main natural atmospheric windows in which the transmission of sub-mm wavelengths improves are at 350μm, 450μm, 770μm and 850μm, with 850μm being the clearest sub-mm atmospheric window. SCUBA and its successor SCUBA-2 operate at 450μm and 850μm in order to take advantage of these atmospheric windows. Similarly the Large APEX Bolometer Camera (LABOCA) on the Atacama Pathfinder Experiment (APEX) and the Atacama Large Millimeter Array (ALMA) in band 7, observe at 850μm.

Shortly after the commissioning of SCUBA, Smail et al. (1997) discovered the SMG population whilst mapping two fields within two massive, concentrated gravitationally lensing clusters at 450 and 850-μm. A similar discovery was then made with SCUBA targeting blank fields in the Hubble Deep Field-North (Hughes et al. 1998) and the Lockman Hole and SSA13 (Barger et al. 1998), identifying a large number of luminous sources at 850μm. The originally detected samples of ~ 200 dusty galaxies has expanded in recent years to detections of more than a million far-infrared and sub-mm bright galaxies. One of the main contributors has been the *Herschel Space Observatory* (*HSO*) which in four years ($2009-2013$) mapped $> 1300\,\mathrm{deg}^2$ of the sky from $100-500\mu$m, providing a huge sample for statistical analysis of dusty star-forming galaxies (HerMES- Oliver et al. 2012; *Herschel*-ATLAS Survey- Eales et al. 2010; PEP- Lutz et al. 2011; GOODS-*Herschel*- Elbaz et al. 2011). This is highlighted in Fig. 1.5 showing the comparison between the APEX 870μm map of the Extended *Chandra* Deep Field South (ECDFS) and the *Herschel* follow-up of
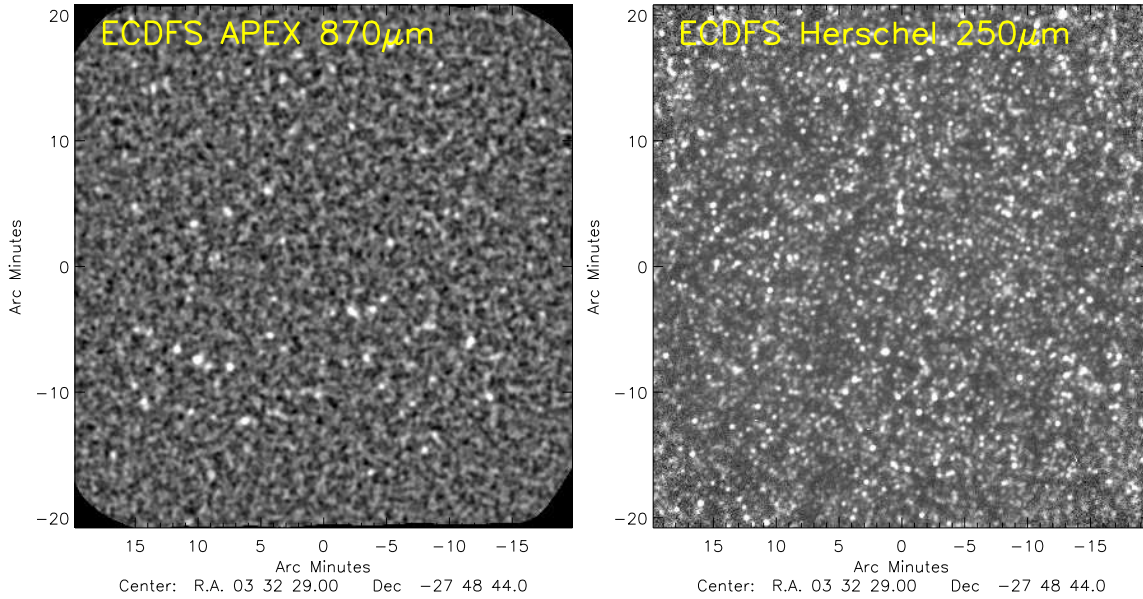
Figure 1.5: This comparison of the APEX 870μm and HerMES *Herschel* 250μm maps of the ECDFS (Weiß et al. 2009; Oliver et al. 2012) demonstrates the dramatic increase in the number of detected dusty galaxies even in the last seven years. Both maps are scaled to a range of $-3 - 5\sigma$. The APEX map combines 310 hours of observing time with LABOCA on the APEX telescope reaching a sensitivity of $\sim 1.2\,\mathrm{mJy\,beam}^{-1}$ and detecting a total of 126 SMGs. This was one of only a few fields mapped at sub-mm wavelengths, detecting hundreds of SMGs. Whereas, the *Herschel* map is one small area of the ~ 380 deg^2 HerMES survey (Oliver et al., 2012) probed with *Herschel* Spectral and Photometric Imaging Receiver (SPIRE) to a typical sensitivity of $\sim 5 - 10\,\mathrm{mJy}$, detecting in total hundreds of thousands of galaxies.

the same 0.5×0.5 deg region at 250μm, demonstrating the huge increase the number of detected sources.

The most recent development in the field of sub-mm Astronomy has been with ALMA, a vast interferometer, comprising 54 dishes of $12\,\mathrm{m}$ diameter and 12 dishes of $7\,\mathrm{m}$ diameter with maximum baselines of $\sim 16\,\mathrm{km}$. It operates at $84 - 950\,\mathrm{GHz}$ and is capable of resolving to scales of $0.006''$ in its most extended configuration. In full operations ALMA will efficiently detect large numbers of SMGs at high precision and in a fraction of the time required by previous surveys.

1.4.2 Dust properties and emission

The majority of the sub-mm emission being detected from SMGs originates from thermal dust emission, with the remaining $\sim 1\%$ arising from line emission from atomic and molecular transitions in the ISM (e.g. rotational transitions of carbon monoxide, discussed in detail in Section 1.6). The thermal dust emission peaks at rest-frame $60 - 200 \mu$m (corresponding to dust temperatures of $\sim 50 - 15$ K) but since most SMGs are found at high-redshift ($z \sim 2$) this emission is redshifted to sub-mm wavelengths. The dust in SMGs contributes a relatively small fraction of the total mass (median $M_{dust} \sim 0.0052 \, M_{gas}$ in the SINGS galaxy sample; Draine et al. 2007) but it has a significant effect on the observed emission and the chemistry in these systems, constituting $\sim 99\%$ of the energy released by galaxies in the sub-mm and far-IR.

Interstellar dust consists mainly of: (1) polyaromatic hydrocarbons (PAHs)- the smallest of the carbonaceous dust grains emitting predominantly in features between $3 - 17 \mu$m; (2) silicates produced largely as a result of supernovae; (3) graphites- released as ejecta from stars and natural condensation in cool stellar atmospheres. The dust particles range in size typically from $0.001 - 1 \mu$m and this grain size has a profound effect on the light passing through the cloud, since the dust scatters or absorbs most effectively at a wavelength comparable to the size of the grain. Dust grains are critical in star formation. They act as catalysts for chemical reactions, in particular in providing the surface for H_2 formation, where two hydrogen atoms are adsorbed onto the surface of the grain and tunnel across the grain to form H_2 molecules which are then released, providing the essential 'fuel supply' for star formation.

Since dust most effectively absorbs light of a similar wavelength to the dust grain size, dust strongly absorbs and scatters rest-frame UV and visible light which is predominantly emitted by young, hot, blue massive stars and accretion disks surrounding active galactic nuclei (AGN). The star light is absorbed by the dust

and thermally re-radiated at infrared and sub-mm wavelengths[1]. Thus, in strongly star-forming dusty systems, such as SMGs, the emission can be described as a modified blackbody spectrum. At wavelengths redward of the peak flux the spectral energy distribution (SED) is described by $S_\nu \propto \nu^{2+\beta}$ (the Rayleigh-Jeans tail of the dust blackbody spectrum), where β is the dust emissivity spectral index. The value of β depends on the chemical composition of the dust, the temperature and the size of the dust grains and is still in debate for SMGs. In extragalactic sources it is typically assumed to be $1.5 < \beta < 2$. Indeed, Magnelli et al. (2012) and Dunne & Eales (2001) independently determine a value of $\beta = 2$ from a sample of 61 *Herschel*-detected SMGs and a sample of 104 SCUBA galaxies selected from the IRAS Bright Galaxy Sample respectively.

As a galaxy of fixed luminosity is shifted to higher redshift two main effects must be considered. The observed flux density decreases/fades $\propto (1+z)^4$ since $S_\nu = L_\nu/4\pi D_{\rm L}^2$ and $D_{\rm L} \propto (1+z)^2$. The observed frequency behaves as $\nu_{obs} = \nu_{rest} \times (1+z)$. Furthermore, an SED-dependent K-correction must be applied when converting from observed to rest-frame broad-band photometric measurements. However, in the Rayleigh Jeans tail of the SED where $S_\nu \propto \nu^{2+\beta}$, the flux density behaves as $S_\nu \propto \nu_{rest}^{2+\beta}/4\pi D_{\rm L}^2 \propto \nu_{obs}^{2+\beta}(1+z)^{2+\beta}/(1+z)^4 \propto (1+z)^{\beta-2}$. Thus, for a value of $\beta = 2$ (discussed previously), galaxies get brighter as they are redshifted to greater distance, described as a negative K-correction. This is one of the huge advantages of observing in the sub-mm/mm regime. Assuming intrinsically similar SEDs, the negative K-correction for wavelengths redward of 250μm implies that distant galaxies, with similar bolometric luminosities, produce similar flux densities at all redshifts up to $z \sim 8$ (for 850μm observations). This is highly advantageous for providing a uniform SMG selection function with redshift with which to develop an understanding of the characteristics of the SMG population. Fig. 1.6 demonstrates the K-correction effect at different wavelengths, as a function of redshift, for a typical distant sub-mm galaxy SED.

---

[1]Re-processed emission from dust illuminated by AGN, as opposed to starlight, is thought to peak at shorter wavelengths ($\sim 40\mu$m) corresponding to higher temperatures (see **?**.
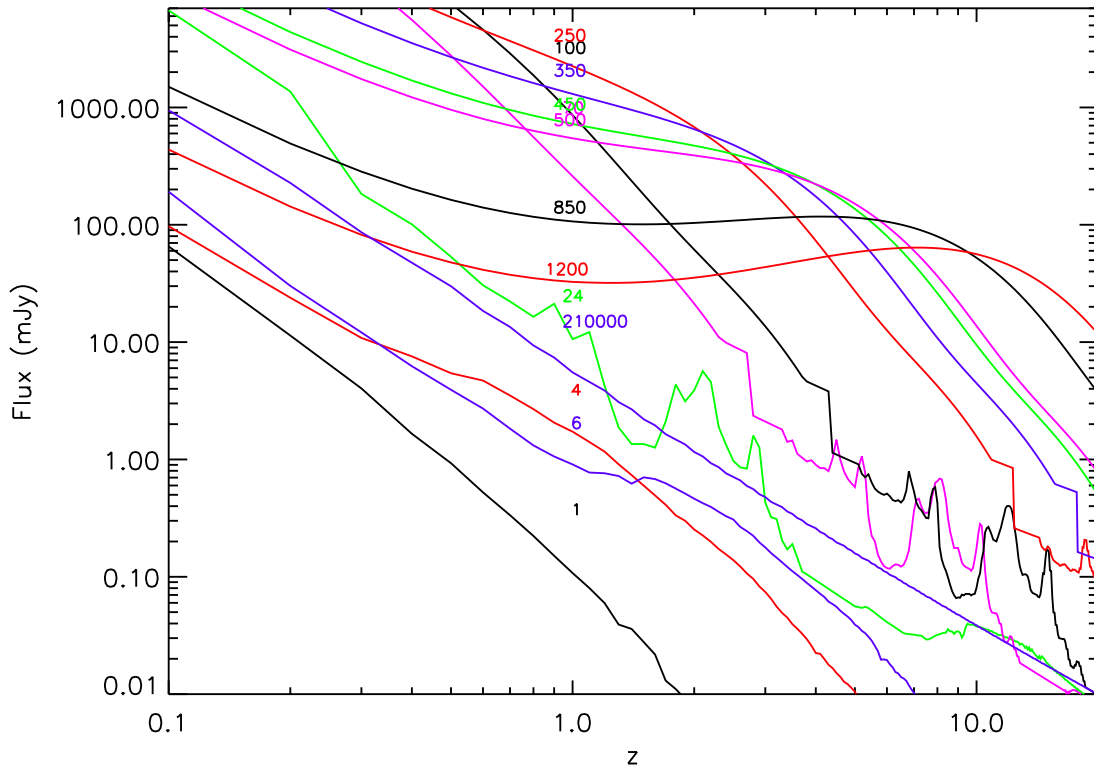
Figure 1.6: The flux density predicted at different wavelengths (in μ m; shown on each line) for the SED of the 'Cosmic Eyelash' (SMM J2135; a representative SMG discussed in Chapters 3 and 4 of this thesis), as a function of redshift. The K-correction at 850μm is such that the flux density is nearly independent of redshift from $z \sim 1 - 10$ allowing SMGs to be uniformly selected over a broad redshift range, making them a fascinating and useful sample to study. This figure is produced from the SED for SMM J2135 presented in Swinbank et al. (2010).

1.4.3 SMG properties

The typical far-infrared luminosity of SMGs exceeds $L_{8-1000\mu m} = 10^{12}\,\mathrm{L_\odot}$, thus they are thought to be high-redshift analogs to local Ultra Luminous Infrared Galaxies (ULIRGs) which make up $\sim 0.1\%$ of galaxies in the local Universe. However, the space density of $L_{8-1000\mu m} > 10^{12}\,\mathrm{L_\odot}$ galaxies is $\sim$1000 times greater at $z \sim 2$ than locally (Daddi et al. 2005, Sanders et al. 2003), thus their contribution to cosmic star formation evolves strongly with redshift. If this powerful far-infrared energy production is mostly from star formation, then this implies that half of all stars were born in highly obscured systems (see Fig. 1.2). More recent galaxy surveys have confirmed this with e.g. Swinbank et al. (2014) determining that over the redshift range $z \sim 1-4$, SMGs contribute over 20% of the total star formation budget (for $S_{870\mu m} \geq 1$ mJy). Local ULIRGs generally appear to be major mergers of gas-rich galaxies with a dense core of cold gas from which the far-infrared luminosity originates (e.g. Tacconi et al. 2008). These gas-rich mergers drive intense star formation such that for a star formation rate of $\sim 1000\,\mathrm{M_\odot\,yr^{-1}}$ (typical of SMGs), in 100 Myr a stellar mass of $10^{11}\,\mathrm{M_\odot}$ can be formed, which is consistent with the mass of a local massive elliptical galaxy (Lagache et al. 2005). Indeed, Eisenstein et al. (2003), for example, demonstrate that the uniformity of the stellar populations within massive elliptical galaxies demonstrates a starburst origin. This is corroborated by studies of the most massive elliptical galaxies which have shown that most of their stars must have indeed formed at $z \sim 2$ (e.g. Whitaker et al. 2013), when SMGs (high-redshift ULIRGs) were very prevalent. Thus it is thought that SMGs are likely candidates for the progenitors of local massive elliptical galaxies (Simpson et al. 2014; Toft et al. 2014).

Much controversy still remains regarding the triggering mechanisms for the extreme star formation observed within SMGs. Whilst the star-formation in most local ULIRGs appears to be driven by gas-rich mergers (e.g., Sanders & Mirabel 1996), numerical models have claimed that there are insufficient major mergers at high redshift to account for the observed SMG population and that secular bursts

in gas-rich disks play an important role (i.e. Davé et al. 2010; Hayward et al. 2011; Hayward et al. 2012). In contrast, semi-analytic models from Baugh et al. (2005) require 95% of SMGs to be triggered by merging systems, with SMGs corresponding to the most extreme starbursts. To distinguish between these models, high-resolution observations of the distribution and kinematics of the gas and star formation are required, to search for interactions, tidal features and assess the relative prevalence of disks and mergers. Such observations cannot be carried out without accurate spectroscopic redshifts to tune follow-up instruments to map SMGs in particular emission lines (see Chapter 6). To begin to understand and interpret every aspect of the SMG population, it is critical to have good constraints on the redshifts (see Chapter 2).

1.4.4 SMG redshifts

Determining redshifts for the SMG population is essential for understanding almost all properties of the sources. Knowing the redshift in combination with the observed brightness of the source allows the intrinsic bolometric luminosity and thus star formation rates to be calculated. It is very important to be able to constrain the far-infrared luminosity in SMGs, in order to understand their contribution to the star formation rate density and how this evolves with redshift. Spectral energy distribution (SED) model fitting can be used to determine the properties of SMGs including, ages, stellar masses, reddening and star formation histories. However, there are significant degeneracies between these parameters. Precise redshifts can break some of the degeneracies in SED fitting, in particular between redshift and reddening (high redshift, low extinction galaxies can have very similar SED fits to low redshift, high extinction galaxies). With precise redshifts we can constrain the stellar masses of SMGs which are still highly uncertain in the literature (see i.e. Michałowski et al. 2010 and Hainline et al. 2011). Furthermore, precise redshifts can be used to determine the environments of galaxies and search for 'associations' between galaxies. Such measurements can be very important for testing if SMGs

reside in sufficiently dense environments to evolve into massive elliptical galaxies to-day. Determining dynamical masses and gas fractions also requires well-constrained redshifts, since for follow-up observations, particularly at mm wavelengths, the band pass of many receivers is typically only $\sim 2000\,\mathrm{km\,s^{-1}}$ so requires precise tuning and precise redshifts.

Redshifts can be determined both photometrically and spectroscopically but spectroscopic redshifts are significantly more reliable and accurate. Despite the many advantages of spectroscopic redshifts, given their low space densities and UV/optical faintness, acquiring them for large samples of SMGs is a huge effort requiring many nights on 10m class telescopes for only about 100 redshifts. As such, much effort now goes into photometric redshifts, which are generally less reliable but easier to determine for large numbers of sources.

Photometric redshift distributions for SMGs have been derived in various fields including the SCUBA Half Degree Extragalactic Survey (SHADES) by Aretxaga et al. (2007) (with radio, mm and far-infrared colours) and Clements et al. (2008) (with the addition of *Spitzer* Infrared Array Camera data), finding peak redshifts of $z \sim 2.4$ and $z \sim 1.5 - 2$ respectively. Inhomogeneity in multiwavelength data in this field means that the same photometric redshift technique cannot be used for all sources and the survey area is too small to fully characterise the bright sub-mm population.

The most complete photometric redshift survey of 850μm-selected galaxies has been carried out by Wardlow et al. (2011), later improved by Simpson et al. (2014), in the public 870μm LABOCA survey on the APEX telescope of the ECDFS; the LABOCA ECDFS Submillimeter Survey (LESS; Weiß et al. 2009; see Fig. 1.5). LESS is the largest, most homogenous and sensitive blind 870μm survey to date. The ECDFS has the advantage of excellent multiwavelength coverage which is essential for constraining photometric redshifts. Wardlow et al. (2011) derive photometric redshifts for 72 out of the 126 LESS sources, using 17-band optical to mid-infrared photometry of 78 robust radio, 24μm and *Spitzer* Infrared Array Camera (IRAC) counterparts. They determine a median photometric redshift of $z = 2.2 \pm 0.1$.

Following ALMA observations of the LESS sources (ALESS) many of the original LESS sub-mm sources were resolved into multiple SMGs. Simpson et al. (2014) re-analyse the photometry in $4-19$ bands and derive photometric redshifts for 77 SMGs deriving a median photometric redshift of $z = 2.3\pm0.1$. Although such work provides an excellent statistical study of the properties of SMGs, certain properties cannot be well-constrained without very accurate redshifts which require spectroscopy and Chapter 2 addresses this problem, measuring spectroscopic redshifts for a large number of the ALMA-identified SMGs in the LESS survey.

Measuring precise redshifts is fraught with difficulties. There have been many limitations and uncertainties in the redshift surveys of SMGs to date. Spectroscopic redshift distributions have been drawn from small numbers of inhomogeneously selected sources, from various different small surveys which are difficult to compare. Furthermore, rest-frame UV and optical, where many of the strong emission lines lie, are severely affected by extinction. Since the positional accuracy of most sub-mm sources is poor (i.e. beam of SCUBA is $\sim15''$), this hampers the identification of the correct multi-wavelength counterparts for spectroscopic follow-up.

Most spectroscopic surveys to date have relied upon radio counterpart identification since there is a strong correlation between far-infrared and radio flux densities both locally (e.g. de Jong et al. 1985; Helou et al. 1985; Condon et al. 1991; Condon 1992; Bell 2003; Murphy et al. 2008) and at high redshift (e.g. Ivison et al., 2010a,b; Magnelli et al., 2010; Casey et al., 2012), and radio observations provide significantly higher resolution than sub-mm, with beam sizes of $\sim1.5''$ (Chapman et al., 2005). This relation was first observed as a correlation between $1.4\,\mathrm{GHz}$ and $10\mu\mathrm{m}$ emission from Seyfert galaxies by van der Kruit (1971). Once it was understood that the infrared emission was thermally driven, the correlation was then understood to be due to fact that both infrared and radio emission are related to short-lived massive stars. A large proportion of the infrared emission from galaxies is due to the thermal re-radiation of UV from dust-enshrouded massive young stars. Such massive stars are short-lived and result in supernovae explosions, generating shocks which accelerate relativistic electrons, resulting in synchrotron emission which emits

strongly at $1.4\,\text{GHz}$. Some of the radio emission also results from free-free emission in HII regions (free electrons scattering off ions). Ivison et al. (2010a) study the far-infrared-radio correlation in Balloon-borne Large Aperture Submillimetre Telescope (BLAST) 250μm-selected galaxies and define the relation to be:

$$q_{\text{IR}} = \log\left(\frac{1.01 \times 10^{18} L_{\text{IR}}}{4\pi D_{\text{L}}[\text{L}_\odot]}\right) - \log\left(\frac{10^{-32} S_{1.4\text{GHz}}}{(1+z)^{\alpha-1}[\mu\text{Jy}])}\right) \qquad (1.4.1)$$

where L_{IR} is the infrared luminosity integrated over $8-1000\mu$m, D_{L} is the luminosity distance, $S_{1.4\text{GHz}}$ is the observed $1.4\,\text{GHz}$ flux density, α is the radio spectral index which Ivison et al. (2010a) demonstrate to be relatively constant over $z = 1-3$. Due to this relation, radio observations can be used to identify SMGs and more accurately define their position.

From the first extragalactic surveys only a few SMGs had reliable redshifts and well-constrained multi-wavelength properties (i.e. Barger et al. 1999). However, Chapman et al. (2005) investigated a sample of 150 SMGs detected with SCUBA on the JCMT in seven well-studied extragalactic survey fields. They selected only those 104 sources with reliable radio counterparts, in order to utilise the radio-far-infrared correlation and determine precise positions for the sub-mm emission and therefore to identify counterparts for spectroscopic follow-up. They measured a median redshift for SMGs of $z \sim 2.2$. However, since radio wavelengths do not benefit from the negative K-correction found at sub-mm wavelengths, SMGs at $z > 3$ are likely to be missed due to radio flux limits and similarly, not all SMGs at $z < 3$ are radio-detected. Therefore, ideally sub-mm surveys with accurate sub-mm positions and consequently unambiguous counterparts are required in order to provide an unbiased spectroscopic survey of SMGs. This requires interferometric observations at sub-mm wavelengths.

ALMA is now facilitating very high-resolution sub-mm surveys. At 870μm, it is capable of resolving down to $< 1''$ scales, thus directly providing accurate positions for the source of the sub-mm emission, leading to unambiguous multiwavelength counterpart identification. ALMA Cycle 0 observations began late in 2011 and

ALMA has already yielded incredible results, some of which are discussed in Chapter 2, where we carry out a spectroscopic follow-up survey of the ALMA-identified SMGs in the LESS field (one of the first fields to be followed-up with ALMA continuum observations; Karim et al. 2013; Hodge et al. 2013).

1.5 Spectral diagnostics of the ISM

1.5.1 UV, optical and near-infrared spectra

Most spectroscopic redshifts are measured from emission or absorption lines in rest-frame UV and optical spectra, with Hα frequently being targeted with near-infrared spectrographs. Spectroscopy is not only an important means of determining precise redshifts but optical and UV spectra are essential probes of the properties of galaxies, such as the metallicities, excitation conditions, dynamics etc. (e.g. Swinbank et al. 2004). Through spectral analysis one can: search for evidence of winds or AGN activity through broad emission lines; measure the abundances of molecules, atoms and ions; derive the temperature, density and chemical composition of a system.

Most spectral emission lines emerge from gas (particularly around newly formed stars) which is heated and re-radiates the energy at specific allowed wavelengths. Emission lines arise from bound-bound transitions within an atom or ion where an electron moves between two bound states (falls from an excited state) and a photon is emitted. In an ion, emission may occur through the recombination of the electron which then cascades down through a series of energy levels. The main mechanisms for exciting or ionising gas resulting in bound-bound emission lines are predominantly through collisional excitation or high-energy photons. De-excitation may occur collisionally or radiatively, where a radiative de-excitation is also termed a spontaneous transition. Absorption lines arise mainly in the atmospheres of stars and in the cold gas in the ISM. Photons are absorbed by an atom/ion and add to the internal energy of the atom by raising an electron to a higher state, whilst removing energy from the passing radiation.

Different spectral regions are dominated by different electromagnetic transitions. UV, optical and infrared spectra are dominated by electronic transitions of atoms, molecules and ions. Some of the brightest emission lines emerge from the various transitions associated with hydrogen. The Lyman series is the series of transitions and UV emission lines corresponding to an electron transitioning to the ground state ($n = 1$; 13.6eV) from a level of $n \geq 2$ (where n is the principal quantum number). As $n \to \infty$, the Lyman series absorption lines converge to a limiting wavelength of $\lambda = 911.75$Å (the Lyman limit) and the interval between the line centres approaches zero. Since the lines are of finite width, they therefore blend into a continuum before this limit is reached. The Lyman limit is equivalent to the energy required to ionise hydrogen. For the Lyman series typically only Lyman-α (Lyα; 1215Å) emission is observed strongly, since a photon with energy greater than 1215Å will tend to be absorbed by intervening neutral hydrogen between the emitting galaxy and the observer. The Balmer series (i.e. Hα, Hβ etc.) is the series of transitions where an electron transitions to the $n = 2$ (3.4eV) state from a level of $n \geq 3$. Balmer lines are prevalent in the H$_{\rm II}$ regions, which are emission nebulae containing newly formed hot, massive, photo-ionising stars, and are therefore a good tracer of the systemic redshifts of galaxies.

Emission lines can be permitted (such as Hα, Hβ), semi-forbidden (such as CIII]λ1909) or forbidden (such as [OII]$\lambda\lambda$3726, 3729, [NII]$\lambda\lambda$6548, 6583, [OIII]$\lambda\lambda$4959, 5007). Permitted lines are electric dipole transitions with a high probability of occurring, i.e. high spontaneous radiative transition rates. Forbidden lines (electric quadrupole, magnetic dipole, or magnetic quadrupole transitions), however, are generally only seen from diffuse gas and occur in atoms which have been excited into a metastable state. Spontaneous decay from a metastable state can take longer than a second to occur as compared to $\sim 10^{-8}$ s for a permitted transition. As such, in a dense medium the electron is likely to be collisionally de-excited before it has time to spontaneously decay. However, if the medium is sufficiently diffuse, the spontaneous decay from a metastable state is possible, accompanied by the emission of a photon. Semi-forbidden transitions (electric dipole) have a lifetime between that

of a permitted and forbidden line. Further detail on emission lines is discussed in Chapter 2 where the spectra of a large sample of SMGs are analysed.

1.5.2 Millimetre spectroscopy

Given that SMGs are typically rest-frame UV/optically faint, it is often difficult to determine spectroscopic redshifts for them at these wavelengths. A more direct method of determining redshifts is in the millimetric regime. Until recently, the bandwidths of detectors at these wavelengths were too narrow to be a useful means of determining redshifts, however, detectors such as the Wideband Express (WideX) correlator on the Institut de Radioastronomie Millimétrique (IRAM) Plateau de Bure Interferometer (PdBI) and the Eight MIxer Receiver (EMIR) receivers on IRAM 30m telescope have made this possible. However, determining millimetric redshifts for galaxies is very time consuming and is still not a feasible method for large samples of SMGs, until ALMA reaches full-science operations.

As discussed previously, as well as the thermal dust emission, the other main source of emission from galaxies at observed sub-mm wavelengths is line emission from atomic and molecular transitions in the ISM. This line emission can be a very useful diagnostic tool for the physical conditions and chemistry within the molecular clouds in which stars are forming, and to trace the kinematics of the molecular gas within high-redshift galaxies. The millimetric regime is dominated by molecular-rotational transitions and rotational-vibrational transitions such as transitions of the carbon monoxide molecule and its isotopologues, which are studied in detail in Chapters 3 and 4 of this thesis and described below.

1.6 The cold ISM

The properties of the ISM of galaxies play a critical role in the evolution of galaxies as it includes the raw material from which stars form. The main sources of heating of the atomic and molecular ISM are the stellar radiation field, cosmic rays and turbulence; as such the ISM exhibits a considerable range of properties, spanning

a wide range in density $\sim 10^{0-7}\,\mathrm{cm^{-3}}$ and temperature $\sim 10^{1-4}\,\mathrm{K}$. The thermodynamic state of the gas is dictated by the balance of this heating with cooling from atomic and molecular species (e.g. [CII], [CI], ^{12}CO and [OI]). This balance may dictate the Jeans mass (the minimum mass necessary for a gas cloud to spontaneously collapse) and initial mass function (IMF; the distribution of initial masses for a population of stars) and therefore the efficiency of star formation (Hocuk & Spaans, 2010). Understanding the balance of heating and cooling within the ISM is thus fundamental to understanding the initial conditions and the detailed physics of the star formation, which drives the formation and evolution of galaxies. Star formation itself takes place in giant molecular clouds (GMCs) where the gas is at its densest ($n(\mathrm{H_2}){>}10^4\,\mathrm{cm^{-3}}$; Gao & Solomon 2004; Bergin & Tafalla 2007) and the temperatures are typically low ($10-20\,\mathrm{K}$), making the denser, cooler ISM phases the more important to study when it comes to defining the star-formation process. An essential element of our understanding of distant galaxies comes therefore from observations of emission from interstellar molecular and atomic gas. In the following two sections we explain the importance of carbon monoxide as a means of tracing $\mathrm{H_2}$ gas using this emission both to determine the gas mass of galaxies and the excitation of the gas in star-forming regions. This forms the basis for the work in Chapters 3 and 4.

1.6.1 ^{12}CO as a tracer of $\mathbf{H_2}$

The most abundant molecule in GMCs is hydrogen ($\mathrm{H_2}$), however, it lacks a permanent dipole and therefore has no dipolar rotational transitions. Furthermore, very high temperatures are required to excite the quadrupolar rotational transitions ($T > 100\,\mathrm{K}$). This means that cold, star-forming $\mathrm{H_2}$ gas is almost impossible to directly observe in emission. The next most abundant molecule in GMCs is Carbon Monoxide ($^{12}\mathrm{C}^{16}\mathrm{O}$, hereafter ^{12}CO), which has very strong emission lines from pure rotational transitions at millimetre wavelengths. The lowest ^{12}CO rotational transitions ($J\,{=}\,1{\rightarrow}0$ and $2{\rightarrow}1$, hereafter $J_{\mathrm{up}} = 1$ and $J_{\mathrm{up}} = 2$) are those typically used

for tracing the bulk of the cold gas in galaxies (e.g. Young & Scoville 1991). The energy of this transition is low ($h\nu/k \approx 5.53\,\mathrm{K}$) and the critical density (the density at which the rate of spontaneous emission and collisional de-excitation balance) is also low ($n_{\mathrm{crit}} \sim 2200\,\mathrm{cm}^{-3}$). Furthermore, the high optical depth to photons capable of exciting ^{12}CO causes radiative trapping which lowers the density required for ^{12}CO excitation. The higher the transition of ^{12}CO, the higher the density and temperature required for excitation. Thus ^{12}CO($J_{\mathrm{up}} = 1$) is readily excited even in cold gas.

Since ^{12}CO readily forms in the conditions within molecular clouds, it is an excellent tracer of the bulk distribution of H_2 gas in galaxies and, with some assumptions, can be used to derive the mass of H_2 likely to be present in the ISM. In order to use ^{12}CO emission to measure the gas mass, an empirical conversion factor is used. This CO-H_2 factor is typically dubbed the 'X-factor', $\mathrm{X_{CO}}$ or α_{CO} (see i.e. Dickman et al. 1986). $\mathrm{X_{CO}}$ relates the column density of H_2 to the observed intensity of ^{12}CO: $\mathrm{N(H_2)} = \mathrm{X_{CO}} \mathrm{W}(^{12}\mathrm{CO}(J_{\mathrm{up}} = 1))$, where $\mathrm{N(H_2)}$ is in cm^{-2} and $\mathrm{W}(^{12}\mathrm{CO}(J_{\mathrm{up}} = 1))$ is in $\mathrm{K\,km\,s}^{-1}$. α_{CO}, which we refer to throughout this thesis, relates the ^{12}CO line luminosity to the total molecular gas mass (the mass of H_2 plus the contribution due to helium, where a factor of 1.36 is applied to the mass of an H_2 molecule) such that $\alpha_{\mathrm{CO}} = M_{H_2}/L'_{^{12}\mathrm{CO}(1-0)}\,\mathrm{M_\odot}\,(\mathrm{K\,km\,s}^{-1}\,\mathrm{pc}^2)^{-1}$ (see Section 4.6.4 for definitions of line luminosity). The $\mathrm{X_{CO}}$ and α_{CO} are related via:

$$\frac{\mathrm{X_{CO}}}{[\mathrm{cm}^{-2}(\mathrm{Kkms}^{-1})^{-1}]} \sim 4.65 \times 10^{19} \frac{\alpha_{\mathrm{CO}}}{[\mathrm{M_\odot}(\mathrm{Kkms}^{-1}\mathrm{pc}^2)^{-1}]} \tag{1.6.2}$$

There has been extensive investigation into determining the value of α_{CO} in different environments, as it is crucial in understanding star formation at different redshifts and under different conditions. This factor can vary significantly depending on the average physical and kinematical state of the cold molecular gas (i.e. UV photodissociation rate, gas density, column density, kinetic temperature, metallicity; see Bolatto et al. 2013 for a review). However, within the Milky Way and Local Group it has been found to be a relatively constant value of $\alpha_{\mathrm{CO}} = 3 - 6\,\mathrm{M_\odot}\,(\mathrm{K\,km\,s}^{-1}\,\mathrm{pc}^2)^{-1}$

(with the independent gas masses being determined from virial mass measurements or from an assumed dust-to-gas ratio). Strong deviation from this local trend is found in low metallicity systems for which α_{CO} is driven to higher values, and in regions of high gas surface density, where α_{CO} is driven to lower values. In literature, typically a bimodal CO-H_2 factor is assumed such that in local ULIRGs a value of $\alpha_{CO} = 0.8 \, M_\odot \, (K \, km \, s^{-1} \, pc^2)^{-1}$ is used (though with considerable uncertainty, i.e. Downes & Solomon 1998; Stark et al. 2008; Papadopoulos et al. 2012a), whereas in normal star-forming galaxies the value in the disk of the Milky Way of $\alpha_{CO} \sim 4.6 \, M_\odot \, (K \, km \, s^{-1} \, pc^2)^{-1}$ is assumed. At high-redshift the situation is considerably more uncertain, with estimates of α_{CO} varying between $\sim (0.4 - 2.3) \, M_\odot \, (K \, km \, s^{-1} \, pc^2)^{-1}$ in high-redshift star-forming galaxies (e.g. Tacconi et al. 2008, Ivison et al. 2011), with lower values $\alpha_{CO} \lesssim 0.5$ being favoured for SMGs. One of the main problems with determining α_{CO} at high-redshift is that often it is difficult to measure $^{12}CO(J_{up} = 1)$ and high-J_{up} transitions must be used. It is therefore necessary to assume a ratio between $J_{up>1}/J_{up=1}$, requiring knowledge of the excitation which is dependent on the density, temperature and optical depth within the ISM. If multiple ^{12}CO transitions are measured, a spectral line energy distribution (SLED) can be determined, which can be used to constrain the conditions within the ISM (discussed below and in Chapters 3 and 4).

1.6.2 Spectral line energy distributions

To date, the majority of the detections of ^{12}CO and atomic fine structure emission from high-redshift galaxies have been in powerful QSOs and intrinsically luminous galaxies, typically with star formation rates $> 10^3 \, M_\odot \, yr^{-1}$ (e.g. Frayer et al. 1998, 1999; Greve et al. 2005; Tacconi et al. 2006, 2008; Hailey-Dunsheath et al. 2010a; Walter et al. 2009). However, the detailed physical properties within the ISM of high-redshift SMGs are still unknown. Critically, the first full ^{12}CO SLEDs, including high-J_{upper} transitions, have recently been completed for local ULIRGs (Papadopoulos et al., 2010; van der Werf et al., 2010) providing an empirical benchmark

for comparison to high-redshift sources, to search for similarities in the thermodynamics of their ISM. The rotational transitions of ^{12}CO are predominantly excited through collisions with H_2 and He and through radiative trapping. Ignoring the effects of radiative trapping (which decreases the density required for thermalisation), then when the gas density is higher than the critical density (n_{crit}) and the excitation temperature $T_{ex,J} >> h\nu_J/k \approx 5.53J(J+1)/2$, then $J_{\rm up}$ will be populated and a strong emission line will be observed. Here $T_{ex,J}$ is the temperature required to recover the relative populations of $J_{\rm up}$ and $J_{\rm up} - 1$ levels from the Boltzmann distribution, which is typically different for each transition. However, at very high densities, $n >> n_{crit,J}$, the population of the $J_{\rm up}$ level in question and the levels below this can be described by Boltzmann statistics and become thermalised at the kinetic temperature of the gas i.e. $T_{ex,J}=T_{kin}$ (also known as local thermodynamic equilibrium- LTE). At this point the intensity of any particular J_{up} level can be described as a Planck function and the SLED will increase as the square of the line frequency. The excitation temperature is expected to increase towards the edges of molecular clouds since the volume densities are lower than the critical density for the ^{12}CO($J_{\rm up} = 1$) transition, whereas in the densest regions the ^{12}CO is in LTE and is therefore a good tracer of the kinetic temperature of the gas. Various local starburst galaxies, such as M 82 (Weiß et al. 2005c; Panuzzo et al. 2010; see Fig. 1.7) demonstrate thermalised SEDs up to $J_{\rm up} \sim 5$. Thus, typically the SLEDs of SMGs have been assumed to be thermalised given that they are extreme star-forming systems. However, sub-thermal excitation can occur when the excitation temperature is below the kinetic temperature and $T_{ex,J}/T_{ex,J-1} < 1$. Furthermore, Narayanan & Krumholz (2014) demonstrate that there is huge diversity in the SLEDs of SMGs such that a 'typical SMG' template SLED cannot easily be defined, and in particular LTE may not be a good description of SMG SLEDs. Measuring a complete ^{12}CO SLED provides essential constraints in modelling the physical and chemical properties within the ISM of galaxies.

A means of using measured line ratios to predict the conditions within the ISM is through radiative transfer codes such as large velocity gradient (LVG) models (i.e.
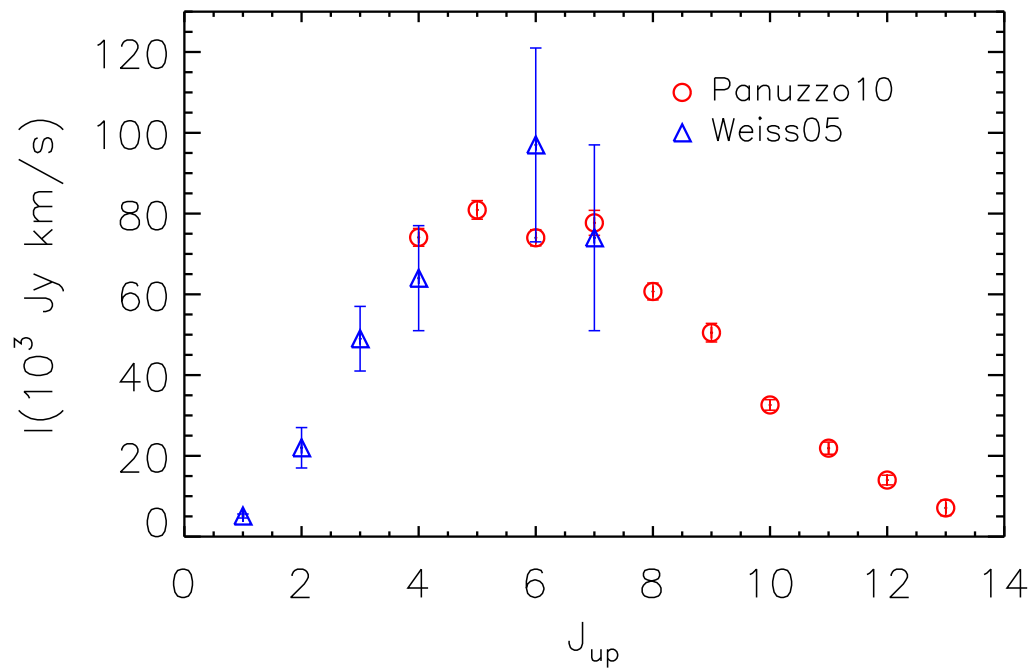
Figure 1.7: The spectral line energy distribution (SLED) of ^{12}CO rotational transition emission from the local starburst galaxy M 82. These data are taken from Weiß et al. (2005c); Panuzzo et al. (2010) and are observed with the IRAM 30 m telescope (triangles) and the *Herschel* SPIRE Fourier-transform spectrometer (FTS; circles). The SLED peaks at $J_{\mathrm{up}} = 6$ and is thermalised below this transition ($\mathrm{T}_{ex,J}=\mathrm{T}_{kin}$).

RADEX- van der Tak et al. 2007; used in Chapters 3 and 4 of this thesis). In particular if very few lines of the SLED are available it is necessary to use other species or theoretical calculations to deduce the excitation. Fundamentally, the intensity of an emitted ray can change due to emission, absorption and scattering within a medium. These processes are mathematically described by the equation of radiative transfer. Various methods have been employed to solve this equation numerically, although typically, simplifying assumptions are first applied. For example, this equation can be significantly simplified through the common assumption of LTE for which the emission and absorption can be described as functions of temperature and density only. An alternative simplifying assumption is the LVG approximation, which can be used to solve the radiative transfer equations when level populations within the molecules are not thermalised. The LVG approximation is such that if a sufficiently large velocity gradient (dv/dr) is assumed across a particular source (i.e. a galaxy) then solving the radiative transfer equation can be considered to be independent of the radius (since dv/dr is significantly larger than the velocity width at a particular point).

In Chapters 3 and 4 of this thesis LVG models are employed to derive the typical densities and kinetic temperatures within the ISM of an SMG. We note that these models do assume the medium to be homogeneous and therefore for complex, structured morphologies, such as those observed within some SMGs (e.g. Swinbank et al. 2010), these models can provide only an average description of the molecular gas.

1.6.3 Photodissociation regions

Much of the atomic and molecular gas emission from galaxies arises from photodissociation regions (PDRs), also known as photon-dominated regions; the surfaces of predominantly neutral molecular clouds where the heating and chemistry is dominated by far-UV (6-13.6 eV) photons from stellar sources, typically OB stars (see Hollenbach & Tielens 1997 for a review). The ISM directly adjacent to a hot massive

star is typically exposed to very high-energy (> 13.6 eV) photons which are capable of ionising the hydrogen, resulting in an HII region. However, beyond this region, the ISM becomes neutral and the remaining lower energy far-UV photons can ionise other atoms of lower ionisation potential (such as carbon; 11.3 eV) and trigger photodissociations. The bulk of the molecular gas ($> 90\%$; Kaufman et al. 1999) within galaxies resides within PDRs which dominate the infrared and sub-mm emission line spectra of star formation regions and galaxies as a whole. Although the term PDRs encompasses a wide range of gas temperatures ($\sim 10 - 8000$ K), hydrogen nucleus densities (i.e. $n \sim 10^{0-7}$ cm^{-3}), incident far-UV extinction (G$_0 \sim 10^{0-6}$, where G$_0$ is measured in Habing fields[2]), in this thesis we are concerned with the dense ($n(\text{H}_2) \sim 10^4$cm^{-3}) PDRs which are exposed to intense far-UV radiation fields in star-forming regions.

Fig. 1.8 shows a schematic of the processes occurring within a PDR. The incident far-UV photons are initially absorbed by dust grains and PAHs, which then re-radiate the bulk of the energy as thermal continuum radiation or infrared PAH emission features as described in Section 1.4.2. However, $0.1-1\%$ of the energy is converted into energetic photoelectrons (~ 1 eV) via photoelectric ejection of electrons from predominantly small dust grains and PAHs. In order to escape, these photoelectrons must overcome both the work function of the grain as well as the Coulomb potential, therefore the photoelectrons are mostly efficiently released from very small grains with a low charge. These energetic photoelectrons carry away some of the kinetic energy and are then free to heat the interstellar gas via elastic collisions. The gas typically reaches higher temperatures than the dust since the gas is less efficient at cooling and there is inefficient coupling between the gas and the dust. Gas and grains can transfer heat through collisions and radiation pressure can accelerate the dust relative to the gas, resulting in viscous heating of the gas.

Fig. 1.8 demonstrates the most simple geometry for understanding the line emission from a PDR, i.e. a slab of gas illuminated by far-UV radiation on one side.

---

[2]A Habing field is the average far-UV radiation field in the Solar neighbourhood, equivalent to 1.6×10^{-3} erg s^{-1} cm^{-2}

The deeper into the cloud/slab the higher the extinction and therefore the more attenuated the illuminating radiation field. Thus the chemistry changes throughout the PDR. PDRs typically comprise a layer of atomic hydrogen, a layer of C^+ and a layer of atomic oxygen, which are maintained by the photodissociation of molecular hydrogen and oxygen and the photoionisation of carbon. However, much of the gas in PDRs comprises molecular CO and H_2. It can be seen in Fig. 1.8 that various major chemical changes occur within the PDR. The first is at the edge of the PDR where atomic hydrogen is converted into H_2. As the gas becomes optically thick to the far-UV photons which are capable of dissociating H_2 (at the energies of the Lyman and Werner absorption bands within H_2) the molecule then becomes self-shielding. The second major chemical change occurs deeper into the PDR, at about 3 mag of extinction (A_V), where the incident far-UV has been sufficiently attenuated to allow the conversion of C^+ to C and subsequently to CO.

The majority of the cooling within PDRs occurs via spontaneous emission of the atomic fine structure lines of [OI], [CII] and the rotational ^{12}CO lines (Kramer et al., 2004). The cooling rate depends on the rate of spontaneous emission as well as the density and optical depth. If the optical depth of the emitting region is high, the released photon is more likely to be absorbed before escaping the PDR. Furthermore, if the density is high ($n >> n_{crit}$) excited states are likely to be collisionally de-excited and the energy is not radiated away.

It is important to note that PDRs specifically refer to the cloud edges near to a far-UV emitting source. In regions of ISM near to a very energetic source the ISM may be strongly influenced by X-ray radiation (X-ray dominated regions- XDRs, i.e. Sternberg 2005), capable of penetrating significantly deeper in molecular clouds. Furthermore, in the densest regions of ISM in the star-forming cores, only cosmic rays are sufficiently energetic to penetrate these regions, thus cosmic ray dominated regions (CRDRs; Papadopoulos et al. 2011) may be essential in determining the initial conditions for star formation. The presence of XDRs and CRDRs may be observed by the presence of unusually high excitation of ^{12}CO e.g. seen in the SLED of the local ULIRG Markarian 231 (van der Werf et al., 2010).

Over the last ~ 30 years, PDR modelling of measured atomic and molecular line ratios has been extensively used to predict the conditions within the PDRs by iteratively solving for the thermal balance, radiative transfer and the chemical balance of molecular gas that is exposed to far-UV radiation, as a function of depth into the cloud. Thus PDR models provide a more sophisticated approach than LVG models. Typically, assuming certain metallicities (thus elemental abundances) and certain grain properties, each model is described by a constant density of hydrogen nuclei (n) throughout the PDR and an incident far-UV radiation field. Most models assume a plane-parallel slab of ISM illuminated from one side by far-UV photons, resulting in the layered structure described previously (i.e. Kaufman et al. 1999; Meijerink & Spaans 2005), or a spherical geometry (i.e. CLOUDY; Ferland et al. 1998), however, some more recent models have considered a clumpy geometry (i.e. KOSMA-τ PDR code; Stoerzer et al. 1996; Röllig et al. 2006), more realistic for the complicated internal structures of high-redshift star-forming galaxies. Models may be steady-state stationary PDR models, in which case they assume thermal and chemical balance and ignore any flow within the PDR, or time-dependent, non-stationary PDRs where the incident far-UV flux or the hydrogen density changes on timescales of shorter than the timescale for H_2 formation on grains ($\tau_{H_2} \sim 10^9 \, \mathrm{cm}^{-3}/n \, \mathrm{yr}$). Different models also have different treatments for infrared and radiative transfer, dust and PAH properties and gas heating and cooling. Röllig et al. (2007) provides a comparison study of the most commonly used models. We discuss PDR modelling further in Chapter 3 of this thesis and compare two different models to determine the typical properties within the ISM of an SMG, using one of the most complete ^{12}CO SLEDs for a high-redshift galaxy.

1.6.4 ^{12}CO isotopologues

Typical molecular clouds have a high optical depth to photons that excite ^{12}CO transitions ($\tau \sim 5-10$ for $J_{\mathrm{up}} = 1$), even at relatively low column densities. This means that in externally-heated clouds, the ^{12}CO emission is dominated by the warm
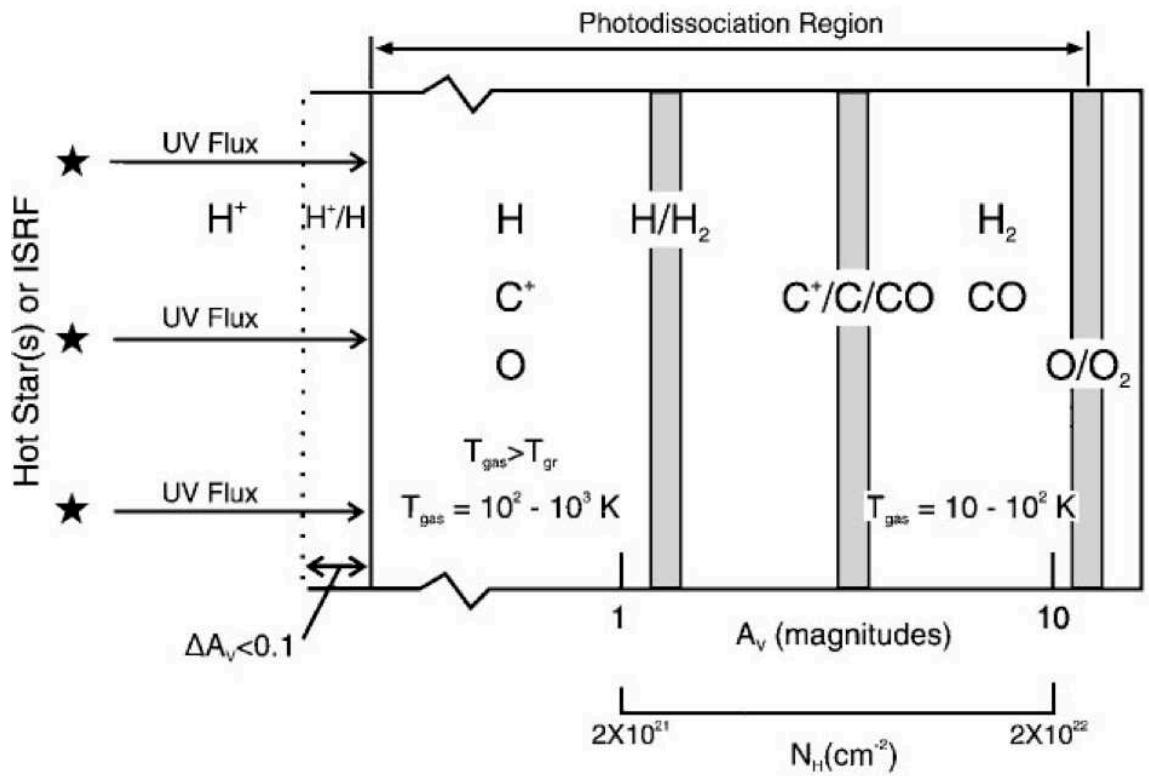
Figure 1.8: Schematic of a photodissociation region (PDR) on the surface of a molecular cloud, illuminated on one side by far-UV photons from massive OB stars or the interstellar radiation field. The column density of hydrogen increases from left to right. This demonstrates how the UV flux and density dictates the chemistry of the cloud surface. This figure is taken from Hollenbach & Tielens (1997).

cloud surfaces, thus limiting the information that can be deduced about the physical properties of the high-density molecular gas. Furthermore, low J_{up} transitions of ^{12}CO are very easily thermalised (where $\mathrm{T}_{ex} = \mathrm{T}_{kin}$) making them very insensitive to dense gas. A more direct tracer of the column density of H_2 can be obtained from optically thin emission lines, providing a reliable probe of the physical conditions of the cold gas and probing all of the column. ^{13}CO and C^{18}O (rare isotopologues of CO) can provide this due to their significantly lower abundances (and hence lower optical depths; $\tau < 1$) than ^{12}CO. ^{13}C is a "secondary" species (a product of the CNO cycle) produced in longer-lived, low-to-intermediate mass stars, compared to the "primary" nature of ^{12}C (a product of helium burning in the cores of stars) which is formed in and ejected from high-mass stars (Wilson & Rood 1994). Thus, ^{13}CO is generally associated with the later stages of star formation. Less is known about the origin of the optically thin molecule C^{18}O, however, it is generally associated with high-mass star formation and ^{18}O is potentially a major constituent of the winds of massive stars (i.e. Henkel & Mauersberger 1993; Prantzos et al. 1996). Given the lower abundance of these isotopes (i.e. $[^{12}\mathrm{C}]/[^{13}\mathrm{C}] \sim 20-140$ Martín et al. 2010; $[^{16}\mathrm{O}]/[^{18}\mathrm{O}] \sim 150-200$ Henkel & Mauersberger 1993), ^{13}CO is expected to be optically thin in all but the highest density, highest extinction, star-forming cores. In the densest cores C^{18}O may provide an even better tracer of H_2 due to its lower abundance and optical depth than ^{13}CO (i.e. in the Milky Way the abundance ratio of $[^{13}\mathrm{CO}]/[\mathrm{C}^{18}\mathrm{O}] \sim 7-8$; Henkel & Mauersberger 1993). In Chapter 4 we discuss some of the first observations of the SLEDs of ^{13}CO and C^{18}O in a high-redshift SMG and discuss the improvement that these constraints provide for LVG modelling of the ISM.

1.6.5   The decline of star formation

In order to address the final question in this thesis we must move forward at least 2.5 Gyr from the peak of cosmic star formation history (the focus of the previous discussion) to probe the conditions within a passive population of galaxies no longer

forming stars; early-type galaxies (ETGs). What limits the star formation in local elliptical galaxies?

(c) Interaction/"Merger"

NGC 4676

- now within one halo, galaxies interact & lose angular momentum
- SFR starts to increase
- stellar winds dominate feedback
- rarely excite QSOs (only special orbits)

(d) Coalescence/(U)LIRG

NGC 6240

- galaxies coalesce: violent relaxation in core
- gas inflows to center: starburst & buried (X-ray) AGN
- starburst dominates luminosity/feedback, but, total stellar mass formed is small

(e) "Blowout"

IRAS Quasar Hosts

- BH grows rapidly: briefly dominates luminosity/feedback
- remaining dust/gas expelled
- get reddened (but not Type II) QSO: recent/ongoing SF in host high Eddington ratios merger signatures still visible

(f) Quasar

PG Quasar Hosts

- dust removed: now a "traditional" QSO
- host morphology difficult to observe: tidal features fade rapidly
- characteristically blue/young spheroid

(b) "Small Group"

M66 Group

- halo accretes similar-mass companion(s)
- can occur over a wide mass range
- M_{halo} still similar to before: dynamical friction merges the subhalos efficiently

(g) Decay/K+A

NGC 7252

- QSO luminosity fades rapidly
  - tidal features visible only with very deep observations
- remnant reddens rapidly (E+A/K+A)
- "hot halo" from feedback
  - sets up quasi-static cooling

(a) Isolated Disk

M81

- halo & disk grow, most stars formed
- secular growth builds bars & pseudobulges
- "Seyfert" fueling (AGN with M_B>-23)
- cannot redden to the red sequence

(h) "Dead" Elliptical

M59

- star formation terminated
- large BH/spheroid - efficient feedback
- halo grows to "large group" scales: mergers become inefficient
- growth by "dry" mergers

Figure 1.9: This schematic taken from Hopkins et al. (2008) (see references therein), describes the theory of evolution of massive galaxies from isolated disks through the merger phase, triggering the SMG phase, through the QSO phase and finally resulting in passive elliptical galaxies. The central figure demonstrates the variation in star formation rate and luminosity of the QSO with time relative to the merger, such that the merger triggers a bright and sudden burst of star formation which is coincident with the increase in brightness of the central QSO.

Various studies have found evidence to suggest that SMGs are the progenitors of local massive, passive galaxies. The proposed evolutionary sequence initiated by the merging of disk galaxies is shown in Fig. 1.9. Swinbank et al. (2006) and Tacconi et al. (2006) demonstrate that SMGs and local elliptical galaxies have similar space densities, whilst Hickox et al. (2012) show that typically SMGs are short-lived ($\sim 110\,\mathrm{Myr}$) and that their clustering implies that they are the progenitors of massive elliptical galaxies. Simpson et al. (2014) find that assuming SMGs undergo a $100\,\mathrm{Myr}$ burst of star formation and then passively evolve, their predicted H-band magnitudes and number density are consistent with $z \sim 0$ elliptical galaxies. Meanwhile, observations of massive local ellipticals suggest that they formed the bulk of their stars at $z > 2$, consistent with the peak of the SMG population (i.e. Heavens et al. 2004). Toft et al. (2014) measure a large sample of compact quiescent systems already in place at $z \sim 2$, consistent with having been formed in $z = 3\,{-}\,6$ SMGs with matching formation redshifts, size distributions, stellar masses and internal dynamics. Similarly, Whitaker et al. (2012) find a large population of recently-quenched quiescent galaxies at $z \sim 1.4\,{-}\,2$ with typical ages of $\sim 1\,\mathrm{Gyr}$. The progenitors of such systems should be rapidly star-forming galaxies at $z \sim 2\,{-}\,3$, thus consistent with the SMG population. However, it is still unclear what caused the star formation rates in these galaxies to rapidly fall from $> 1000\,\mathrm{M_\odot yr^{-1}}$ to almost zero in local massive elliptical galaxies.

By investigating the various heating and cooling mechanisms within the gas in passive galaxies we can hope to understand what prevents stars from forming in these systems and why the star formation rate density of the Universe has fallen so rapidly since $z \sim 1.9$. In this thesis we investigate one of the possible mechanisms that resulted in the decline of the star formation rate density: AGN feedback.

1.7 SMBHs and AGN

It has long been believed that a supermassive black hole (SMBH) resides at the centre of every galaxy with a mass proportional to the mass of the galaxy spheroid

(e.g. Kormendy & Richstone 1995; Magorrian et al. 1998). It is therefore believed that the SMBH is integral to the growth and evolution of the host galaxy, since both processes require a good supply of cold gas, however, their connection is still not well-understood (see Alexander & Hickox 2012 for a review), in particular given the huge difference in size of the SMBH and the bulge ($\sim 8-9$ orders of magnitude in linear scale and ~ 3 orders of magnitude in mass).

As the SMBH grows at the centre of a galaxy, primarily through accretion, it begins to increase in luminosity until it is revealed as an active galactic nucleus (AGN). An accretion rate of just $1\,\mathrm{M_\odot}\,\mathrm{yr}^{-1}$ is sufficient for the AGN to dominate the bolometric output of the whole galaxy. The term 'AGN' covers a very broad range of characteristics, e.g. broad/narrow permitted/forbidden luminous emission lines in optical spectra; luminous nonthermal radio emission; luminous high-energy continuum emission (UV/X-ray). However, all these classifications have been unified under one 'unified model' (Antonucci 1993; Urry & Padovani 1995) which states that the different classifications arise from the AGN being viewed along different lines-of-sight. Chapter 5 of this thesis focuses only on radiatively-inefficient AGN (also known as 'radio-mode', 'mechanical mode', 'maintenance mode' or 'jet mode' AGN). These are low accretion rate AGN where the bulk of their energy is converted into mechanical energy in the form of radio jets (see Heckman & Best 2014 for a review). Radio-mode AGN typically reside within massive passive galaxies with very little cold gas or ongoing star formation (i.e. Best et al. 2005; Smolčić et al. 2009; Herbert et al. 2010; Smolčić & Riechers 2011). This is in contrast to the 'quasar mode' (or 'radiative-mode') feedback which occurs in radiatively-efficient, high accretion rate AGN and is the mode of feedback more likely to be responsible for the rapid and dramatic quenching of star-formation in SMGs.

1.7.1 Feedback

The most successful theoretical models of galaxy evolution (e.g. Bower et al. 2006 and Croton et al. 2006) require that feedback, in the form of energetic outflows from

active galactic nuclei (AGNs), will have a fundamental influence on the evolution of intermediate and massive galaxies. In these models, energy injected from AGN heats the interstellar and intergalactic medium of massive ETGs (ETGs) and further drives interstellar gas out of these systems. This energy injection effectively quenches star formation and supermassive black hole (SMBH) accretion and prevents galaxies and SMBHs growing. The interstellar gas itself is thought to be produced by evolving stars ejecting material through stellar winds and supernovae (at a rate of $\sim 1.3[L_{\rm B}/10^{11}L_{\rm B,\odot}]\,{\rm M_\odot yr^{-1}}$; e.g., Mathews & Brighenti 2003 and Bregman & Parriott 2009), as well as gas infall from the intergalactic medium.

The hot gas in massive ($\gtrsim 10^{11}\,{\rm M_\odot}$) ETGs has been found to radiate powerfully at X-ray wavelengths through thermal bremsstrahlung and yet it does not appear to be cooling as expected. The X-ray SEDs of massive ETGs demonstrate that hot gas ($kT = 0.3 - 1\,{\rm keV}$) typically dominates the $0.5 - 2\,{\rm keV}$ emission (e.g., Boroson et al. 2011). The temperatures and densities in the central regions imply relatively short radiative cooling times of $\sim 10^8$ yr (Mathews & Brighenti 2003). However, large quantities of cool ($10^{4-5}\,{\rm K}$) gas are not observed in the ETGs, which would be predicted by simple cooling flow models (see, e.g., Mathews & Brighenti 2003 for a review). By these observational arguments, it is necessary that some mechanism keeps the gas hot and/or expels the cool gas reservoirs. The most favoured mechanism is the transfer of mechanical energy by radio jets launched from AGN (see McNamara & Nulsen 2012 for a review).

Direct observational evidence for the interaction of AGN radio jets with hot gas has been obtained via X-ray and radio observations of massive ETGs in the local universe (e.g., Boehringer et al. 1993; Bîrzan et al. 2004; Forman et al. 2005; Rafferty et al. 2006; McNamara & Nulsen 2012; Hlavacek-Larrondo et al. 2013). These observations have revealed relativistic radio outflows, inflating large X-ray-emitting gas cavities with cool gas observed at the cavity rims. Measurements of X-ray cavity sizes and their surrounding gas densities and temperatures can give estimates of the mechanical energy input required by the radio jets to inflate the cavities against the pressure of the surrounding gas. The derived mechanical energy

and jet power are in the ranges 10^{55-62} ergs and 10^{40-46} erg s^{-1}, respectively (Nulsen et al. 2007; McNamara et al. 2009). This radio-mode heating is sufficient to suppress gas cooling in the galaxy and impede star formation and cold gas SMBH accretion (Allen et al. 2006).

Previous studies clearly indicate that heating by radio jets is an important process in galaxy evolution. Investigations of the influence of radio AGN on gas cooling in the general ETG population (Best et al. 2005) found that more than 30% of the most massive ($\sim 5 \times 10^{11}$ M$_\odot$) galaxies host a radio AGN, which is consistent with radio AGN activity being episodic with duty cycles of $\sim 10^{7-8}$ yr (Best et al., 2006). Evidence of such episodic radio luminous activity is also implied by the presence of multiple bright rims and shocks in the X-ray and radio images of individual ETGs (e.g., M87; Forman et al. 2005). Therefore the prevention of the cooling of large quantities of gas is thought to be maintained by a self-regulating AGN feedback loop. Cooling gas in the ETG centre initially provides a slow deposition of fuel for SMBH accretion, which in a radiatively-inefficient accretion mode, leads to the production of a radio outburst. Surrounding cool gas is physically uplifted by the radio outbursts, which increases the gravitational potential energy of the gas or removes it from the system entirely (e.g. Giodini et al. 2010). As the gas further cools via X-ray emission, it falls back towards the SMBH where it can re-ignite a new cycle of accretion, thus completing the feedback loop (Best et al. 2006; McNamara & Nulsen 2007). The importance of the role of feedback from moderately radio luminous AGN is becoming increasingly apparent, since the feedback energy can be directly diffused into the ISM (Smolčić et al., 2009).

Lehmer et al. (2007) have demonstrated that there is very modest cooling in the hot gas in ETGs out to $z \sim 0.7$. In Chapter 5 we push these limits to higher redshift ($z \sim 1.2$) and measure the hot gas cooling and the potential influence of radio-mode heating on the gas in ETGs.

1.8 Outline of this thesis

The star formation rate density of the Universe reached a peak at $z \sim 2$, an epoch when SMGs were most common and were forming thousands of stars per year. To understand how SMGs formed stars so rapidly we need to probe the ISM within SMGs. Furthermore, to understand why the star formation rate density of the Universe has rapidly declined since $z \sim 2$ we need to investigate the possible descendants of SMGs, the massive passive ETGs we see today and probe the balance of heating and cooling within these systems.

Chapters 3, 4 and 5 of this thesis are published work. Chapter 2 investigates the redshift distribution and overall properties of SMGs via UV, optical and near-infrared spectroscopy. Chapters 3 and 4 then consider the detailed observations of the molecular emission from the ISM of a gravitationally-lensed SMG. In Chapter 5 a large sample of massive ETGs are investigated, seeking to constrain the contribution of radio-mode heating in these systems and the resultant suppression of star formation. The overall conclusions are summarised in Chapter 6 followed by a discussion of the future directions of this work. Finally, the Appendix contains additional data from Chapter 5 and a glossary of acronyms used in this thesis.

Chapter 2

An ALMA survey of the Extended *Chandra* Deep Field South: the spectroscopic redshift distribution

2.1 Motivation

The LESS survey was the first deep, wide-field extragalactic survey at 870μm carried out with the LABOCA on the 12-m APEX telescope. This extragalactic survey covers the full $0.5{\times}0.5\,\mathrm{deg}^2$ extent of the ECDFS, which is one of the best-studied regions of the sky, with excellent multiwavelength coverage from X-ray to radio wavelengths. In 310 hours of observing time the full region was covered to a uniform noise level of $1.2\,\mathrm{mJy\ beam}^{-1}$, making LESS the largest contiguous deep submillimetre survey published to date. The LESS catalog (Weiß et al., 2009) comprises 126 SMGs detected above 3.7σ. Multiwavelength counterparts were identified for the sub-mm sources (Biggs et al. 2011) and the photometric redshifts were determined from 17-band photometry in the ECDFS (Wardlow et al., 2011). However, spectroscopic redshifts are required to facilitate detailed follow-up of SMGs. We therefore undertook a 180-hr large programme on the Very Large Telescope (VLT) with FORS2 and VIMOS to measure the spectroscopic redshifts for a majority of

the LESS SMGs. These data are discussed in this Chapter. Due to various delays in the programme, it was not completed until late in 2012, by which time we had been granted ALMA Cycle 0 time to observe the full LESS population.

The ALMA Cycle 0 study obtained 120s Band 7 (870μm) images of 122 of the 126 LESS SMGs, providing significantly deeper, higher resolution images than LABOCA and resolving many of the original sources into multiple SMGs. We therefore carried out further spectroscopic surveys with MOSFIRE, XSHOOTER, DEIMOS and GNIRS to target these newly-identified SMGs. These data are also discussed in this Chapter.

There is a wealth of multiwavelength data in the ECDFS providing an ideal region in which to constrain the properties and evolution of the SMG population and their environments and properties relative to other coeval galaxy populations. However, to unambiguously interpret many of these properties we require secure spectroscopic redshifts and detailed follow-up of a sub-sample of SMGs (see Chapters 3 and 4). This Chapter discusses how the redshifts were determined for the ALESS SMGs and uses the redshifts to measure an SMG redshift distribution and to provide improved constraints on various SMG properties. We search for strong emission/absorption features and continuum breaks within both the individual spectra and the composite spectra over various wavelength ranges to attempt to characterise the SMG emission. This work will be the basis of a paper which is currently near submission.

2.2 Abstract

We present the spectroscopic redshift distribution of the 131 ALMA-identified SMGs in the ECDFS (ALESS); follow-up of 126 single-dish sources from the LESS survey. We have carried out a large spectroscopy programme with a combination of FORS2, VIMOS and XSHOOTER on the VLT; GNIRS on GEMINI-SOUTH; DEIMOS and MOSFIRE on Keck and ALMA (Cɪɪ detections). In total we have targeted 109 ALESS SMGs and determined redshifts for 52 of the 131 SMGs in the ALESS sur-

vey. This is the first redshift distribution of unambiguously-identified SMGs. We find a median redshift for the MAIN+SUPPLEMENTARY ALESS catalog of $z = 2.3 \pm 0.2$ which increases to $z = 2.4 \pm 0.1$ if we include our tentative redshifts. This peak redshift is within 1σ of previous surveys of radio-identified SMGs. Spectral diagnostics imply that the SMGs are generally young starbursts with many emitting strong star formation driven winds of up to $3000\,\mathrm{km\,s^{-1}}$. Interestingly, using the spectroscopic redshifts, we find very little evidence of associations between SMGs. However, we note that spectroscopic incompleteness and cosmic variance may play a role here.

2.3 Introduction

As described in Chapter 1, SMGs were discovered by Smail et al. (1997), Barger et al. (1998), Hughes et al. (1998) using the SCUBA detector on the JCMT. They are a population of heavily dust-obscured galaxies which, through spectroscopic and photometric redshift surveys, have been shown to be most prevalent at $z \sim 2.3$ (Chapman et al. 2005- hereafter C05; Simpson et al. (2014)- hereafter S14). They typically form stars at a rate of $\sim 100\text{--}1000\mathrm{M_\odot\,yr^{-1}}$, inferred from their infrared luminosities, which is analogous to the most extreme local ULIRGs. However, SMGs are nearly 1000 times more common at $z = 2$ than ULIRGs are today and they are thought to be a key step in the evolution of galaxies, potentially being the progenitors of massive elliptical galaxies in the local Universe (e.g. Swinbank et al. 2006; Simpson et al. 2014; Toft et al. 2014). Since the discovery of the SMG population and the realisation of their important contribution to the cosmic star formation history, it has become a priority to measure their redshifts both for the purpose of further detailed follow-up and to aid in characterising the emission from these massive star-forming galaxies.

Measuring spectroscopic redshifts is observationally very expensive, therefore much effort has been put into photometric redshift estimates for SMGs (i.e. Aretxaga et al. 2007; Clements et al. 2008; Wardlow et al. 2011; S14). Although such work provides an excellent statistical study of the properties of SMGs, certain properties,

such as their environments, cannot be well-constrained without very accurate red-shifts which can only be measured through spectroscopy. Furthermore, spectroscopy can provide valuable information about the composition, dynamics, energetics and ages of galaxies. However, there are many difficulties in determining spectroscopic redshifts. Firstly, optical counterparts to the sub-mm emission are typically very difficult to precisely determine given the large beamsize of sub-mm telescopes (in particular single-dish telescopes) and even when radio counterparts are identified these are frequently very faint in the UV-to-optical. Many of the strong emission features from which spectroscopic redshifts can be measured (i.e. Lyα, [OII]), lie at rest-frame UV-to-optical wavelengths which suffer from significant extinction due to dust, and it is common to detect emission lines but no continuum in SMG spectra (i.e. C05).

The largest spectroscopic survey of SMGs was carried out by C05 who studied a sample of 150 SCUBA-detected SMGs spread across seven extragalactic survey fields. They focussed on the 104 sources with reliable radio counterparts, in order to utilise the radio-far-infrared correlation to more precisely determine the position for UV-to-optical spectroscopic follow-up of the SMG. Using rest-frame UV spectroscopy with the Low-resolution Imaging Spectrograph (LRIS) on Keck, they were able to derive 73 spectroscopic redshifts with a median redshift of $z \sim 2.2$ for the radio-selected sample, a predicted peak of $z \sim 2.3$ for a sub-mm flux-limited sample, a highest redshift of $z = 3.6$ and an interquartile range of $z = 1.7 - 2.8$. Unfortunately UV and optical spectroscopy alone result in spectroscopic incompleteness due to the instrument dependent redshift desert, i.e. for LRIS at $z = 1.5$, no strong spectral features lie within its wavelength range. Banerji et al. (2011) attempt to fill in this desert by using the red-sensitive Keck-II DEIMOS in order to target emission-line galaxies at $z \sim 1.3$ through their [OII]$\lambda 3727$ emission. However, the requirement of a radio detection introduces bias in that around half of all SMGs remain undetected in the radio (Ivison et al. 2005) since a large fraction of SMGs do not have a radio counterpart. Furthermore, those with radio counterparts may be missed due to radio flux limits, since radio data does not benefit from the same

negative K-correction as sub-mm wavelengths, due to the shape of the SEDs. The radio flux limit in C05 is 30μJy, thus at $z > 3.5$, radio counterparts are very difficult to detect unless they are particularly bright in radio. Various examples of high-redshift SMGs have been identified via particularly bright radio counterparts or millimetre-detected emission lines such as transitions of ^{12}CO (e.g. Capak et al. 2008; Schinnerer et al. 2008; Coppin et al. 2009; Daddi et al. 2009; Knudsen et al. 2009; Riechers et al. 2010; Cox et al. 2011; Smolčić et al. 2011; Combes et al. 2012; Walter et al. 2012). There is a need for an unbiased 850μm-selected sample with accurate positions, without necessitating the use of radio counterparts. For detailed study of the properties of SMGs, it is essential to be able to pinpoint their precise positions.

This situation has been vastly improved with the use of ALMA, which can provide high-resolution ($< 1''$) 870μm images allowing the source of the sub-mm emission to be accurately pinpointed without recourse to statistical associations at other wavelengths. In order to provide an unbiased sample of SMGs with unambiguous IDs, we recently undertook an ALMA survey of 122 SMGs in the ECDFS: the "ALESS" survey (Karim et al. 2013; Hodge et al. 2013). This survey followed up 122 of the 126 SMGs originally detected in the LESS survey. Each LESS source was targeted with ALMA at 870μm (Band 7) in compact configuration, which provides a beam of $\sim 1''$, allowing direct comparison to the LABOCA observations and providing maps which are $3\times$ deeper than the original LESS survey and with a beam area $\sim 200\times$ smaller. The typical FWHM of the ALMA observations was $\sim 1.5''$, thus allowing us to directly pinpoint the source of the SMG emission. Interestingly, $> 35\%$ of the original sources were resolved into multiple SMGs, in particular, all sources with $S_{870\mu m} > 12\,$mJy in the LESS sample were found to comprise multiple sources with $S_{870\mu m} > 9\,$mJy (Karim et al. 2013; Hodge et al. 2013). Thus a new ALESS SMG catalog was defined comprising 131 SMGs (Hodge et al. 2013). We now have a large unbiased dataset from which to build a firm understanding of the properties of the SMG population.

In this Chapter we describe the UV, optical and near-infrared spectroscopic

follow-up of the ALESS galaxies and we use these redshifts to investigate the redshift distribution, the SMG environments and typical SMG spectral features, as well as using them to better constrain the SED fitting from UV-to-radio wavelengths and provide improved stellar masses for the ALESS SMG population. The structure of the Chapter is as follows: We discuss the observations and the data reduction in Section 2.4, followed by redshift identification and sample properties in Section 2.5. In Section 2.6 we show the ALESS redshift distribution and discuss the spectroscopic completeness. In Section 2.7 we discuss the velocity offsets of various different spectral lines searching for evidence of stellar winds and galaxy-scale outflows, the environments of SMGs and the individual and composite spectral properties. We also investigate the SEDs of the ALESS SMGs when using the spectroscopic redshifts as a constraint in the SED fitting.

Unless otherwise stated the errors on quoted medians are determined through bootstrap analysis. We use a Salpeter IMF unless otherwise stated. Throughout the Chapter we use a ΛCDM cosmology with $H_0 = 72\,\mathrm{km\,s^{-1}\,Mpc^{-1}}$, $\Omega_m = 0.27$ and $\Omega_\Lambda = 1 - \Omega_m$ (Spergel et al., 2003).

2.4 Observations and reduction

2.4.1 Sample definition

The original LESS survey (Weiß et al. 2009) was undertaken using the LABOCA camera on APEX, operating at 870μm. This survey covered the full 0.5×0.5 degrees of the ECDFS and had a uniform noise level of $\sigma_{870\mu\mathrm{m}} \sim 1.2\,\mathrm{mJy\,beam^{-1}}$. In 310 hours of observing time, 126 SMGs were detected above 3.7σ. The measured angular resolution of each beam was $19.2''$. To identify likely counterparts for photometric and spectroscopic follow-up, it was therefore necessary to use radio imaging (discussed in Wardlow et al. 2011).

Once the optical counterparts were determined, we commenced a VLT Large Programme with the FOcal Reducer and low dispersion Spectrograph (FORS2) and

VIsible MultiObject Spectrograph (VIMOS) with the goal of measuring redshifts for the LESS SMGs as a priority but also a large number of other galaxies in the ECDFS. However, whilst the programme was $< 30\%$ complete, we were allocated a Cycle 0 ALMA programme to target the complete sample of the LESS SMGs. The details of the ALMA observations are described in Hodge et al. (2013) but in summary, the observations were taken in ALMA's Band 7 (centred at 870μm) between 2011 October 18 and 2011 November 3 as part of the Cycle 0 Project #2011.1.00294.S. The observations were 120s exposures centred on the 126 LESS sources. The ALMA follow-up survey of the LESS SMGs found that up to 50% of the originally detected LESS SMGs were resolved into multiple SMGs and further sources were found to have previously mis-identified counterparts, therefore many of the source IDs changed. Thus a new ALESS SMG catalog was formed comprising a main (hereafter MAIN) catalog of the 99 most reliable SMGs, coming from within the primary beam FWHM of the good-quality maps (RMS$< 0.6\,$mJy beam^{-1}, signal-to-noise > 3.5, beam axial ratio< 2.0). Furthermore a supplementary (hereafter SUPP) catalog was defined comprising 32 sources extracted from outside the ALMA primary beam, or in lower quality maps (RMS$> 0.6\,$mJy beam^{-1} or axial ratio > 2.0; Hodge et al. 2013). Karim et al. (2013) demonstrate that in the MAIN catalog only one source is expected to be spurious and one source is expected to be missed, however, up to $\sim30\%$ of the SUPP sources are likely to be spurious. In this work we include both the MAIN and SUPP sources but we highlight the MAIN sources in the analysis. Using the ALMA data, we observed the counterparts to the newly-identified SMGs (those that differed from the original LESS counterparts) with various spectrographs in order to form a complete redshift catalog for the ALESS SMGs.

To increase the wavelength coverage and so increase the probability of determining a redshift, we also obtained observations with XSHOOTER on the VLT, Gemini Near-Infrared Spectrograph (GNIRS) on Gemini South and the Multi-Object Spectrometer for Infra-Red Exploration (MOSFIRE) on Keck I, all of which probe into the near-infrared, allowing us to reach a greater range of spectroscopic features (if present), in particular Hα at $z \sim 2$. We also used the DEep Imaging Multi-Object

Spectrograph (DEIMOS) on Keck II, as infill in another observing programme, in order to probe a similar wavelength range to FORS2 but targeting some of the ALMA-identified SMGs not targeted in the original VLT programme. In total, out of 131 ALESS SMGs we targeted 109 with spectrographs. In many cases we have ALESS SMGs with spectra from five different spectrographs covering a broad wavelength range. We now discuss the various instruments involved in our survey. See Table. 2.1 for a summary of the instrumental setups.

2.4.2 VLT FORS2/VIMOS

Our initial spectroscopy programme began in 2009 to target all the LESS SMGs with a dual approach of the FORS2 and VIMOS spectrographs on the VLT, aiming to reduce the 'redshift desert' incompleteness problems of i.e. C05. We observed a total of $\sim$180 hours with these multi-object spectrographs as part of the large programme 183.A-0666, targeting $\sim$2500 galaxies (see Swinbank et al. in prep) in the ECDFS including nearly all 126 of the original LESS SMGs. Due to various delays the programme spanned periods 83–90 (July 2009 – Feb 2012). All observations were carried out in grey time for FORS2 and dark time for VIMOS, with a seeing of ≤ 0.8 and thin cirrus (transparency variations above 10%). This dual-instrument approach allowed us to probe a large wavelength range using VIMOS LR-Blue grism (400 – 670nm) and FORS2 300I (600 - 1100nm) such that for an expected mean redshift of the SMGs of $z \sim 2$ we expected to be able to detect Lyα and UV ISM lines with VIMOS and [OII] λ3727 with FORS2. In designing the slit masks, priority was given to the SMGs, supplemented by far-infrared selected galaxies from the FIDEL *Spitzer* survey, the HerMES *Herschel* survey of this field, 2000μJy radio sources and *Chandra* X-ray sources.

Figs. 2.1 and 2.2 give the spectroscopic coverage of the LESS field in our FORS2 and VIMOS programmes respectively. There was much overlap between the pointings in the VIMOS coverage therefore these are shown in Fig. 2.2 with the darkest areas demonstrating the areas with the longest total exposure time. There is little

overlap in the FORS pointings therefore these are shown in Fig. 2.1 as boxes overlaid on the original LESS survey map.

FORS2

FORS2 operates over the wavelength range from 330–1100 nm and provides an image scale of $0.25''$/pixel (or $0.125''$/pixel with the high resolution collimator) in the standard readout mode (2×2 binning). FORS2 was used in its multi-object spectroscopy mode with exchangeable masks. The slit lengths and widths can be defined by the observer. We varied the slit length and orientation in order to observe the maximum number of sources on each mask, but we consistently used a slit width of $1''$. We used the OG590 order-sorting filter and the 300I grism resulting in a wavelength range of 600–1100 nm for our setup. The typical resolution in this configuration is $R = \lambda/\Delta\lambda \sim 660$. We targeted 16 main pointings and in some cases we targeted the same pointing multiple times but with a few slits moved around if there were multiple SMGs near each other which could not be simultaneously observed on the same mask. Each mask was observed in OBs of 3×900s exposures nodded up and down the slits by $\sim 1.0''$ in order to aid sky-subtraction and cosmic-ray removal when the images were combined. Each mask was then typically targeted between three and six times resulting in a exposure time of $2.25 - 6.75$ hrs per pointing. We typically used $\sim 40 - 70$ slits per mask.

We initially reduced the data using the FORS2 pipeline as part of the ES-OREX data reduction package. Using pipeline-generated master calibration products, this pipeline produces 2D bias-corrected, flat-fielded, wavelength-calibrated, sky-subtracted images. We then extracted 1D spectra over the full y-extent of the continuum/emission lines visible, or in the case where no emission was obvious in the 2D image, we extracted over the region where the source should have been. However, we found that the sky-subtraction was poor in the initial reduction. We therefore re-reduced the data using the Kelson Spectroscopy Software[1] adapted for

---

[1]http://www.ucolick.org/~holden/datareducetext/kelsonware.html
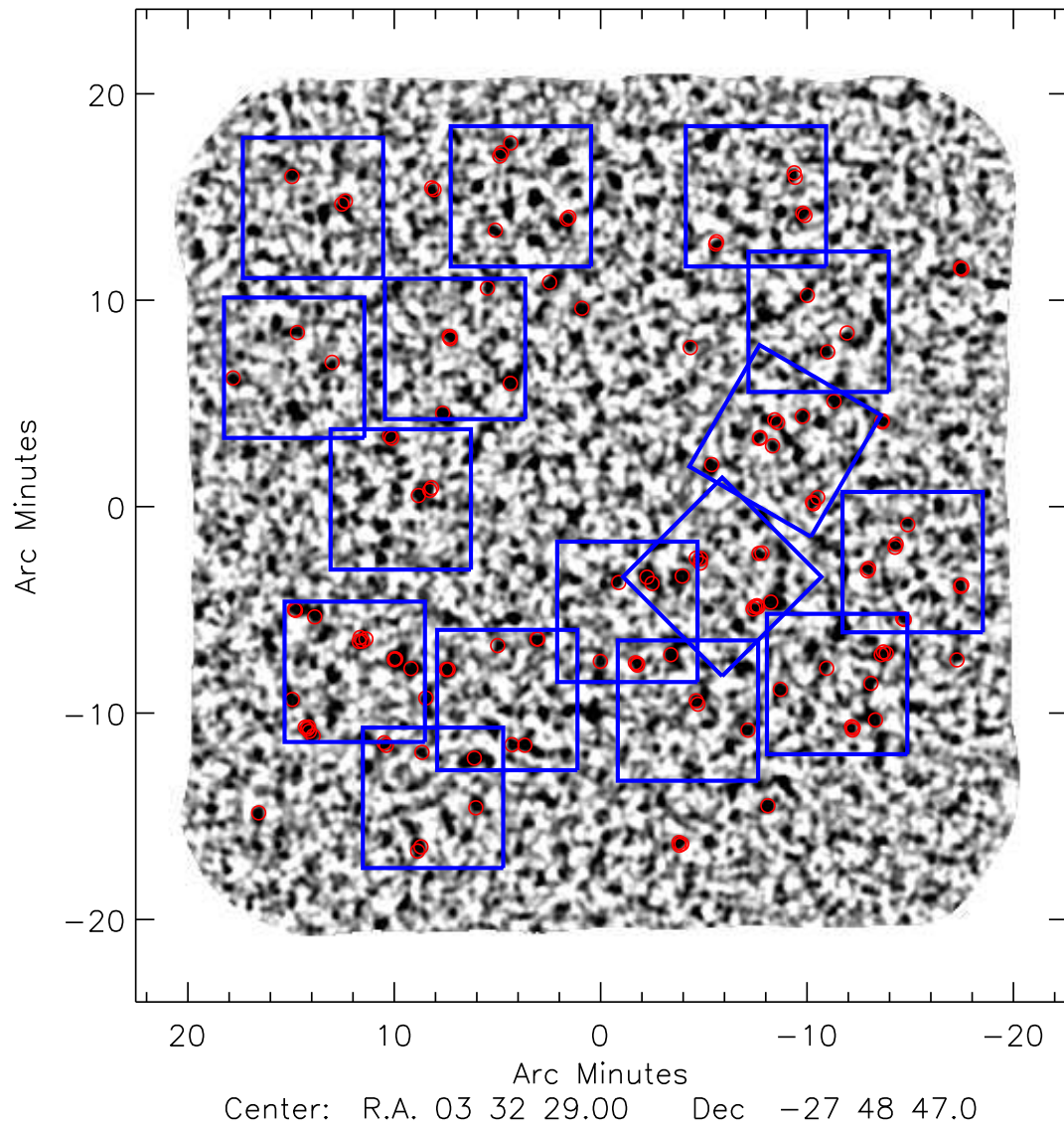
Figure 2.1: The LABOCA/APEX map of the ECDFS with the 16 FORS2 pointings overlaid as blue boxes and the ALESS SMG positions as small red circles. There is little overlap between the FORS pointings. The LABOCA image has a beam with an angular resolution of $19.2''$ compared to $\sim 1.5''$ for ALMA.
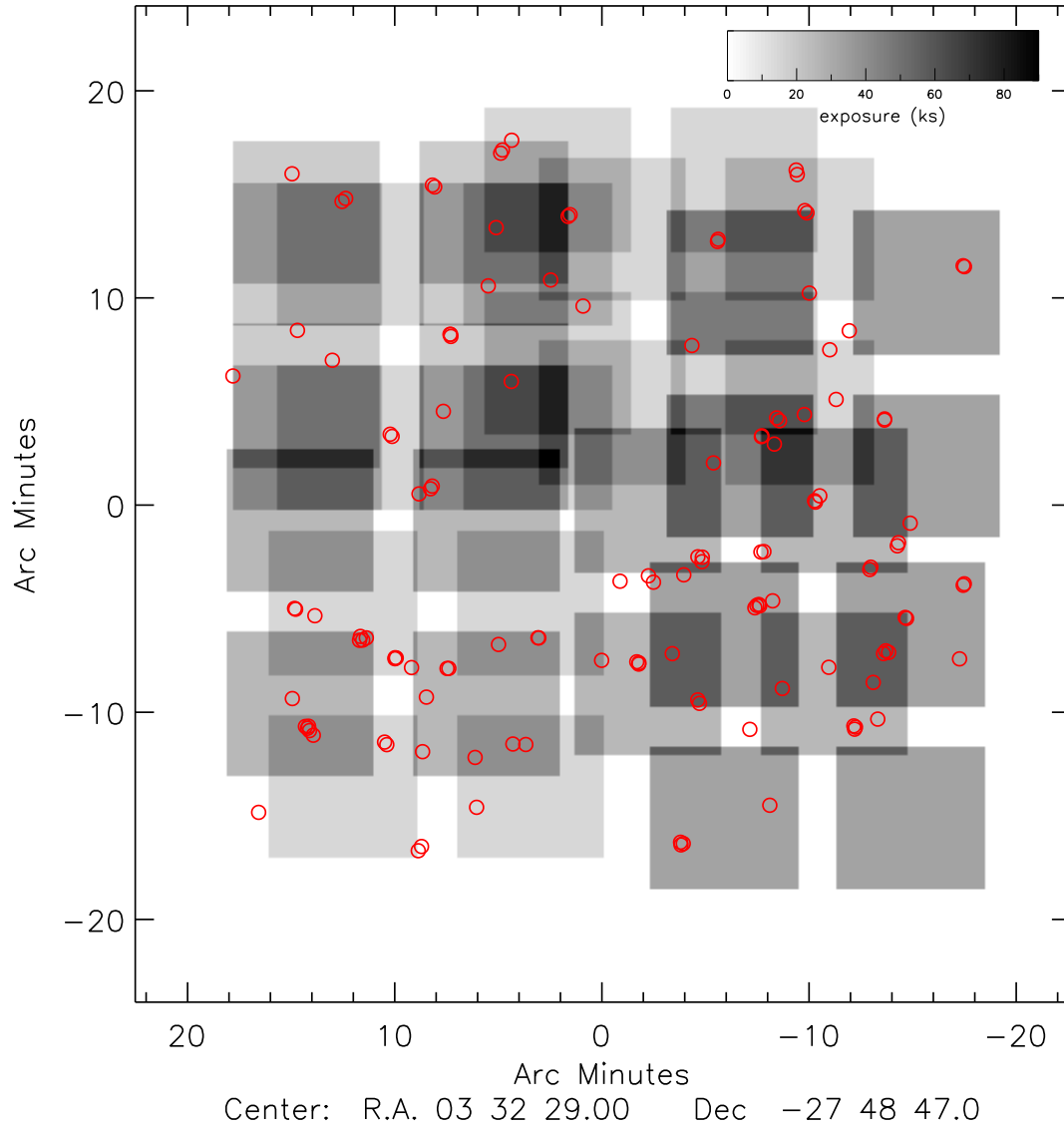
Figure 2.2: The coverage of the 10 VIMOS pointings in the ECDFS. VIMOS has four quadrants separated by small gaps. There is significant overlap between the VIMOS pointings, we therefore show the pointings here with the darkest areas corresponding to the areas with the longest total exposure time. The ALESS SMG positions are shown as small red circles.

use with FORS2 data. This provided more manual versatility with the sky subtraction which was important for the fainter sources. Frames were combined in 2D by taking a median of the frames and sigma clipping before extracting the 1D spectra.

VIMOS

The VIMOS observations were undertaken in MOS-mode. VIMOS consists of four quadrants each of a field of view of $7' \times 8'$ with a detector pixel scale of $0.205''$. Each OB comprised 3×1200s exposures dithering $\pm 1.0''$ along the slit. The typical exposure time per mask was $3-9$ hrs. Slit widths of $1.0''$ were used, for which the typical resolution is $R \sim 180$ and the dispersion is 5.3Å/pix, for the LR_blue grism with the OS_blue order sorting filter ($\sim 400-670$ nm). We typically used $40-160$ slits per quadrant, totalling $160-400$ over the four quadrants. The data was reduced using the standard ESOREX pipeline package for VIMOS. The frames were stacked in 2D before extracting the 1D spectra. In some cases there was an issue of overlapping spectra since in the low-resolution mode, a spectrum spans 640 pixels along the dispersion direction, which will allow four slits to be placed along the dispersion direction. However, this can lead to a second order spectrum at $2\times$ higher spectral resolution overlapping the adjacent spectrum (this can be seen in the VIMOS spectrum of ALESS 057.1 in Fig. 2.3).

2.4.3 XSHOOTER

To improve the wavelength coverage of our observations, we also obtained XSHOOTER observations of 20 ALESS SMGs. XSHOOTER simultaneously observes from UV to near-infrared wavelengths covering wavelength ranges of $300-560$ nm, $550-1020$ nm and $1020-2480$ nm for the UV (UVB), visible (VIS) and near-infrared (NIR) arms respectively. Targets were selected for XSHOOTER follow-up mainly based on their K-band magnitude. Our XSHOOTER observations were taken in visitor mode as part of programme 090.A-0927(A) (PI: Smail). We were granted four nights from $7-10$ December 2012 in dark time to target 20 ALESS SMGs for ~ 1hr per source.

The conditions were generally clear with a typical seeing of $\sim 1.0''$. Our observing strategy was taking four exposures per source of 600s and nodding the source up and down the slit. The pixel scales were 0.16, 0.16 and $0.21''$/pix for the UVB, VIS and NIR arms respectively. The slits were all $11''$ long and $0.9''$ wide for the VIS and NIR arms and $1.0''$ wide for the UVB arm. The typical resolution was $R \sim 4350$, 7450, 5300 for the UVB, VIS and NIR arms respectively. The data reduction was carried out using the standard ESOREX pipeline package for XSHOOTER.

2.4.4 MOSFIRE

36 ALESS SMGs were targeted with MOSFIRE on Keck as mask infill targets in the programmes 2012B_H251M, 2013B_U039M, and 2013B_N114M (PI: Casey) in H-band ($1.46-1.81\mu$m) and K-band ($1.93-2.45\mu$m) only. Observations were taken in clear-to-photometric conditions with the seeing varying from $0.4-0.9''$. In all cases we used $0.7''$ slits and an ABBA sequence with a $1.5''$ nod. Five different pointings were used. The individual exposures were 120s in H-band and 180s in K-band resulting in a total exposure per mask of $2.16-3.6$ ks. The pixel scale of MOSFIRE is $0.18''$/pix and the typical spectral resolution for this slit width is $R = 3270$. The wavelength coverage is $1460-1810$ nm and $1930-2450$ nm for the H and K bands respectively. Data reduction was completed with MOSPY, the publicly available python reduction package for MOSFIRE data written by Nick Konidaris.

2.4.5 DEIMOS

71 of the ALESS SMGs were used as mask infill in the programme 2012B_H251 (PI: Casey). The data were taken in visitor mode on $9-10$ Dec. 2012. The conditions were generally clear with seeing between $1-1.3''$. The setup used the 600ZD (600 lines mm^{-1}) grating with a 7200Å blaze angle and the GG455 blocking filter resulting in a wavelength range of $4850-9550$ nm. Slit widths of $0.75''$ were used and the masks were filled with $40-70$ slits per mask. Since many of the sources were near the edge of the slits the observations were taken without dithering and 1200s exposures

were used. The pixel scale of DEIMOS is 0.1185"/pix and the typical resolution was $R \sim 3000$. The data was reduced using the DEEP2 DEIMOS data reduction pipeline.

2.4.6 GNIRS

GNIRS on Gemini was used to observe 8 ALESS SMGs as part of the programme GN-2012B-Q-90 (PI: Smail) undertaken on the $10-15$ November 2012 and the $4-23$ December 2012. The targets were selected based on their K-band magnitude and whether they had a photometric redshift placing strong lines within the wavelength coverage of GNIRS. The instrument was in cross-dispersing mode (via the SXD prism with 32 lines/mm), using the short camera, with slit widths of $0.3''$, slit lengths of $7''$ and a pixel scale of $0.15''$/pix. The wavelength coverage with this setup is 900–2560 nm. The resolution in this set-up was typically $R \sim 1700$. Our observing strategy was using 200s exposures and nodding up and down the slit and by $\sim 1''$. Each OB comprised eight coadds of three exposures, resulting in an exposure of ~1.3 hrs per source. The GNIRS data was reduced using the Gemini IRAF package.

Table 2.1: Observation details

Instrument/pointing[a]	RA (J2000)	Dec J2000)	Obs dates[b]	Filter/Grism(/Grating)	λ range[c] (nm)	FOV (arcmin)	t_{exp} (ks)	#SMGs
F-1	53.041948	-27.978522	July 2009-Dec 2012	OG590/GRIS_300I	600–1100	6.8 × 6.8	10.8	6
F-2	52.905575	-27.956958	July 2009-Dec 2012	OG590/GRIS_300I	600–1100	6.8 × 6.8	16.2	19
F-3	53.010735	-27.870523	July 2009-Dec 2012	OG590/GRIS_300I	600–1100	6.8 × 6.8	13.5	8
F-4	52.953363	-27.760699	July 2009-Dec 2012	OG590/GRIS_300I	600–1100	6.8 × 6.8	21.6	11
F-5	52.836796	-27.858372	July 2009-Dec 2012	OG590/GRIS_300I	600–1100	6.8 × 6.8	16.2	8
F-6	52.923031	-27.664484	July 2009-Dec 2012	OG590/GRIS_300I	600–1100	6.8 × 6.8	8.1	4
F-7	52.980313	-27.563316	July 2009-Dec 2012	OG590/GRIS_300I	600–1100	6.8 × 6.8	21.6	9
F-8	53.207129	-27.969997	July 2009-Dec 2012	OG590/GRIS_300I	600–1100	6.8 × 6.8	21.6	10
F-9	53.346543	-27.947061	July 2009-Dec 2012	OG590/GRIS_300I	600–1100	6.8 × 6.8	18.9	12
F-10	53.304287	-27.807922	July 2009-Dec 2012	OG590/GRIS_300I	600–1100	6.8 × 6.8	8.1	8
F-11	53.401298	-27.701462	July 2009-Dec 2012	OG590/GRIS_300I	600–1100	6.8 × 6.8	8.1	6
F-12	53.254538	-27.686497	July 2009-Dec 2012	OG590/GRIS_300I	600–1100	6.8 × 6.8	13.5	11
F-13	53.383834	-27.572420	July 2009-Dec 2012	OG590/GRIS_300I	600–1100	6.8 × 6.8	13.5	4
F-14	53.194435	-27.563368	July 2009-Dec 2012	OG590/GRIS_300I	600–1100	6.8 × 6.8	24.3	12
F-15	53.097372	-27.898818	July 2009-Dec 2012	OG590/GRIS_300I	600–1100	6.8 × 6.8	10.8	6
F-16	53.275153	-28.048890	July 2009-Dec 2012	OG590/GRIS_300I	600–1100	6.8 × 6.8	8.1	5
V-1	52.924738	-27.991344	July 2009-Dec 2012	OS_BLUE/LR_BLUE	400–670	4 × 7 × 8	32.4	14
V-2	53.026533	-27.664861	July 2009-Dec 2012	OS_BLUE/LR_BLUE	400–670	4 × 7 × 8	10.8	7
V-3	53.305875	-27.651358	July 2009-Dec 2012	OS_BLUE/LR_BLUE	400–670	4 × 7 × 8	18.0	7
V-4	53.272729	-27.966083	July 2009-Dec 2012	OS_BLUE/LR_BLUE	400–670	4 × 7 × 8	14.4	8
V-5	53.076596	-27.625639	July 2009-Dec 2012	OS_BLUE/LR_BLUE	400–670	4 × 7 × 8	14.4	7
V-6	53.312683	-27.899536	July 2009-Dec 2012	OS_BLUE/LR_BLUE	400–670	4 × 7 × 8	25.2	9
V-7	52.994858	-27.883456	July 2009-Dec 2012	OS_BLUE/LR_BLUE	400–670	4 × 7 × 8	25.2	10
V-8	52.910208	-27.708119	July 2009-Dec 2012	OS_BLUE/LR_BLUE	400–670	4 × 7 × 8	32.4	7
V-9	53.305517	-27.685317	July 2009-Dec 2012	OS_BLUE/LR_BLUE	400–670	4 × 7 × 8	18.0	2

Table 2.1 – *Continued from previous page*

Instrument/pointing[a]	RA (J2000)	Dec J2000)	Obs dates[b]	Filter/Grism(/Grating)	λ range[c] (nm)	FOV (arcmin)	t_{exp} (ks)	#SMGs
V-10	53.265846	-27.685342	July 2009-Dec 2012	OS_BLUE/LR_BLUE	400–670	$4 \times 7 \times 8$	14.4	2
M-1-H	53.018500	-27.859814	21 Dec. 2012	H/H	1460–1810	6.12×6.12	2.16	7
M-3-H	53.315458	-27.957108	21 Dec. 2012	H/H	1460–1810	6.12×6.12	2.16	7
M-A2-H	52.844708	-27.880444	19 Jan. 2014	H/H	1460-1810	6.12×6.12	2.88	7
M-A3-H	53.280208	-27.942242	19 Jan. 2014	H/H	1460-1810	6.12×6.12	2.88	8
M-0-K	52.879583	-27.943317	21 Dec. 2012	K/K	1930–2450	6.12×6.12	2.16	7
M-1-K	53.018500	-27.859814	21 Dec. 2012	K/K	1930–2450	6.12×6.12	2.52	7
M-3-K	53.315458	-27.957108	21 Dec. 2012	K/K	1930-2450	6.12×6.12	2.52	7
M-A3-K	53.280208	-27.942242	31 Dec. 2013	K/K	1930-2450	6.12×6.12	3.6	8
M-A2-K	52.844708	-27.880444	19 Jan. 2014	K/K	1930-2450	6.12×6.12	3.6	7
D-1	52.861126	-27.914778	10 Dec. 2012	GG455/600ZD	4850–9550	16.7×5.0	7.2	17
D-2	52.270164	-27.974695	9 Dec. 2012	GG455/600ZD	4850–9550	16.7×5.0	8.4	20
D-4	52.473042	-27.697083	9 Dec. 2012	GG455/600ZD	4850–9550	16.7×5.0	8.9	17
D-5	53.011581	-27.893778	10 Dec. 2012	GG455/600ZD	4850–9550	16.7×5.0	9.2	17
X-UVB	-	-	7–10 Sep. 2012	UVB	300–560	-	96.0	20
X-VIS	-	-	7–10 Sep. 2012	VIS	560–1024	-	96.0	20
X-NIR	-	-	7–10 Sep. 2012	NIR	1024–2480	-	96.0	20
G	-	-	10–15 Nov. 2012	SXD/32l/mm	900–2560	-	38.4	8
	-	-	4–23 Dec. 2012					

NOTES: The RA and DEC correspond to the pointing centres for the multi-object masks. [a]F=VLT/FORS2, V=VLT/VIMOS, X=VLT/XSHOOTER, M=Keck/MOSFIRE (Band *H* or *K*), D=Keck/DEIMOS, G=Gemini/GNIRS. [b]Specific observing dates are not given for the FORS2 and VIMOS data as they were observed as part of a VLT large programme over a period of more than three years. [c]For multi-object spectroscopy, wavelength coverage varies with source position on the slit-mask therefore the quoted range is the *typical* wavelength range.

We note that the redshifts for ALESS 061.1 and ALESS 065.1 were determined from ALMA detections of [CII]$\lambda158\mu$m in Swinbank et al. (2012) and we allocate a 'secure' quality flag to their redshifts (see Section 2.5).

For all observations, flux calibration was carried out using standard stars to remove filter response, but in the case of FORS2 and VIMOS, one standard star was utilised per observing run.

Once all the data were collected from the different spectrographs, we collated the information for each ALESS SMG. Some ALESS SMGs were covered with five different instruments (see Table. 2.3) and we combined the information to determine the redshifts of the ALESS SMGs. The instruments used to observe each SMG are listed in Table. 2.3 and the number of SMGs covered with each pointing for each instrument is listed in Table. 2.1.

2.5   Analysis

2.5.1   Redshift identification

To determine redshifts for the ALESS SMGs, all spectra were interactively examined in both one and two dimensions and independently confirmed by two investigators (ALRD and AMS). Any emission/absorption features identified were fit with a Gaussian profile to determine their central wavelength. In the FORS2, VIMOS and DEIMOS data the most commonly identified lines were Lyα and [OII]. Whereas, in the NIR spectra we were frequently able to detect Hα and [OIII] $\lambda\lambda$4959, 5007 (see Tables. 2.2 and 2.3).

We assigned four different quality flags to our data:

1. Q=1 is a secure redshift where multiple lines were identified,

2. Q=2 is a relatively secure redshift but derived from only one or two bright detected lines,

3. Q=3 is a tentative redshift based on one or two tentative (low signal-to-noise)

lines and often using the photometric redshifts as a guide to the line iden-
tification. These redshifts are therefore not independent of the photometric
redshifts and are thus highlighted in some of the analysis,

4. Q=4 means no lines or continuum were detected or no redshift could be de-
termined.

Representative examples of spectra from which Q=1 redshifts were determined
are shown in Fig. 2.3, giving one example for each instrument used, whilst Fig. 2.4
gives examples of spectra from which Q=2 and 3 redshifts were determined.

We also searched for literature redshifts for the ALESS SMGs and found six
matches, one of which is a secure redshift in disagreement with our Q=1 redshift.
These SMGs are flagged in Table. 2.3 but the exact redshifts given in the table are
those derived through line-fitting in this work. The following SMGs already had
secure redshifts from literature:

1. ALESS 018.1- listed as ID 66 in Casey et al. (2011), with a redshift of $z = 2.252$ derived from an Hα detection with the Infrared Spectrometer And Array Camera (ISAAC) on the VLT.

2. ALESS 057.1- listed as ID 112a in Szokoly et al. (2004) with a redshift of $z = 2.940$ derived from detections of HeII, Ovi and Nv with FORS1/FORS2. It is classed as a QSO with strong high-ionisation emission lines.

3. ALESS 067.1- listed as ECDFS-45 in Kriek et al. (2008) with a redshift of $z = 2.122$, derived from emission lines in NIR spectra observed with GNIRS.

4. ALESS 073.1- listed as GDS J033229.29-275619.5 in the Vanzella, et al. (2008) collection of 1019 spectroscopic redshifts for GOODS/CDFS. The redshift of $z = 4.762$ was determined via the detection of Lyα and Nv using FORS2. Vanzella, et al. (2008) also class this source as a QSO.

5. ALESS 098.1- listed as ID J033129 in Casey et al. (2011). The redshift, $z = 1.4982$ is derived through a tentative detection of Hα, however, it is also
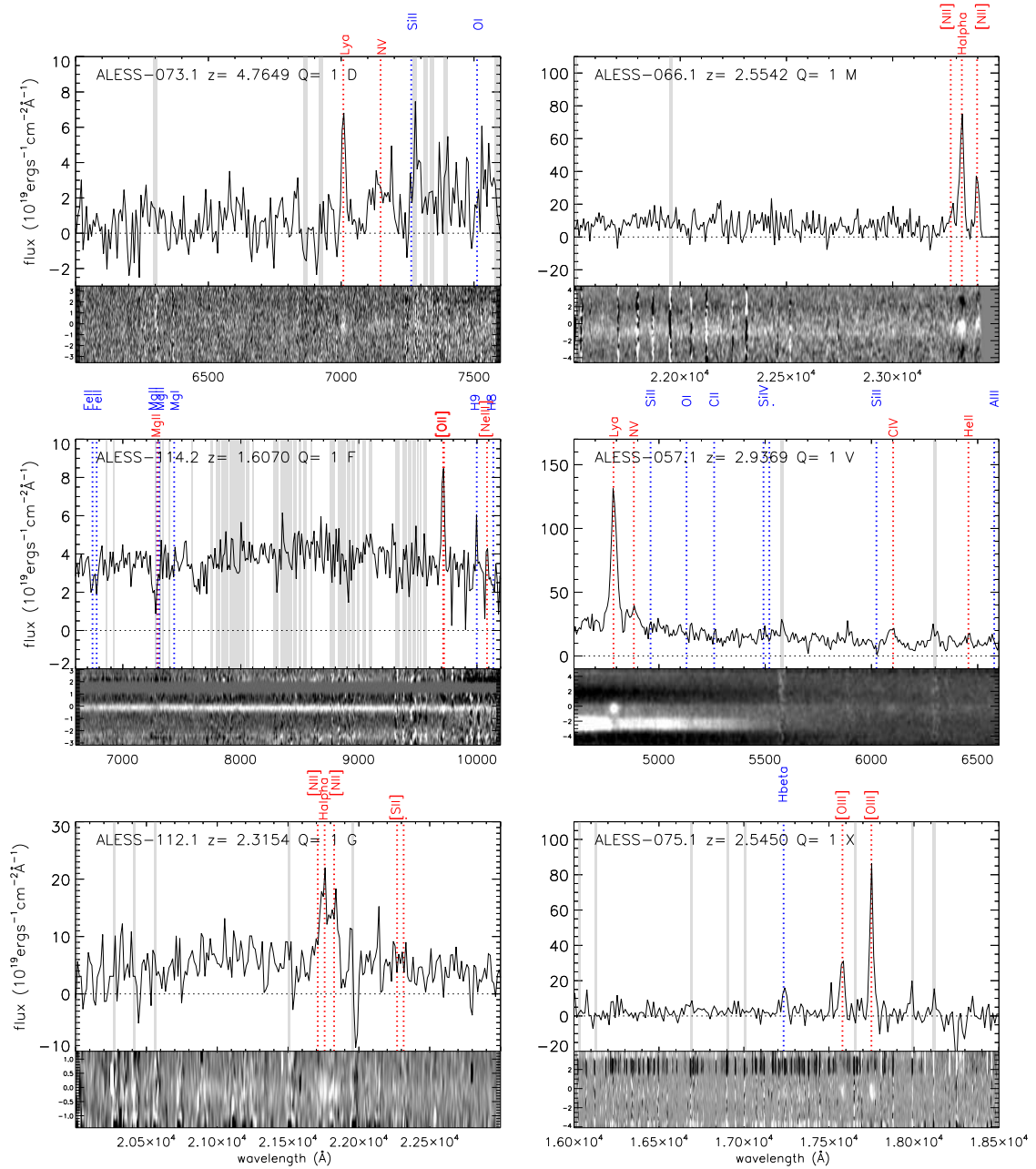
Figure 2.3: Representative 1D and 2D Q=1 spectra of ALESS SMGs from each spectrograph used. The strongest skylines are marked as grey regions and the flux at these wavelengths has been set to the median of the spectrum for display purposes. *Top left:* ALESS 073.1- Lyα and Nv are clearly detected in this DEIMOS spectrum (rebinned to ∼6Å/bin). *Top right:* ALESS 066.1- Hα and the [NII] λλ6548, 6583 are strongly detected in this MOSFIRE *K*-band spectrum (rebinned to ∼7Å/bin). *Middle left:* ALESS 114.2- Very strong continuum, [OII] emission and absorption features of broad MgII (P-Cygni profile) and FeII are identifiable in this FORS2 spectrum (rebinned to ∼12Å/bin). *Middle right:* ALESS 057.1- X-ray AGN with very strong Lyα, Nv and CIV. The bright feature below the source continuum is contamination from higher order emission from an adjacent slit on the mask in VIMOS (rebinned to ∼7Å/bin). *Bottom left:* ALESS 112.1- strong Hα and [NII] are identifiable in this GNIRS spectrum (rebinned to ∼13Å/bin). *Bottom right:* ALESS 075.1- Strong detections of [OIII] λλ4959, 5007 and Hβ in this X-SHOOTER NIR spectrum (rebinned to ∼12Å/bin).
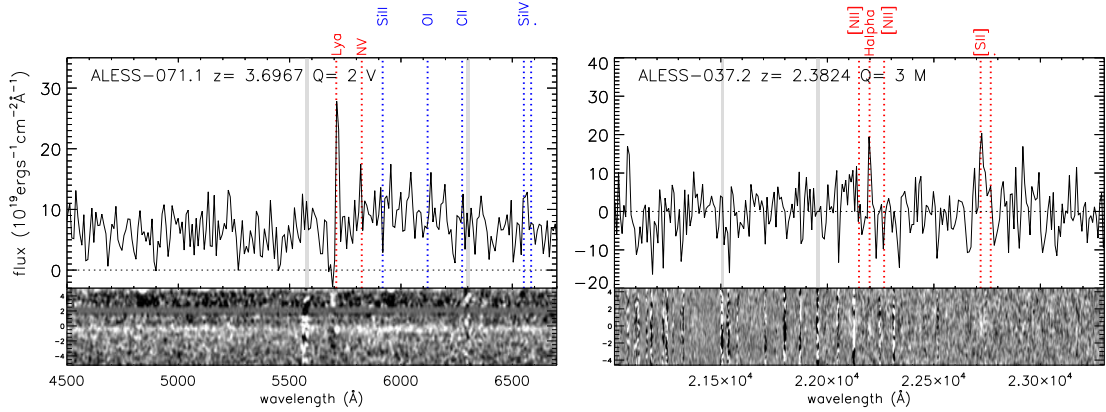
Figure 2.4: Example 1D and 2D Q=2 and 3 spectra of ALESS SMGs. Again, the strongest skylines are marked as grey regions and the flux at these wavelengths has been set to the median of the spectrum for display purposes. The spectra have been rebinned to ∼8Å/bin. *Left:* ALESS 071.1- A continuum break, very narrow Lyα and Nv are detected in this Q=2 VIMOS spectrum. There is some ambiguity in the redshift since the break is not strong, hence the Q=2 flag. *Right:* ALESS 037.2- This single line-detection is identified as Hα in this Q=3 MOSFIRE K-band spectrum.

spectroscopically-identified in the rest-frame UV in the same paper and therefore it is given a 'secure' status. This redshift is, however, in disagreement with our Q=1 redshift of $z = 1.3735$ derived from fitting to an [Oii] detection in the FORS2 observations, with a tentative detection of Hα at the same redshift under a sky line in the XSHOOTER NIR spectrum. We use our redshift in the analysis in this work.

6. ALESS 122.1- listed as radio ID 149 in Bonzini et al. (2012). The redshift of $z = 2.03$ is determined from UV ISM absorption features observed with VIMOS on the VLT. Bonzini et al. (2012) give this redshift a Q=3, which in their case indicates a 'secure' redshift.

For each instrument used, there are redshift ranges for which none of the brightest spectral features lie within the wavelength coverage of the spectrograph. The 'redshift desert' is typically described as the redshift range between which [Oii] shifts out of the range of the spectrograph and Lyα shifts into the range. Since we use various different instruments we have different redshift deserts. Our origi-

nal dual FORS2/VIMOS approach attempted to reduce the redshift desert suffered in i.e. C05, through the sole use of LRIS. For VIMOS the wavelength range is $400-670$ nm, resulting in a redshift desert of $z = 0.80-2.29$. Whereas, for FORS2, with a wavelength coverage of 600–1100nm, the redshift desert is $z = 1.95-3.90$. Similarly DEIMOS, with the GG455 blocking filter has a wavelength coverage of $\sim470-880$ nm, therefore the redshift desert extends from $z = 1.36-2.95$. It is still possible to measure redshifts in this range, mainly through the detection of CIV λ1549, CIII] λ1909 and MgII λ2800. MOSFIRE does not suffer from this same redshift desert as in the near-infrared various other emission and absorption features can be observed over a wide range of redshifts. However, other deserts exist such as the redshift ranges between which [OIII]λ5007 shifts out of the range of the spectrograph and [OII] shifts into the range, or the range between which Hα shifts out of the range of the spectrograph and [OIII]λ5007 shifts into the range. For MOSFIRE these deserts correspond to $z = 1.76-1.92$ and $z = 2.73-2.86$ for the H and K bands respectively for the [OII] to [OIII] desert and $z = 2.61-2.92$ and $z = 3.89-4.18$ for the H and K bands respectively for the [OIII] to Hα desert. XSHOOTER and GNIRS do not suffer from these redshift deserts since the wavelength coverage of XSHOOTER is $300-2480$ nm and GNIRS is $900-2560$ nm. The redshift deserts for all instruments are shown in Fig. 2.5, which gives the ALESS redshift distributions for each instrument.

A further comparison demonstrating our spectroscopic completeness is shown in Fig. 2.6 where we show the photometric redshift distribution of the ALESS SMGs, highlighting both those sources for which we were able to determine a spectroscopic redshift and those for which we were unable to determine a redshift. In both cases the MAIN catalog SMGs and MAIN+SUPP catalog SMGs are highlighted differently. Fig. 2.6 is used to determine whether we are systematically unable to determine redshifts in particular regions of redshift space. The median photometric redshift for spectroscopic failures is $z = 2.4 \pm 0.2$, compared to the median photometric redshift of those SMGs with a spectroscopic redshift and a photometric redshift of $z = 2.2\pm0.1$, which are within 1σ of each other. Furthermore, we overlay on Fig. 2.6,
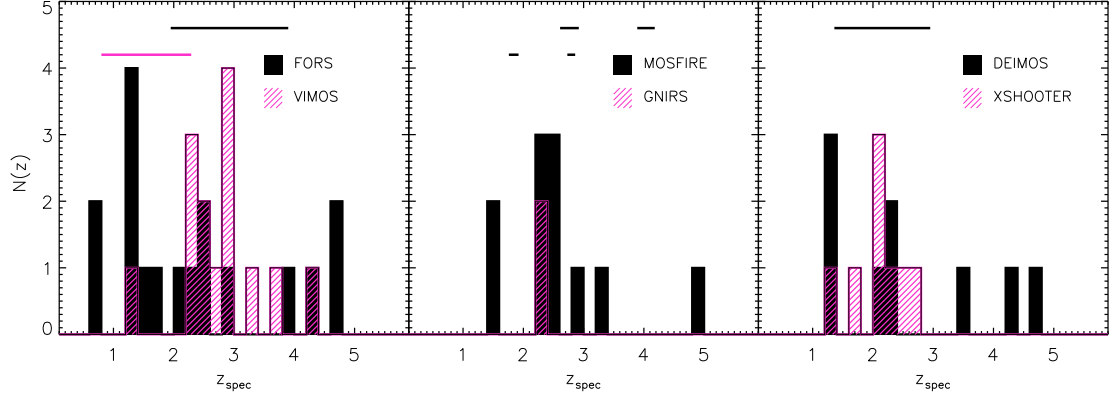
Figure 2.5: The individual redshift distributions for each spectrograph. Sources were included in these distributions if spectral features were observed with that particular instrument which were sufficient to determine a redshift, without the aid of other instruments. There are therefore some cases where the same source appears in multiple distributions, as identifiable features were observed with various spectrographs. The 'redshift deserts' are shown as solid lines at the top of all the figures. For FORS2, VIMOS and DEIMOS the deserts are based on the redshift range between which [OII] shifts out of the range of the spectrograph and Lyα shifts into the range. For MOSFIRE the deserts are based on the same concept but for [OIII] to [OII] and Hα to [OIII]. The K-band deserts are the lower lines and the H-band deserts are the upper lines. Some redshifts have still been measured even in 'desert' regions and this is typically through observations of other features such as UV ISM absorption, CIV emission/absorption, CIII] emission, MgII emission/absorption.

the ratio of $N(z_{\mathrm{spec}})/(N(z_{\mathrm{spec}})+N(z_{\mathrm{phot}}))$, where $N(z_{\mathrm{spec}})$ is the photometric redshift distribution of SMGs with spectroscopic redshifts, and $N(z_{\mathrm{phot}})$ is the photometric redshift distribution of those SMGs without spectroscopic redshifts, and we find that the ratio remains flat at a value of ~ 0.6 across $z \sim 1-4$ with a dip at $z = 4-5$ down to ~ 0.3 demonstrating that it is marginally more difficult to determine spectroscopic redshifts for very high-redshift SMGs, as it is more difficult to detect their optical counterparts. Therefore there is no particular region of redshift space for which it is more difficult to measure a spectroscopic redshift in our sample.

For most ALESS SMGs we have more than one spectrum and for many we have coverage in UV, visible and NIR. Thus, for those SMGs with Q=1 redshifts, generally we have been able to determine the redshifts using multiple strong lines across a large wavelength range. Ideally the redshift is determined from a nebular line i.e. Hα, [OII] or [OIII]. In some cases the only strong line available is Lyα, however, this is only used to determine the redshift if it is the sole detected line.
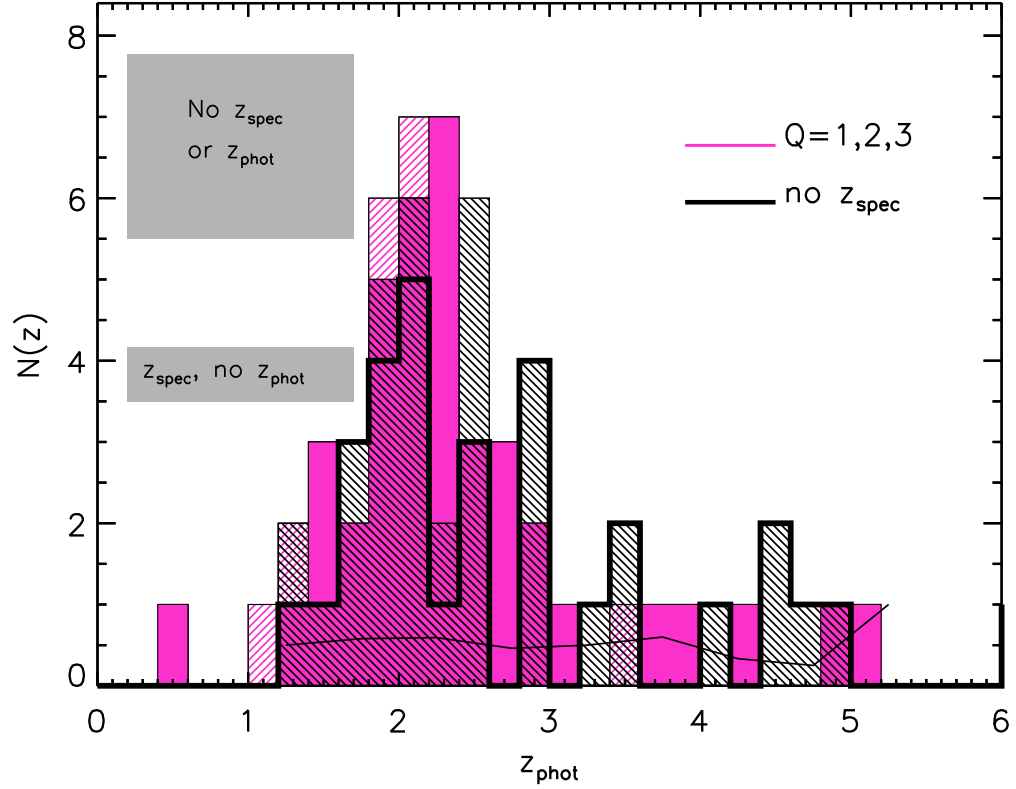
Figure 2.6: The photometric redshift distribution of the ALESS SMGs. The magenta solid and hashed histograms show the photometric redshifts for the ALESS SMGs in the MAIN and MAIN+SUPP catalogs respectively, for which we determined a Q=1, 2 or 3 spectroscopic redshift. The black hashed histogram shows the photometric redshift distribution for the ALESS SMGs (MAIN+SUPP) for which we were unable to determine a redshift (no z_{spec}). The thick solid histogram marks the MAIN catalog SMGs. The binsize is $\Delta z = 0.2$. The grey box regions show the number of sources with either no spectroscopic redshift and no photometric redshift, or a spectroscopic redshift but no photometric redshift. These regions are placed at arbitrary positions on the plot. Overlaid on the histograms is a solid line demonstrating ratio of $\mathrm{N}(z_{\mathrm{spec}})/(\mathrm{N}(z_{\mathrm{spec}})+\mathrm{N}(z_{\mathrm{phot}}))$, where $\mathrm{N}(z_{\mathrm{spec}})$ is the photometric redshift distribution of SMGs with spectroscopic redshifts, and $\mathrm{N}(z_{\mathrm{phot}})$ is the photometric redshift distribution of those SMGs without spectroscopic redshifts. A binsize of $\Delta z = 0.5$ was used to calculate this ratio. The line is relatively flat, demonstrating that there is no particular region of redshift space for which it is more difficult to determine a spectroscopic redshift than a photometric one.

Lyα frequently exhibits a distinctly asymmetric profile with a sharp cut-off on the blue side of the emission line. This asymmetry is observed almost ubiquitously in high-redshift Lyα emitters (i.e. Shapley et al. 2003) and is caused by the resonant neutral hydrogen absorption in the ISM of the galaxy along the line of sight. Often the redshifted emission arises from a strong galactic wind where photons can escape by scattering from the far-side of the outflow, redshifting them with respect to the neutral medium within the galaxies and thus allowing them to pass through the galaxy without being absorbed. In Table 2.3 the redshifts quoted for each SMG are determined as follows:

1. The systemic redshifts are determined from fitting Hα, [OII] $\lambda\lambda$3726,3729, [OIII] $\lambda\lambda$4959,5007 and/or Hβ and in some cases, if none of these lines are available we use HeII or CIII] λ1909 in emission if they are sufficiently narrow. All these lines should be associated with HII regions and stellar emission and should therefore be good tracers of the systemic redshift, in particular Hα. HeII λ1640 in emission, if narrow, is typically a nebular recombination emission line, however it can originate from the stellar winds from Wolf-Rayet stars, making it less reliable as a systemic velocity tracer than the typical nebular lines (i.e. Hα). CIII] λ1909, is a collisionally-excited semi-forbidden electron dipole transition which should not be affected by outflowing gas. If many nebular lines are detected the recorded redshift is that of the mean of the redshifts determined from fitting to the different nebular lines.

2. If no nebular lines are detected, we take a mean of the fits to the other detected lines, such as UV ISM absorption lines of CII λ1334.53, SiIV λ1393.76 and SiII λ1526.72, or other strong lines such as NV λ1240, MgII λ2800 and HeII.

3. If Lyα is the *only* detected line then the redshift is determined via fitting to this line. Similarly, where possible we avoid using CIV λ1549 in redshift measurements, since it can be strongly influenced by winds and frequently exhibits a profile which is a superposition of P-Cygni emission and absorption, nebular emission and interstellar absorption.

Table 2.2: Summary of spectroscopic features

Condition	Number of galaxies		
	MAIN	SUPP	TOTAL
TOTAL	99	32	131
Q=1	20	1	21
Q=2	8	3	11
Q=3	17	3	20
Observed with specz	45	7	52
Observed but no specz	42	15	57
Not observed	12	10	22
Lyα	21	1	22
[O II]	8	3	11
[O III]	6	0	6
Hα	11	3	14
[O III] and Hα	3	0	3
Hβ	4	0	4

For the ALESS SMGs, $\sim 30\%$ of the redshifts are determined from a single line (compared to $\sim 25\%$ in C05) and generally these redshifts are allocated Q=3 unless strong continuum features such as breaks across Lyα are also identified. Single line redshifts are typically backed up by either continuum breaks across Lyα, the absence of other emission lines that do not correspond to the proposed redshift, line profiles (i.e. asymmetric Lyα profile, close doublet of [OII] $\lambda 3726$, 3729) and photometric redshifts. In seven cases single line redshifts are based on detections of Lyα; in three cases they are determined from Hα detections in NIR spectra and in five cases they are from detections of the [OII] doublet. These Hα and [OII] single-line redshifts are predominantly determined through the lack of line detections which would correspond to a different redshift.

We summarise the main spectroscopic features that we observed in Table. 2.2 and provide detailed information on each of the 109 observed SMGs in Table. 2.3.

Table 2.3: ALESS spectroscopic redshift catalog

ALESS ID	RA (J2000)	DEC (J2000)	$z_{\rm spec}$	$Q_{\rm spec}$	$z_{\rm phot}^a$	M/S^b	Instruments^c	Notes
ALESS 001.1	53.310270	-27.937366	4.9540	3	$4.34^{+2.66}_{-1.43}$	M	GMX	[OII] in M-K
ALESS 001.2	53.310059	-27.936562	-99	4	$4.65^{+2.34}_{-1.02}$	M	FVX	BLANK
ALESS 001.3	53.309069	-27.936759	-99	4	$2.85^{+0.20}_{-0.30}$	M	X	BLANK
ALESS 002.1	53.261188	-27.945211	2.1913	3	$1.96^{+0.27}_{-0.20}$	M	DV	poss. CIII] em in D
ALESS 002.2	53.262800	-27.945252	-99	4	-	M	D	BLANK
ALESS 003.1	53.339603	-27.922304	4.2373	3	$3.90^{+0.50}_{-0.59}$	M	FMV	poss. Lyα em in F+V
ALESS 003.2	*53.342461*	*-27.922486*	*-99*	*4*	$1.44^{+0.43}_{-0.38}$	*S*	*M*	*BLANK*
ALESS 003.3	*53.336294*	*-27.920555*	*-99*	*4*	*-*	*S*	*M*	*BLANK*
ALESS 003.4	*53.341644*	*-27.919379*	*-99*	*4*	*-*	*S*	*M*	*BLANK*
ALESS 005.1	52.870467	-27.985840	-99	4	$2.86^{+0.05}_{-0.04}$	M	DMX	BLANK
ALESS 006.1	53.237331	-28.016856	2.3338	1	$0.45^{+0.06}_{-0.04}$	M	GX	cont. from bright sources above SMG; Lyα em ($z = 2.3295$) and CIV em ($z = 2.3314$) in X-UVB; Hα and [OIII]5007 in G ($z = 2.3338$)
ALESS 007.1	53.314242	-27.756750	2.6923	1	$2.50^{+0.12}_{-0.16}$	M	DFXS	strong cont.; z from Hα in X-NIR; HeII in X-VIS ($z = 2.6901$)
ALESS 007.2	*53.312522*	*-27.758499*	*-99*	*4*	*-*	*S*	*D*	*BLANK*
ALESS 009.1	53.047244	-27.869981	-99	4	$4.50^{+0.54}_{-2.33}$	M	D	BLANK
ALESS 010.1	53.079418	-27.870781	0.7616	1	$2.02^{+0.09}_{-0.09}$	M	FV	[OII] in V; [OII] ($z = 0.7613$), [OIII]4959 ($z = 0.7619$), Hβ ($z = 0.7617$) in F; z is mean from [OII], [OIII], Hβ, possible lens
ALESS 011.1	53.057688	-27.933403	2.6832	2	$2.83^{+1.88}_{-0.50}$	M	FV	Lyα em in V, no cont.
ALESS 013.1	53.204132	-27.714389	-99	4	$3.25^{+0.64}_{-0.46}$	M	DG	BLANK
ALESS 014.1	52.968716	-28.055300	-99	4	$4.47^{+2.54}_{-0.88}$	M	VX	BLANK
ALESS 015.1	53.389034	-27.991547	-99	4	$1.93^{+0.62}_{-0.33}$	M	DFGVX	BLANK
ALESS 015.2	*53.391876*	*-27.991724*	*-99*	*4*	*-*	*S*	*M*	*BLANK*
ALESS 015.3	53.389976	-27.993176	3.4252	3	-	M	DM	Lyα em ($z = 3.4399$) and CIV em ($z = 3.4106$) in D
ALESS 015.6	*53.388192*	*-27.995048*	*-99*	*4*	*-*	*S*	*M*	*BLANK*
ALESS 017.1	53.030410	-27.855765	1.5397	1	$1.51^{+0.10}_{-0.07}$	M	DFMV	strong cont.; z from Hα in M-H; MgII abs in F ($z = 1.5382$)

Continued on next page

Table 2.3 – *Continued from previous page*

ALESS ID	RA (J2000)	DEC (J2000)	z_{spec}	Q_{spec}	z_{phot}^a	M/S[b]	Instruments[c]	Notes
ALESS 017.2	*53.034437*	*-27.855470*	*2.4431*	*3*	$2.10^{+0.65}_{-1.37}$	*S*	*M*	*poss. Hα in M-K*
ALESS 017.3	*53.030718*	*-27.859423*	*-99*	*4*	$2.58^{+0.16}_{-0.32}$	*S*	*D*	*BLANK*
ALESS 018.1[d]	53.020343	-27.779927	2.2520	1	$2.04^{+0.10}_{-0.06}$	M	V	cont. in V; archival z from Casey+11
ALESS 019.1	53.034401	-27.970609	-99	4	$2.41^{+0.17}_{-0.11}$	M	FV	BLANK
ALESS 020.1	*53.319834*	*-28.004431*	*-99*	*4*	$2.58^{+0.16}_{-0.32}$	*S*	*DFV*	*cont. in F*
ALESS 020.2	*53.317807*	*-28.006470*	*-99*	*4*	*-*	*S*	*D*	*BLANK*
ALESS 022.1	52.945494	-27.544250	-99	4	$1.88^{+0.18}_{-0.23}$	M	FV	cont. in F+V
ALESS 023.1	53.050039	-28.085128	-99	4	$4.99^{+2.01}_{-2.55}$	M	V	BLANK
ALESS 025.1	52.986997	-27.994259	2.8719	3	$2.24^{+0.07}_{-0.17}$	M	V	Lyα + break, cont.
ALESS 029.1	53.403749	-27.969259	1.4389	2	$2.66^{+2.94}_{-0.76}$	M	DGMV	Hα in M-H
ALESS 031.1	52.957448	-27.961322	-99	4	$2.89^{+1.80}_{-0.41}$	M	FVX	BLANK
ALESS 034.1	*53.074833*	*-27.875910*	*2.5115*	*2*	$1.87^{+0.29}_{-0.32}$	*S*	*M*	*broad Hα in M-K*
ALESS 035.1	52.793776	-27.620948	-99	4	*-*	M	V	BLANK
ALESS 037.2	53.401514	-27.896742	2.3824	3	$4.87^{+0.22}_{-0.40}$	M	M	Hα ($z = 2.3824$) and [SII] ($z = 2.3831$)
ALESS 038.1	*53.295153*	*-27.944501*	*-99*	*4*	$2.47^{+0.11}_{-0.05}$	*S*	*D*	*strong cont.+emission lines from contaminating source*
ALESS 039.1	52.937629	-27.576871	-99	4	$2.44^{+0.17}_{-0.23}$	M	X	poss. faint lines, no cont.
ALESS 041.1	52.791959	-27.876850	2.5460	2	$2.75^{+4.25}_{-0.72}$	M	FV	strong cont. in F+V; CIII]1909 em ($z = 2.5459$),
								CII]2326 em ($z = 2.5500$) in F; cont. break in V
ALESS 041.3	52.792927	-27.878001	-99	4	*-*	M	M	weak cont.
ALESS 043.1	53.277670	-27.800677	-99	4	$1.71^{+0.20}_{-0.12}$	M	DFV	possible faint lines, no cont.
ALESS 043.3	*53.276120*	*-27.798534*	*-99*	*4*	*-*	*S*	*D*	*BLANK*
ALESS 045.1	53.105255	-27.875148	-99	4	$2.34^{+0.26}_{-0.67}$	M	FV	no cont.; poss. Lyα em $z = 2.9690$ from V and CIV $z = 2.9867$ from F
ALESS 046.1	*53.402937*	*-27.547072*	*-99*	*4*	*-*	*S*	*FV*	*faint cont. in F*
ALESS 049.1	52.852998	-27.846406	2.9417	2	$2.76^{+0.11}_{-0.14}$	M	DFV	strong cont. in F + V; HeII em ($z = 2.9417$), CIV em ($z = 2.9436$),
								broad CIII] em in F; Lyα ($z = 2.9516$) in V
ALESS 049.2	52.851956	-27.843914	-99	4	$1.47^{+0.07}_{-0.10}$	M	M	BLANK

Continued on next page

Table 2.3 – *Continued from previous page*

ALESS ID	RA (J2000)	DEC (J2000)	z_{spec}	Q_{spec}	z_{phot}^a	M/S[b]	Instruments[c]	Notes
ALESS 051.1	52.937754	-27.740922	1.3638	3	$1.22^{+0.03}_{-0.06}$	M	FV	strong cont. in F+V, [OII] ($z=1.3638$) and break ~ 8000Å
								and poss. MgII em ($z=1.3681$) in F
ALESS 055.1	53.259242	-27.676513	1.3564	2	$2.05^{+0.15}_{-0.13}$	M	DF	strong cont. in F+D; MgII em ($z=1.3556$)
								and H+K abs. (K abs. $z=1.3572$) in F
ALESS 055.2	53.258983	-27.678148	-99	4	-	M	D	BLANK
ALESS 057.1[d]	52.966348	-27.890850	2.9369	1	$2.95^{+0.05}_{-0.10}$	M	FV	cont. + Lyα em ($z=2.9387$), CIV em ($z=2.9332$),
								HeII em ($z=2.9388$) in V
ALESS 059.2	53.265897	-27.738390	-99	4	$2.09^{+0.78}_{-0.29}$	M	X	BLANK
ALESS 061.1	53.191128	-28.006490	4.4190	1	$6.52^{+0.36}_{-0.34}$	M	A	ALMA [CII]158μm
ALESS 062.1	*53.150677*	*-27.580258*	*-99*	*4*	*-*	*S*	*D*	*BLANK*
ALESS 062.2	*53.152410*	*-27.581619*	*1.3614*	*1*	*$1.35^{+0.08}_{-0.11}$*	*S*	*DFV*	*[OII] in D+F*
ALESS 063.1	53.285193	-28.012179	-99	4	$1.87^{+0.10}_{-0.33}$	M	G	poss. faint em lines
ALESS 065.1	53.217771	-27.590630	4.4445	1	-	M	AD	z from ALMA [CII158]μm, Lyα
ALESS 066.1	53.383053	-27.902645	2.5542	1	$2.33^{+0.05}_{-0.04}$	M	FMV	Hα and [NII] in M; lensed?
ALESS 067.1[d]	53.179981	-27.920649	2.1230	1	$2.14^{+0.05}_{-0.09}$	M	FVX	cont. in F+V; Hα, [OIII]5007 in X-NIR; merging with 067.2
ALESS 067.2	53.179253	-27.920749	2.1230	3	$2.05^{+0.15}_{-0.13}$	M	X	BLANK but likely merging with 067.1
ALESS 068.1	53.138888	-27.653770	-99	4	-	M	VX	BLANK
ALESS 069.1	52.890731	-27.992345	4.2071	3	$2.34^{+0.27}_{-0.44}$	M	D	single line, poss. Lyα with asymmetric profile
ALESS 069.2	52.892226	-27.991361	-99	4	-	M	M	BLANK
ALESS 069.3	52.891524	-27.993990	-99	4	-	M	DM	BLANK
ALESS 070.1	52.933425	-27.643200	2.0918	3	$2.28^{+0.05}_{-0.06}$	M	FX	strong cont. in F; poss. Lyα in X-UVB
ALESS 071.1	53.273528	-27.557831	3.6967	2	$2.48^{+0.21}_{-0.11}$	M	V	Lyα ($z=3.7006$); very bright line; Nv em ($z=3.6927$)
ALESS 072.1	53.168322	-27.632807	-99	4	-	M	DX	poss. faint lines, no cont.
ALESS 073.1[d]	53.122046	-27.938807	4.7649	1	$5.18^{+0.43}_{-0.45}$	M	DF	very broad Lyα and Nv em in D+F; Lyα ($z=4.7648$),
								Nv ($z=4.7649$)
ALESS 074.1	53.288112	-27.804774	-99	4	$1.80^{+0.13}_{-0.13}$	M	DFV	BLANK

Continued on next page

Table 2.3 – *Continued from previous page*

ALESS ID	RA (J2000)	DEC (J2000)	z_{spec}	Q_{spec}	z_{phot}^a	M/S^b	Instruments^c	Notes
ALESS 075.1	52.863303	-27.930928	2.5450	1	$2.39^{+0.08}_{-0.06}$	M	FVX	very interesting source; strong cont. in V+F; [OIII]4959 ($z = 2.5452$), [OIII]5007 ($z = 2.5447$) broad red components to [OIII], Hβ ($z = 2.5451$), [OII] doublet ($z = 2.5446$), Hα ($z = 2.5452$), Lyα in X ($z = 2.5440$)
ALESS 075.2	*52.865276*	*-27.933116*	*2.2944*	*2*	*$0.39^{+0.02}_{-0.03}$*	*S*	*DM*	*Hα, [NII] ($z = 2.2941$), [SII] ($z = 2.2886$) in M-K*
ALESS 075.4	52.860715	-27.932144	-99	4	$2.10^{+0.29}_{-0.34}$	M	DM	BLANK
ALESS 076.1	53.384731	-27.998786	3.3895	2	-	M	DFMV	[OIII]5007 + [OIII]4959 in M; poss. Lyα ($z \sim 3.3984$) in V
ALESS 079.1	53.088064	-27.940830	-99	4	$2.04^{+0.63}_{-0.31}$	M	D	BLANK
ALESS 079.2	53.090004	-27.939988	1.7693	1	$1.55^{+0.11}_{-0.18}$	M	FVX	Strong Hα, [NII]6548, 6583 in X-NIR; structured lines- 2 components
ALESS 079.4	53.088261	-27.941808	-99	4	-	M	D	BLANK
ALESS 080.1	52.928347	-27.810244	4.6649	3	$1.96^{+0.16}_{-0.14}$	M	FV	poss Lyα in F
ALESS 080.2	52.927570	-27.811376	-99	4	$1.37^{+0.17}_{-0.08}$	M	D	BLANK
ALESS 080.5	*52.923654*	*-27.806318*	*1.3078*	*3*	*-*	*S*	*D*	*tentative [OII] + [NeIII]*
ALESS 081.1	*52.864805*	*-27.744336*	*-99*	*4*	*$1.70^{+0.29}_{-0.20}$*	*S*	*V*	*BLANK*
ALESS 082.1	53.224989	-27.637470	-99	4	$2.10^{+3.27}_{-0.44}$	M	DFV	BLANK
ALESS 084.1	52.977090	-27.851568	3.9651	3	$1.92^{+0.09}_{-0.07}$	M	DFM	Lyα ($z = 3.9639$), Nv ($z = 3.9672$) in F; cont. in F
ALESS 084.2	52.974388	-27.851207	-99	4	$1.75^{+0.08}_{-0.19}$	M	DF	cont. in F; poss faint lines
ALESS 087.1	53.212016	-27.528187	2.3086	1	$3.20^{+0.08}_{-0.47}$	M	FV	Lyα em ($z = 2.3188$), SiIV abs ($z = 2.3050$), SiII abs ($z = 2.3019$) in V; Lyα offset from cont.
ALESS 088.1	52.978175	-27.894858	1.2679	1	$1.84^{+0.12}_{-0.11}$	M	FVMX	[OII] ($z = 1.2679$); [OII]3726,3729 visible in X-VIS
ALESS 088.2	52.980797	-27.894529	2.5192	3	-	M	DM	CII]2326 em ($z = 2.5227$), CIV em ($z = 2.5156$) in D
ALESS 088.5	52.982524	-27.896446	2.2941	2	$2.30^{+0.11}_{-0.50}$	M	DFV	strong cont. in V, poss break; Lyα em ($z = 2.3021$), HeII ($z = 2.2941$) in V
ALESS 088.11	52.978949	-27.893785	2.3583	3	$2.57^{+0.04}_{-0.12}$	M	D	CIII] em ($z = 2.3585$), Lyα em ($z = 2.3581$) + break
ALESS 089.1	*53.202879*	*-28.006079*	*0.6830*	*3*	*$1.17^{+0.06}_{-0.15}$*	*S*	*F*	*bright [OII] + cont*
ALESS 094.1	53.281640	-27.968281	-99	4	$2.87^{+0.37}_{-0.64}$	M	DV	BLANK
ALESS 098.1^d	52.874654	-27.956317	1.3745	1	$1.63^{+0.17}_{-0.09}$	M	DFMVX	[OII] ($z = 1.3745$) brightest in F; cont. in M and F,

Continued on next page

Table 2.3 – *Continued from previous page*

ALESS ID	RA (J2000)	DEC (J2000)	z_{spec}	Q_{spec}	$z^a_{\rm phot}$	M/S[b]	Instruments[c]	Notes
								real Hα under sky in X-NIR
ALESS 099.1	53.215910	-27.925996	-99	4	-	M	D	BLANK
ALESS 101.1	*52.964987*	*-27.764718*	*2.7999*	*2*	*$3.49^{+03.52}_{-0.88}$*	*S*	*V*	*Lyα*
ALESS 102.1	53.398333	-27.673061	2.2960	3	$1.76^{+0.16}_{-0.18}$	M	FV	cont. in V, Lyα ($z = 2.2931$), Ciii] ($z = 2.2960$) in V
ALESS 106.1	*52.915187*	*-27.944236*	*-99*	*4*	*$7.00^{+0.00}_{-4.07}$*	*S*	*DM*	*BLANK*
ALESS 107.1	52.877082	-27.863647	2.9965	3	$3.75^{+0.09}_{-0.08}$	M	VM	Lyα em ($z = 2.9757$), Civ em ($z = 2.9965$) in V; cont. in V+M;
								poss. [Oii], [Oiii] in M
ALESS 107.3	52.878013	-27.865465	-99	4	$2.12^{+1.54}_{-0.81}$	M	D	BLANK
ALESS 110.1	52.844411	-27.904784	-99	4	$2.55^{+0.70}_{-0.50}$	M	FMV	BLANK
ALESS 110.5	52.845677	-27.904005	-99	4	-	M	DM	BLANK
ALESS 112.1	53.203596	-27.520362	2.3154	1	$1.95^{+0.15}_{-0.26}$	M	FGV	Lyα em ($z = 2.3122$) + cont. in V , Hα ($z = 2.3145$),
								poss [Oiii]5007 ($z = 2.3157$), Hβ em ($z = 2.3160$) in G
ALESS 114.2	52.962945	-27.743693	1.6070	1	$1.56^{+0.07}_{-0.07}$	M	FV	strong cont in F+V, [Oii] doublet in F ($z = 1.6070$)
ALESS 115.1	53.457070	-27.709609	3.3631	3	-	M	V	cont., poss Lyα em ($z = 3.3631$)
ALESS 116.1	52.976342	-27.758039	-99	4	$3.54^{+1.47}_{-0.87}$	M	FV	BLANK
ALESS 116.2	52.976826	-27.758735	-99	4	$4.02^{+1.19}_{-2.19}$	M	F	BLANK
ALESS 118.1	52.841347	-27.828161	2.3984	3	$2.26^{+0.50}_{-0.23}$	M	DFV	strong cont in F+V, Lyα abs + break, Civ em ($z = 2.3984$) in V
ALESS 119.1	53.235993	-28.056988	-99	4	$3.50^{+0.95}_{-0.35}$	M	V	BLANK
ALESS 122.1[d]	52.914768	-27.688792	2.0232	1	$2.06^{+0.05}_{-0.06}$	M	FV	very strong blue cont. and abs. lines. V: Cii] abs ($z = 2.0197$),
								Siiv abs ($z = 2.0229$), HeII em ($z = 2.0282$),
								VERY broad Civ and SiII blended abs.; Ciii] ($z = 2.0222$).
								F: FeII 2344, FeII 2375, FeII 2383 abs
ALESS 124.1	53.016843	-27.601769	-99	4	$6.07^{+0.94}_{-1.16}$	M	FV	poss faint lines
ALESS 126.1	53.040033	-27.685466	-99	4	$1.82^{+0.28}_{-0.08}$	M	V	BLANK

NOTES: The 22 ALESS SMGs not targeted in our spectroscopy programme (and without redshifts from literature) are not listed here. The SUPP SMGs are shown in italics.

$z_{spec} = -99$ means we could determine a spectroscopic redshift. ^{a}Photometric redshifts from S14. Those SMGs without a photometric redshift have poor photometric constraints (detections in < 4 bands). ^{b}M=MAIN catalog, S=SUPP catalog. ^{c}F=VLT/FORS2, V=VLT/VIMOS, X=VLT/XSHOOTER, M=Keck/MOSFIRE (Band H or K), D=Keck/DEIMOS, G=Gemini/GNIRS. ^{d}These redshifts are the six redshifts which also have literature spectroscopic redshifts described in Section 2.5.

2.5.2 Sample properties

We now discuss some of the characteristics of the ALESS SMGs and how these characteristics may have influenced our spectroscopic completeness. Throughout our analysis we compare to the C05 SMG sample in order to understand the relative sample selection and properties. The C05 sample comprised a radio-identified subset of SMGs.

In Fig. 2.7 we show the distributions of the R, z, 4.5μm magnitudes and $1.4\,$GHz flux density for the ALESS SMGs, showing only the 109/131 SMGs which were targeted in our spectroscopy programmes. The median R-band magnitude of the ALESS SMGs with spectroscopic redshifts is $R = 24.1 \pm 0.2$ (comparable to 24.3 ± 0.2 in C05) whereas the median magnitude of all targeted ALESS SMGs (with or without spectroscopic redshifts) is $R = 24.3 \pm 0.2$. In the z-band, the median apparent magnitude of the ALESS SMGs with spectroscopic redshifts is $z = 23.1 \pm 0.2$, compared to $z = 23.2 \pm 0.2$ for all targeted ALESS SMGs. In the mid-infrared, the median magnitude in IRAC 4.5μm is $m_{4.5\mu\mathrm{m}} = 20.9 \pm 0.2$ for the ALESS SMGs with spectroscopic redshifts, with a median of $m_{4.5\mu\mathrm{m}} = 21.2 \pm 0.1$ for all 109 targeted SMGs. As noted in S14, at $3.6\,\mu$m the C05 sample of radio-detected SMGs are a magnitude brighter than the ALESS SMGs ($m_{3.6\mu\mathrm{m}} = 20.63 \pm 0.18$; Hainline et al. 2009). On average therefore, the ALESS SMGs for which we were able to determine a redshift are marginally brighter in R, z and $m_{4.5\mu\mathrm{m}}$ than those for which we were not able to determine a redshift. Furthermore, the ALESS SMGs are typically fainter than those presented in C05. Due to the heavy optical extinction in SMGs, we detect continuum in only $\sim 50\%$ of the 52 SMGs for which we determine a redshift, compared to $\sim 75\%$ in C05. However, we are also less biased towards AGN and lower-redshift counterparts since we do not have the prerequisite of radio detections. Radio emission may be brighter in AGN and furthermore, SMGs with $z > 3.5$ would typically fall below the radio detection limit since radio does not benefit from a negative K-correction observed at sub-mm wavelengths.

Fig. 2.8, a colour-magnitude diagram of all the SMGs targeted in our spec-

troscopy program, demonstrates that there is little difference in the $R - m_{4.5\mu m}$ colours or 4.5μm apparent magnitudes of the SMGs for which we were able to determine a redshift compared to those for which we could not determine a redshift. Only $\sim 40\%$ of the SMGs targeted in our spectroscopy programme are detected in R, whereas, $\sim 85\%$ are detected at 4.5μm. At $z \sim 2.4$ (the median redshift of the ALESS SMGs), R-band approximately traces $\sim 0.2\mu$m (the rest-frame UV) and therefore the young stars, however, this wavelength is heavily dust-obscured. Whereas, 4.5μm approximately traces the stellar bump at rest-frame 1.6μm and is therefore dominated by older stellar populations. Since our spectroscopy programme is predominantly UV-to-optical, one might expect to find that the more dust-obscured SMGs should be more difficult to determine a redshift for than the less dust-obscured sources. Also, the more dust-obscured the source, the larger the expected values of $R - m_{4.5\mu m}$ (redder colours). However, the colours of the spectroscopically-identified SMGs are only marginally (within 1σ) bluer than those for which we could not determine a redshift.
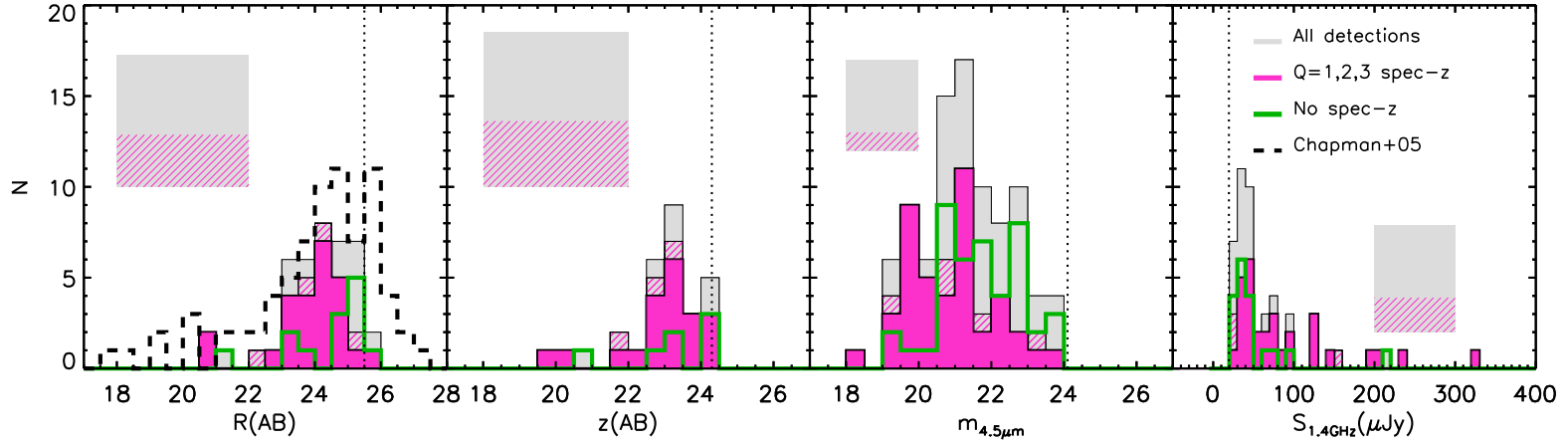
Figure 2.7: Sample properties showing histograms of the whole sample at different magnitudes (where the whole sample includes ONLY the 109/131 that were targeted in our spectroscopic survey). Grey represents the whole sample (with or without spectroscopic redshifts). Solid magenta represents the SMGs with Q=1, 2 or 3 spectroscopic redshifts in the MAIN ALESS catalog, with the magenta hashed histogram showing the SUPP SMGs. The green line represents SMGs with photometry but no spectroscopic redshift. The grey inset box shows the area covered by SMGs with no photometry in the specified band and no spectroscopic redshift, and the magenta hashed box shows the area covered by SMGs with spectroscopic redshifts but no photometry in the specified band. These inset boxes are placed at arbitrary positions. The dotted lines show the 3σ detection limits in the specified bands. We note that ALESS 020.1 has a radio flux density of $(4193 \pm 8)\,\mu\mathrm{Jy}$ and is not plotted here. The dashed line shows the comparison with the R-band magnitude distribution of the 73 C05 SMGs. The binning is 0.5 magnitudes for R, z and $m_{4.5\mu\mathrm{m}}$ and $10\mu\mathrm{Jy}$ for the $S_{1.4\mathrm{GHz}}$. This demonstrates that, on average, the SMGs for which we were able to determine a redshift are marginally brighter in R, z and $\mathrm{m}_{4.5\mu\mathrm{m}}$ than those for which we were not able to determine a redshift.

In Fig. 2.9 we study the redshifts of the ALESS SMGs versus their apparent magnitudes in K-band and at 4.5μm. K-band is typically used as a tracer of stellar mass since it is generally widely available, however, at the median redshift of our sample ($z \sim 2.4$), 4.5μm better traces the stellar mass, since observed frame 4.5μm traces rest-frame 1.3μm, which is close to the 1.6μm (H-band) stellar bump. The K-z relation is a tight correlation between the K-band magnitudes of radio host galaxies and their redshifts that was discovered by Lilly & Longair (1984). We highlight the radio-detected SMGs and demonstrate that the radio detections pick out the most massive galaxies (brightest in K-band). However, it can be observed that the relation is not tight for the ALESS SMGs, in fact, at a fixed redshift the ALESS SMGs span $4-5$ magnitudes in both K-band and at 4.5μm, across all redshifts. Serjeant et al. (2003) find a similarly large spread in the K-band magnitudes of their SMG sample, which is interpreted as either a large mass range in the SMGs (a demonstration of the diversity of the SMG population), or that there may be varying levels of heavy dust extinction even in the K-band. In Section 2.7.6 we find that the stellar masses, determined from SED model fitting, range between $\sim 2 \times 10^{9-12}$M$_\odot$ thus over three orders of magnitude, which is a significant range and may explain the large spread in the K-band magnitudes at each redshift (demonstrated in Fig. 2.25).

In order to better understand the evolution in the K-band properties of the ALESS SMGs we generate a track for a non-evolving starburst, based on the composite SED for the ALESS SMGs (shown in S14 but adapted to contain the spectroscopic redshift information in Fig. 2.23). The comparison track has been normalised to the median apparent magnitudes measured in the K and 4.5μm filters for the SED at the median redshift of $z \sim 2.4$. The evolution is consistent with this track but, as previously mentioned, with a very broad spread in magnitudes at a fixed redshift.

The 10 SMGs identified and discussed in Section 2.7.5 as lying in pairs or triples with redshift offsets of $\leq 2000\,\mathrm{km\,s^{-1}}$ are highlighted in Fig. 2.9. The median apparent magnitude at 4.5μm for the 10 SMGs is $m_{4.5\mu\mathrm{m}} = 20.8 \pm 0.6$ as compared to a median of $m_{4.5\mu\mathrm{m}} = 21.1 \pm 0.2$ for the 51 ALESS SMGs with spectroscopic red-
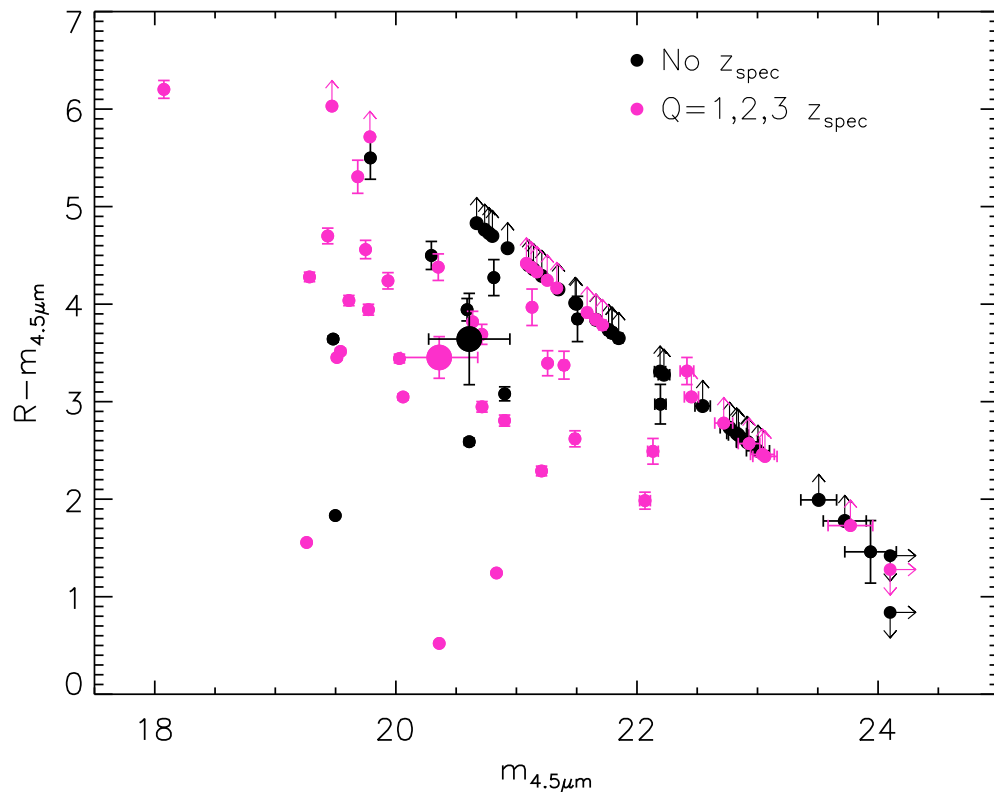
Figure 2.8: A colour-magnitude diagram of the whole spectroscopically targeted ALESS sample (i.e. 109/131 SMGs). All magnitudes are apparent. Limits are given for non-detections in R or 4.5μm and are based on 3σ detection limits in the two bands. The errors shown are 1σ errors on the photometry. The colours of the spectroscopically-identified SMGs are only marginally (within 1σ) bluer than those for which we could not determine a redshift.
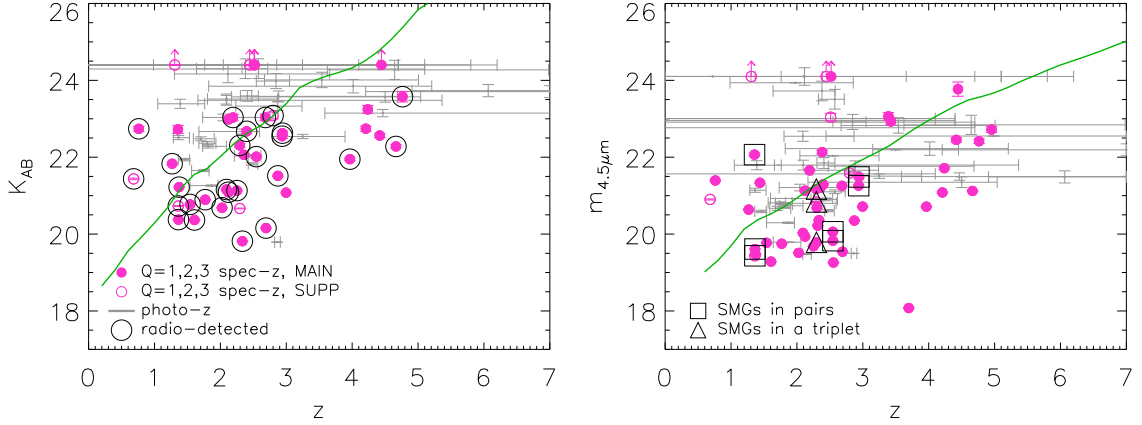
Figure 2.9: *Hubble* plots of apparent TENIS K-band ($2.15\mu m$) magnitude and apparent IRAC-$4.5\mu m$ magnitude versus redshift. Q=1, 2 and 3 spectroscopic redshifts are shown as filled circles for the MAIN SMGs and open circles for the SUPP SMGs. Photometric redshifts (where spectroscopic redshifts are not available) are shown as their ranges given in S14 and Table. 2.3. The upper limits shown are the 3σ detection limits of $K = 24.4$ and $m_{4.5\mu m} = 24.1$. Both K and $4.5\mu m$ can be used to trace the stellar mass for high-redshift galaxies. $4.5\mu m$ is a better tracer at $z \sim 2$. *Left:* We highlight the radio-detected SMGs with large black open circles. They do not follow the usually tight K-z relation but they do generally pick out the most massive galaxies (brightest in K-band). Finally, the solid green line provides the expected variation with redshift for a non-evolving fixed luminosity galaxy, assuming the composite ALESS SED determined in Fig. 2.23. It is normalised to the median apparent magnitude in K and $4.5\mu m$ at a median redshift of $z = 2.4$. *Right:* Those SMGs which are found in associations with other SMGs are highlighted with large open triangles for those found in triplets and squares for those found in pairs. Those in associations tend to be massive SMGs. This is discussed in Section 2.7.5.

shifts and $4.5\mu m$ detections. Thus the SMGs in 'associations' are slightly brighter and thus more massive than those not in 'associations', though the magnitudes are within 1σ of each other.

We note that in cases where the SMG is lensed (which we believe to be the case for at least two of the ALESS SMGs) the photometry will be dominated by the lensing source, resulting in SMGs which are at high redshift but with unusually high apparent magnitudes.

2.5.3 Spectroscopic versus photometric redshifts

S14 derived photometric redshifts for 77 of the ALESS SMGs based on $4-19$ band photometry. Photometric redshifts can produce catastrophic errors. In Fig. 2.10 we compare our spectroscopic redshifts to these photometric redshifts. We highlight the Q=3 redshifts as these are typically guided by the photometric redshifts, where the photometric redshifts are well-constrained. In general there is good agreement between the photometric and spectroscopic redshifts with a median offset of $\Delta z/(1+z_{\mathrm{spec}})) = 0.00 \pm 0.02$ and a variance of $\sigma^2 = 0.1$. The four main outliers (for which $|\Delta z/(1+z_{\mathrm{spec}}))| > 0.5$) are:

1. ALESS 006.1 for which the photometry is contaminated by an adjacent low-redshift unassociated source (the SMG is potentially lensed by the foreground contaminating galaxy);

2. ALESS 010.1 for which the Q=1 spectroscopic redshift is significantly lower than predicted by the photometry. There is a blue source slightly offset ($< 1''$) from the ALMA position and an IRAC source coincident with the ALMA position. *HST* imaging (Chen. in prep) reveals two objects and it is possible that this source is a lens. In S14 the SED is blue compared to the other sources, with a relatively flat slope between the UV and the mid-infrared emission, varying by only a factor of 100 from $3000-100000$Å. Given the proximity of the two sources, the photometry is likely to have strong contributions from the two sources, which are at different redshifts;

3. ALESS 037.2 for which the spectroscopic redshift is significantly lower than the $z > 4$ predicted by the photometry. However, the spectroscopic redshift is based on two tentative line detections at the correct separation for Hα and [S\textsc{ii}] (see Fig. 2.4, [N\textsc{ii}], if present would lie under sky lines) and the photometric redshift is poorly constrained, based on detections in only six bands and limits in a further six;

4. ALESS 101.1 which has a Q=2 redshift based on a single detection of Lyα. It

is a SUPP SMG with poor constraints on the photometric redshift and photometric detections in only five bands with no detections below J-band.

We now discuss the redshift distribution of our sample and the variation in source properties with redshift.

2.6 Results

2.6.1 Spectroscopic redshift distribution

The redshift distribution of the ALESS SMGs is shown in Fig. 2.11. In total 52 redshifts have been determined for the ALESS SMGs: 45 MAIN catalog SMGs and seven SUPP catalog SMGs. We also overlay the probability density function of the photometric redshift distribution from S14, scaled to the peak of the spectroscopic redshift distribution. The MAIN and the MAIN+SUPP SMGs are shown separately to demonstrate that the inclusion of the seven SUPP SMGs does not significantly change the shape of the redshift distribution. Furthermore, the Q=1, Q=1, 2 and Q=1, 2 and 3 distributions are shown as individual histograms. The redshifts range between $z = 0.683 - 4.954$.

In order to determine the final sample to include in our analysis it is important to analyse the effect on the sample of including the SUPP SMGs and those with only Q=3 redshifts. Karim et al. (2013) demonstrate that up to $\sim$30% of the SUPP sources are likely to be spurious. However, SUPP sources which have a counterpart are significantly less likely to be spurious. Here, we assess the validity of including the SUPP sources in further analysis. The median redshift of the MAIN catalog SMGs with Q=1, 2 or 3 redshifts is $z = 2.5 \pm 0.1$ with an interquartile range of $z = 2.1 - 3.4$, whereas the median redshift of the MAIN+SUPP catalog with Q=1, 2 or 3 redshifts is $z = 2.4 \pm 0.1$ with an interquartile range of $z = 2.1 - 3.0$. The median redshift of the Q=1, 2 and 3 SMGs in the SUPP sample alone is $z = 2.3 \pm 0.5$. The median redshifts of the samples are within 1σ of each other. Furthermore, we carry out a two-sided Kolmogorov-Smirnov (K-S) test between the MAIN and SUPP samples to test the
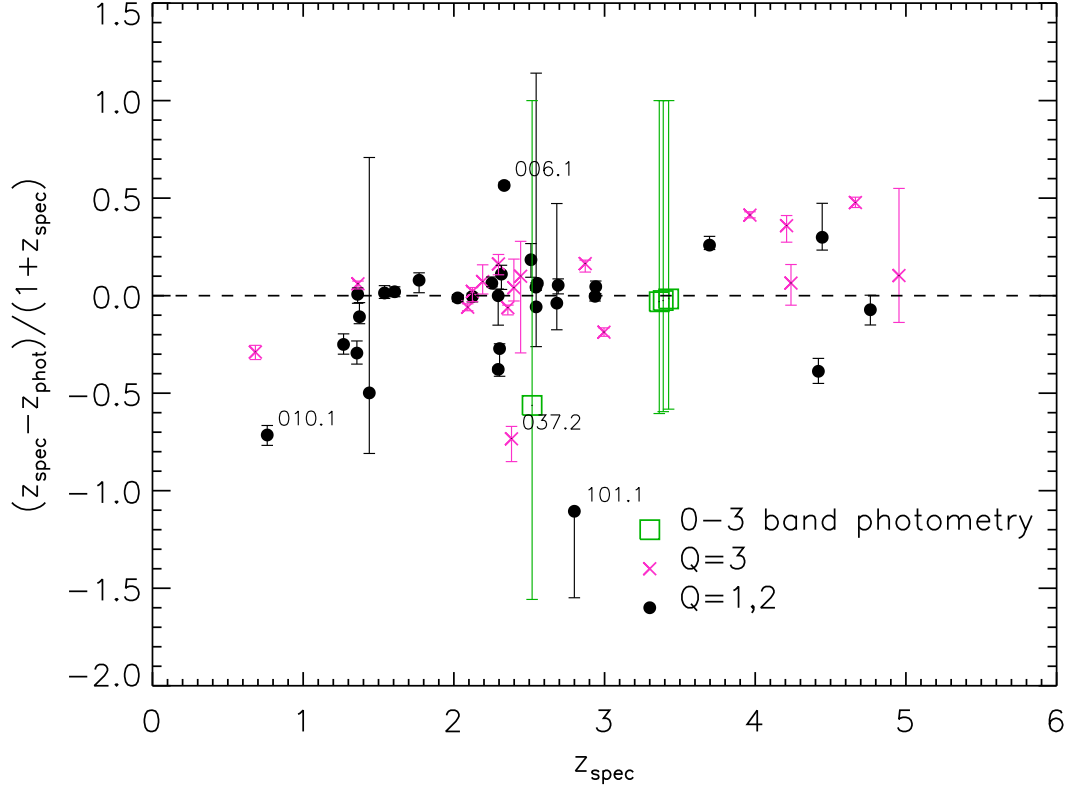
Figure 2.10: A comparison of the spectroscopically and photometrically derived ALESS redshifts (S14). The filled circles represent SMGs with a Q=1 or 2 spectroscopic redshift. The crosses represent SMGs with Q=3 spectroscopic redshift and the green squares represent those SMGs with detections in only $0-3$ bands where the redshift has been determined by assuming these SMGs have an absolute H-band magnitude distribution comparable to that of a complete sample of $z \sim 1-2$ SMGs. For SMGs with $0-1$, and $2-3$ band photometry we set the photometric redshift at the median for those sources of $z \sim 4.5$ and $z \sim 3.5$ respectively. The errors represent the errors on the photometric redshifts determined from the SED fitting in S14. There is good agreement between the photometric and spectroscopic redshifts with a median $\Delta z/(1 + z_{\mathrm{spec}}) = 0.00 \pm 0.02$.
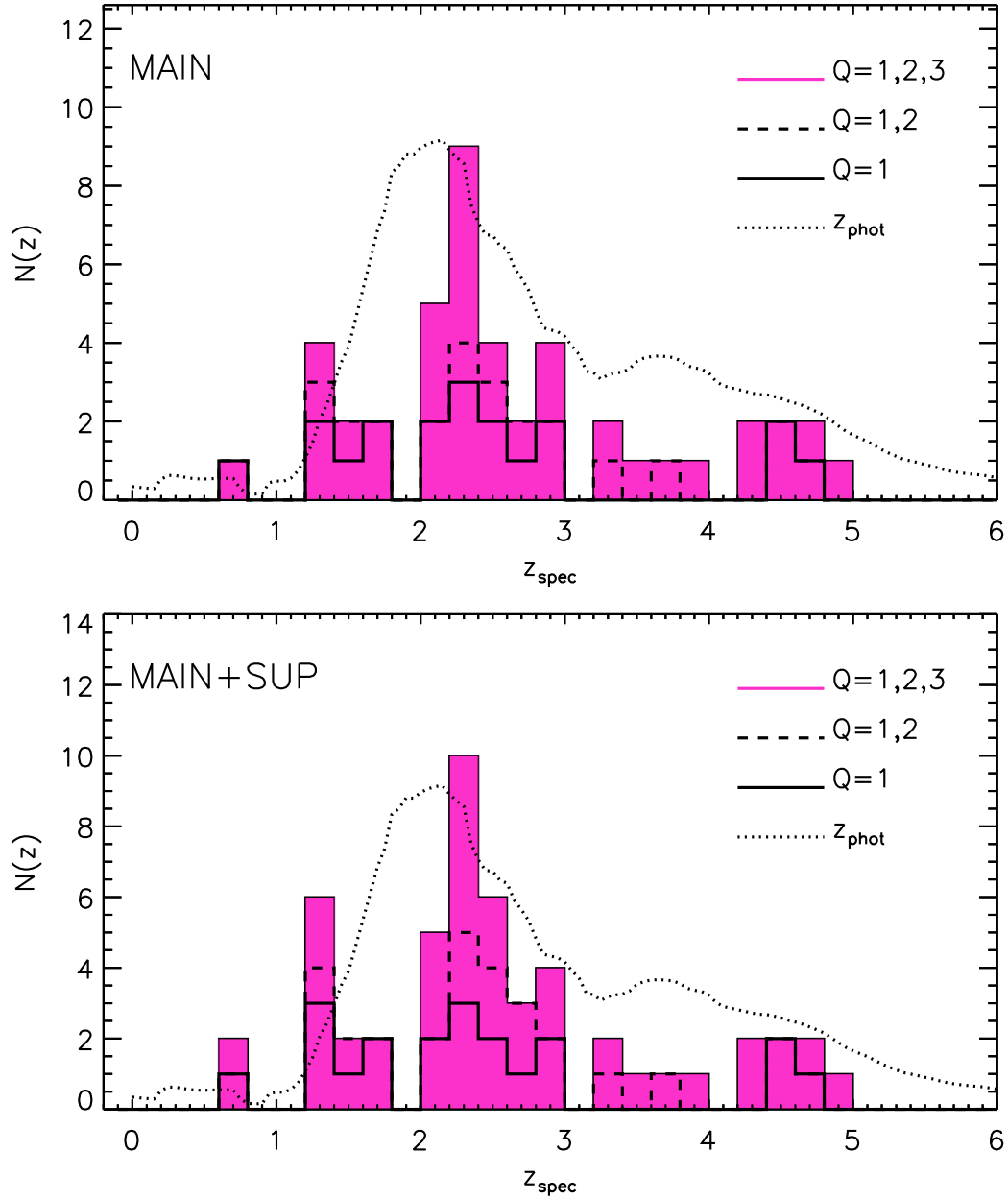
Figure 2.11: *The spectroscopic redshift distribution of the SMGs in the ECDFS. The secure redshifts (Q=1) are shown as a solid line; secure redshifts plus the single line redshifts (Q=1 and Q=2 respectively), are shown as a dashed line; all redshifts, including tentative redshifts (Q=1, 2 and 3) are shown as a filled histogram. We compare the distribution to the probability density function of the photometric redshifts from S14 shown as a dotted line. Top panel: MAIN ALESS catalog only. Bottom panel: MAIN + SUPP ALESS SMGs, including those sources with emission lying outside the primary beam of ALMA and sources from lower quality ALMA maps. The binsize is $\Delta z = 0.2$. The median redshift of the MAIN+SUP SMGs with Q=1, 2 or 3 redshifts is $z = 2.4 \pm 0.1$ which is within 1σ of the distribution of just the MAIN SMGs or with the tentative redshifts removed.*

likelihood that they are drawn from the same distribution and we find no statistical evidence that they are drawn from different parent samples. The statistics of the sample do not vary strongly with the inclusion of the SUPP sources. We therefore include the SUPP sources in our further analysis but in some cases we highlight them to demonstrate that their source properties do not systematically differ from those of the MAIN sample.

It is also important to test whether it is valid to include the SMGs which we have allocated a Q=3 spectroscopic redshift. These redshifts are typically based on one or two tentative line detections (see Fig. 2.4) and are in some cases guided by the photometric redshifts from S14. In order to test the validity of our lowest quality redshifts we carried out a K-S test to compare their redshift distribution to that of the secure (Q=1) and single-line redshifts (Q=2). We find that when comparing the Q=3 sample to the Q=1, 2 sample there is a 56% probability that they are drawn from the same parent distribution. Furthermore, in Section 2.7.2, we stack the emission from the Q=3 around the strongest emission lines i.e. Lyα, [OII]. These features do appear in the stacks emphasising the statistical viability of the Q=3 redshifts. The median redshift of the MAIN+SUPP catalog SMGs with Q=1, 2 redshifts is $z = 2.3 \pm 0.2$ and the inclusion of the Q=3 redshifts shifts the median to $z = 2.4 \pm 0.1$. Although we emphasise that on an individual basis the Q=3 redshifts are tentative, they are statistically viable. We therefore include these SMGs in most of our analysis. The median redshift is marginally higher ($\delta z = 0.2$) than that estimated in C05 of $z \sim 2.2$, however, it is within 1σ of their prediction of $z \sim 2.3$ for a purely submillimetre flux-limited sample as we have in this work.

In order to better understand our spectroscopic completeness and any bias in our sample, in the upper panel of Fig. 2.12 we plot the distribution of $S_{870\mu m}$ flux for both those sources for which we were able to determine a spectroscopic redshift and those we targeted but were unable to measure a redshift for. Fig. 2.12 demonstrates that spectroscopic success does not depend on the $S_{870\mu m}$ flux density, since the flux distributions of $S_{870\mu m}$ for SMGs for which we were able to determine a spectro-scopic redshift, compared to those for which we could not determine a spectroscopic

redshift are almost identical. For the 52 SMGs with spectroscopic redshifts, the median $S_{870\mu m} = 4.2 \pm 0.3 \, \mathrm{mJy}$ with a standard deviation of 2.1, whereas for those 57 SMGs where we could not determine a redshift the median $S_{870\mu m} = 4.3 \pm 0.3 \, \mathrm{mJy}$ with a standard deviation of 2.0. Therefore the sub-mm brightness does not noticeably influence the success rate of spectroscopic redshifts. Our sample is marginally fainter than the C05 sample at $870\mu m$, for which the median sub-mm brightness is $S_{870\mu m} = 5.8 \pm 0.5 \, \mathrm{mJy}$. However, the C05 sub-mm fluxes are derived from single-dish sub-mm observations which assume that all the flux measured emerges from the ID, whereas our ALMA observations have suggested that up to $\sim 50\%$ of the single-dish sources in fact comprise multiple SMGs, therefore, a large fraction of the flux in a single-dish observation may come from other SMGs. Therefore, one would expect the C05 average sub-mm flux to be an over-estimate, such that the actual average sub-mm flux in C05 may be more consistent with our sample. We also note that various literature (i.e. Ivison et al. 2002) would argue for a trend of increasing sub-mm brightness with increasing redshift. However, we do not observe this evolution in Fig. 2.12 and it is difficult to constrain above $\sim 7 \, \mathrm{mJy}$ as the SMG number counts decrease rapidly towards higher flux densities (Karim et al. 2013).

Since previous SMGs redshift surveys have depended on radio detections of the SMGs in order to identify the correct optical/near-infrared counterparts, we briefly discuss the properties of the radio-detected subset of the ALESS SMGs, as this is a better comparison to previous work than the complete ALESS sample. One of the advantages of the ALESS spectroscopic survey over previous SMG redshift surveys is that the high-resolution achieved with ALMA provides precise positions for the SMGs and thus the multiwavelength counterparts can be reliably identified in order to analyse the multiwavelength properties of the SMGs. Furthermore, ALMA observations provide the true sub-mm flux of the SMGs. However, previous work i.e. C05 relied upon the radio - far-infrared correlation to pinpoint the spectroscopic counterparts to the submillimetre emission, thus requiring the SMGs to be radio-detected. Of the 98 radio-detected sources in C05 they measured redshifts for 73 of them ($\sim75\%$ success rate). In our sample we targeted 52 of the 53 radio-detected
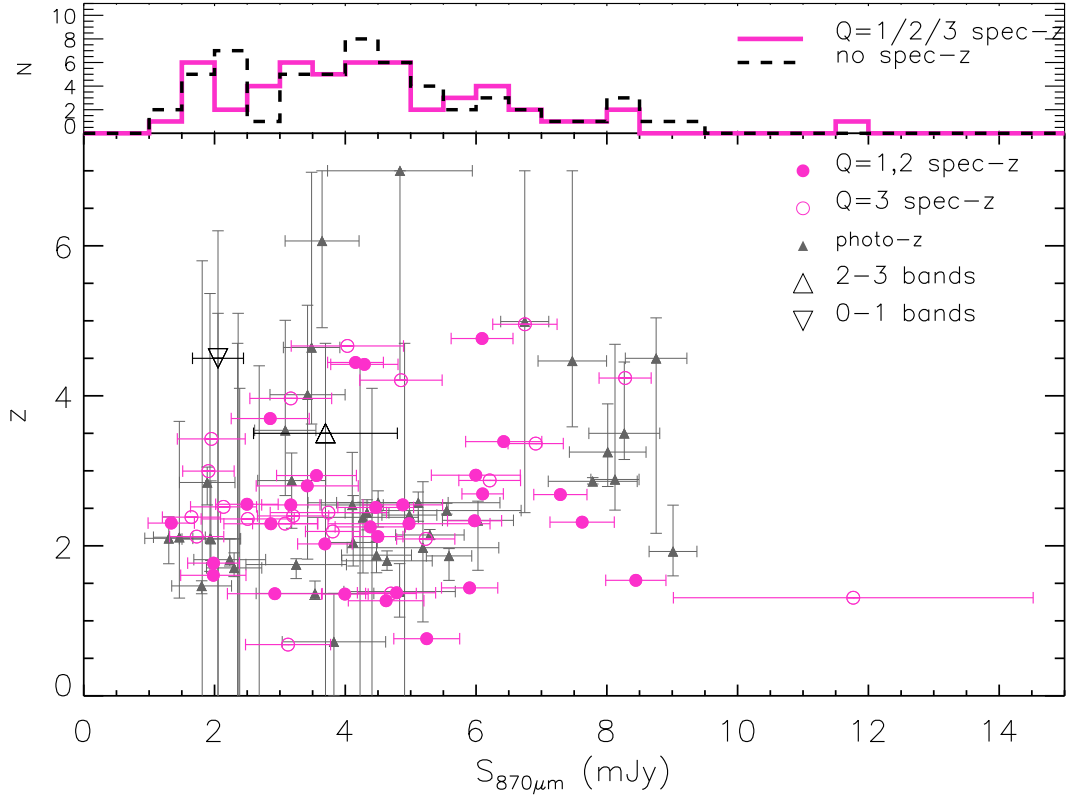
Figure 2.12: *Lower:* Spectroscopic redshift versus observed ALMA 870μm flux density. The filled circles are those SMGs with Q=1 or 2 spectroscopic redshifts. The open circles are those SMGs with Q=3 spectroscopic redshifts. The filled grey triangles represent the photometric redshift for SMGs for which we did not measure a spectroscopic redshift. The open triangles represent the median 870μm flux density and standard deviation for SMGs with $0-1$ and $2-3$ band photometry plotted at their median redshifts of $z \sim 4.5$ and $z \sim 3.5$ respectively. *Upper:* the distribution of ALMA 870μm detections. The magenta solid line shows those SMGs for which we were able to determine a Q=1, 2 or 3 spectroscopic redshift. The black dashed line is the distribution of the SMGs that were targeted with spectrographs but we were not able to determine a redshift. These distributions are relatively similar demonstrating that the likelihood of determining a spectroscopic redshift is independent of the 870μm flux density.

SMGs with spectrographs and measured redshifts for 34 of them (65%). The median 1.4 GHz radio flux density of the 34 radio-detected ALESS SMGs with Q=1, 2 or 3 spectroscopic redshifts is $63 \pm 12 \mu$Jy (as compared to $50 \pm 7 \mu$Jy for *all* 52 radio-detected SMGs) whereas the median radio flux density of the 73 radio-detected SMGs in C05 with spectroscopic redshifts is $75 \pm 6 \mu$Jy. On average our radio-detected sample with redshifts is $\sim$20% fainter at 1.4 GHz than the C05 sample and our spectroscopic completeness is 10% lower. It is possible that the C05 sample has a higher AGN fraction compared to our sample, since radio emission may be brighter in AGN. Typically AGN spectra have stronger, more easily identifiable emission features and thus our 10% lower spectroscopic completeness may be due to a lower AGN fraction. Fig. 2.7 demonstrates that there is no strong difference in the radio flux distributions of the SMGs with spectroscopic redshifts and those for which we could not determine a redshift.

In Fig. 2.13, the C05 redshift distribution is compared to the ALESS spectroscopic redshift distribution and the radio-detected ALESS SMGs are highlighted, since this is a more direct comparison to the C05 work. There are no strong differences between the distributions of the radio-detected ALESS SMGs, the C05 sample and the whole ALESS sample, however, the prerequisite of radio detections in C05 clearly results in a sharper fall-off at $z > 3$ as compared to our sample. Since the spectroscopic incompleteness is not dependent on the sub-mm or radio brightness, the properties of the SMGs at these longer wavelengths give a less biased view of the SMG population than the UV-to-optical emission which is heavily affected by dust obscuration.

Although, as described in Section 2.3, various examples of high-redshift SMGs have been previously identified, this is the first time that the high-redshift tail of the SMG redshift distribution has been clearly measured for ALMA-identified SMGs within a single field, finding 12 ALESS SMGs at $z > 3$. Five of these are radio-detected with a median radio flux density of $\sim 45 \mu$Jy. We find that 23% of the ALESS SMGs for which we measure a spectroscopic redshift are found in a high redshift tail as compared to $35 \pm 5\%$ in the S14. Our estimate is likely to be a lower

limit given that the higher redshift SMGs will be fainter and therefore more difficult to determine a redshift for, however, we should not be biased towards radio-bright SMGs in the high-redshift tail as in C05. They find that $\sim 11\%$ of their SMGs lie at $z > 3$, with a median radio flux of $\sim 60\mu$Jy as compared to the median radio flux of the ALESS SMGs at $z > 3$ of $\sim 45\mu$Jy. Thus the fact that we do not require a radio detection allows us to observe the high-redshift tail and furthermore we are less biased towards radio-bright sources at high redshift and thus less likely to be biased towards AGN than the C05 sample. Given the high redshift tail, the interquartile range of the distribution is more informative than the median and we find an interquartile range of $z = 2.1 - 3.0$ for the Q=1, 2, 3 MAIN+SUP sample. Two of the $z > 3$ ALESS redshifts have been determined through ALMA detections of [CII] which is an important future avenue for redshift detection in SMGs, given their optical faintness.

2.7 Discussion

Although the primary aim of this work was to determine the redshift distribution of a large sample of unambiguously identified SMGs, there is also a huge amount of information contained within the spectra themselves concerning the chemical composition and dynamics of these SMGs. Furthermore, the redshifts can be used as constraints in SED model fitting to better constrain the properties of the SMG population. We begin by discussing the observational features within the spectra themselves, both individually and in composite spectra and consider the evidence of AGN activity within these systems. We then discuss the velocity offsets of different emission and absorption lines within the individual spectra and the implications of these offsets for the dynamics of the systems, followed by a discussion of the environments of the SMGs. Finally we use the newly-determined redshifts to provide better constraints in SED fitting.
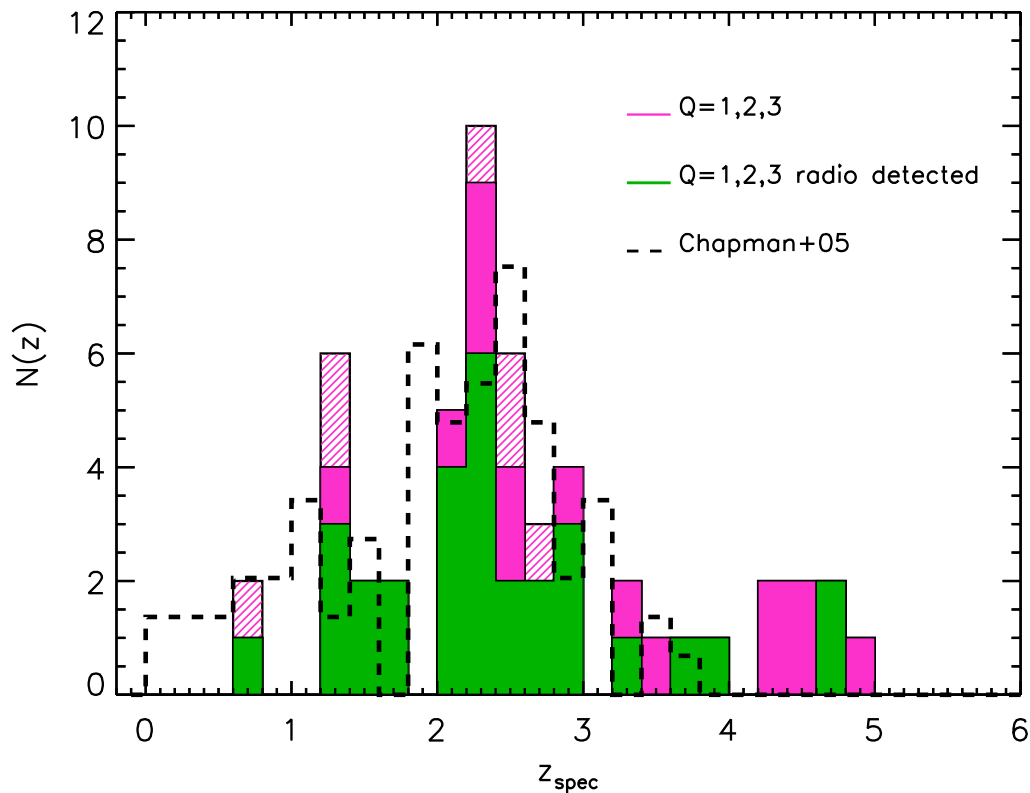
Figure 2.13: The spectroscopic redshift distribution of the ALESS SMGs. The magenta hashed and solid histograms show the distribution of Q=1, 2 and 3 redshifts in the MAIN+SUPP and MAIN catalogs respectively. The subset of radio-detected galaxies with a redshift are shown in green. The dashed histogram shows the comparison to the redshift distribution from C05. The binsize is $\Delta z = 0.2$. There are no strong differences between the distributions of the radio-detected ALESS SMGs, the C05 sample and the whole ALESS sample.

2.7.1 Individual spectra

Since we now have a wealth of spectroscopic data we can utilise the spectra not only for the purpose of determining redshifts but also to search for interesting features indicative of AGN activity, powerful star-formation, strong stellar winds etc. Here we highlight and discuss some of more interesting, high signal-to-noise spectra.

ALESS 057.1: This SMG is shown to be an X-ray AGN in Wang et al. (2013). The VIMOS spectrum is shown in Fig. 2.3 and exhibits strong, broad, symmetric Lyα emission, broad Nv and very broad Civ emission which is significantly blue-shifted ($\sim 1600\,\mathrm{km\,s^{-1}}$) with respect to both the detection of HeII and Lyα (which have velocities that are consistent within measurements errors). The Civ emission also demonstrates a P-Cygni profile with excess emission towards the blue and absorption towards the red. The FWHM $\sim 3700\,\mathrm{km\,s^{-1}}$ which is typical of the broad-line regions of AGN. Civ and Nv are high-ionisation, resonance metal lines which are thought to arise from optically thin, broad line region clouds in which it is also expected to find very strong HeII lines (Blandford et al. 1990), which agrees with the findings for this SMG. The blueshifting of Civ with respect to the systemic velocity has been found to be ubiquitous amongst high-redshift quasars (QSOs) and is thought to be due to a lack of flux in the red wing as opposed to a bulk shift. Furthermore, the blueshift may correlate with the orientation of the QSO, with a large blueshift corresponding to an equatorial viewing angle (Richards et al. 2002). However, Richards et al. (2011) study a larger sample and find that the SEDs (i.e. the shape of the ionising continuum) and strong outflowing winds may play a more important role in the blueshifting of the Civ.

ALESS 066.1: This SMG is listed as an X-ray AGN at $z = 1.310$ in Wang et al. (2013), however, following this paper, our MOSFIRE observations of this SMG revealed in fact that the photometry and X-ray emission are dominated by a foreground QSO at $z = 1.310$ (hence the low-redshift determined from the photometry in S14) but the SMG lies at $z = 2.5542$ and may be lensed by the foreground QSO

which is offset by $\sim 1''$ south of the 870μm position. The MOSFIRE spectrum is shown in Fig. 2.3 where the continuum from the QSO can clearly be observed just south of the SMG emission lines. Also, in Fig. 2.14 we show the colour image (VJK) with the ALMA contours overlaid demonstrating the distinct offset in the ALMA position and the very bright foreground QSO.

ALESS 073.1: A further X-ray AGN listed in Vanzella, et al. (2008) and described in detail in Coppin et al. (2009) and De Breuck et al. (2014). Again, this is an X-ray AGN listed in Wang et al. (2013). Strong, broad Nv is detected with a FWHM $\sim 3000\,\mathrm{km\,s^{-1}}$ as compared to a relatively narrow and weaker Lyα detection with a FWHM $\sim 700\,\mathrm{km\,s^{-1}}$. This is strongly indicative of AGN activity. In Fig. 2.15 we show the spectrum from FORS2 and in Fig. 2.3 we show the spectrum from DEIMOS.

ALESS 075.1: This is one of the SMGs which has been targeted in our ongoing follow-up programme with the Spectrograph for INtegral Field Observations in the Near Infrared (SINFONI), described briefly in Chapter 7. We have excellent spectroscopic coverage of this SMG and have strong detections of [OII], [OIII]λ4959, 5007, Hβ and Hα with XSHOOTER. The Hα detection is relatively narrow at only FWHM $\sim$160 $\mathrm{km\,s^{-1}}$. The [OIII] emission is not fit well with a single Gaussian as it is an asymmetric line with a red wing. In Fig. 2.15 we fit a double Gaussian to the [OIII] lines, giving a fit with $\chi^2 = 20.4$. In the fitting procedure we constrain the [OIII]λ5007/[OIII]λ4959 $= 2.98$ (i.e. Storey & Zeippen 2000) and we constrain the velocity dispersion of the two lines to be the same but allow it to vary between the two components in each line. We find that in the best fit, both components are relatively narrow, with a FWHM $\sim$260 $\mathrm{km\,s^{-1}}$ and $\sim$180 $\mathrm{km\,s^{-1}}$, but offset from each other by $\sim$300 $\mathrm{km\,s^{-1}}$. The Hα is $\sim 2\times$ brighter than the [OIII]λ5007. It is difficult to determine whether the Hα exhibits the same wing, as it is in a particularly low signal-to-noise region of the spectrum and it is therefore also difficult to separate out the [NII] emission from the Hα. Similarly, the Hβ appears to exhibit a broad red wing but it has a skyline through the centre of the emission making it very difficult to accurately fit to this line. The red wing observed in the [OIII] is indicative of

winds which, given the high [OIII] luminosity and the lack of an X-ray detection, may
be accelerated by an obscured AGN (i.e. outflows in high-redshift ULIRGs hosting
AGN activity; Harrison et al. 2012). However, although we detect Lyα with the UVB
arm of XSHOOTER, we do not detect the UV high-ionisation lines such as NV or
CIV which we may expect to be strong if this is an AGN. In Fig. 2.19, ALESS 075.1
is consistent with the ionising radiation originating from Type 2 AGN activity (ac-
cording to locally-derived classification schemes). From the two-component fit to
the [OIII]λ5007, the [OIII] luminosity is $L_{[OIII]} \sim 1 \times 10^{43}\,\mathrm{erg\,s^{-1}}$, which would be
unusually high for a system dominated by star formation, and is similar to that of
the SMGs containing AGN identified in Takata et al. (2006), through their optical
spectra.

Strong [OIII] can also be the result of ionising radiation from young massive
($>10\,\mathrm{M_\odot}$) stars. Rupke et al. (2005) study a large sample of local LIRGs and
ULIRGs and find that starburst-driven galactic winds are ubiquitous in the pop-
ulation with velocities of up to $600\,\mathrm{km\,s^{-1}}$, though more typically 100–$200\,\mathrm{km\,s^{-1}}$.
These winds could explain asymmetry in the observed line profile wings. Indeed
Takata et al. (2006) find that [OIII] excess may be shock-induced in systems under-
going superwind activity, which could result in strong, asymmetric [OIII] emission.
Our further detailed work with SINFONI will provide a significantly more detailed
picture of the dynamics in this system (see Chapter 6).

ALESS 079.2: This SMG has strong detections of Hα and [NII] with XSHOOTER.
The 2D and 1D spectra demonstrate structured emission (see Fig. 2.15). In the 1D
spectrum the Hα and [NII] lines are truncated at their red end and appear to be more
extended towards the blue or indeed they appear to have an additional weaker com-
ponent towards the blue. This is also apparent in the 2D. Both the Hα and the [NII]
are relatively narrow with FWHM $\sim 150\,\mathrm{km\,s^{-1}}$. The flux ratio of [NII]λ6583/Hα
is consistent with the ionising radiation arising from HII regions as opposed to an
AGN, however, we have no constraints on the [OIII] or Hβ fluxes.

ALESS 087.1: Strong continuum is detected in this SMG with UV ISM absorption
lines consistent with the Lyα emission derived redshift, however, the Lyα is signif-

icantly offset northwards of the continuum in the 2D spectrum. We thus produce two 1D spectra taken from the position of the Lyα and the continuum and compare them. The Lyα profile is marginally asymmetric with a truncated blue edge. The continuum spectrum (Fig. 2.15) shows an obvious break and relatively strong SiIV absorption. Unfortunately, there is very poor photometric coverage of this SMG (3.6–8μm only) so although the offset Lyα may be due to a close companion or an interaction with another system, it may also be simply gas which is being illuminated by star-formation, or a less-obscured part of a single galaxy.

ALESS 122.1: This SMG has very blue continuum with strong UV ISM absorption lines in both the FORS2 and VIMOS spectra which are shown in Fig. 2.15. In particular there is very strong CIV absorption which is blended with the SiII feature and overall the feature has a FWHM of $> 7000\,\mathrm{km\,s^{-1}}$ with a significant broad red wing. CIV is a strong line in most typical starburst galaxies as it is formed above the photosphere in the stellar winds from O stars or Wolf-Rayet stars (the descendants of O stars). It is either observed as blueshifted absorption in stars with weak winds or a P-Cygni profile for high wind densities. The CIV exhibits a strong, narrow component associated with the interstellar absorption and a very broad red component associated with stellar winds. The strength of this redshifted component indicates the presence of a large number of very massive stars ($> 30\,\mathrm{M_\odot}$; Leitherer et al. 1995). We observe a P-Cygni profile similar to that found in Leitherer et al. (1995) for a top heavy IMF and in the presence of $> 30\,\mathrm{M_\odot}$ stars. Very hot, massive stars are capable of driving winds of up to $3000\,\mathrm{km\,s^{-1}}$ powered by radiation pressure (i.e. Groenewegen et al. 1989). The strength of the observed absorption profile is indicative of recent star formation but the CIV is not a good indicator of burst or continuous star formation. The SiIV, however, is relatively weak for continuous star formation but transforms into a strong P-Cygni profile for bursty star formation with a flat IMF and massive stars (Leitherer et al. 1995). Detection of a P-Cygni profile for SiIV is therefore a strong indicator that the burst duration is short relative to the burst age. We observe the SiIV absorption feature to be unusually broad ($> 3000\,\mathrm{km\,s^{-1}}$) in particular in the bluer line. This is the

blueshifted wind absorption. The Si IV profile is qualitatively most similar to the line profiles expected for a very recent instantaneous burst of star formation with the intensity of the absorption implying very massive stars and a top heavy IMF. Swinbank et al. (2014) determine $L_{FIR} = (6.0 \pm 0.4) \times 10^{12} \, L_{\odot}$ for this SMG which implies a star formation rate (SFR) of SFR $\sim 1040 \pm 70 \, M_{\odot} yr^{-1}$ (using Kennicutt 1998a) which is particularly high compared to the median for the ALESS SMGs of SFR$\sim (310 \pm 30) \, M_{\odot} yr^{-1}$ (Swinbank et al. 2014). Thus we would expect to observe strong C IV and Si IV absorption features in this system. However, we note that AGN may also exhibit strong C IV absorption and given the very strong continuum and the large width of the C IV in this SMG, it is plausible that it may be a broad absorption line (BAL) QSO (Turnshek 1988). In BAL QSOs the absorption features are indicative of outflowing absorbing material being accelerated from the nucleus of the galaxy. The high outflow velocities and presence of high-ionisation lines are also an indication that the winds are associated with the nuclear regions. However, the VIMOS spectrum is very similar to that of the hyperluminous $z = 2.38$ infrared galaxy N2 850.4, discussed in Smail et al. (2003), which comprises two interacting components and is demonstrated to be a very young starburst.

Overall, these high signal-to-noise spectra indicate a diverse range of characteristics, in particular, they demonstrate the difficulty of isolating the relative contributions of AGN and star formation within SMGs.

2.7.2 Stacked spectral properties

Given that most of the SMGs are heavily dust-obscured in the UV and optical, the signal-to-noise in many of the spectra is low. Stacking spectra is useful for detecting weak features that are not visible in individual spectra and for determining average properties of the stacked galaxies. We therefore produce composite spectra over various wavelength ranges, covering Lyα and the UV ISM lines (1000 – 2000Å), [O II] (2500 – 4500Å) searching for evidence of continuum breaks, and stacks of Hβ, [O III] and Hα. In order to construct the composites, we de-redshift each of the spectra,
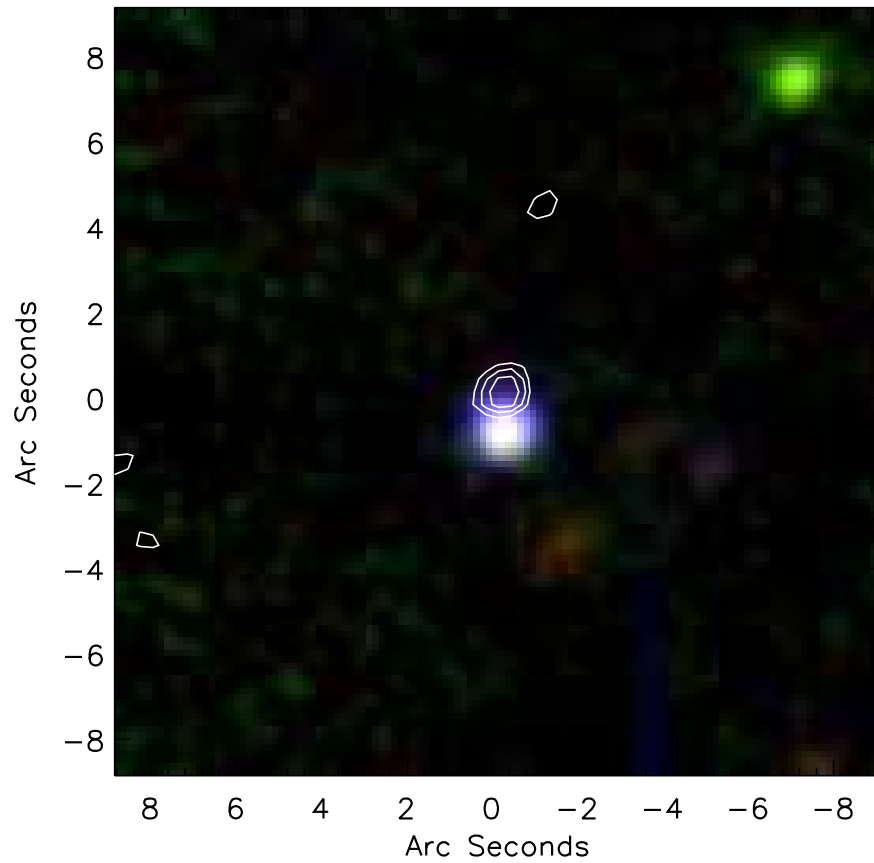
Figure 2.14: A VJK colour image of ALESS 066.1 with the ALMA contours overlaid demonstrating the $\sim 1.5''$ offset of the $z = 2.5542$ SMG north of the $z = 1.310$ QSO. This source is likely to be a lens and the bright foreground QSO dominates the photometry.
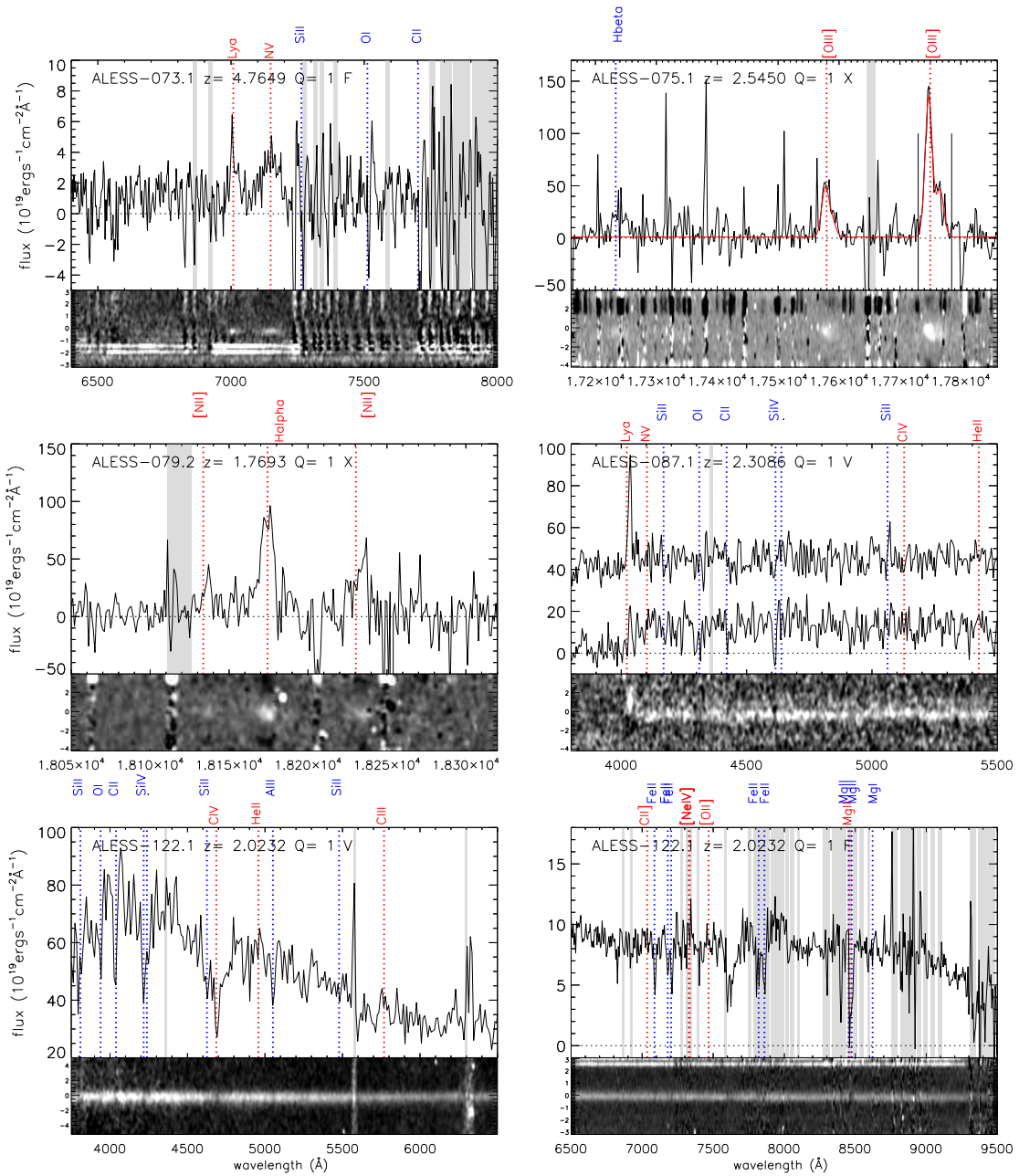
Figure 2.15: Some of the most interesting spectra in the sample, featuring evidence of winds, AGN activity, and multiple components. The sky subtraction is poor in some of the spectra and is a particular problem in the NIR and in the FORS2 spectrum of ALESS 073.1. The main skylines have been highlighted in grey but the spectra have not been smoothed and the skylines have not been masked.

then interpolate them onto the same flux scale. Where the original sky subtraction has been poor, the region within ± 5Å of the sky lines are masked when stacking. We use the Rousselot et al. (2000) catalog of OH emission lines in the near-infrared taking only the brightest 1% of the lines in the catalog. The wavelength coverage of the catalog is $0.997 - 2.25\mu$m. We then sum all the spectra, weighted by the noise (the standard deviation in the region of continuum over which they have been normalised). In the case of the $1000 - 2000$Å composite, we normalise the spectra by their median continuum value beyond 1250Å and in the case of the $2500 - 4500$Å composite, we normalise by the median continuum value between $2900 - 3600$Å. The Hα and [OIII] composites are normalised by their line fluxes.

We note that the redshift used to de-redshift each spectrum is the 'best' redshift listed in Table. 2.3 (i.e. the systemic/nebular redshift where possible). However, as we demonstrate in Fig. 2.20, both the UV ISM lines and Lyα can be significantly offset in velocity from this systemic value. In a composite spectrum this could result in certain features being smeared out or broadened.

We first discuss the composite spectra over Lyα. In Fig. 2.16 all galaxies with spectroscopic coverage within the range $1000 - 2000$Å are stacked. First we combine only the Q=1 and 2 spectra. This composite demonstrates strong Lyα and a continuum break at ~ 1200Å. There is strong SiII absorption, potentially offset SiIV absorption and CIV and CIII] emission. A composite is then produced comprising only the X-ray AGN identified in Wang et al. (2013) in order to determine if certain features in the total composite are dominated by AGN features. The high-ionisation NV feature and possibly HeII (slightly offset to the red) become more obvious, which may be expected since they are often strong in the broad-line regions of AGN. We then re-stack the spectra, removing the AGN from the sample. Again, CIII] and CIV remain strong. There appears to be a significantly blueshifted SiIV feature and potentially blueshifted CIV which may (as described previously) be indicative of strong stellar winds. Overlaid in this composite is a composite spectrum of ~ 200 'Lyman break galaxies' (LBGs) taken from Shapley et al. (2003). The Shapley et al. (2003) sample is divided into four quartiles based on the strength of the Lyα emission and

we select the sub-sample with the closest Lyα equivalent width to our sample for comparison (the 2nd brightest quartile in Lyα). Though the signal-to-noise of the Shapley et al. (2003) spectrum is significantly higher than the ALESS composite (it comprises ~ 300 galaxies), they are qualitatively similar, in particular with regard to the blueshifted ISM absorption features. Finally the Q=3 composite aids in validating the Q=3 redshifts since Lyα and CIII] are identifiable in the composite.

We then produce a rest-frame composite of the Q=1 and 2 spectra over the wavelength range of $3400 - 4400$Å (Fig. 2.17) in order to search for evidence of continuum breaks which can provide an indication of the average age of the stellar population. In this composite we detect strong [OII], Ca H and K and Hδ. Furthermore, there is clearly a break across the [OII]. The continuum begins to fall off bluewards of ~ 3900Å and flattens again bluewards of ~ 3800Å. A break in this region can be due to the 4000Å break, typically observed in older stellar systems due to a deficiency of young, hot blue stars and a build up of metals. Alternatively it can can due to a break at ~ 3650Å, which is the Balmer break/jump, and is indicative of an established stellar population and caused by hydrogen absorption lines in the Balmer series crowding to their series limit. The jump is at the limit of the Balmer series, 3646Å, representing the energy absorbed when electrons originally in the second energy level are ionised. The strength of the Balmer break is dependent on both the temperature and the surface gravity and is strongest for A-type stars (T~ 10000 K). Thus the Balmer break arises in stellar populations which are either experiencing ongoing star formation on timescales of > 100 Myr, or in post-starburst stellar populations, $0.3 - 1$ Gyr after the episode of star formation (Shapley, 2011). Here the break is more consistent with the Balmer jump than a 4000Å break. The continuum at $3500 - 3600$Å is $(1.5 \pm 0.1) \times$ lower than it is at $3900 - 4000$Å. There is strong absorption from high-order Balmer lines, in particular H9 and Hδ. In starbursts the higher-order Balmer lines are often observed in absorption towards the Balmer jump due to absorption in the photospheres of relatively young massive stars (i.e. González Delgado et al. 1999; González Delgado & Leitherer 1999).

In order to gauge the average age of the stellar populations within the ALESS
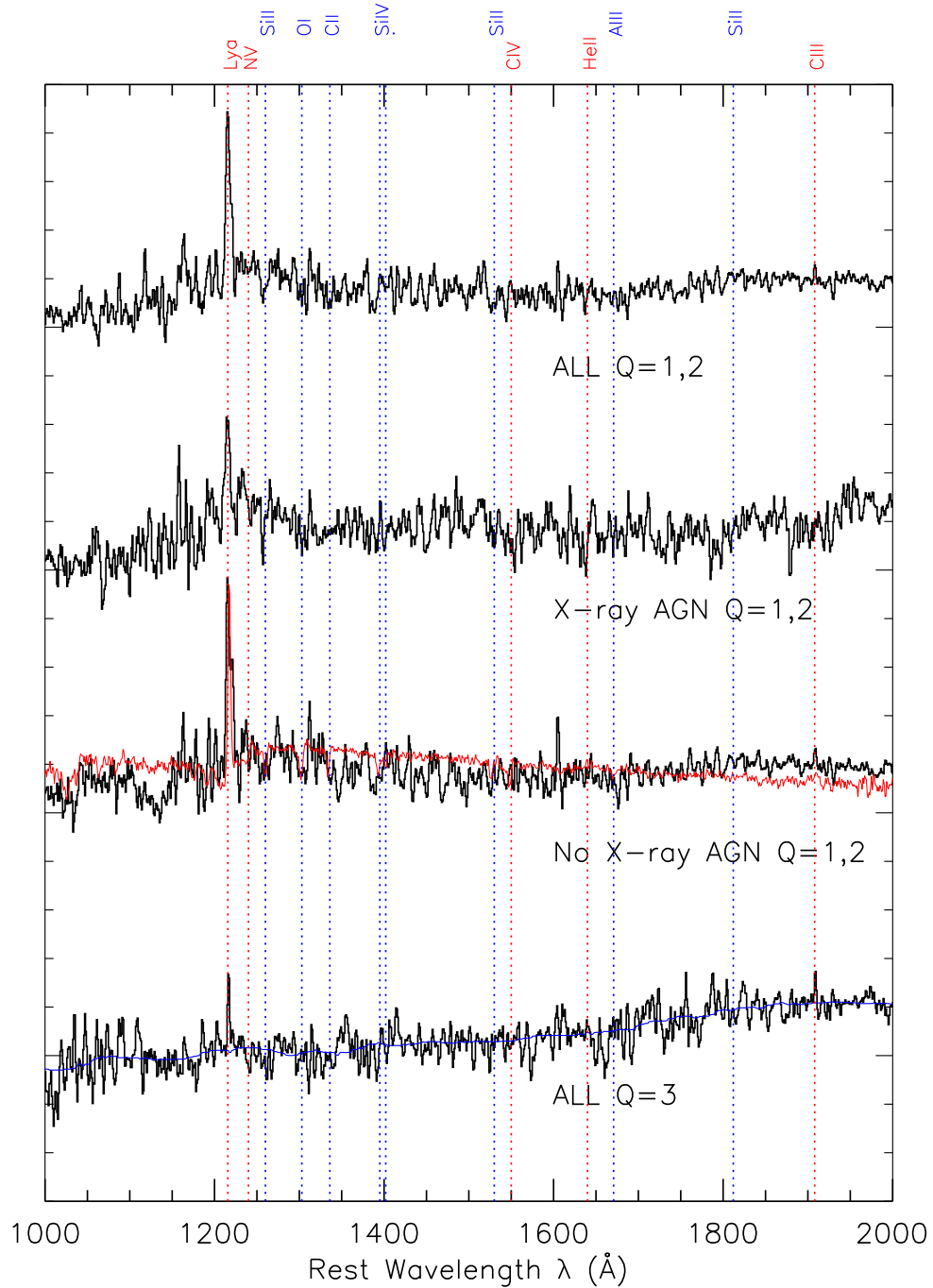
Figure 2.16: Composite spectra over the Lyman break (~ 1215Å). The spectra are summed and weighted by the noise. The top spectrum is a stack of all the spectra. The X-ray AGN are those identified in Wang et al. (2013). The X-ray AGN were then removed and the remaining galaxies were stacked. Overlaid in red on the spectrum is a composite spectrum of LBGs taken from Shapley et al. (2003). The Q=3 stack was produced in order to validate the Q=3 redshifts and ensure that there are obvious features in the composite. The solid blue line is a running median of the Q=3 composite. There are detections of both Lyα and CIII] λ1909 in the composite. There is also potentially a very weak break across Lyα. The stacks are not shown below 1000Å as we have very few detections and the composite becomes dominated by noise at these wavelengths.

SMGs, we use the SED templates of Bruzual & Charlot (2003) to predict the resultant spectra from a starburst of 100 Myr duration observed at 10 Myr, 100 Myr and 1 Gyr. We redden the model spectra using the reddening law from Calzetti et al. (2000) and the median extinction ($A_V = 2$) for the ALESS SMGs, as derived from SED fitting (see Fig. 2.24 and Section 2.7.6). We find that our composite spectrum is most similar to the youngest starburst. We overlay the composite SED from Fig. 2.23 and observe a clear agreement with the composite spectrum, in particular with regard to the strength and position of the continuum break. The ALESS [OII] composite is very similar to the Banerji et al. (2011) SMG composite over the same region, again with regard to the Balmer break and the strength of the H9 absorption (a high-order Balmer line) and [NeIII] emission. [NeIII] is a high-ionisation line typically associated with AGN. The Banerji et al. (2011) composite has been produced through stacking all the SMGs in their sample (including AGN), thus a strong [NeIII] may be expected, however, our [OII] composite does not include the X-ray AGN from Wang et al. (2013). Although it is possible to observe [NeIII] emission from HII regions, it is likely that our [OII] composite still contains some obscured AGN.

In order to study the excitation of the gas and determine the typical line profile, in Fig. 2.18 we combine those spectra for which we detect Hα. We also produce a composite over the region of Hβ to [OIII] for those SMGs detected in [OIII]. For these emission line composites, we normalise the spectra by their Hα or [OIII] fluxes instead of the continuum level, and inverse weight by the noise in the spectra. If [OIII] or Hα are covered but not detected in a spectrum, we include them in the composite but normalise by the 3σ upper limit on the [OIII] or Hα flux respectively, assuming a FWHM $\sim 250\,\mathrm{km\,s^{-1}}$ for [OIII] and $350\,\mathrm{km\,s^{-1}}$ for Hα (i.e. Swinbank et al. 2004). Again, to produce the composite spectrum, we take the weighted mean of the spectra.

For the [OIII] stack we combine the five Q=1 and 2 spectra in which [OIII] is detected. We observe very little difference in the strength of the emission lines between the composites including X-ray AGN ('ALL') and excluding the X-ray
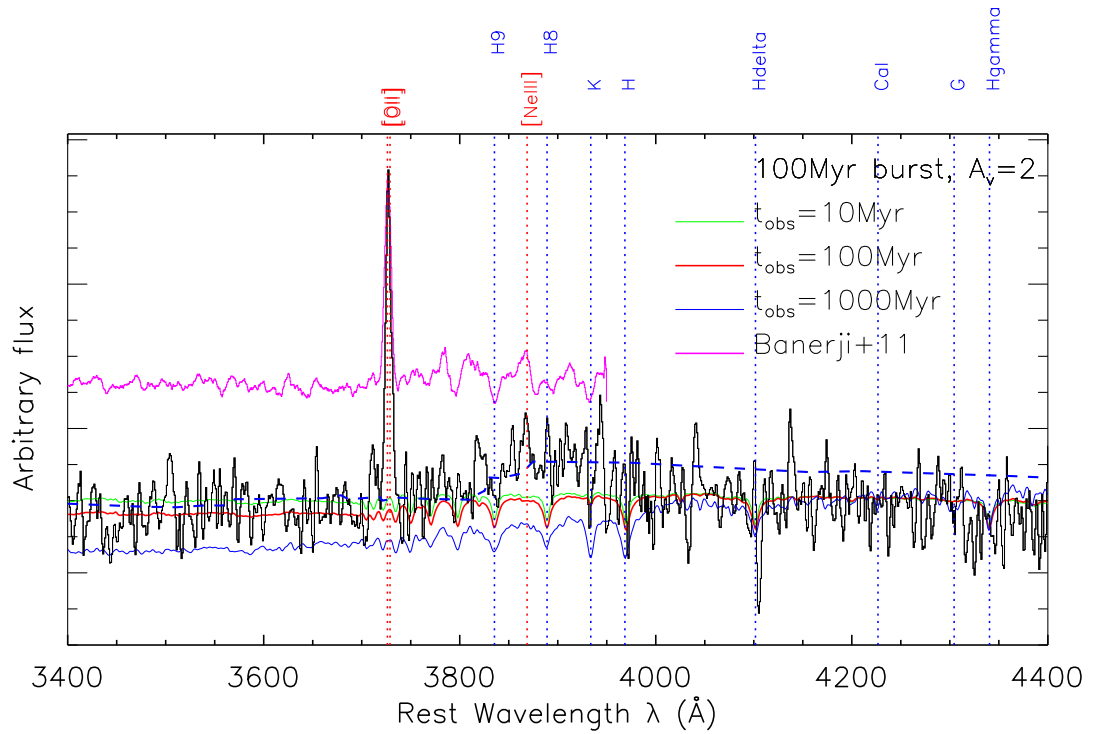
Figure 2.17: A composite spectrum from rest-frame 3400 – 4400Å of the Q=1 and 2 ALESS spectra with the spectra of X-ray AGN removed from the sample. The spectra were normalised by their median continuum flux between 2900 – 3600Å and sky-subtracted by the same method as in Fig.2.16. We overlay predicted SEDs for a continuous starburst observed at 10, 100 and 1000 Myr and find our sample to be most consistent with a younger starburst. In magenta, we overlay the composite SMG spectrum from Banerji et al. (2011) which is in good agreement with our composite. The dashed line is the composite ALESS SED from Fig. 2.23.

AGN ('No X-ray AGN'), as there is only one X-ray AGN (ALESS 067.1) in the total stack and removing it has no effect on the stack. We fit the composite [OIII] emission lines and the Hβ with Gaussian profiles, fixing the ratio of the [OIII] lines at [OIII]λ5007/[OIII]λ4959 = 2.98 (Storey & Zeippen 2000) and fixing the velocity dispersion of the [OIII] lines to be the same. This provides a reasonable fit but qualitatively it can be seen that there is an excess in the spectrum towards the red, possibly implying the presence of strong winds. The FWHM of the [OIII] is $\sim 380\pm80\,\mathrm{km\,s^{-1}}$ for the 'ALL' and 'AGN-removed' sample. The fit to the Hβ is not as good, since the line is asymmetric, again with a broader red wing. The FWHM of the Gaussian clearly over-predicts the total width, with a FWHM $\sim 760\pm700\,\mathrm{km\,s^{-1}}$. The [OIII]$\lambda$5007/H$\beta$ ratio is $\sim 3 \pm 2$ in the 'ALL' composite spectrum which, in Fig. 2.19, indicates very high ionisation, however it is shown to be consistent with the ionisation being dominated by star formation as opposed to AGN.

The signal-to-noise of the Hα composite is low, since in all cases the Hα emission lines lie in the NIR in which the sky emission is very strong. Of the 12 Q=1 and 2 SMGs with Hα detections we combine nine of the spectra to produce the composite (excluding ALESS 006.1, 007.1 and 098.1 as either a strong skyline lies through the line or the signal-to-noise is particularly poor). We fit a model to the Hα and [NII] lines comprising three Gaussians, where the velocity dispersion of the two [NII] lines are fixed to be the same as each other, with a flux ratio between the [NII] lines constrained to be [NII]6583/[NII]6548 = 3.06 (Osterbrock & Ferland 2006). In the best fit, the Hα has a FWHM of $\sim 400\,\mathrm{km\,s^{-1}}$ in both composites, whereas, a FWHM of $\sim 700\,\mathrm{km\,s^{-1}}$ is required for the [NII]. The 'ALL' composite exhibits relatively high [NII]λ6583/Hα ratios of $\sim 0.2\pm0.2$, however, this ratio is very poorly constrained, as demonstrated in Fig. 2.19. It is not clear from these diagnostics whether the ionising radiation within these systems is on average predominantly from star formation or AGN activity. This issue is discussed further in Section 2.7.3.
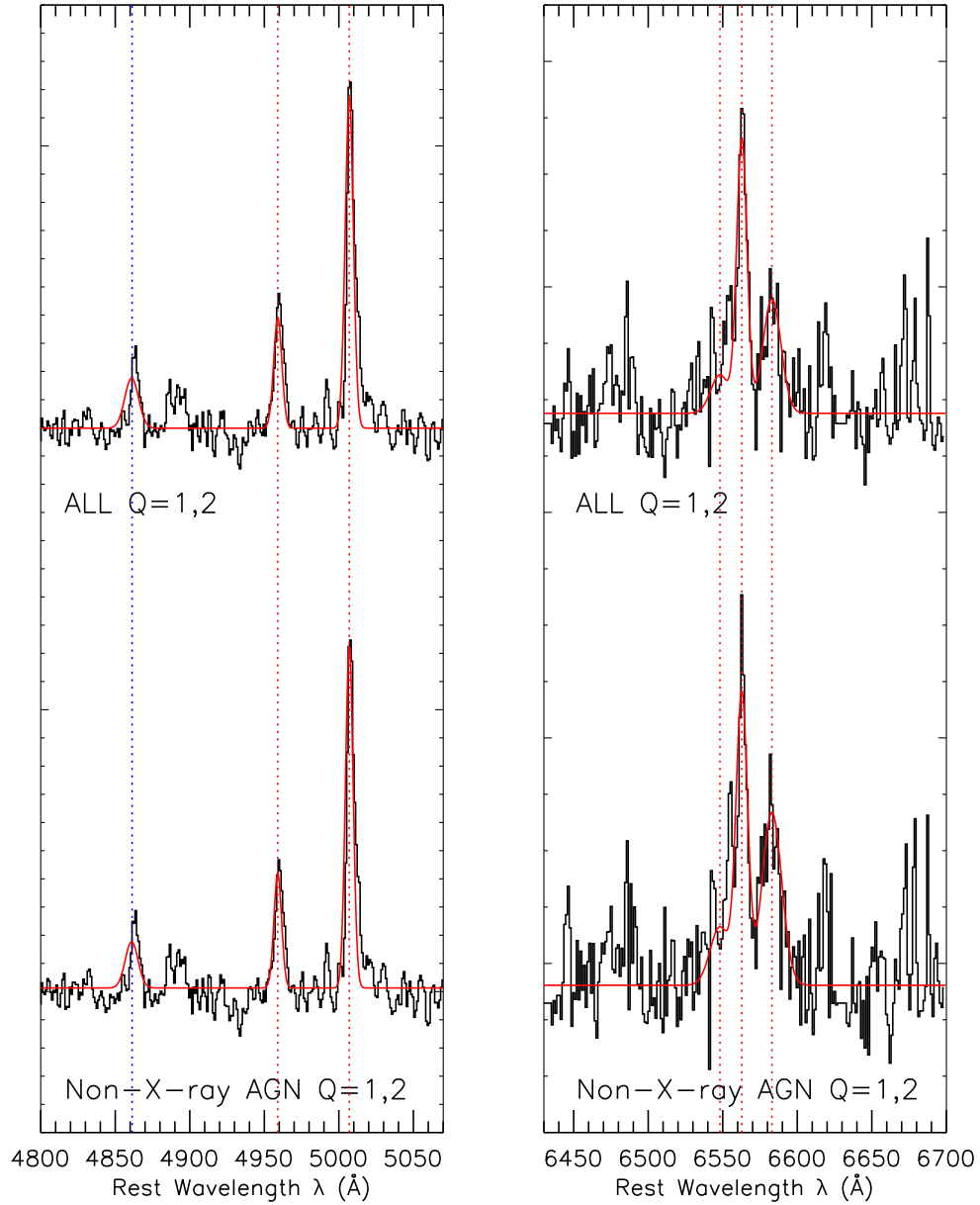
Figure 2.18: A composite spectrum from rest-frame $4800-5070$Å and $6400-6700$Å of the ALESS spectra, covering detections of Hβ, [O III]λ4959,5007, Hα and [N II]. The spectra were continuum-subtracted, normalised by their line fluxes, sky-masked and combined via a noise-weighted mean. The flux scale is arbitrary. The top composite spectra on both the left and right comprise all ALESS SMGs whilst the lower composite spectra have had the spectra of X-ray AGN removed. In the 4800–5070Å composite, the emission lines were each fit with a single Gaussian, fixing the ratio of the [O III] lines at [O III]λ5007/[O III]λ4959 $= 2.98$ (Storey & Zeippen 2000) and fixing the velocity dispersion of the [O III] lines to be the same. For the 6400–6700Å composite, the emission was fit with three Gaussians where the flux ratio of the [N II] lines was constrained to be [N II]6583/[N II]6548 $= 3.06$ (Osterbrock & Ferland 2006) and the velocity dispersion of the lines was fixed to be the same for the two [N II] lines. There is very little difference between the samples including and not including X-ray AGN.

2.7.3 Spectral diagnostics

BPT (Baldwin, Phillips and Televrich) diagnostics were first proposed Baldwin et al. (1981) as a method of using nebular emission line ratios to identify the dominant ionisation mechanism of the nebular gas within galaxies. There are various versions of these diagrams but here we use the most commonly used diagram of [NII]λ6584/Hα versus [OIII]λ5007/Hβ (Baldwin et al. 1981). Given the hard SED of AGNs (they emit strongly at very high-energies), they are capable of exciting high-ionisation lines such as the forbidden lines [OIII] and [NII], thus resulting in higher ratios of both [NII]λ6584/Hα and [OIII]λ5007/Hβ in AGN than in HII regions, which are ionised by star formation. The most commonly used BPT classification schemes were determined by Veilleux & Osterbrock (1987) and Kauffmann et al. (2003) to broadly distinguish star-forming galaxies from AGN, which we show in Fig. 2.19. We note, however, that the BPT diagnostics have only been well-constrained locally, though attempts have been made to make it more applicable to high-redshift galaxies, i.e. Kewley et al. (2013) demonstrate a new model where at higher redshifts the divide between AGN and HII regions is pushed to higher ratios of both [NII]λ6584/Hα and [OIII]λ5007/Hβ.

In order to place the ALESS SMGs on a BPT diagram to determine the dominant ionisation mechanism within these systems, we require at least a detection in Hα. We detect Hα in 14 SMGs, however, only 12 of these are Q=1, 2 spectra. Furthermore, in only three cases out of 12 do we have sufficient line detections (at least Hα and [OIII]) to carry out BPT diagnostics (ALESS 006.1, 067.1 and 075.1) which we show in Fig. 2.19. Two of the three sources are consistent with Type 2 AGNs (ALESS 006.1 and ALESS 075.1), however, paradoxically, ALESS 067.1 (an X-ray AGN; Wang et al. 2013) is consistent with the ionising radiation originating predominantly from HII regions, although, it is a lower limit and may therefore be consistent with an AGN.

Considering only the ratio of [NII]λ6583/Hα, for the four SMGs for which we strongly detected Hα *and* [NII], in ALESS 066.1, 075.2, 079.2 the flux ratio of

[NII]λ6583/Hα varies between $0.37 - 0.47$ which are consistent with the ionising radiation originating from HII regions. However, for ALESS 075.1 the flux ratio of [NII]λ6583/Hα=0.86 which is consistent with an AGN. Furthermore, the FWHM of the Hα lines (including in ALESS 075.1) is significantly below $1000\,\mathrm{km\,s^{-1}}$ and therefore these systems are unlikely to be AGN-dominated. Three of these sources do not have detections of [OIII]λ5007 or Hβ and are therefore placed at zero in the y-axis (an arbitrary value).

In order to extend this analysis further, we also include SMGs which can only be represented as limits constrained in one axis. Two SMGs (ALESS 017.1 and ALESS 112.1) have detections in Hα but only upper limits in [NII] with (in the case of ALESS 112.1) very tentative detections of [OIII] and Hβ. These are therefore also shown as upper limits in [NII]λ6583/Hα at an arbitrary value in [OIII]λ5007/Hβ. We also show the line ratios determined from fitting to the 'ALL' composite spectrum in Fig. 2.18. Though the errors are very large in the ratio of [NII]/Hα, the ionisation is marginally more typical of HII regions than AGN, in particular if the Kewley et al. (2013) higher-redshift trends are to be believed, and the boundaries between the HII regions and AGN shift to higher line ratios.

Since the sample for which we are able to calculate BPT diagnostics are limited to strong line emitters we emphasise that these sources are by no means representative of the SMG population and in fact there is a selection effect such that the sources with the strongest observed emission lines are likely to be AGN. This is demonstrated by the fact that $\sim 40\%$ of the eight SMGs shown in Fig. 2.19 are X-ray detected, compared to 17% of the whole sample of SMGs for which we have spectroscopic redshifts. Furthermore, the median K-band magnitude of the eight SMGs shown is nearly two orders of magnitude brighter than the median of whole ALESS sample and the 870μm flux density of the eight SMGs is $5 \pm 1\,\mathrm{mJy}$ as compared to $4.0 \pm 0.3\,\mathrm{mJy}$ in the whole ALESS sample. However, we are less biased than many previous attempts, since this work is based on a redshift survey instead of targeted follow-up of the brightest SMGs with known redshifts (e.g. Takata et al. 2006). Takata et al. (2006) use near-infrared spectrographs to target 22 SMGs and

optically faint radio galaxies (OFRGs) with redshifts that place [OII], Hβ, [OIII] and Hα within spectroscopically accessible wavelength ranges. They find that 14 out of their 22 sources are consistent with AGN or QSOs based on the spectral diagnostics. In particular, eight out of the nine sources with sufficient line detections to place them on a BPT diagram are found to be AGN. However, they note that they are strongly biased towards this result. They also note that BPT diagnostics may not be a particularly useful indicator of the dominant ionisation mechanisms, given that extreme star formation may drive 'superwind' activity which could mimic the behaviour of an AGN on the BPT diagram. Takata et al. (2006) suggest that this wind activity could cause an enhancement in the [OIII] through shock-induced ionisation, which on a BPT diagram would appear to be produced by a Compton thick AGN. Furthermore, various studies are demonstrating that the BPT diagram classifications vary with redshift. Kewley et al. (2013) argue that the extreme ISM conditions within high-redshift star-forming galaxies mean that galaxy classifications derived from local galaxies cannot be used to clearly classify $z > 1$ galaxies. They therefore present a redshift-dependent classification line which we overlay as a dotted line on Fig. 2.19, using our median ALESS SMG redshift of $z \sim 2.4$ to define it. According to this classification, both the composite and all the individually-detected SMGs in our sample are consistent with the dominant ionising mechanism arising from star-formation, aside from ALESS 075.1 (discussed in detail in Section 2.7.1) and ALESS 006.1 (a possible lens). This relation does, however, assume that the populations are either purely star-forming or contain an AGN and in reality composite systems are common, for example with a heavily obscured AGN and strong star formation.

It is also important to note that rest-frame optical spectroscopy of heavily dust-obscured sources is unlikely to be sensitive to the dominant luminosity source in the inner regions of a galaxy and that the absence of AGN features in an optical spectrum does not rule out the possibility of a heavily obscured AGN (i.e. Goldader et al. 2002).

Further details on the energetics within the ALESS SMGs can be determined
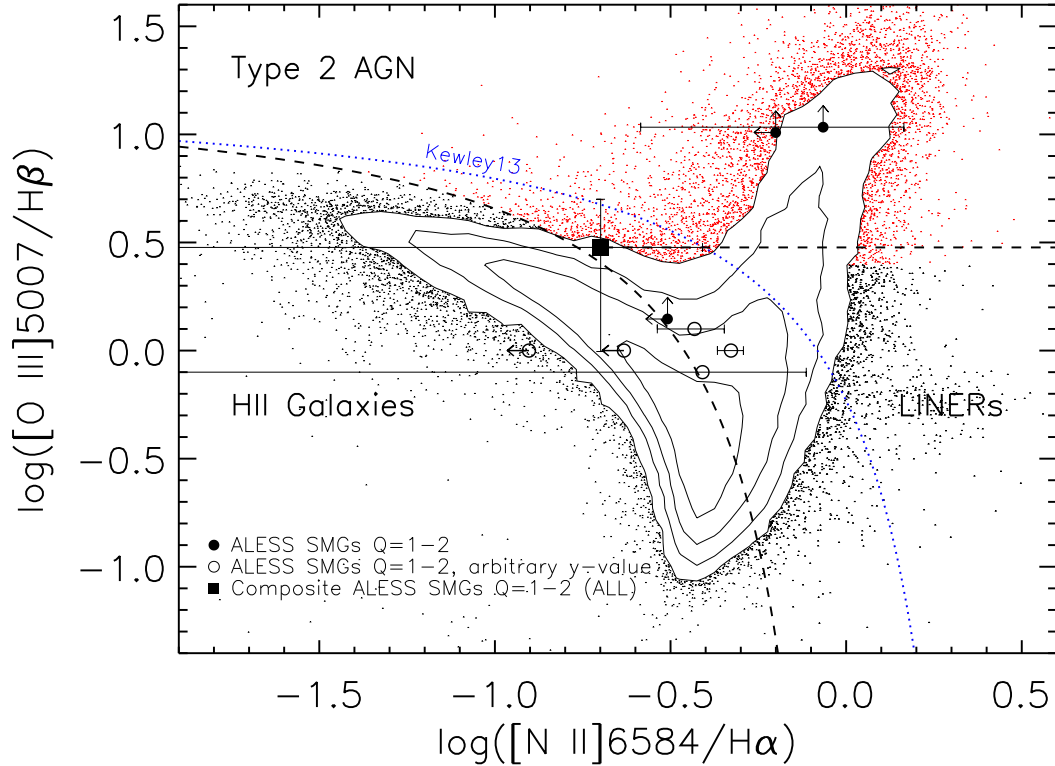
Figure 2.19: A BPT diagram highlighting the position of the three ALESS SMGs for which we have reasonable constraints in two or more of the required emission lines. This figure is an adapted version of Fig. 1 from Mullaney et al. (2013). The data are taken from the SDSS DR7 database for extragalactic sources with $z < 0.4$. We overlay with filled circles, ALESS 006.1, ALESS 067.1 and ALESS 075.1 and use a square for the value determined from the 'ALL' composite spectrum in Fig. 2.18. We also overlay with open circles the [NII]/Hα ratios for ALESS 017.1, ALESS 066.1, ALESS 075.2, ALESS 079.2 and ALESS 112.1 at arbitrary values of [OIII]/Hβ. The classification schemes are taken from Veilleux & Osterbrock (1987) and Kauffmann et al. (2003) for the dashed lines. The redshift-dependent scheme defined by Kewley et al. (2013) set at the median ALESS SMG redshift of $z \sim 2.4$, is shown as a dotted blue line. Using the Kewley et al. (2013) classification scheme, the composite and the individual SMGs highlighted in this figure are consistent with being star formation dominated.

through investigating the velocity offsets of various spectral lines from the nebular emission, searching for evidence of winds which may be driven by star formation or AGN. We now investigate the dependency of the redshift determination on the choice of the emission/absorption lines from which it is measured.

2.7.4   Velocity offsets

In Steidel et al. (2010) it is shown that for LBGs redshifts derived from UV ISM absorption lines typically show a systematic offset bluewards of the systemic redshift (determined from Hα), whereas redshifts determined from Lyα emission show a systematic offset redward of the systemic redshift. This effect is largely due to galaxy-scale outflows, blueshifting the absorbing material between the galaxy and the observer and scattering Lyα photons from the far-side of the galaxy outflows, redshifting them with respect to the neutral medium within the galaxies and allowing them to pass through. For some of the ALESS SMGs we were able to determine nebular redshifts, UV ISM redshifts and Lyα redshifts allowing us to compare to the results for LBGs.

In Table. 2.3 we summarise the lines detected for each ALESS SMG and the redshift associated with fitting to each line. From this information we compare to the Lyα and UV ISM-derived redshifts for the SMGs in C05 and show this in Fig. 2.20. The C05 galaxies broadly agree with the Steidel et al. (2010) such that on average the Lyα is redshifted and the UV ISM lines are blueshifted, however, they are significantly more scattered than the Steidel et al. (2010) sample, with offsets ranging between $\sim -1100 - 700\,\mathrm{km\,s^{-1}}$ for the UV ISM-derived redshifts and between $\sim -1500 - 1200\,\mathrm{km\,s^{-1}}$ for the Lyα-derived redshifts for the C05 sample, as compared to $-600 - 100\,\mathrm{km\,s^{-1}}$ for the UV ISM-derived redshifts and $\sim 100 - 900\,\mathrm{km\,s^{-1}}$ for the Lyα-derived redshifts in Steidel et al. (2010). The ALESS SMGs do not show the same trend as Steidel et al. (2010) of redshifted Lyα and blueshifted UV ISM lines. In particular there is a significantly broader distribution in the velocity offsets of the ALESS SMGs, with Lyα redshifts being up to $+3000\,\mathrm{km\,s^{-1}}$

offset from the systemic redshift, possibly indicating high velocity outflows. The large spread in the velocity offsets emphasises the diversity of conditions within these SMGs, in particular with regard to the strength of large-scale winds. The median bolometric luminosities of our sample in Fig. 2.20 compared to the C05 sample (C05: $(9 \pm 2) \times 10^{12}\,\mathrm{L_\odot}$, ALESS: $(3.6 \pm 0.6) \times 10^{12}\,\mathrm{L_\odot}$) demonstrate that on average our sample is significantly fainter in bolometric luminosity for those sources for which we were able to detect multiple spectral lines. The main outliers on Fig. 2.20 are ALESS 088.5 and ALESS 049.1, with Lyα offset from the nebular velocity by $> 2000\,\mathrm{km\,s^{-1}}$. For both ALESS 088.5 and ALESS 049.1 the only line available to determine a nebular/systemic velocity was HeII λ1640, which, as we described previously can originate from the stellar winds from Wolf-Rayet stars, making it less reliable as a systemic velocity tracer than the typical nebular lines (i.e. Hα).

To attempt to understand the SMG population further, we now investigate the typical environments in which they reside.

2.7.5 Environments

Various studies have investigated the environments and clustering of SMGs and demonstrated that SMGs are strongly clustered, inferring them to reside in very massive haloes ($> 10^{12}h^{-1}\mathrm{M_\odot}$). Clustering measurements provide constraints in cosmological models predicting the nature of SMGs and provide an estimate of the halo masses in order to determine whether different galaxy populations may be evolutionarily linked. Much work has been carried out to measure SMG clustering via their angular, on-sky correlation. In particular Weiß et al. (2009) used the projected on-sky distribution of the LESS survey to determine a correlation length of $(13 \pm 6)\,h^{-1}\,\mathrm{Mpc}$ for the LESS SMGs. Other work has included redshift information in order to improve the clustering measurements. Blain et al. (2004) discovered an over-density of five SMGs within $1200\,\mathrm{km\,s^{-1}}$ of $z = 1.99$ in the GOODS-N field which was later expanded to six SMGs and two radio galaxies with additional red-
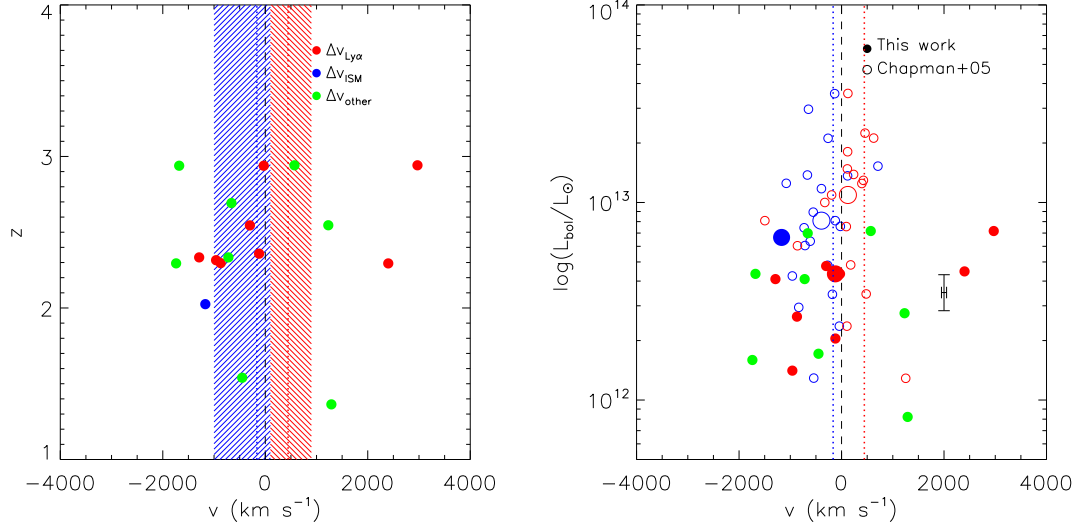
Figure 2.20: The velocity offsets of UV ISM absorption lines and Lyα from the systemic redshifts (shown as a vertical dashed line) for all ALESS SMGs where multiple lines are detected (most of which are Q=1 redshifts). The systemic redshifts are determined from fitting to nebular emission lines. *Left:* The red points represent the offsets between the Lyα emission and the systemic velocity. The green points represent the offsets between lines which can be either nebular or ISM lines and are frequently strongly influenced by winds, such as CIV λ1549, NV λ1240, CIII] λ1909, MgII λ2800 and HeII (if other nebular lines are available). The blue point is the only SMG (ALESS 122.1) for which we have spectra covering both UV ISM lines and nebular lines, where we exclusively use CII λ1334.53, SiIV λ1393.76 and SiII λ1526.72 to determine ISM line velocity offsets. We show the velocity offsets versus the systemic redshift. The red and blue dotted lines represent the mean of the distribution of Lyα and ISM velocity offsets respectively from the Steidel et al. (2010) sample of $z = 2 - 3$ LBGs. We see significant scatter in our sample as compared to the range (hashed regions) and mean (dotted lines) of the Steidel et al. (2010) sample, where blue represents the distribution of ISM velocity offsets and red represents the distribution of Lyα velocity offsets. *Right:* here we show the velocity offsets versus the bolometric luminosity ($L_{8-1000\mu m}$). The median of each sample is shown as a larger symbol. For comparison we show the SMG sample from C05 which demonstrates a similarly large scatter to our sample. Again, we compare to the mean offsets in the Steidel et al. (2010) sample (dotted lines). In contrast to C05 and Steidel et al. (2010) the median velocity offset of the Lyα is blueshifted as opposed to redshifted. We show a representative error bar for our data derived from the median error on the bolometric luminosity and we estimate a typical redshift measurement error of $\sim 100 \, \mathrm{km \, s^{-1}}$ from fitting the spectral lines.

shift data by Chapman et al. (2009). Their clustering length of $(6.9\pm2.1)\,h^{-1}\,\mathrm{Mpc}^{-1}$ determined in Blain et al. (2004), through a pair counting analysis (number of pairs within $1200\,\mathrm{km\,s^{-1}}$), is consistent with the SMGs evolving into passive red galaxies at $z\sim1$, and subsequently the members of rich galaxy clusters. However, the spatial density of the SMGs is too high for them to evolve into rich clusters. Adelberger (2005) criticised this method of pair counting suggesting that it was unnecessarily noisy and would overestimate the correlation length. However, Chapman et al. (2009) attempted to determine whether the discrepancy in Blain et al. (2004) may be due to the fact that SMGs are in fact not necessarily tracing the most massive structures in the Universe. They compare the overdensity of SMGs to that of UV-selected galaxies in the same field and find that the UV-selected galaxies exhibit only a modest overdensity. They therefore conclude that searching for galaxy clusters via the highest luminosity systems (i.e. the brightest SMGs which are typically those most rapidly star-forming systems) tends to trace brief periods of rapid evolution in systems of lower matter overdensity as opposed to the largest, densest mass structures.

Hickox et al. (2012) built on the angular correlation work of Weiß et al. (2009) in the LESS survey and used photometric redshift constraints from Wardlow et al. (2011), some of the spectroscopic redshifts from this work, and a sample of 50,000 Spitzer IRAC/MUSYC Public Legacy Survey galaxies in the ECDFS to better constrain the clustering amplitude of SMGs. They applied a method from Myers et al. (2009) which incorporates the photometric probability distribution into the calculation of the projected spatial cross-correlation between SMGs and other galaxies to then determine an SMG auto-correlation length of $(7.7\pm2.3)\,h^{-1}\mathrm{Mpc}$ and a characteristic halo mass of $\sim6\times10^{12}\,h^{-1}\mathrm{M_\odot}$. This halo mass is consistent with the $z\sim2$ SMGs being the progenitors of $z=0$ massive elliptical galaxies. This is the best constraint to date on SMG clustering. However, the Hickox et al. (2012) results were based on the original LESS survey, in which we now know there to be some incorrectly identified counterparts and some faint sources which were missed.

In order to search for associations and structures in the ALESS SMG population

we first study each ALESS map individually, since Karim et al. (2013) demonstrate that $> 35\%$ of the original LESS sources were resolved into multiple SMGs. However, there are only four ALESS maps in which we were able to determine a spectroscopic redshift for two or more of the SMGs within the pointing (ALESS 017.1, 017.2, 067.1, 067.2, 075.1, 075.2, 088.1, 088.2, 088.5, 088.11), none of which are within the $2000\,\mathrm{km\,s^{-1}}$ of each other. Also, in most of these cases, only one of the redshifts found is Q=1 and typically the SMG for which we were able to determine a redshift in each map is the brightest at 870μm. Thus, there are no pairs found at the same redshift within the same map.

Since we suffer from spectroscopic incompleteness, we therefore use the photometric redshifts from S14 where the spectroscopic redshifts are missing. Including photometric redshifts we have redshifts for a total of 92 SMGs. We first search within each map, going to each SMG with a spectroscopic redshift and measuring the velocity offsets to all other SMGs in the map via either their spectroscopic (where available) or photometric redshifts. We include the errors on the photometric redshifts by allowing the redshift to randomly vary within the constraints of the 1σ error bars and we repeat the procedure 1000 times, taking a median of the result. Furthermore, we apply error bars of $500\,\mathrm{km\,s^{-1}}$ to the spectroscopic redshifts, in order to allow for the uncertainty introduced from the lack of availability of nebular lines for accurate spectroscopic redshift determination (highlighted in Fig. 2.20). By this method we still find no matches within $2000\,\mathrm{km\,s^{-1}}$ within the maps, compared to $10-29$ matches (factoring in the error bars) within $2000\,\mathrm{km\,s^{-1}}$ when matching an SMG with a spectroscopic redshift to any SMG in the field with either a spectroscopic or photometric redshift.

We then crudely compare the spectroscopic redshift distributions of the ALESS SMGs with that of the other galaxy populations in the ECDFS where we have spectroscopic redshifts, in order to search for correlation between the different populations. Most of the spectroscopic redshifts for the other galaxy populations were taken from an extended version of a sample compiled in Luo et al. (2011) of $> 15,000$ redshifts for galaxies in the ECDFS with a median redshift of $z \sim 0.670 \pm 0.001$ and

an interquartile range of $z = 0.3$–1.0, with references therein of: a compilation of redshifts in the CDFS[2], including redshifts from Cristiani et al. (2000), Croom et al. (2001), Bunker et al. (2003), Dickinson et al. (2004), Stanway et al. (2004a), Stanway et al. (2004b), Strolger et al. (2004), Szokoly et al. (2004), van der Wel et al. (2004), Le Fèvre et al. (2005), Doherty et al. (2005), Mignoli et al. (2005), Ravikumar et al. (2007), Vanzella, et al. (2008), Popesso et al. (2009), Balestra et al. (2010), Silverman et al. (2010), Kurk et al. (2013); further redshifts are taken from Kriek et al. (2008), Boutsia et al. (2009), Taylor et al. (2009), Treister et al. (2009), Wuyts et al. (2009), Casey et al. (2011), Xia et al. (2011), Bonzini et al. (2012), Cooper et al. (2012), Coppin et al. (2012), Iwasawa et al. (2012), Mao et al. (2012), Le Fèvre et al. (2013), Georgantopoulos et al. (2013), and the 2df galaxy redshift survey (2dFGRS). From this catalog, we select only secure redshifts and remove the duplicates. We also remove any cases in which two secure but differing redshifts are given from two different references. Redshifts are also included from the Williams et al. (2014) and ~ 1100 of the redshifts for the other galaxy populations are taken from Swinbank et al. (in prep) and are the other galaxies targeted on the masks in our FORS2/VIMOS large spectroscopy programme.

In Fig. 2.21 we plot the spectroscopic redshift distribution in bins of $6000\,\mathrm{km\,s^{-1}}$ to search for correlation between the peaks of the SMG distribution and the field galaxy population redshift distribution. This figure demonstrates that there is little correlation between overdensities in the SMGs and in the other galaxy populations. We then search for associations within $2000\,\mathrm{km\,s^{-1}}$ ($\Delta z = 0.0067$) of each other, in a similar approach to that in Chapman et al. (2009), both between SMGs and SMGs and SMGs and galaxies. An offset of $2000\,\mathrm{km\,s^{-1}}$ is larger than the typical velocity dispersion of rich clusters ($< 1200\,\mathrm{km\,s^{-1}}$; Blain et al. 2004) and it is also larger than random velocity offsets caused by emission from randomly-oriented galactic winds at high-z (i.e. Erb et al. 2003), however, we note that we find offsets of up to $3000\,\mathrm{km\,s^{-1}}$ for Lyα in Section 2.7.4. Thus, although $2000\,\mathrm{km\,s^{-1}}$ is a large offset, it

---

[2]http://www.eso.org/sci/activities/garching/projects/goods/MASTERCAT_v3.0.dat
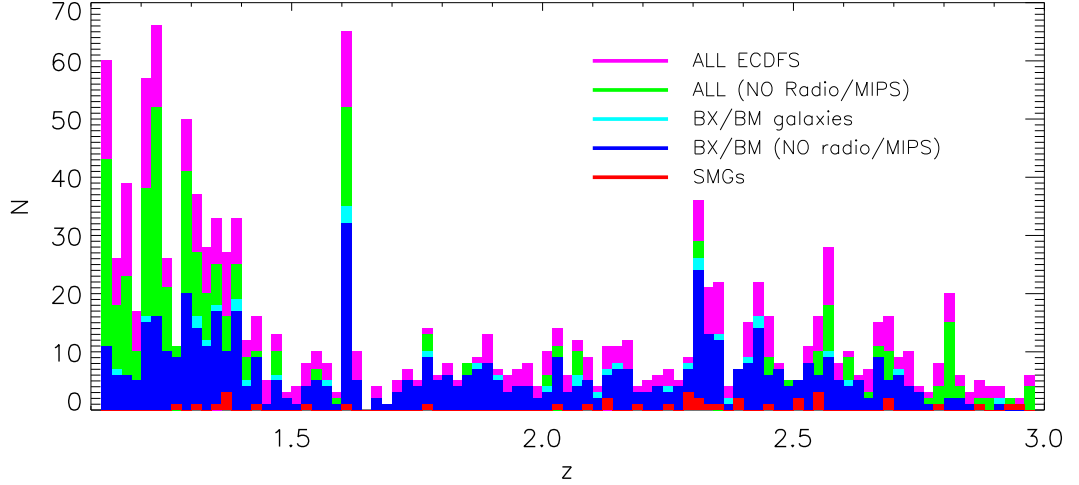
Figure 2.21: The redshift distribution of Q=1, 2 and 3 SMGs overlaid on the redshift distribution of field galaxies, compiled by Bin Luo with the addition of recent redshifts from Swinbank et al. in prep and Williams et al. (2014). The binning is $6000\,\mathrm{km\,s^{-1}}$. There is very little correlation between the peaks in the galaxy redshift distribution and the peaks in the SMG population.

is fair given the measurement errors on the redshifts and in particular the uncertainty on the systemic redshifts due to the absence of nebular lines etc. (see Fig. 2.20). In the few cases where > 1 SMG lies within $2000\,\mathrm{km\,s^{-1}}$ of another SMG, these 'spikes' do not coincide with 'spikes' in the background galaxy populations. This can be seen more clearly in Fig. 2.22 which focuses in on the densest 'structures'. We find only three pairs within $2000\,\mathrm{km\,s^{-1}}$ (one of which is ALESS 067.1 and ALESS 067.2 which is likely to be a merger based on the *HST* imaging to be presented in Chen et al. in prep) and one triple at $z \sim 2.294$ comprising ALESS 075.2, ALESS 088.5 and ALESS 102.1.

In Fig. 2.22 we show the comparison between the redshift distributions of SMGs and field galaxies in bins of $2000\,\mathrm{km\,s^{-1}}$, centred around the main 'associations' within the SMG population. This figure demonstrates that there are other SMGs within $\sim 2000\,\mathrm{km\,s^{-1}}$ of the 'spikes' and therefore that this method of identifying 'associations' is somewhat dependent on the binning. Furthermore, Fig. 2.20 demonstrates that depending on the choice of spectral lines from which the redshift
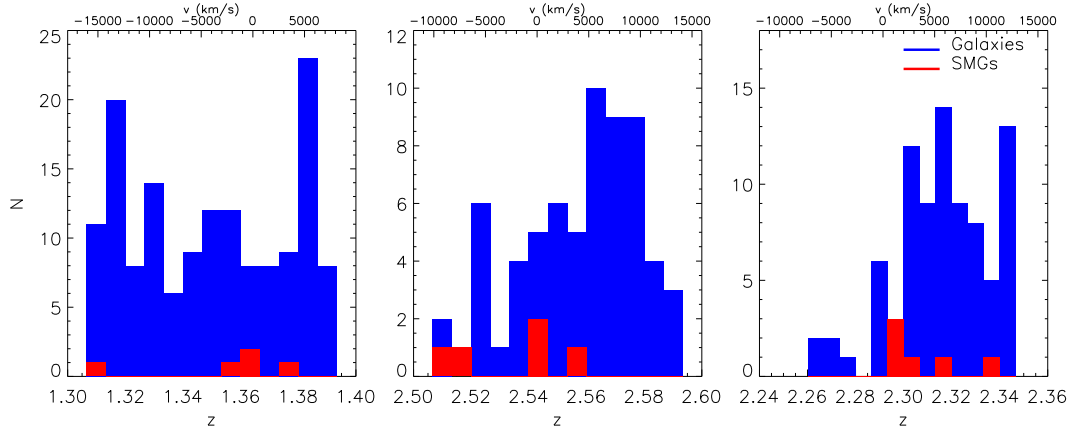
Figure 2.22: A zoomed in view of the 'spikes' in the ALESS SMG spectroscopic redshift distribution to search for coincidence with peaks in the overall galaxy redshift distribution. The maximum number of SMGs in a $2000 \, \mathrm{km \, s^{-1}}$ bin is three and there are three other bins containing two SMGs. The top axis gives the velocity offsets, with 0 being set at the position of the redshift 'spike' to demonstrate that the neighbouring SMGs are sometimes within $3000 \, \mathrm{km \, s^{-1}}$ from the 'spikes' and thus, depending on which line was used to determine their redshifts, they may scatter into the 'spike' (see Fig. 2.20).

is determined the derived redshifts may vary significantly (up to $3000 \, \mathrm{km \, s^{-1}}$). Thus some of the SMGs neighbouring the redshift 'spikes' may in fact scatter into these 'spikes' if nebular emission lines were available for all SMGs and others may scatter out. We therefore cross-match the SMG redshifts with themselves and find seven pairs of SMGs within $2000 \, \mathrm{km \, s^{-1}}$ of each other and therefore 10 SMGs lying within 'associations' (ALESS 041.1, 049.1, 051.1, 055.1, 057.1, 062.2, 075.1, 075.2, 088.5 and 102.1). ALESS 075.2, ALESS 088.5 and ALESS 102.1 lie in a triple 'association'. For these 10 sources we then also look at the spatial (on-sky) associations and we find that none of the pairs lie within 2 Mpc of each other and in fact, the median offset on sky is 11 Mpc with a range of 9–39 Mpc; the maximum of 39 Mpc meaning they may lie within the same large-scale structure but are unlikely to be within the same haloes. These 10 SMGs are highlighted in Fig. 2.9 and shown to be ~ 0.3 magnitudes brighter at 4.5μm than the average of the ALESS sample with spectroscopic redshifts.

To compare this result with the random probability of finding these 'associations'

we use the probability density function of the photometric redshift distribution as an input probability function to generate 52 random redshifts (matching the number of SMGs for which we have a Q=1, 2 or 3 redshift) 100,000 times in order to estimate the random likelihood of detecting two or more SMGs within $2000\,\mathrm{km\,s^{-1}}$ of each other. We only search over the redshift range $z = 1 - 3$ where a majority of the SMGs lie, and all the observed spikes in the redshift distribution. For $2000\,\mathrm{km\,s^{-1}}$ offsets, there is a 68% chance of finding four pairs of SMGs and a 28% chance of finding one or more groups of three SMGs, thus our observed 'associations' are not significant.

It is interesting to find so little coincidence between the background galaxy population and the SMGs and also to find so little structure within the SMG population itself given the results in Hickox et al. (2012). Spectroscopic incompleteness is still an obvious factor here, even when including the photometric redshifts. The lack of overdensities is interesting considering the most infrared luminous galaxies at $z > 1$ are expected to preferentially lie in groups (Popesso et al. 2014) and given the various measurements of clustering lengths which have implied that SMGs reside in very massive haloes. It is possible that most of the ALESS SMGs in fact reside in relatively isolated environments and that the strong clustering signal may be dominated by strong but brief merger-driven burst activity in relatively low mass structures, as discussed in Chapman et al. (2009). Finally, we note that the ECDFS appears to be underdense in bright ($> 3\,\mathrm{mJy}$) SMGs compared to other blank field surveys (see Weiß et al. 2009) which may be due to cosmic variance.

2.7.6 Spectral energy distributions and derived properties

The photometry of the ALESS SMGs, SED fitting and inferred average source properties are discussed thoroughly in S14 (optical to mid-infrared properties) and Swinbank et al. (2014) (far-infrared to radio properties). In Fig. 2.23 we plot the rest-frame composite SED (as in Fig. 11 from S14) based only on the photometry for the 52 ALESS SMGs for which we have determined a spectroscopic redshift. The

SEDs of both the optical to mid-infrared and the far-infrared to radio have been re-fit using the spectroscopic redshifts as constraints following exactly the same procedures as in S14 and Swinbank et al. (2014). Using the spectroscopic redshifts, the photometry has been de-redshifted and normalised by the rest-frame H-band luminosity. A running median is then calculated and convolved with the photometric filters to produce the 'average' SED. As in S14, the composite SED is found to be strongly dust reddened, however, the Balmer break in the composite SED is much stronger than observed in S14, as it is not smeared-out by inaccurate photometric redshift estimates.

To better understand the star formation history (SFH) of the ALESS SMGs we compare the composite to the constant and burst SFH models derived in S14 which were derived through fitting the average photometry for the whole ALESS sample redshifted to $z = 2.5$ using HYPERZ. The ALESS SMG composite SED is systematically offset from the models highlighting the fact that the SMGs for which we were able to determine a redshift are brighter than average across all wavelengths. Furthermore, the models look marginally redder than the composite meaning that those SMGs for which we were able to determine a spectroscopic redshift are bluer than the average of the total ALESS sample. This is biased since our spectroscopic redshift determinations typically required UV and optical detections and only the intrinsically brightest galaxies would have been detected at these wavelengths, thus resulting in a bluer than average SED. Aside from this, the shape of the composite is in good agreement with the models (which S14 find to be statistically indistinguishable from each other), in particular the strength and wavelength position of the break are very similar. These constant and burst models from S14 have burst ages of 2.3 Gyr and 30 Myr respectively and it is very difficult to distinguish between these two SFHs for the ALESS composite SED.

UV-to-radio SED fitting using MAGPHYS

As a comparison to the SED fitting of the photometry for the ALESS SMGs presented in S14 and Swinbank et al. (2014) we use MAGPHYS (da Cunha et al. 2008),
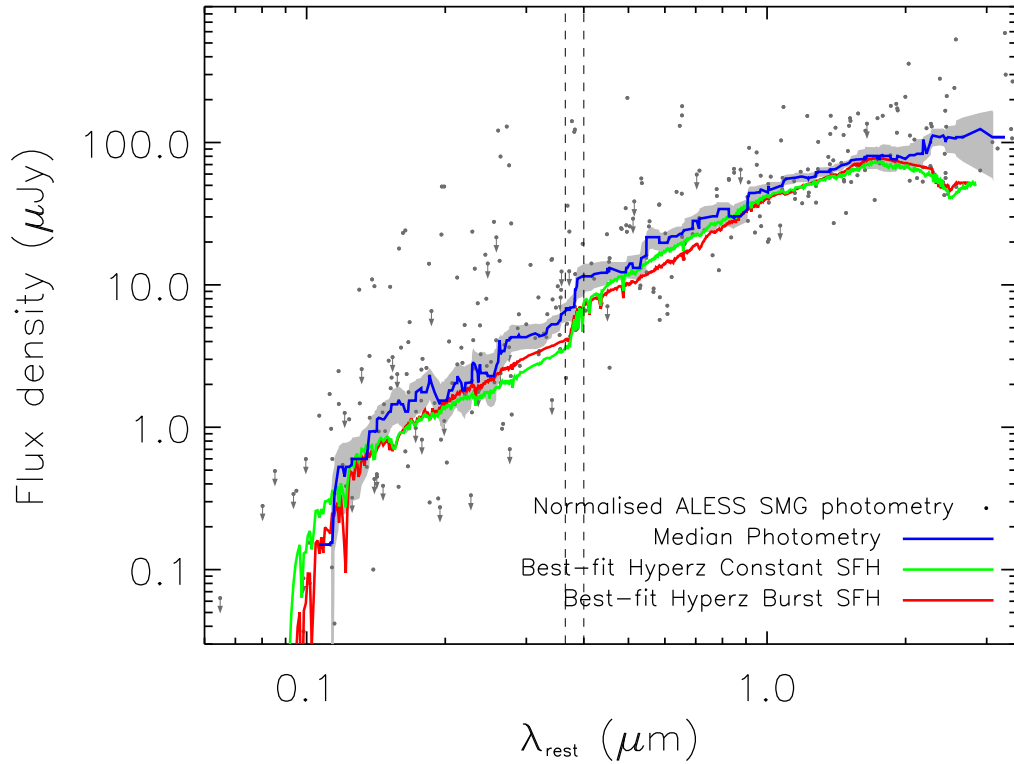
Figure 2.23: A composite SED using only the photometry from S14 for those ALESS SMGs with Q=1, 2, 3 spectroscopic redshifts. The photometry have been de-redshifted and normalised by their H-band luminosity. The blue solid line represents the running median over 20 sources per box. The grey region represents the bootstrap error on the running median. The overlaid fits are taken from S14 and are the SED fits to the average photometry for all ALESS SMGs using HYPERZ and assuming a constant SFH and an instantaneous burst respectively. The de-redshifted photometry and limits are shown as grey points and arrows respectively. Limits are set to zero in the calculation of the running median. The vertical dashed lines are positioned at the Balmer (3646Å) and 4000Å breaks. We observe a strong Balmer break in the composite SED.

an SED fitting code which consistently interprets the UV-to-radio emission. We use the spectroscopic redshifts determined in this work as a constraint in fitting to the 4–19 band (UV to mid-infrared) photometry presented in S14 and the far-infrared to radio photometry presented in Swinbank et al. (2014). These MAGPHYS SED fits and the derived sample properties can then be compared to those derived via fitting to the UV to mid-infrared and far-infrared to radio separately. MAGPHYS is described in detail in da Cunha et al. (2008) but we summarise some features of the code here:

MAGPHYS uses the Bruzual & Charlot (2003) stellar population synthesis code (with the Marigo & Girardi 2007 prescription for thermally-pulsating asymptotic giant branch stars- TP-AGB stars) to compute the light produced by the stars within the model galaxies. The attenuation by dust is then calculated via the Charlot & Fall (2000) model, which is also used to determine the total infrared luminosity of the re-radiated dust emission in star-forming clouds and the ISM. The SED of the dust emission is modelled as three main components: near-infrared PAH emission; mid-infrared emission from small hot dust grains ($< 0.01\mu$m); far-infrared emission from large dust grains ($0.01 - 0.25\mu$m) which are in thermal equilibrium and are either warm grains ($30 - 60\,$K) in stellar birth clouds or cold grains ($15 - 25\,$K) in the ambient ISM. These equilibrium temperatures are adjustable within the models, as are the relative contributions of the different dust emission components. The SFHs for each model are parameterised to rise linearly at early ages and then exponentially decay. The stellar emission and dust emission are simultaneously modelled via a basic energy balance argument such that the energy emitted by stars and absorbed by dust is re-emitted in the infrared.

In Fig. 2.24 the observed-frame SEDs are shown for each of the 52 ALESS SMGs with a spectroscopic redshift. The multiwavelength photometry from S14 and Swinbank et al. (2014) are shown, with both the attenuated and unattenuated flux models, fit using MAGPHYS overlaid. An updated version of MAGPHYS was used which is more applicable to high-redshift SMGs (described in da Cunha. in prep)

where the main improvements to the code were: (1) the prior likelihood distributions for each model parameter have been extended to include higher dust optical depths, higher SFRs and younger ages, since the stellar populations within SMGs at high-redshift are typically young; (2) absorption by the intergalactic medium has been incorporated into the UV region of the model SEDs. In Fig. 2.24 we show the best fits to the photometry whilst fixing the redshift at the spectroscopic value determined in this work. As well as providing strong constraints on the properties of the galaxies, such as stellar masses, extinction and bolometric luminosities, we can also study the fits to search for evidence of AGN which have been missed by the X-ray classifications in Wang et al. (2013). Since AGN templates are not currently included within the MAGPHYS library, SMGs with strong AGN emission will not be fit well by the models. Furthermore, we can use the fitting procedure as a sanity check for the Q=3 redshifts.

In general the SED fits in Fig. 2.24 are good, with $\chi^2 < 5$, however, as expected the poorest fits are to sources known to be AGN and sources with very few photometry points. The best fit SEDs to the ALESS photometry, with no constraints being applied to the redshifts will be presented in da Cunha (in prep). Where the fits are particularly poor this is generally due to a lack of photometric detections (i.e ALESS 080.5, ALESS 088.2), contamination from a nearby bright source (i.e. ALESS 006.1, 084.1), poorly constrained photometry points (i.e. U-band in ALESS 011.1, ALESS 017.2), Q=3 redshifts may be wrong (i.e. ALESS 080.5, 084.1, 088.2) or AGN contamination (i.e. ALESS 011.1, 084.1). Comparing the dust-attenuated and the unattenuated SED fits in Fig. 2.24 shows that on average there is very significant attenuation in the rest-frame UV; in some cases reaching ~ 4 orders of magnitude.

The main advantages of these SED fits over those determined in S14 and Swinbank et al. (2014) is that the UV-to-radio emission is simultaneously and consistently fit. However, the main parameters derived from the two different models do not strongly differ. In Fig. 2.25 we compare the stellar masses, far-infrared luminosities and extinction between the S14 and the MAGPHYS model outputs. The

median extinction derived from the S14 fits is $A_V = 1.7 \pm 0.2$ whilst the median from the MAGPHYS fits is $A_V = 1.9 \pm 0.2$, which are within 1σ of each other. Furthermore, the median difference between the MAGPHYS and S14 estimates of A_V as a fraction of the MAGPHYS estimate is $\Delta A_V / A_{V\_MAG} = 0.1 \pm 0.1$, consistent with them being the same. There are some very obvious outliers, namely, ALESS 006.1, ALESS 017.2, ALESS 075.2, ALESS 107.1, with $\Delta A_V / A_{V\_MAG} < -2$, two of which have Q=3 redshifts which may be incorrect. In some cases the extreme offset between the two models may be due to a poor fit to a small number of photometry points in the SED fit or in the case of ALESS 006.1, contaminated photometry due to the SMG being lensed. The scatter in $\Delta A_V / A_{V\_MAG}$ highlights the degeneracy between the SFHs, age and reddening in the SED fitting.

We compare the far-infrared luminosities $(8-1000\mu m)$ from Swinbank et al. (2014) with the 'dust' luminosities from MAGPHYS $(3-2000\mu m)$ and find almost linear agreement between them, with median values of $L_{FIR} = (3.5 \pm 0.4) \times 10^{12}\,L_\odot$ and $L_{FIR} = (3.2 \pm 0.4) \times 10^{12}\,L_\odot$ for the Swinbank et al. (2014) and MAGPHYS models respectively (within 1σ of each other) and with $\Delta L_{FIR}/L_{FIR\_MAG} = -0.06 \pm 0.09$ (consistent with zero). These compare to $L_{FIR} = (3.0 \pm 0.3) \times 10^{12}\,L_\odot$ (Swinbank et al. 2014) and $L_{FIR} = 3.5 \times 10^{12}\,L_\odot$ (da Cunha. in prep) for the whole ALESS sample, thus the ALESS SMGs with spectroscopic redshifts are not statistically distinct in terms of far-infrared luminosity from the whole ALESS sample. Again, in Fig. 2.25, there are two distinct outliers, ALESS 015.3 and ALESS 017.2 both of which have SED fits based on only three and seven photometry points respectively.

Estimating the masses of SMGs has been the subject of much controversy in literature. Estimates depend strongly on the SFHs assumed, the stellar population synthesis model parameters and the IMF adopted. Furthermore, historically, rest-frame K-band magnitudes have been used as a tracer of the stellar mass, in part due to the accessibility of data in this waveband, but also because it is not as strongly affected by dust (at shorter wavelengths), and is more sensitive to older, lower mass stars which dominate the stellar mass of galaxies. More recently, Hainline et al. (2011) and S14, used rest-frame H-band luminosities, which more closely

probe the peak of the stellar emission, benefit from the lower extinction at near-infrared wavelengths and minimise the effects of TP-AGB stars which contribute more strongly in the K-band. However, large systematic uncertainties in determining the stellar mass remain. This is exemplified in studies by Hainline et al. (2011) and Michałowski et al. (2010), which for the same sample of galaxies determine median stellar masses of $M_* \sim 7 \times 10^{10}\,\mathrm{M_\odot}$ (Chabrier IMF) and $\sim 3.7 \times 10^{11}\,\mathrm{M_\odot}$ (Salpeter IMF) respectively; a factor of five difference, which was attributed to differences in the IMF, SFHs and population synthesis models applied. The stellar masses in S14 are calculated via their dust-corrected (and single SFH) H-band luminosities, whereas the stellar masses output from MAGPHYS are determined from the full SED fits with a range of complex SFHs, ages and dust attenuations. Since in our MAGPHYS analysis, we also have spectroscopic redshifts as constraints in the SED fits the stellar masses determined are some of the strongest constraints on SMG stellar masses to date. S14 find a median stellar mass for the whole ALESS sample (with photometric redshifts) of $M_* \sim 8 \times 10^{10}\,\mathrm{M_\odot}$ for a Salpeter IMF. To make this more comparable to the work of Hainline et al. (2011) and the MAGPHYS models we divide this by a factor 1.8 to convert from the Salpeter IMF to the Chabrier IMF resulting in a median mass of $M_* \sim 4.4 \times 10^{10}\,\mathrm{M_\odot}$. This is lower than the median of $M_* = (7 \pm 1) \times 10^{10}\,\mathrm{M_\odot}$ derived here from refitting the SEDs with spectroscopic redshifts. Using MAGPHYS we find a median stellar mass for our SMGs of $M_* = (6 \pm 1) \times 10^{10}\,\mathrm{M_\odot}$ (Chabrier IMF) compared to $M_* \sim 8.9 \times 10^{10}\,\mathrm{M_\odot}$ in the whole ALESS sample (da Cunha. in prep). Thus, on average, the MAGPHYS and S14 masses are comparable with a median fractional difference between the masses derived from the two models of $\Delta \mathrm{M_*}/\mathrm{M_{*\_MAG}} = -0.1 \pm 0.5$. The ALESS SMG masses are significantly closer to those determined in Hainline et al. (2011) than those determined in Michałowski et al. (2012) even with the correction applied to the Michałowski et al. (2010) masses to scale from a Salpeter to a Chabrier IMF.

The main outliers in the stellar mass comparison in Fig. 2.25 are ALESS 010.1, ALESS 037.2, ALESS 061.1 and ALESS 075.1. ALESS 010.1 (discussed in Section 2.5.3) is found to be more consistent with a redshift of $z \sim 2$ in S14. There appear to be

two components $< 1''$ from each other, which if physically unassociated from each other will result in contaminated photometry. ALESS 037.2 is a Q=3 redshift with only seven detections across the whole SED thus the fit is poorly constrained in both S14 and MAGPHYS. ALESS 061.1 has a redshift determined from an ALMA detection of [CII]$\lambda 158\mu$m and the SED is fit to only eight photometry points, with a particularly poor fit in the UV. ALESS 075.1 is discussed in Section 2.7.1 and may have strong contributions from an AGN. Neither S14 nor MAGPHYS include AGN templates in the SED fitting, thus one might expect the fits be poor, in particular in the mid-infrared, which is the case for ALESS 075.1 in Fig. 2.24. Fig. 2.25 highlights the degeneracy in SED fitting between different models and the difficulty in constraining the stellar masses of SMGs, since they are rapidly evolving, dusty, heavily reddened galaxies. This degeneracy is exacerbated by poorly constrained SEDs with few photometry points. However, given the broad range in complex SFHs utilised by MAGPHYS and the capability of simultaneously fitting the whole SED from UV-to-radio, we are able to place some of the best constraints on the stellar masses of SMGs to date.
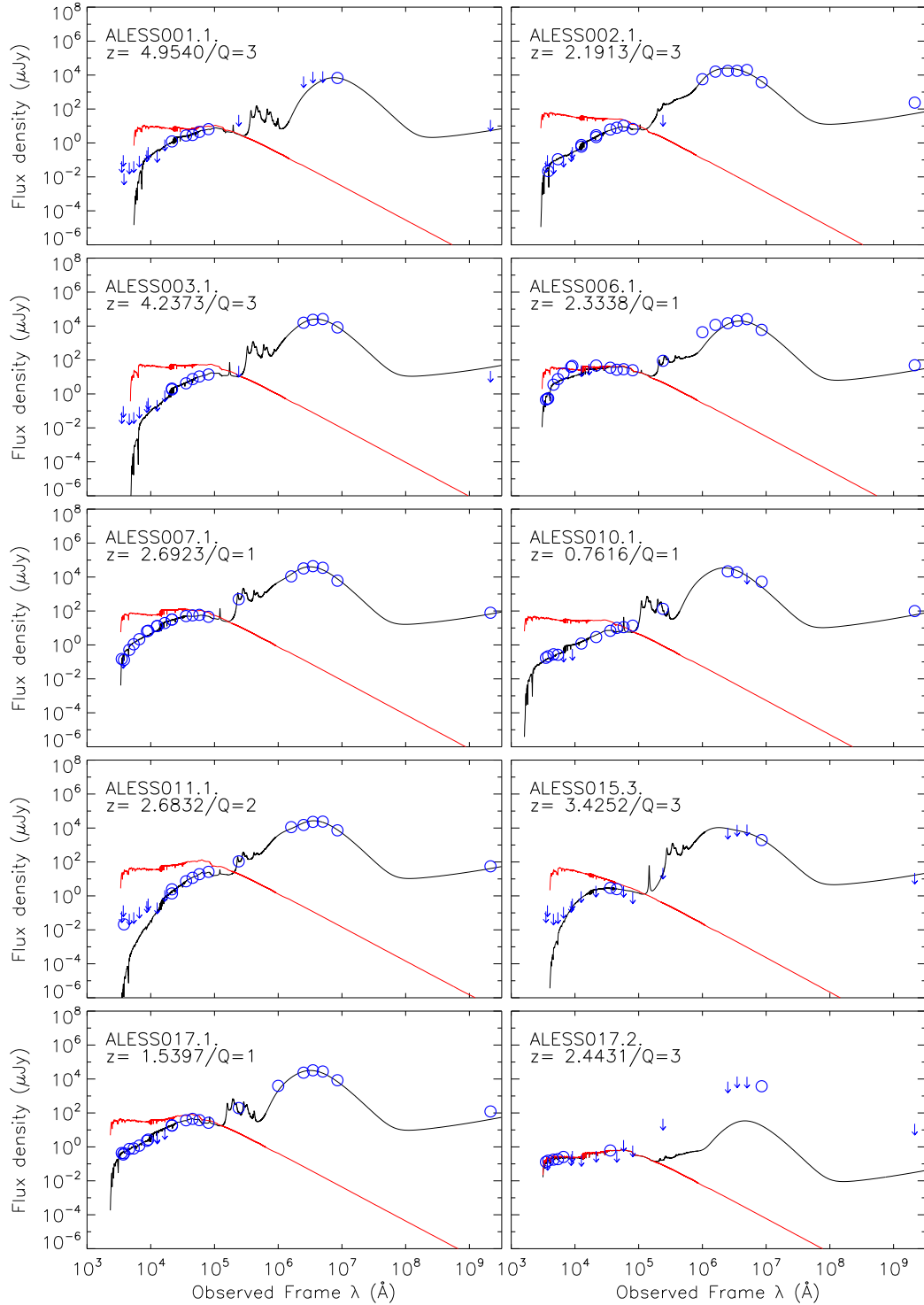
Figure 2.24: These SEDs have been fit to the photometry from S14 and Swinbank et al. (2014) using the MAGPHYS SED fitting code (da Cunha et al. 2008). These are the fits based on the spectroscopic redshifts and are therefore not always the optimum fit that would result from placing no constraint on the redshift. The data points are the observed photometry, and arrows indicate 3σ detection limits in each band. We do not show the errors as they are typically relatively small ($< 5\%$). In black is the dust attenuated model and in red is the unattenuated model. In some cases there are ~ 4 orders of magnitude of extinction in the rest-frame UV.
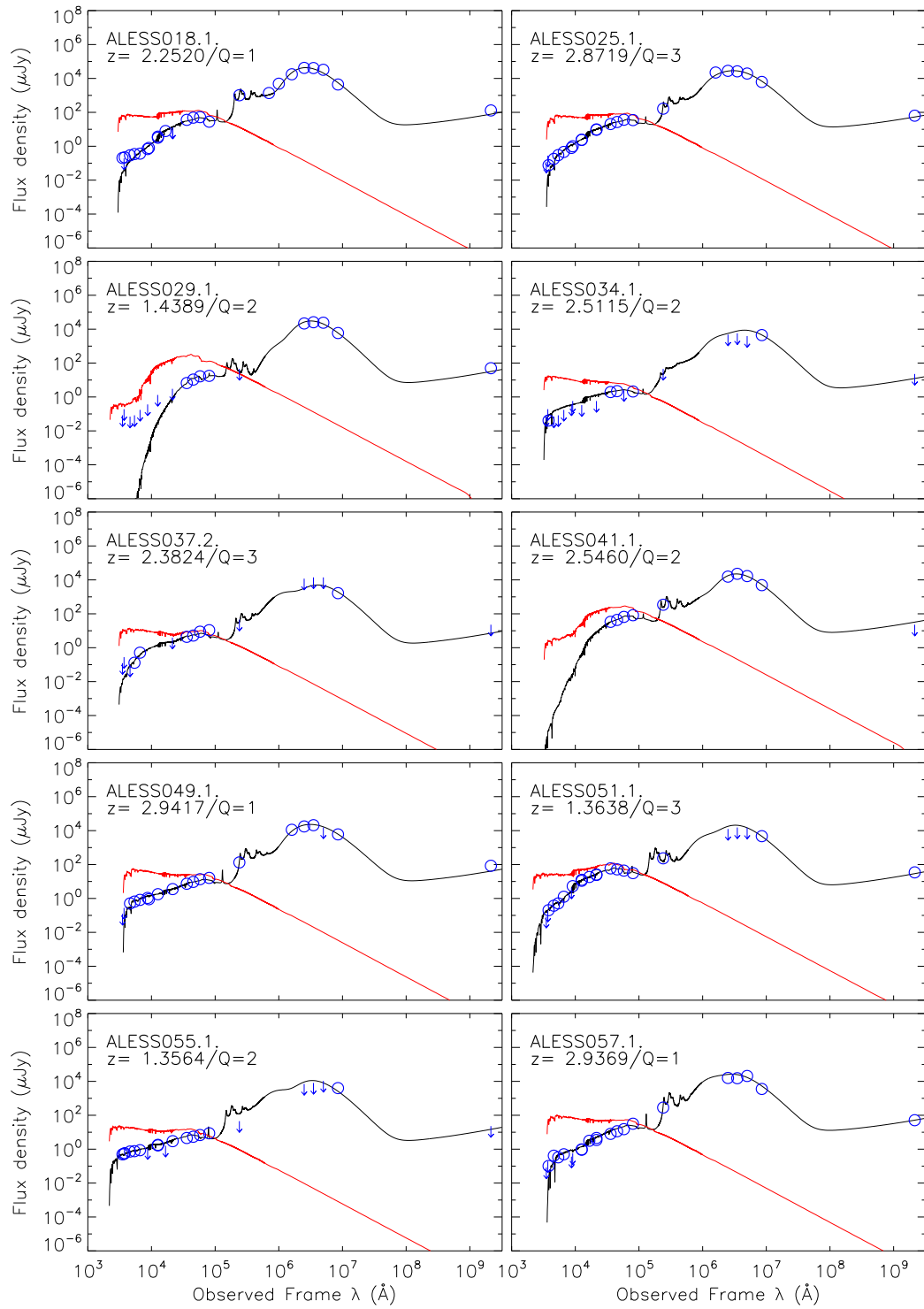
Figure 2.24 *cont.*
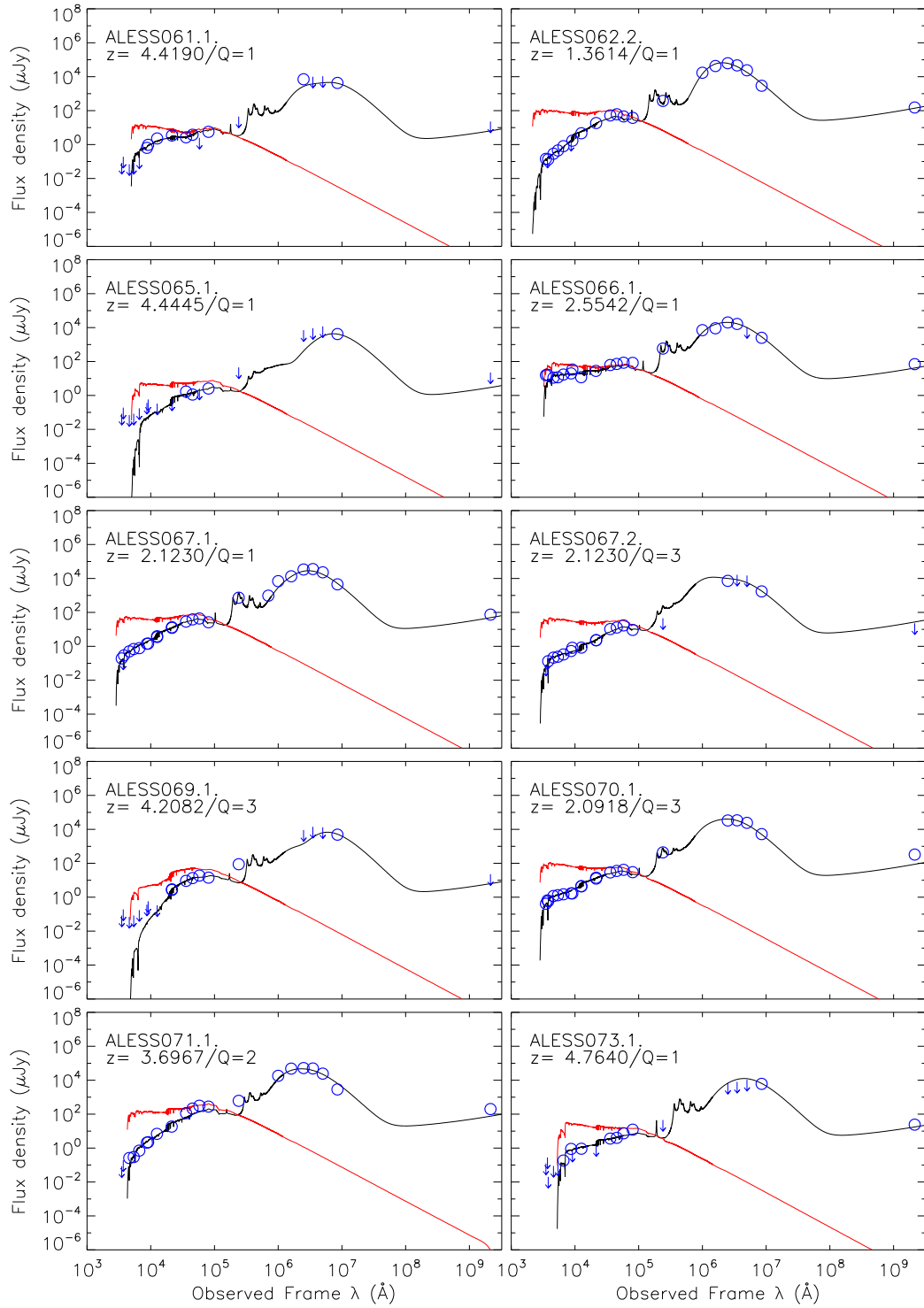
Figure 2.24 *cont.*
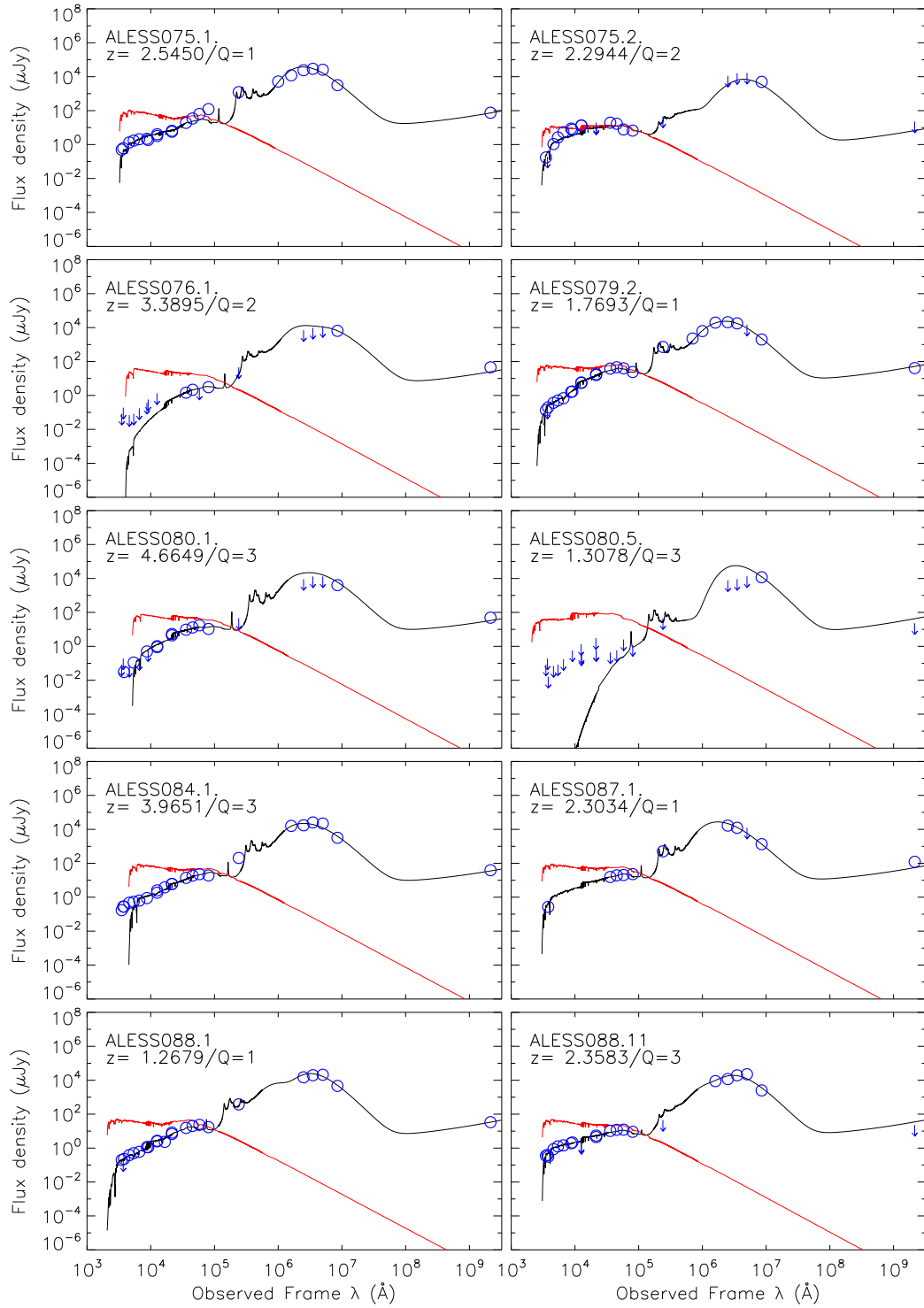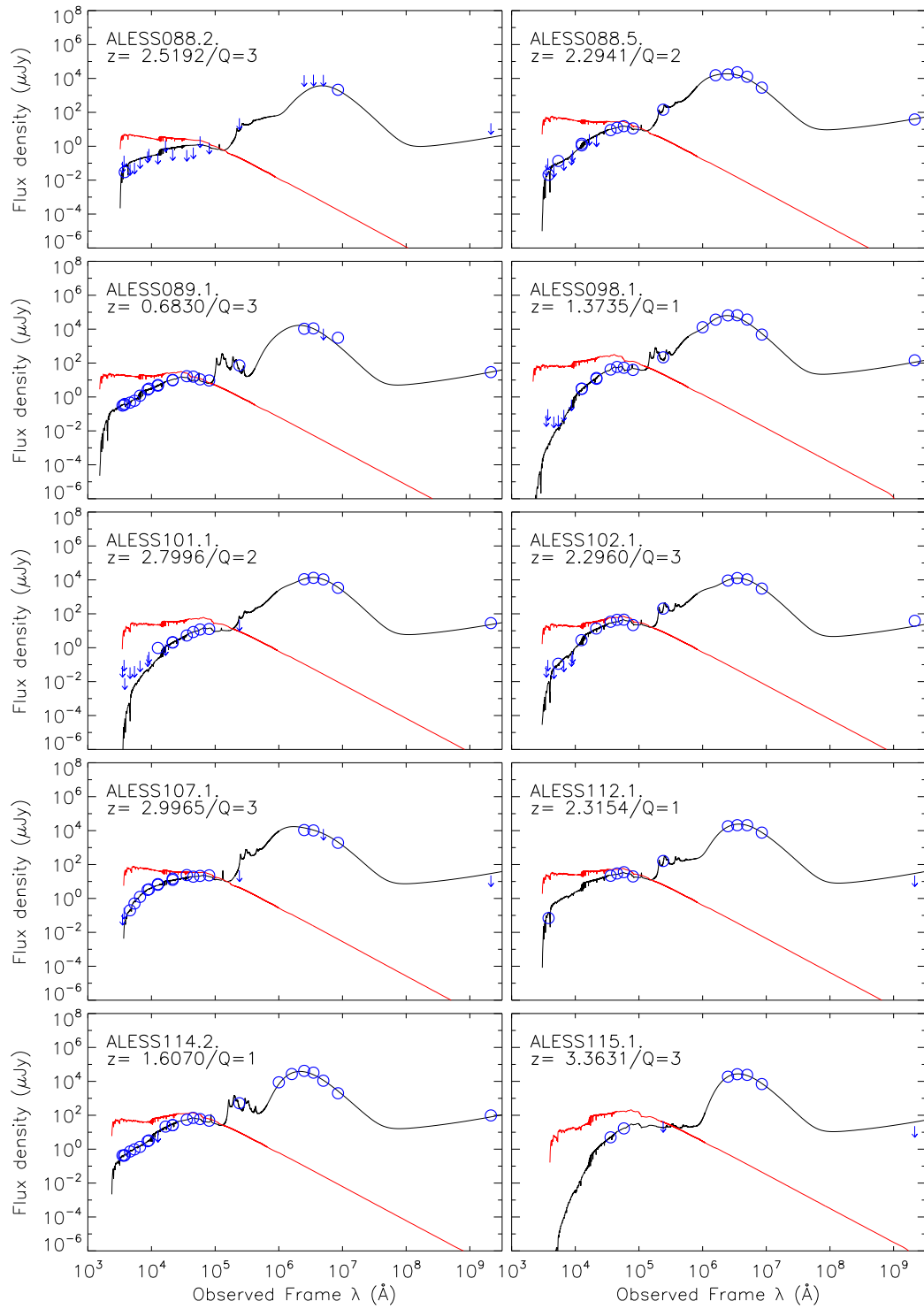
Figure 2.24 *cont.*
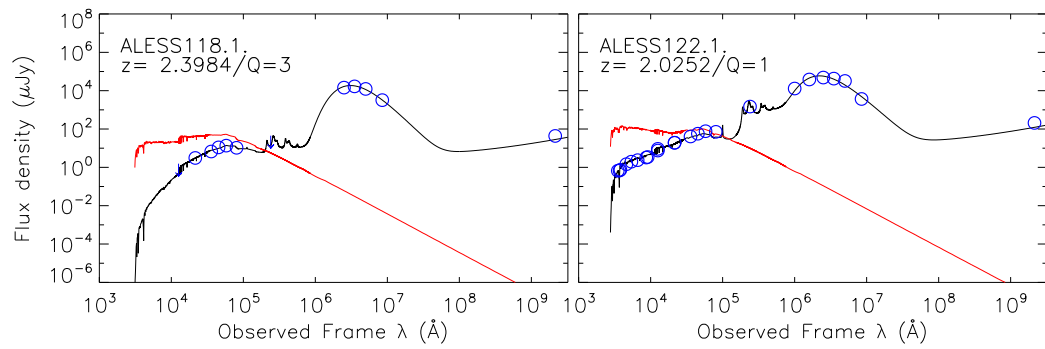
Figure 2.24 *cont.*

Figure 2.24 *cont.*
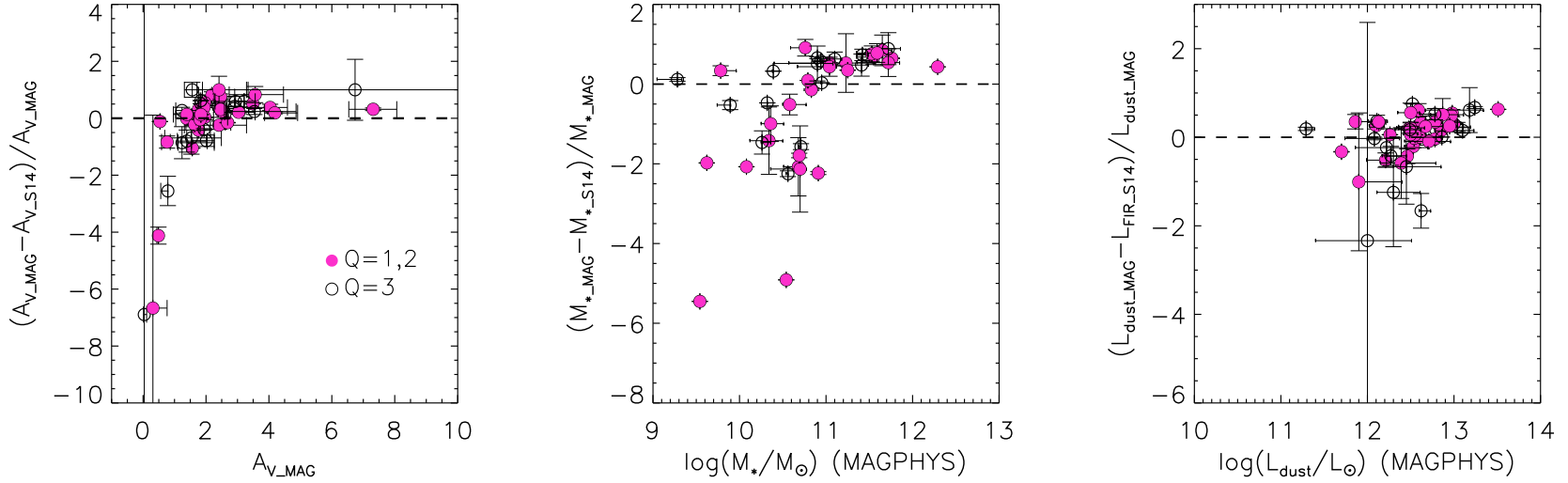
Figure 2.25: We compare the properties of the ALESS SMGs as derived from S14 and Swinbank et al. (2014), and from MAGPHYS. The extinction (A_V), stellar masses and far-infrared luminosities are compared. The far-infrared luminosities from MAGPHYS are the 'dust' luminosities, integrating the SEDs over $3-2000\mu m$ which are comparable to bolometric ($8-1000\mu m$) luminosities determined in Swinbank et al. (2014). We exclude the data for ALESS 080.5 since the fit is based on only one photometry point. All quantities are shown as the difference between the estimates from MAGPHYS and S14, as a fraction of the MAGPHYS estimates versus the MAGPHYS estimates. A one-to-one relation is shown as a dashed line. The stellar masses from S14 have been shifted to Chabrier IMF to be consistent with those from MAGPHYS. There is generally good agreement between the properties derived using MAGPHYS and those derived in S14 and Swinbank et al. (2014) with median values of $\Delta A_V/A_{V\_MAG} = 0.1 \pm 0.1$, $\Delta M_*/M_{*\_MAG} = -0.1 \pm 0.5$ and $\Delta L_{FIR}/L_{FIR\_MAG} = -0.06 \pm 0.09$. Some of the error bars are very large and therefore extend beyond the plot boundaries.

IRX-β

The SED fits can be used to infer various properties of the SMGs. Here we use inferred properties to compare the dust attenuation of SMGs to that in local galaxies via the IRX-β relation, which relates the dust reddening to the dust attenuation in galaxies. In the absence of dust, the best tracer for measuring SFR is the UV, since it directly traces the bulk of the emission from young massive O/B stars which are short-lived. However, star formation produces large quantities of dust which in turn absorbs the UV emission and re-emits it at infrared wavelengths causing reddening of the UV continuum. This reddening can be described as $f_\lambda \propto \lambda^\beta$ where β is the rest-frame UV slope. The attenuation caused by dust can then be described as the infrared excess or the ratio of the far-infrared dust emission to residual UV emission (IRX=$L_{\rm IR}/L_{\rm UV}$). The strong correlation between IRX and β was first observed and constrained in Calzetti et al. (1994) and Meurer et al. (1999). In Meurer et al. (1999) a large sample of local starbursts were used to empirically constrain the IRX-β relation, where $L_{\rm IR}$ is $L_{8-1000\mu m}$, $L_{\rm UV}$ is $L_{1600 \text{\AA}}$ and β is determined from the slope of the UV continuum between $1216-3200\text{\AA}$. The relation was found to be very tight for local starbursts (Meurer et al. 1999) and historically, IRX-β has been used as a method of estimating the dust obscuration and thus the total SFRs of galaxies where $L_{\rm FIR}$ measurements are not available or are difficult to obtain (for example at high redshift). However, a recent re-analysis of the Meurer et al. (1999) sample by Takeuchi et al. (2012) uses better constrained photometry and finds a shift in the IRX-β relation resulting in lower IRX values and redder slopes.

Normal, non-starburst galaxies have been found to typically lie below the relation, in the sense of having lower values of IRX at a fixed UV slope, likely due to contamination from intermediate-age populations contributing strongly in the UV (Seibert 2004). Other work i.e. Kong et al. (2004) argues that offsets from the IRX-β relation may be due to more complex SFHs. Furthermore, various studies have demonstrated that the dustiest systems, such as ULIRGs and high redshift SMGs, lie significantly above the locally calibrated relation and appear to be uncorrelated

(i.e. Goldader et al. 2002; Reddy et al. 2010; Overzier et al. 2011). In part this may be due to the fact that for the IRX-β relation to work, the geometry of the dust must be assumed to be a shell, physically close to the UV-emitting sources. The likely complex and disturbed geometries of ULIRGs and SMGs may have a strong effect on their position in IRX-β space. Goldader et al. (2002) attribute the offset of ULIRGs to a decoupling of the far-infrared and UV emission within the galaxies, such that the some of the UV emission is not being emitted from the same spatial regions as that which is absorbed and re-emitted by the dust. Such decoupling of the UV and infrared could be due to a recent merger-driven starburst.

In Fig. 2.26 we show the IRX-β distribution of the ALESS SMGs, colour coded by redshift. L_{IR} values are from the photometry presented in Swinbank et al. (2014), with the SEDs re-fit using the spectroscopic redshifts as constraints. We determined L_{UV} by interpolating the S14 SEDs (re-fit to the spectroscopic redshifts) at 1600Å. Similarly the UV slope is determined by fitting the slope of the SEDs between $1216-3200$Å. We only determine these quantities from SEDs which are well-constrained in the UV (i.e. multiple photometry points between $1216-3200$Å).

We find the ALESS SMGs to be scattered around the IRX-β relation from Takeuchi et al. (2012) with a median UV slope of $\beta = -0.3 \pm 0.2$ and a median infrared excess of IRX $= 30 \pm 10$, which is only marginally offset from the IRX-β relation. We also compare to the IRX-β relation determined in Casey et al. (in prep) which has been derived from a large local sample with a range of galaxy properties (SFR$\sim 1-100\,M_\odot yr^{-1}$) and a sample of high-redshift dusty star-forming galaxies (up to $z \sim 3.5$). We find the median IRX and β values of the ALESS SMGs are $\delta IRX \sim 13$ above the relation from Casey et al. (in prep) with the slope being $\delta\beta \sim 0.3$ bluer for the ALESS SMGs than the IRX-β relation. Unlike Goldader et al. (2002) we do not find the ALESS SMGs to be systematically above the IRX-β relation. The points are grouped into four redshift ranges to search for evidence of evolutionary trends. The mean and bootstrap error is calculated for each redshift bin and we find that towards the present day, the ALESS SMGs move to higher values of IRX and UV slope. In part this trend with redshift may be due to the

fact we are biased to detecting only the UV-brightest SMGs at high redshift, thus resulting in a decrease in IRX towards higher redshift.

We then investigate the deviation of the observed UV slope from that predicted by the Casey et al. (in prep) relation versus the far-infrared luminosity and find a marginal evolution, such that the IRX-β relation predicts bluer slopes than observed at $z > 3.5$ and redder slopes than observed towards the present day. However, overall the $z > 3.5$ SMGs have slopes which are $\Delta\beta \sim 0.5$ bluer than those at $z < 1.5$. Furthermore, the figure clearly demonstrates that the far-infrared luminosity increases with increasing redshift (thus also the derived SFRs).

Thus, we find that both the IRX increases and the L_{FIR} decreases towards the present day. Also, we find marginally redder slopes towards the present day ($\Delta\beta \sim 0.5$ between $z = 1.5 - 3.5$). Thus, in order for the IRX to decrease despite increasing L_{FIR}, the emergent UV must be significantly attenuated. Since the scatter of the ALESS SMGs is so broad it could also be argued that the UV and infrared emission are decoupled (tracing different components) which may explain why the IRX increases towards to the present day despite an order of magnitude decrease in L_{FIR} from $z > 3.5$ to $z < 1.5$. The reddening observed towards the present day may be indicative of an increase in metallicity towards lower redshifts or possibly a varying IMF such that at high redshifts the UV slope appears bluer due to the presence of a top-heavy IMF which over-produces massive, hot blue O/B stars (e.g. Marks et al. 2012). Again, this analysis highlights the diversity in the SMG population and the variation in the properties of SMGs with redshift. These are complex systems with varying levels of star formation and dust attenuation and further detailed work is required to understand what drives the lack of correlation between the IRX and β, in particular whether spatial dissociation of the UV and far-infrared emitting components play a role.
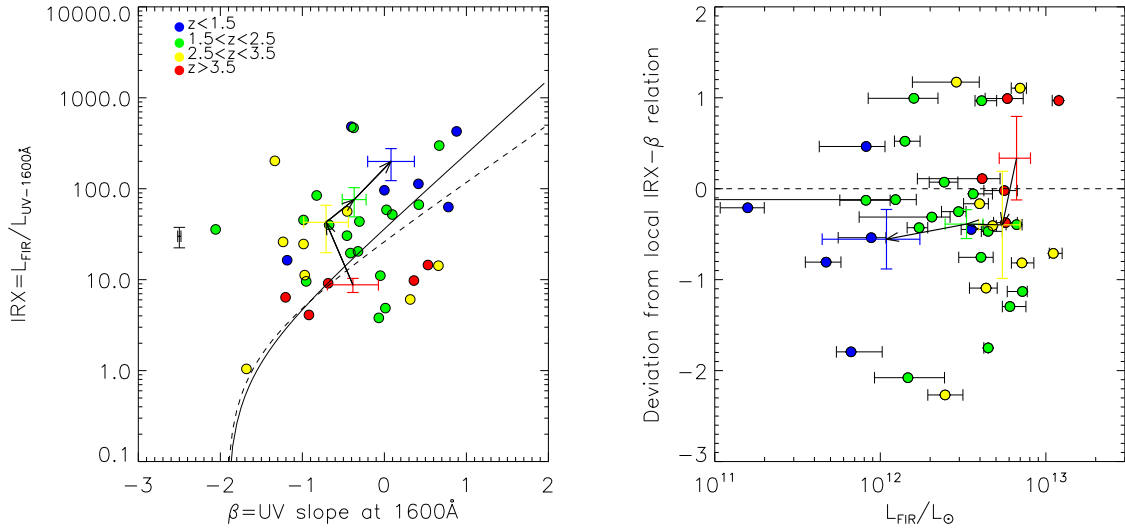
Figure 2.26: *Left:* The ratio of the far-infrared dust emission to residual UV emission (infrared excess- IRX) versus the UV spectral slope β ($f_\lambda \propto \lambda^\beta$) for the 36 ALESS SMGs with Q=1, 2 and 3 redshifts and reasonable constraints on the photometry for constraining the UV slope and luminosity. For normal star-forming galaxies the correlation between IRX and β is tight, however, as demonstrated with our sample, high redshift ULIRGs typically fall well above the relation. Overlaid as a solid line is the best-fit model derived in Casey et al. (in prep) and shown as a dashed line is the relation from Takeuchi et al. (2012). We show a median representative error bar in black. In both figures, the points are colour-coded by redshift and the mean of each redshift bin is highlighted with corresponding coloured error bars, and linked with arrows to highlight potential evolutionary trends. At higher redshifts SMGs appear to be marginally bluer with a lower IRX than at low redshifts. *Right:* The deviation of the observed UV slope from that predicted by the Casey et al. (in prep) relation ($\beta_{\rm obs} - \beta_{\rm exp}$), versus the far-infrared luminosity.

2.8 Conclusions

In this work we carry out a redshift survey of a large sample of ALMA-identified sub-mm selected SMGs with unambiguously identified counterparts. We determine redshifts for 52 out of the 131 ALESS SMGs, 32 of which are high quality (Q=1 or 2) and 27 of these are in the MAIN ALESS catalog (SMGs within the primary beam of ALMA and in high-quality maps). ALMA detections of the SMGs enables unambiguous and unbiased counterpart identification without the need to select radio-identified SMGs and use the radio-far-infrared correlation to pinpoint the SMG emission, therefore removing the bias against high-redshift SMGs and radio-undetected SMGs. Furthermore, the high resolution of ALMA allows the true sub-mm flux of the SMGs to be measured. Here we summarise the main conclusions of this work:

- The spectroscopic redshift distribution of all the ALESS SMGs has a range of $z = 0.683 - 4.954$, an interquartile range of $z = 2.1 - 3.0$, and a peak at a median of $z = 2.4 \pm 0.1$. In our analysis we include both the SUPP ALESS SMGs and the lower quality Q=3 spectroscopic redshifts, which we find to be individually tentative but statistically viable. Excluding these two populations changes the median redshift to $z = 2.5 \pm 0.1$ when the SUPP SMGs are excluded and $z = 2.3 \pm 0.2$ when the Q=3 SMGs are excluded. We find the spectroscopic redshift distribution to be in good agreement with the ALESS photometric redshift distribution in S14. The distribution is also similar to that determined from the large sample of radio-detected SMGs across multiple fields discussed in C05, however, we have a high redshift tail such that 23% of the ALESS SMGs lie at $z > 3$, which was not found in the C05 sample due to their radio flux limits.

- We discuss the dependency of the measured redshift on the choices/availability of emission/absorption features. We find velocity offsets of up to $\sim 3000 \, \mathrm{km \, s^{-1}}$ between the redshifts measured from nebular emission lines (i.e. Hα, [OIII], Hβ and [OII]) and those measured from Lyα or UV ISM absorption lines. We

conclude that it is likely that the extreme SFRs within the SMGs (typically $\sim 300 \pm 30\,\mathrm{M}_\odot\mathrm{yr}^{-1}$) are driving strong galaxy-scale outflows in many of the SMGs.

- Using the accurate spectroscopic redshifts we investigate the environments of the SMGs to search for associations both between SMGs and between SMGs and other galaxy populations in the ECDFS. We find very little evidence of structures within the SMG population, or correlation between peaks in the SMG redshift distribution and those of other galaxy populations in the ECDFS. In particular, though >35% of the original LESS SMGs were found to comprise multiple SMGs in the ALMA maps, there are only four maps for which we were able to determine spectroscopic redshifts for more than one of the components, none of which were found to be within $2000\,\mathrm{km\,s}^{-1}$ of each other, and in most of these cases only one of the redshifts was Q=1. Even when including photometric redshifts for the SMGs for which we could not measure a spectroscopic redshift we found *no* cases where two or more SMGs within the same map had a photometric or spectroscopic redshift within $2000\,\mathrm{km\,s}^{-1}$ of each other. This may imply that the ALESS SMGs reside in relatively isolated environments. However, it is important to note that spectroscopic completeness is a problem for this analysis.

- We identify interesting spectra with strong emission/absorption/continuum features. There are a number of lensed sources with a bright foreground galaxy lensing the higher redshift SMG. Such cases highlight the difficulty of counterpart identification without the benefit of high-resolution sub-mm detections. In such cases the photometry may be contaminated or dominated by the foreground source which can affect the SED modelling and the derived photometric redshifts and properties. The highest signal-to-noise spectra show a diverse range in spectral classifications from QSOs to star-forming galaxies with very strong galactic winds. We note that the spectra with strong emission lines may be biased towards containing AGN.

- BPT diagnostics of those SMGs for which we have at least Hα and [NII] information demonstrate that most of the SMGs are consistent with the dominant ionisation mechanism arising from star-formation in HII regions as opposed to AGN activity, if we use the Kewley et al. (2013) classification scheme which is more suitable for the highly disturbed ISM found within high-redshift star-forming galaxies.

- Since many of the spectra are too faint to exhibit any obvious emission or absorption features (in fact continuum is only detected in ∼50% of the spectra), we produce composite spectra over various redshift ranges to search for interesting features in the 'typical' ALESS SMG optical-to-near infrared spectrum. Over $1000-2000$Å we find strong asymmetric Lyα emission and blueshifted SiIV and CIV absorption indicative of strong stellar winds. Over $3400-4400$Å we observe a strong Balmer break, indicative of ongoing star formation on timescales of > 100 Myr. Comparing our composite to various evolutionary models we find that it is most consistent with a young starburst of 100 Myr duration observed at 10 Myr. The [OIII] composite exhibits a broadened red wing indicative of stellar winds. The Hα composite exhibits a high [NII]/Hα ratio. Although the [OIII]/Hβ and the [NII]/Hα ratios are extreme, they are consistent with the ionisation being star-formation driven, within the Kewley et al. (2013) high-redshift star-forming galaxy classification scheme.

- We use the newly-derived redshifts as constraints in SED model fitting for each SMG using MAGPHYS and find the average stellar mass of the spectroscopically-confirmed SMGs to be $M_* = (6 \pm 1) \times 10^{10}$ M$_\odot$ (with a Chabrier IMF) similar to the typical SMG mass derived in Hainline et al. (2011).

- We find the ALESS SMGs to be widely scattered about the local star-forming galaxy IRX-β relation. There is a trend of the IRX (L$_{\text{FIR}}$/L$_{\text{UV}}$) increasing with redshift, however, this is likely to be mostly due to the fact that the UV is only detected from the brightest SMGs at high redshift, especially since we find that the L$_{\text{FIR}}$ increases with redshift. We also find a trend such that

the typical UV slope at $z > 3.5$ is bluer than that at $z < 1.5$ which may imply an increase in the metallicity towards the present day, evolution in the IMF, or possibly spatial decoupling of the UV and far-infrared emitting galaxy components.

Overall, we find that the SMG population is a diverse population of dusty galaxies most common at $z \sim 2.4$, with strong contributions to their energetics from both AGN activity and extreme star formation. These contributions can be very challenging to disentangle since powerful star formation can result in strong galactic winds which appear spectroscopically similar to AGN. Further detailed integral field unit (IFU) follow-up observations, facilitated by the knowledge of the spectroscopic redshifts of these SMGs will allow us to separate out the relative contributions of star formation and AGN and to better understand this extreme and diverse population of galaxies.

Chapter 3

The properties of the interstellar medium within a star-forming galaxy at z=2.3

3.1 Motivation

In the previous chapter we derived redshifts for a large sample of SMGs. One of the incentives for deriving spectroscopic redshifts for SMGs is to facilitate detailed follow-up observations, in particular using instruments with narrow bandwidths, where the redshift must be known to a high degree of accuracy in order to correctly tune the detector. As discussed in Chapter 6, we are in the process of undertaking follow-up observations of a number of the brightest LESS SMGs, however, since a majority of the population lies at a redshift of $z \sim 2$, these sources are typically very faint and difficult to resolve, since at this redshift the scale is $\sim 8\,\mathrm{kpc}/''$. Some of the most detailed studies of SMGs have been able to probe to scales of 1–2 kpc, however, this is far larger than the characteristic size of individual star-forming regions ($< 100\,\mathrm{pc}$ locally, Milky Way GMCs $\sim 40\,\mathrm{pc}$; Bolatto et al. 2008). Therefore, a spatial resolution approaching $\sim 100\,\mathrm{pc}$ is essential to resolve the gravitationally unstable regions within SMGs and investigate the environments in which the stars

form and evolve.

Much controversy remains about the main driver of the very high star formation rates within SMGs. Are they predominantly merger-driven, like their low-redshift analogues, ULIRGs, or do secular bursts within massive disks play a role? It is therefore critical to take high-resolution observations of the star-forming gas within SMGs to probe the composition, distribution and kinematics, in order to begin to undertand the main drivers of the star formation in these systems. This is one of the key science drivers for ALMA in full science operations, however, we can begin to answer these questions by exploiting rare examples of high-redshift starburst galaxies which have been strongly gravitationally lensed by massive foreground galaxy clusters. This effect can boost both the apparent size and the observed flux of the galaxy image, facilitating high spatial resolution observations without the need for ALMA.

In this and the following Chapter we focus on the $z = 2.3259$ gas-rich, starburst galaxy SMM J2135−0102 (hereafter SMM J2135; R.A./Dec.: 21 35 11.6, −01 02 52; J2000), also known as the 'Cosmic Eyelash'. This was discovered serendipitously during an 870μm LABOCA observation of the massive galaxy cluster MACSJ2315-010217 at $z = 0.325$ (Swinbank et al. 2010; Ivison et al. 2010d). The redshift for this SMG, was derived through blind detection of ^{12}CO(1–0) using Zpectrometer on the Green Bank Telescope (GBT). The 'Cosmic Eyelash' has an extremely high observed flux at 870μm of (106.0 ± 7.0) mJy (brighter even than the brightest submillimetre detected QSOs) due to the strong magnification from the foreground cluster of $37.5 \pm 4.5\times$. The lens produces two mirror images of the SMG, straddling the critical curve. Intrinsically (correcting for the lens magnification) it has a flux of $S_{870\mu m} = 3.0\pm0.4$ mJy, which is typical of high-redshift ULIRGs (i.e. the median flux in the ALESS sample is $S_{870\mu m} \sim 4$ mJy). This makes it an even more interesting galaxy to study as it provides a uniquely detailed insight into a fairly 'representative' example of the gas rich star-forming galaxies that contribute a large fraction of the submillimetre background.

This and the following Chapter are published papers which describe our detailed

analysis of the chemistry of the interstellar medium within the 'Cosmic Eyelash' leading to a better understanding of the properties and environment of the cool star-forming gas within this relatively normal SMG. The content of this Chapter is published, as written here, in Danielson et al. (2011), MNRAS, 410, 1687, however, Section 3.3 has been shortened and modified from the published work.

3.2 Abstract

We present an analysis of the molecular and atomic gas emission in the rest-frame far-infrared and submillimetre, from the lensed $z = 2.3$ SMG, SMM J2135−0102. We obtain very high signal-to-noise detections of 11 transitions from three species and limits on a further 20 transitions from nine species. We use the ^{12}CO, [CI] and HCN line strengths to investigate the gas mass, kinematic structure and ISM chemistry, and find strong evidence for a two-phase medium within this high-redshift starburst galaxy, comprising a hot, dense, luminous component and an underlying extended cool, low-excitation massive component. Employing a suite of photodissociation region models we show that on average the molecular gas is exposed to a UV radiation field that is $\sim 1000\times$ more intense than the Milky Way, with star-forming regions having a characteristic density of $n \sim 10^4\,\mathrm{cm}^{-3}$. Thus, the average ISM density and far-UV radiation field intensity are similar to those found in local ULIRGs. These densities and radiation fields are similar to those found in the central regions of typical starburst galaxies, even though the star formation rate is far higher in this system. The ^{12}CO spectral line energy distribution and line profiles give strong evidence that the system comprises multiple kinematic components with different conditions, including temperature, and line ratios suggestive of high cosmic ray flux within clouds, likely as a result of high star formation density. We find tentative evidence of a factor ~ 4 temperature range within the system. We expect that such internal structures are common in high-redshift ULIRGs but are missed due to the poor signal-to-noise of typical observations. We show that, when integrated over the galaxy, the gas and star-formation surface densities appear to follow the Kennicutt-

Schmidt relation, although by comparing our data to high-resolution submillimetre imaging, our data suggest that this relation breaks down on scales of $<100\,\mathrm{pc}$. By virtue of the lens amplification, these observations uncover a wealth of information on the star formation and ISM at $z \sim 2.3$ at a level of detail that has only recently become possible at $z < 0.1$, and show the potential physical properties that will be studied in unlensed galaxies when ALMA is in full operation.

3.3 Introduction

To understand what drives the intense star formation within SMGs it is essential to understand the conditions and composition of the ISM. Since the ISM cools mainly through emission from atomic and molecular species (e.g. [CII], [CI], ^{12}CO and [OI]), measuring these emission lines will give a strong indication of the ISM properties. In particular the various rotational transitions of ^{12}CO are strongly detected at millimetre wavelengths and provide an excellent tracer of the cold molecular gas available for star formation.

Prior to full science operations of ALMA, the most promising route to gaining high signal-to-noise, submillimetre spectroscopy of star-forming galaxies at high redshift is to use the natural amplification from strong gravitational lensing (e.g. Smail et al., 2002; Weiß et al., 2005a,b, 2007; Maiolino et al., 2009; Hailey-Dunsheath et al., 2010a; Ivison et al., 2010c). In particular, measuring the chemistry of the ISM through emission line flux ratios in strongly-lensed galaxies is especially advantageous since gravitational lensing is achromatic (in the absence of differential amplification) and so the apparent line ratios (and the implied chemistry) are unaffected. As such, intrinsically faint emission lines which are sensitive probes of the ISM chemistry (such as ^{13}CO or HCN) can be measured, if suitably bright targets can be identified.

SMM J2135 provides an ideal opportunity to investigate the detailed properties of the ISM within a galaxy which is representative of the high-redshift starburst population. In this Chapter we analyse observations of the ^{12}CO ladder (up to

$J_{\mathrm{upper}} = 10$), as well as other dense gas tracers and more complex molecules in the rest-frame frequency range 80–1100 GHz. To put the current molecular/atomic line data obtained for the *global* line emission of this distant starburst in perspective, we note that they are rivalled only by those obtained for local ULIRGs, e.g. Arp 220, Mrk 231 and NGC 6240 (Greve et al., 2009; van der Werf et al., 2010), which are some $\sim 250\times$ closer to us.

In Section 3.4 we describe our observations of the molecular and atomic emission from SMM J2135. Our analysis is described in Section 3.5 where we first examine the integrated properties of the system, deriving and comparing gas masses calculated from ^{12}CO, [CI] and HCN. We produce a ^{12}CO SLED for this galaxy and use this to investigate excitation conditions within its ISM. We use PDR models to investigate the characteristic density of the ISM and the incident far-UV intensity. We then decompose the spectra into three distinct kinematic components, and measure the ^{12}CO SLED of each in order to search for excitation structure within the system. We give our conclusions in Section 3.6. Throughout the Chapter we use a ΛCDM cosmology with $H_0 = 72\,\mathrm{km\,s^{-1}\,Mpc^{-1}}$, $\Omega_m = 0.27$ and $\Omega_\Lambda = 1 - \Omega_m$ (Spergel et al., 2003). Unless otherwise stated, a lensing amplification correction of a factor of 37.5 has already been applied to all quoted luminosities.

3.4 Observations

An essential requirement for the study of the molecular and atomic emission lines from SMM J2135 is a precise redshift for the gas reservoir in this system. This was obtained soon after the discovery of the source using Zpectrometer on GBT (Swinbank et al. 2010, see Section 3.4.1). With this accurate systemic redshift, it was then possible to precisely tune to the expected frequencies of molecular and atomic emission lines.

Table 3.1: Log of IRAM 30 m and GBT observations

Band	ν_{obs} (GHz)	Emission lines	t_{int} (ks)
Ka	25.6–36.1	^{12}CO(1–0), CS(2–1), CN(1–0) HNC(1–0), ^{13}CO(1–0) HCO$^+$(1–0)	18.0
E0	79.00–83.00	HCN(3–2), HCO$^+$(3–2), HNC(3–2)	28.8
	96.75–100.75	^{13}CO(3–2), H$_2$O 325.141	18.0
	101.97–105.97	^{12}CO(3–2), CN(3–2), CS(7–6)	18.0
E1	131.00–135.00	^{13}CO(4–3), HCO+(5–4), HCN(5–4), CS(9–8)	14.4
	135.92–139.92	^{12}CO(4–3), CN(4–3), HNC(5–4)	10.8
	146.00–150.00	[CI](1–0), CS(10–9), O$_2$ 487.3	7.2
	171.26–174	^{12}CO(5–4)	10.8
E2	205.90–209.90	^{12}CO(6–5)	8.4
	224.11–228.11	H$_2$O 731.681	3.6
	240.53–244.53	^{12}CO(7–6), [CI](2–1)	12.6
E3	275.16–279.16	^{12}CO(8–7)	9.6
	309.77–313.77	^{12}CO(9–8)	7.2

The log of the IRAM 30m and GBT Zpectrometer observations giving the frequency ranges of Zpectrometer Ka band and the IRAM/EMIR receiver backends (E0–E3), the emission lines observed and integration time for each set-up.
Note: These set-ups have beam sizes of Ka:$\sim$ 15$''$–23$''$, E0:$\sim$ 30$''$, E1:$\sim$ 17$''$, E2:$\sim$ 11$''$ and E3:$\sim$ 8.5$''$ respectively.

Table 3.2: Emission line properties

Species	$\nu_{\rm rest}$ (GHz)	Flux[a,b] $(\mathrm{Jy\,km\,s^{-1}})$	L′ $(10^8\,\mathrm{K\,km\,s^{-1}\,pc^2})$
^{12}CO(1–0)	115.2712	2.16 ± 0.11	173 ± 9
^{12}CO(3–2)	345.7959	13.20 ± 0.10	117.6 ± 0.9
^{12}CO(4–3)	461.0408	17.3 ± 1.2	87 ± 6
^{12}CO(5–4)	576.2679	18.7 ± 0.8	60 ± 3
^{12}CO(6–5)	691.4731	21.5 ± 1.1	48 ± 2
^{12}CO(7–6)	806.6518	12.6 ± 0.6	21 ± 1
^{12}CO(8–7)	921.7997	8.8 ± 0.5	11 ± 1
^{12}CO(9–8)	1036.9124	3.6 ± 1.7	4 ± 2
^{12}CO(10–9)	1151.9855	< 1.1	< 0.9
^{13}CO(1–0)	110.2013	< 0.3	< 29
^{13}CO(3–2)	330.5880	< 1.8	< 18
^{13}CO(4–3)	440.7651	< 0.3	< 1.4
[CI](1–0)	492.1607	16.0 ± 0.5	71 ± 2
[CI](2–1)	809.3435	16.2 ± 0.6	26 ± 1
HCN(1–0)	88.6300	< 0.3	< 45
HCN(3–2)	265.8900	1.2 ± 0.4	18 ± 6
HCN(5–4)	443.1200	< 0.3	< 1.4
HNC(1–0)	90.6600	< 0.3	< 43
HNC(3–2)	271.9800	< 1.2	< 17
HCO+(1–0)	89.190	< 0.3	< 44
HCO+(3–2)	267.560	< 1.2	< 17
HCO+(5–4)	445.90	< 0.3	< 1.3
CN(1–0)	113.320	< 0.3	< 27
CN(3–2)	339.450	< 1.6	< 14
CS(2–1)	97.981	< 0.3	< 37
CS(7–6)	342.883	< 1.6	< 14
CS(9–8)	428.875	< 0.3	< 14
CS(10–9)	489.751	< 1.6	< 7
O_2	487.246	< 1.6	< 7
H_2O	325.141	< 1.8	< 18
H_2O	731.681	< 4.8	< 9.5
[CII][c]	1910	850 ± 180	2500 ± 500
[OII][d]	2065.40	620 ± 200	155 ± 50

[a]We quote 3-σ limits for all lines which are not formally detected.

[b]Uncertainties on fluxes denote measurement errors and do not include the calibration uncertainties, which we estimate as $\sim 5\%$ for 30–200 GHz, $\sim 10\%$ for 200–300 GHz and $\sim 15\%$ for > 300 GHz.

[c]The [CII] flux is taken from Ivison et al. (2010d).

[d]Ivison et al. (2010d) report a $\sim 3\sigma$ from [OI]146μm and we have used the flux of this feature in our analysis, although we note that removing this line from our analysis changes our results negligibly. We also note that the since the [CII] and [OI] 146μm lines are of comparable strength, this would imply that the [OI] 63μm line would be much brighter than the [CII] line thus making this an interesting source for Herschel/PACS follow-up.

3.4.1 GBT Zpectrometer observations

Details of the observations with Zpectrometer are given in Swinbank et al. (2010) and Table 3.1. Briefly, Zpectrometer is a wide-band spectrometer optimised for ^{12}CO(1–0) emission line searches between $z = 2.2$–3.5 (with $\sim 150\,\mathrm{km\,s^{-1}}$ resolution) using the GBT's Ka-band receiver (see Harris et al. 2007 and Harris et al. 2010 for more detail on the instrument and observing mode). Observations of SMM J2135 were conducted in two equal shifts on 2009 May 19 and May 27 for a total integration time of 5 hours. Data reduction was carried out with the standard Zpectrometer GBT reduction scripts. The final spectrum reaches an rms noise level of $\sigma = 0.50\,\mathrm{mJy\,beam^{-1}}$. From the spectrum, shown in Fig. 3.1, we determine the heliocentric redshift as $z = 2.32591$ from the ^{12}CO(1–0) emission at 34.648 GHz. The observed velocity-integrated flux in ^{12}CO(1–0) is given in Table 3.2.

3.4.2 IRAM PdBI & 30m observations

We used the six-element IRAM Plateau de Bure Interferometer (PdBI) to observe the redshifted ^{12}CO(3–2) and ^{12}CO(4–3) emission lines and the continuum at 104 GHz and 139 GHz respectively. Observations were made in D configuration in Directors Discretionary Time (DDT) on 2009 May 29 and 31 with good atmospheric phase stability and precipitable water vapour (seeing $= 0.6$–$1.6''$, pwv $= 5$–15mm). The receivers were tuned to the systemic redshift determined from the GBT ^{12}CO(1–0) spectrum. We observed SMM J2135 for total on-source exposure times of 4 hrs and 2 hrs for ^{12}CO(3–2) and ^{12}CO(4–3) respectively. The correlator was adjusted to a frequency resolution of 2.5 MHz, yielding 980-MHz coverage. The overall flux scale for each observing epoch was set from observations of MWC 349, with additional observations of 2134+004 for phase and amplitude calibrations. The data were calibrated, mapped and analysed using the GILDAS software package. Inspection of the velocity datacubes shows very good detections of both ^{12}CO(3-2) and ^{12}CO(4–3) emission lines (S/N $\sim$ 300 in each) at the position of SMM J2135 (see Fig. 3.1) and we give line fluxes in Table 3.2.

To constrain the high-J_{upper} ^{12}CO emission (and search for other emission lines such as [CI]) we used the Eight MIxer Receiver (EMIR) multi-band heterodyne receiver at the IRAM 30-m telescope. Observations were made on 2009 June 29–30, and 2010 February 5–8 and April 3–6, in good to excellent conditions, typically with ~ 2–$6\,\mathrm{mm}$ pwv and $\lesssim 1\,\mathrm{mm}$ pwv for some of the April observations. Data were recorded using the E0–E3 receivers with $4\,\mathrm{GHz}$ of instantaneous, dual-polarisation band-width covering frequency ranges from ~ 70–$310\,\mathrm{GHz}$ (see Table 3.1 for the details of the setups). For each observation, we used eight 1-GHz bandwidth units of the Wide-band Line Multiple Autocorrelator (WILMA) to cover $4\,\mathrm{GHz}$ in both polarizations. WILMA provides a spectral resolution of $2\,\mathrm{MHz}$ which corresponds to 5–$7\,\mathrm{km\,s^{-1}}$ in the 3-mm band. The observations were carried out in wobbler-switching mode, with a switching frequency of $1\,\mathrm{Hz}$ and an azimuthal wobbler throw of $90''$. Pointing was checked frequently on either the nearby QSO J2134+004 or Venus and was found to be stable to within $3''$. Calibration was carried out every $12\,\mathrm{mins}$ using the standard hot/cold-load absorber, and the flux calibration was carried out using the point source conversion between temperature and flux as measured from celestial objects. We note that, even at the highest frequency (i.e. $345\,\mathrm{GHz}$) the beam is $8.5''$ and so the lensed galaxy is likely to be smaller than the beam at all wavelengths (Swinbank et al., 2010). The data were first processed with the CLASS software (Pety, 2005), and then using custom IDL routines. We omitted scans with distorted baselines and subtracted only linear baselines from individual spectra. For the 2010 April observations of ^{12}CO(5–4), an upward correction was made to the flux of 10% since the line extends into the wings of an atmospheric water band (although for these observations the pwv $\lesssim 1\,\mathrm{mm}$). In total, we observed twelve different set-ups, each for ~ 2–$5\,\mathrm{hrs}$ (Table 3.1); the spectra of the detections are shown in Fig. 3.1. These observations provide detections or limits on 31 transitions listed in Table 3.2.

3.4.3 APEX SHFI observations

Observations of the redshifted ^{12}CO(7–6) emission line were also carried out in DDT using the Swedish Heterodyne Facility Instrument (SHFI) between 2009 July 10 and July 20 (ESO programme ID 283.A-5014). SHFI consists of four wide-band heterodyne receiver channels for 230–1300 GHz (Vassilev et al. 2008). We used APEX-1 tuned at 242.4 GHz to search for the ^{12}CO(7–6) emission from the galaxy, and obtained a total integration time of ~ 5.5 hrs in excellent conditions (0.4–0.6 mm pwv). The data reduction was carried out using the CLASS software, omitting scans with poor baselines. To create the final spectrum we binned the data onto a velocity scale of $50\,\mathrm{km\,s^{-1}}$ and averaged it together with 4 hours of observations from IRAM/EMIR, which has similar signal-to-noise; we show this spectrum in Fig. 3.1.

3.4.4 SMA observations

We mapped the 870μm continuum emission from SMM J2135 using the Submillimeter Array (SMA) in a number of different array configurations (see Swinbank et al. 2010). During four of these tracks (in the sub-compact, compact, extended and very-extended configurations) we tuned the upper side band of the receiver to 346.36699 GHz to search for ^{12}CO(10–9). Details of the data reduction are given in Swinbank et al. (2010) and we show the spectrum in Fig. 3.1. The resulting combined spectrum reaches an rms of $2\,\mathrm{mJy}$ per $100\,\mathrm{km\,s^{-1}}$ channel and although ^{12}CO(10–9) is not detected, we place a 3-σ limit on the flux of $\leq 0.2\,\mathrm{Jy\,km\,s^{-1}}$.
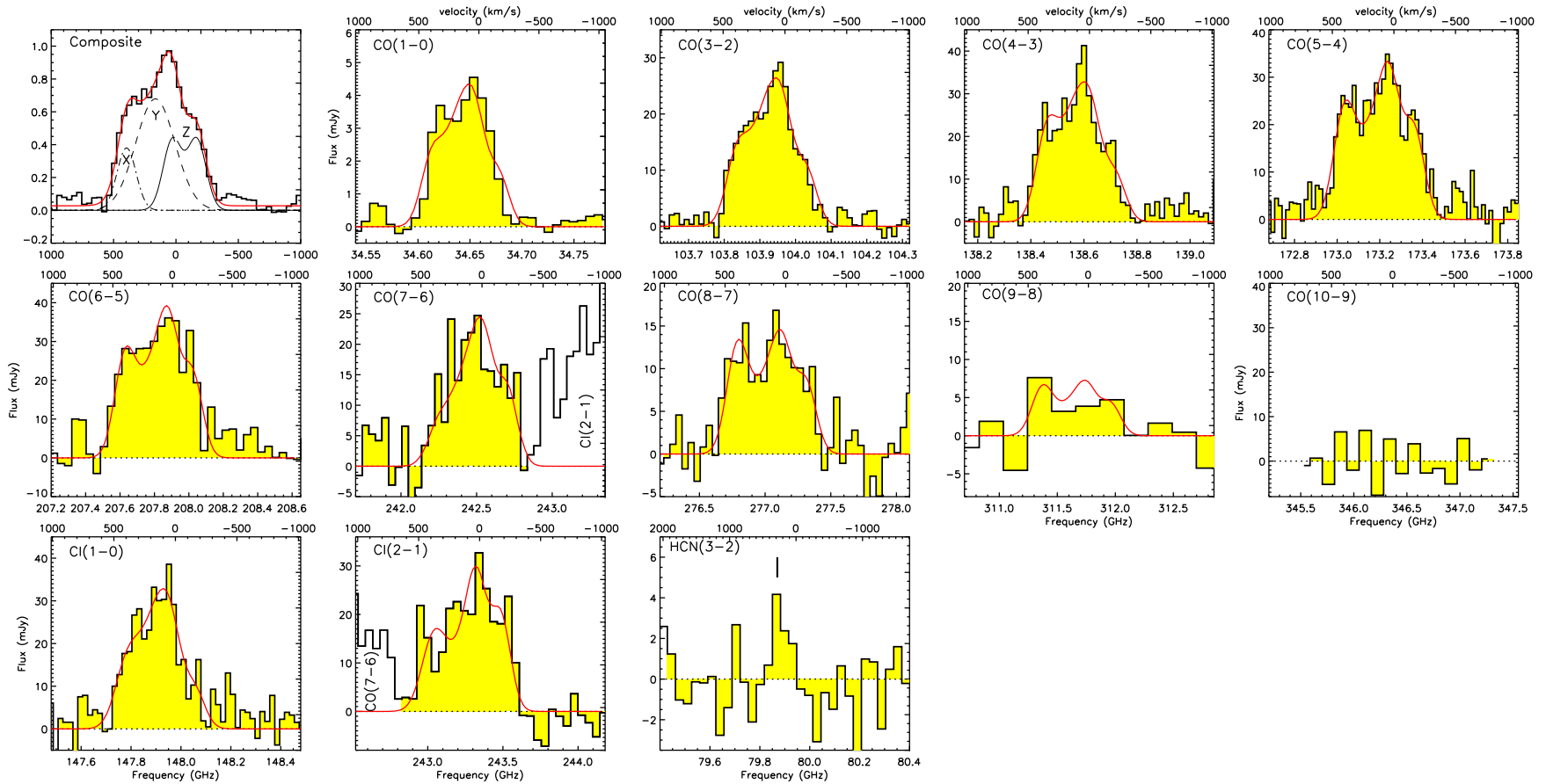
Figure 3.1: Molecular and atomic emission from the lensed submillimetre galaxy SMM J2135. The top two rows show spectra of the ^{12}CO emission arising from $J_{upper} = 1$ up to $J_{upper} = 10$. These are followed by the spectra of the [Ci] fine-structure lines and our detection of HCN(3–2). In all cases, the emission profiles show multiple velocity components whose intensity appears to vary between transitions. To better constrain the kinematic structure of the lines we derive an average ^{12}CO spectrum (which does not include ^{12}CO(9–8) or ^{12}CO(10–9)) and we overplot on this the resulting three-component parametric model as described in Section 3.5.3. We fit this three-component kinematic model to the various lines, allowing the intensities of the components to vary between lines, and overlay this on all the ^{12}CO emission lines making up the average, clearly highlighting the evidence of different excitation in the different velocity components. The spectra have been binned into channels of width 30–100 km s^{-1}. The spectra for ^{12}CO(3–2), ^{12}CO(4–3) and ^{12}CO(6–5) are the combined data from our PdBI and EMIR observations, the ^{12}CO(7–6) spectrum is a combination of EMIR and SHFI data. The ^{12}CO(1–0) line was measured by GBT and the ^{12}CO(10–9) line by SMA, all other observations were taken with IRAM 30m and PdBI. The axes are flux (mJy) and frequency (GHz) (with the velocity shown on the upper horizontal axes) in all cases except for the average spectrum which has been plotted as km s^{-1} and flux normalised to the peak value. Note that ^{12}CO(7–6) and [Ci](2–1) lines abut each other in the spectrum.

3.5 Analysis and discussion

Our observations have detected 11 individual transitions arising from three molecular or atomic species in SMM J2135 and place upper limits on the line fluxes of a further 20 transitions arising from seven other species. We list these in Table 3.2 with the fluxes quoted with their respective measurement uncertainties and we show the spectra for all detections in Fig. 3.1. We estimate additional calibration uncertainties of 5%, 10% and 15% for those lines at 30–200 GHz, 200–300 GHz and > 300 GHz respectively.

With the very high signal-to-noise of our data (particularly the ^{12}CO lines), we clearly identify multiple velocity components within the spectra (at approximately -180, 0 and $+200$ km s^{-1} relative to the ^{12}CO(1–0) flux-weighted mean velocity), implying multiple physical components in the source. We believe that the detection of this structure in the ^{12}CO spectra is not due to this galaxy's being unusual, but instead reflects the high signal-to-noise of our observations, which is uncommon for observations of other (even local) galaxies. We discuss these multiple components in Section 3.5.3, modelling the system as three components which we label X, Y and Z. However, so that fair comparisons can be made to other galaxies (at low and high redshift), we begin (in Section 3.5.1, 3.5.1 and 3.5.2) by discussing the integrated properties of the system to see what can be learnt about the bulk properties of its ISM.

As Fig. 3.1 shows, the ^{12}CO and [CI] emission lines are broad, with a typical FWHM of ~ 500 km s^{-1}. Since there is significant kinematic structure within the ^{12}CO and [CI] emission, we first define the width of the emission lines by constructing a composite ^{12}CO spectrum by combining the spectra from ^{12}CO(1–0) to ^{12}CO(8–7) (normalised by peak flux). This composite has a full width at zero intensity of 900 km s^{-1}, with a range from -350 to 550 km s^{-1} (Fig. 3.1), although we note that there may be faint emission extending to ± 1000km s^{-1}. We use the velocity range, -350 to 550 km s^{-1}, to measure the fluxes of the ^{12}CO lines, [CI]($^3P_1 \rightarrow \ ^3P_0$) and [CI]($^3P_2 \rightarrow \ ^3P_1$), while for HCN(3–2) we use a range of -100 to 550 km s^{-1}. To

determine the errors on the fluxes we measure the variance in the spectra away from the emission line, although in most cases the dominant error is from the calibration; these errors are used in Fig. 3.2 (see also Table 3.2).

3.5.1 Integrated properties

Gas mass and dust SED

We begin by estimating the total molecular gas mass of the galaxy from ^{12}CO. Low-J_{upper} transitions of ^{12}CO are commonly used to obtain estimates of the total gas mass of a galaxy using a conversion factor, $\alpha = M_{H_2} / L'_{^{12}CO(1-0)}\,M_\odot\,(\text{K km s}^{-1}\,\text{pc}^2)^{-1}$ which converts the ^{12}CO line luminosity to total gas mass, (where M_{H_2} is defined to include the mass of Helium such that $M_{H_2} = M_{\text{gas}}$; see Solomon & Vanden Bout 2005 for a review).

There is considerable uncertainty about the correct value of α to adopt in high-redshift galaxies (e.g. Baker et al. 2004; Coppin et al. 2007; Tacconi et al. 2008 and Ivison et al. 2010c) and similar uncertainty about the conversion factor to transform high-J_{upper} CO transitions to the equivalent CO(1–0) fluxes (if required). However, we can estimate a minimum mass (and so a lower limit on α) assuming the ^{12}CO(1–0) emission is optically thin (which is unlikely to be the case) and has solar abundance, following Ivison et al. (2010c):

$$\frac{M(\text{H}_2)}{L'_{\text{CO}(1-0)}} \sim 0.08 \left(\frac{g_1}{Z} e^{-T_o/T_k} \left(\frac{J(T_k) - J(T_{bg})}{J(T_k)} \right) \right)^{-1}$$
$$\times \left(\frac{[^{12}\text{CO}/\text{H}_2]}{10^{-4}} \right)^{-1} \frac{M_\odot}{\text{Kkms}^{-1}\text{pc}^2}$$

where $T_o = E_1/k_B \sim 5.5\,\text{K}$, $J(T) = T_o(e^{T_o/T} - 1)^{-1}$, $T_{\text{bg}} = (1+z)T_{\text{CMB}} \sim 9.1\,\text{K}$ ($T_{\text{CMB}} = 2.73\,\text{K}$ at $z = 0$), $z = 2.3259$, $g_1 = 3$ (the degeneracy of level $n = 1$), $Z \sim 2(T_k/T_0)$ and $[^{12}\text{CO}/\text{H}_2] \sim 10^{-4}$ for a solar metallicity environment (Bryant & Scoville 1996). For typical star-forming gas, $T_k \sim 40$–$60\,\text{K}$, so to derive a minimum mass we use $T_k = 40\,\text{K}$. With $L'_{^{12}\text{CO}(1-0)} = 173 \pm 9 \times 10^8\,\text{K km s}^{-1}\,\text{pc}^2$, this gives us

a minimum gas mass of $M_{gas} \gtrsim 1 \times 10^{10} \, M_\odot$ and a lower limit on $\alpha \gtrsim 0.54$.

We can then compare this to the dynamical mass adopting $M_{dyn} = 5 \, R\sigma^2/G$ (Solomon & Vanden Bout, 2005). This assumes the dynamics of the CO emission trace the virialised potential well of the system and that the CO is distributed in a sphere of constant density with $r \sim 1 \, kpc$ (see Section 3.5.4 and Swinbank et al. 2010). Using the width of the $^{12}CO(1–0)$ line, $\sigma \sim 200 \, km \, s^{-1}$, we estimate a dynamical mass of $M_{dyn} \sim 5.3 \times 10^{10} \, M_\odot$. If this mass is dominated by gas, then the upper limit on α is $\alpha = M_{gas}/L'_{^{12}CO(1-0)} < 3$.

Using this dynamical mass and the minimum gas mass, we place a lower limit on the gas fraction of $M_{gas}/M_{dyn} \gtrsim 0.19$. This ratio is similar to the ratio for typical starburst nuclei and the ratio of 30% found in M 82 (Devereux et al., 1994). Compared to other high-redshift submillimetre galaxies (SMGs), using the $^{12}CO(3–2)$ observations from Greve et al. (2005) and adopting $\alpha = 0.8 \, M_\odot \, (K \, km \, s^{-1} \, pc^2)^{-1}$ and $R_{3,1} = 0.58 \pm 0.05$ from Ivison et al. (2010c), we find a median gas mass ratio of 50% for luminous SMGs, whilst Tacconi et al. (2008) derive a gas mass fraction of 0.3 for more typical star-forming galaxies at similar redshifts. We stress, however, that compared to the gas mass of $6 \times 10^8 \, M_\odot$ within the central 1.2 kpc of M 82 (Young & Scoville, 1984), our gas mass is nearly two orders of magnitude higher, underlining the more extreme conditions in the central regions of SMM J2135.

In order to provide a simple comparison with previous studies, we estimate the gas mass of SMM J2135 using a conversion factor of $\alpha \sim 0.8 \, M_\odot \, (K \, km \, s^{-1} \, pc^2)^{-1}$ which applies to the smoothly distributed, high-pressure, largely molecular ISM measured in local ULIRGs (Downes & Solomon 1998; Solomon & Vanden Bout 2005, although recent local studies on high-J_{upper} CO lines imply multi-phase ISM in ULIRGs as opposed to smoothly distributed) and is also the canonical value used for high-redshift LIRGs and ULIRGs (Tacconi et al., 2008; Stark et al., 2008). This value of α is comfortably between the upper and lower limits calculated above. With this assumption the $^{12}CO(1–0)$ line luminosity yields a total gas mass of $M_{H_2} = (1.4 \pm 0.1) \times 10^{10} \, M_\odot$ (see also Swinbank et al. 2010).

Taking our estimate of the total gas mass and the expected size of $\sim 1 \, kpc$

for the system (Swinbank et al., 2010), we derive an average column density of $N_H \sim 10^{24}\,cm^{-2}$, which is comparable to the molecular hydrogen density in Arp 220, averaged over a similar region (Gerin & Phillips, 1998), but much higher than the density in typical starburst galaxies such as M 82. However, this estimate gives an average over the system which we know to be structured and so indicates that the column density is very high in parts of this source. The associated extinction is expected to exceed $A_V \sim 10^3$, suggesting significant absorption even in the far-infrared and moreover that the emission from some of the more common species we see is optically thick. With this extinction, coupled with our high value for G_0 (derived in Section 3.5.2), high infrared luminosity and potentially high cosmic ray flux (see below), it is probable that momentum-driven outflows will result. These outflows could be either photon-driven (Thompson et al., 2005) or cosmic ray-driven (Socrates et al., 2008) and will impact both the dynamics of the gas in the system and the steady-state assumption in our PDR modelling (Section 3.5.2).

We can now compare the star-formation efficiency in SMM J2135 to that in the wider SMG and ULIRG populations. First we note that the far-infrared luminosity of SMM J2135 is $L_{FIR} = (2.3 \pm 0.1) \times 10^{12}\,L_\odot$ (Ivison et al., 2010d) which indicates a star formation rate (SFR) of $\sim 400 \pm 20\,M_\odot yr^{-1}$ (Kennicutt, 1998b) assuming a Salpeter IMF. We combine the SFR and gas mass to estimate the star formation efficiency (SFE) following Greve et al. (2005), $SFE = L_{FIR}/M_{H_2}$ resulting in $SFE \sim 165 \pm 7\,L_\odot\,M_\odot^{-1}$. This is comfortably within the limit derived by Scoville (2004) of $[L_{FIR}/M_{H_2}]_{max} = 500\,L_\odot\,M_\odot^{-1}$, assuming Eddington-limited accretion of gas onto OB star clusters. $^{12}CO(1–0)$ measurements in local ULIRGs derive a SFE of $180 \pm 160\,L_\odot\,M_\odot^{-1}$, which is comparable to that in our source. The SFE of our source is also comparable to the median SFE of $210 \pm 80\,L_\odot\,M_\odot^{-1}$ for the sample of luminous SMGs of Greve et al. (2005), after correcting the latter using $R_{3,1} = 0.58$ as appropriate for SMGs (Harris et al. 2010; Ivison et al. 2010c).

We begin modelling this system by noting that the 870-μm SMA observations and comparison to the LABOCA flux reveal four bright, compact clumps embedded in a much more extended system with the clumps emitting $\sim 80\%$ of the total luminosity,

and the rest of the emission emerging from a more extended component (Swinbank et al., 2010). Motivated by this structure we fit a two-component model to the dust SED, fixing the characteristic temperature of the cool (presumably more extended) component at 30 K and allowing the size and the characteristic temperature of the clumps to vary. The best fit yields a characteristic size for the clumps of $r \sim 200 \, \text{pc}$ at a temperature of $T_{\text{d,warm}} = 57 \pm 3 \, \text{K}$, while the extended component has a size of $r \sim 1000 \, \text{pc}$ at $T_{\text{d,cool}} = 30 \, \text{K}$. The dust mass of both the extended component and the clumps is then $(1.5 \pm 0.2) \times 10^8 \, \text{M}_\odot$, which is similar to the mass determined for the cool dust component in Ivison et al. (2010d). The inferred clump size is somewhat larger than the size of the dust emission regions seen in the highest resolution 870-μm SMA maps, where the clumps appear to be 100–200 pc in diameter (Swinbank et al., 2010). However, we note that forcing the clump sizes down to that size requires an increase in the characteristic temperature up to $\sim 80 \, \text{K}$, and to keep the emission consistent with the integrated SED the clumps must then be optically thick at $\sim 200 \mu$m in the rest-frame. Clearly this two-component model is not a unique description of the dust emission from SMM J2135, but it does suggest that the system could be modelled by a combination of warm, compact and cooler, more extended dust components.
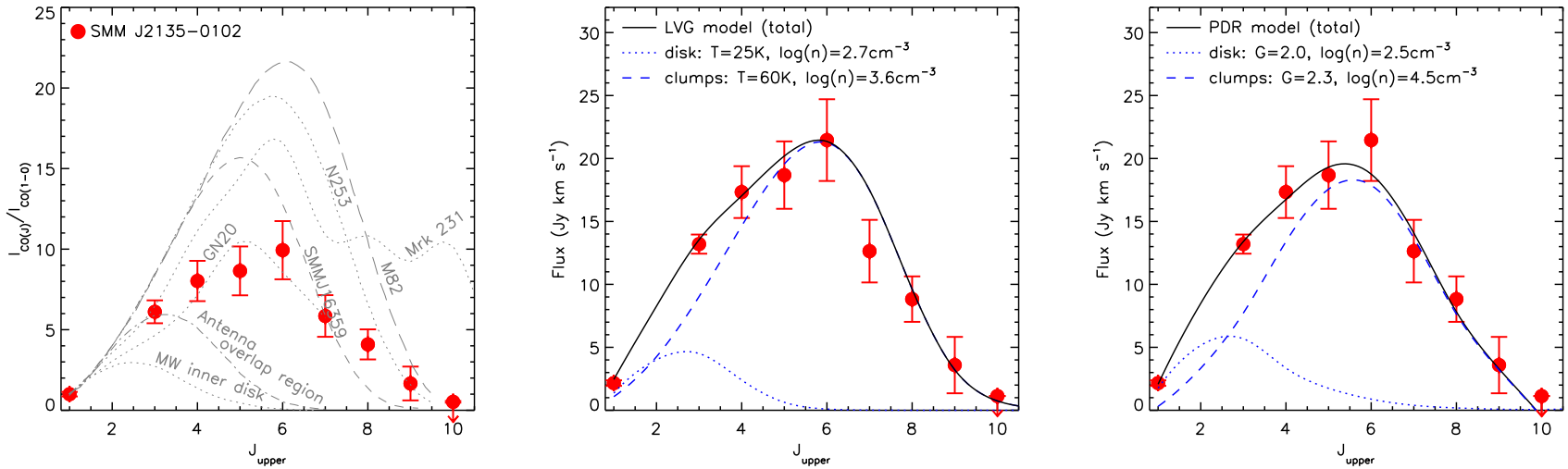
Figure 3.2: The integrated ^{12}CO SLED for SMM J2135 showing that the SLED peaks around $J_{upper} = 6$ (similar to M 82, but with proportionally stronger ^{12}CO(1–0)). The central panel shows the results of LVG modelling applied to the integrated SLED, which requires two temperature phases to yield an adequate fit. In this model they have characteristic temperatures of $T_{kin} = 25\,K$ and $60\,K$ and densities of $n = 10^{2.7}$ and $10^{3.6}\,cm^{-3}$ respectively (we associate these two phases with a cool, extended disk and hotter, more compact, clumps). The right-hand panel shows a similar comparison but now using a PDR model (Meijerink et al. 2007; see Section 3.5.2) which again requires a combination of both low- and high-density phases to adequately fit the integrated SLED.

^{12}CO SLED

To investigate the excitation within the ISM, we next construct the ^{12}CO SLED by calculating the ^{12}CO flux of each transition over the velocity range defined by the composite spectrum; we show the resulting SLED in Fig. 3.2. In Table 3.4 we also give the velocity-averaged brightness temperature ratios between ^{12}CO(J_{upper}) and ^{12}CO(1–0), which we define as $R_{J,1} = L'(J + 1 \rightarrow J)/L'(1 \rightarrow 0)$ (Greve et al. 2003; Harris et al. 2010). The ^{12}CO SLED shows a continuous rise out to $J_{\text{upper}} = 6$, followed by a sharp decline as far as $J_{\text{upper}} = 10$. The brightness ratios of all of the $J_{\text{upper}} > 2$ line luminosities compared to the ^{12}CO(1–0) are < 1, which interpreted in the framework of a single phase ISM would indicate that the gas is sub-thermalised (the thermalised prediction is ~ 1; Devereux et al. 1994). Indeed the $L'_{^{12}\text{CO}(3-2)}/L'_{^{12}\text{CO}(1-0)}$ line luminosity ratio for SMM J2135, 0.68 ± 0.03, is similar to that seen in local starburst galaxies, 0.64 ± 0.06 (Devereux et al., 1994). However, as Harris et al. (2010) discuss and as we show later in Section 3.5.2, these ratios are more likely to indicate a multi-phase ISM as found in star-forming regions locally.

The peak of the SLED at $J_{\text{upper}} = 6$ is similar to that seen in nearby starburst galaxies such as NGC 253 and M 82 (Bradford et al. 2003; Weiß et al. 2005c; Panuzzo et al. 2010) and AGN, e.g. Mrk 231 (Papadopoulos et al., 2007; van der Werf et al., 2010). However, the overall shape of the SLED suggests that SMM J2135 has proportionally stronger ^{12}CO(1–0) emission (compared to the higher J_{upper} transitions) than any of these galaxies, indicating the presence of an additional low-excitation gas phase. Nevertheless, the bulk of the cooling, 60%, arises through the ^{12}CO $J_{\text{upper}} = 5$–7 line emission, with a further 20% at ^{12}CO $J_{\text{upper}} \geq 8$. van der Werf et al. (2010) have recently constrained the ^{12}CO in Mrk 231 up to $J_{\text{upper}} = 13$ with *Herschel*, building upon the earlier study of Papadopoulos et al. (2007), and show that, unlike nearby starbursts (e.g. NGC 253 or M 82), the ^{12}CO line luminosity is roughly flat across $J_{\text{upper}} = 5$–13. They calculate that only 4% of the total ^{12}CO line luminosity arises from the three lowest transitions, compared to $\sim 20\%$ in the three lowest transitions of our ^{12}CO SLED (and 43% in the Milky Way). The luminous

high-J_{upper} emission they see is likely due to the presence of additional excitation phases in Mrk 231, either high excitation PDRs or more likely an X-ray dominated region (XDR) (Spaans & Meijerink, 2008). As we see later, we also find evidence for at least two phases of material in SMM J2135.

In comparison to higher-redshift sources, we see that the ^{12}CO SLED for SMM J2135 has a broadly similar shape to that seen in other high-redshift SMGs, e.g. GN 20 (Carilli et al., 2010) or SMM J16359 (Weiß et al., 2005b). Indeed, recent progress with EVLA and GBT has started to provide ^{12}CO(1–0) detections of SMGs to complement the earlier ^{12}CO(3–2) studies from PdBI (e.g. Greve et al. 2005). Using these two transitions, we find that the $R_{3,1}$ brightness temperature ratio we derive for SMM J2135 (Table 3.4) is comparable to typical SMGs: $R_{3,1} = 0.55 \pm 0.05$ (Ivison et al. 2010c) and $R_{3,1} = 0.68 \pm 0.08$ (Harris et al., 2010), suggesting that the CO SLED results we derive for SMM J2135 may be applicable to the wider SMG population.

To investigate the excitation of the gas reservoir within this galaxy in more detail we exploit the fact that the shape of the ^{12}CO SLED can provide information on the underlying gas density and temperature distributions and use a spherical large velocity gradient model (LVG; Weiß et al. 2005b) to attempt to fit the observed SLED. LVG techniques are the most widely used radiative transfer model which can account for photon transport when spectral lines are optically thick, and can be used for efficiently solving the radiative transfer equation when the molecule level populations are not thermalised (Bayet et al. 2006).

Thus we next use the LVG code to model the ^{12}CO SLED. The model assumes spherical symmetry and uniform kinetic temperature and density, a CMB background temperature of $T_{\text{CMB}} = 2.73\,\text{K}(1+z)$ which at $z = 2.3$ is $\sim 9\,\text{K}$, the collision rates from Flower (2001) with an ortho/para H_2 ratio of 3 and a ratio of the CO abundance to the velocity gradient of CO $/dv/dr = 10^{-5}\,\text{pc}\,(\text{km s}^{-1})^{-1}$. To fit absolute line intensities the model further uses the source solid angle size, Ω_S, which can be expressed in terms of the equivalent radius of a face-on disk, $r_0 = D_A\sqrt{(\Omega_S/\pi)}$. The model returns the temperature, density and size of the emission region.

Modelling the ^{12}CO SLED in this way, we find that a single temperature and density phase is unable to fit the SLED, and that two or more phases are required. This is consistent with the implication of the model of the dust SED and the sub-millimetre morphology: we need at least two temperature phases to adequately describe this system. This need for multiple phases to fit the ISM in a high-redshift galaxy is unusual (however cf. Carilli et al. 2010), although it is not unexpected given that such multi-phase ISMs are commonly required in local galaxies (e.g. Wild et al. 1992; Guesten et al. 1993; Aalto et al. 1995; Mao et al. 2000; Ward et al. 2003). Thus, motivated by the fit to the dust SED we identify a two-phase fit to the SLED comprising four clumps and an extended phase, which provides an adequate fit (Fig. 3.2). In this model, the low-excitation phase peaks at $J_{\mathrm{upper}} \sim 3$ and is diffuse, with $n \sim 10^{2.7}\,\mathrm{cm}^{-3}$ and $\mathrm{T}_{\mathrm{kin}} \sim 25\,\mathrm{K}$. The denser, mildly-excited phase peaks around $J_{\mathrm{upper}} = 5\text{--}6$, has $\mathrm{T}_{\mathrm{kin}} \sim 60\,\mathrm{K}$ and $n \sim 10^{3.6}\,\mathrm{cm}^{-3}$ and contributes $\sim 60\%$ of the total luminosity over all the ^{12}CO lines (Fig. 3.2). The low-excitation phase has a ^{12}CO SLED which is very similar to the inner disk of the Milky Way, while the warmer phase is well matched to the inner few hundred parsecs of the starburst region in NGC 253. Within this two phase model, the total gas mass is $\mathrm{M}_{gas} \sim (4.0 \pm 0.1) \times 10^{10}\,\mathrm{M}_{\odot}$, a factor of $\sim 3\times$ the mass we determine from ^{12}CO(1–0), assuming $\alpha = 0.8\,\mathrm{M}_{\odot}\,(\mathrm{K\,km\,s}^{-1}\,\mathrm{pc}^2)^{-1}$, corresponding to an effective $\alpha = 2.0\,\mathrm{M}_{\odot}\,(\mathrm{K\,km\,s}^{-1}\,\mathrm{pc}^2)^{-1}$ (similar to that derived for the nucleus of Arp 220; (Scoville et al., 1997)). From here on we adopt this value as the gas mass of our system, but note some of the differences if we had used the ^{12}CO line luminosity and $\alpha = 0.8\,\mathrm{M}_{\odot}\,(\mathrm{K\,km\,s}^{-1}\,\mathrm{pc}^2)^{-1}$, as is commonly assumed in the analysis of high-redshift galaxies. The combination of this higher value for α and our estimate of $R_{3,1}$ would increase the gas mass by a factor of $\sim 4\times$ over that estimated by assuming $\alpha = 0.8\,\mathrm{M}_{\odot}\,(\mathrm{K\,km\,s}^{-1}\,\mathrm{pc}^2)^{-1}$ and $R_{3,1} = 1$ as usually assumed at high redshift (see also Ivison et al. 2010c; Harris et al. 2010). Adopting $\alpha \sim 2\,\mathrm{M}_{\odot}\,(\mathrm{K\,km\,s}^{-1}\,\mathrm{pc}^2)^{-1}$ results in a gas mass fraction in the central 1 kpc radius region of SMM J2135 of 75% (and closer to the 100% for typical SMGs, Greve et al. 2005) subject to uncertainties on the dynamical mass due to the unknown configuration of the gas within

the system.

Atomic carbon

We have also obtained strong detections of the $[\mathrm{CI}](^3P_1 \to {}^3P_0)$ and $[\mathrm{CI}](^3P_2 \to {}^3P_1)$ emission lines, and from these we can begin to investigate the properties of the ISM. We start by noting the similar detailed morphologies of the $[\mathrm{CI}](^3P_1 \to {}^3P_0)$ and the $^{12}\mathrm{CO}(3\text{–}2)$ and $^{12}\mathrm{CO}(1\text{–}0)$ lines in Fig. 3.1, which suggests that the emission is arising from the same mix of phases with characteristic temperatures of $T \lesssim 40\,\mathrm{K}$. Indeed observations of neutral carbon transitions have shown that the ratio of $L'_{[\mathrm{CI}](^3P_2 \to {}^3P_1)} / L'_{[\mathrm{CI}](^3P_1 \to {}^3P_0)}$ provides a sensitive probe of the temperature of the interstellar medium at moderate densities. Both lines have modest critical densities $(n_{\mathrm{crit}} \sim 0.3\text{–}1.1 \times 10^3\,\mathrm{cm}^{-3})$ and are therefore often thermalised in molecular clouds with $n \gtrsim 10^3\,\mathrm{cm}^{-3}$. The lines arise from states with energy levels $\mathrm{T}_1 = 23.6\,\mathrm{K}$ and $\mathrm{T}_2 = 62.5\,\mathrm{K}$ above the ground state, and thus their ratio is sensitive to the gas temperature if $\mathrm{T}_{\mathrm{gas}} \lesssim 100\,\mathrm{K}$. We derive $L'_{[\mathrm{CI}](^3P_2 \to {}^3P_1)} / L'_{[\mathrm{CI}](^3P_1 \to {}^3P_0)} = 0.37 \pm 0.02$, which is similar to that measured in nearby starbursts and galactic nuclei such as $\mathrm{M}\,82$ and $\mathrm{NGC}\,253$ where $L'_{[\mathrm{CI}](^3P_2 \to {}^3P_1)} / L'_{[\mathrm{CI}](^3P_1 \to {}^3P_0)} \sim 0.33$ (Bennett et al., 1994; White et al., 1994; Israel et al., 1995; Bayet et al., 2004), but larger than typically found in the cooler, dense cores of giant molecular clouds (e.g. Zmuidzinas et al. 1988). To be compatible with previous studies we define $\mathrm{R}_{[\mathrm{CI}]}$ as the ratio of the $[\mathrm{CI}](^3P_2 \to {}^3P_1)$ to $[\mathrm{CI}](^3P_1 \to {}^3P_0)$ temperature integrated line intensities in $\mathrm{K\,km\,s}^{-1}$. In SMM J2135 we derive an integrated line ratio of $R_{[\mathrm{CI}]} = 0.88 \pm 0.01$. We can use this ratio to estimate the excitation temperature T_{ex} following Stutzki et al. (1997), $T_{\mathrm{ex}} = 38.8\,\mathrm{K}/\ln(2.11/R_{[\mathrm{CI}]})$, and derive $\mathrm{T}_{\mathrm{ex}} = 44.3 \pm 1.0\,\mathrm{K}$ for SMM J2135.

We also follow Weiß et al. (2005a) to derive the total mass of neutral carbon via:

$$M_{\mathrm{CI}} = 1.902 \times 10^{-4} Q(T_{\mathrm{ex}}) e^{T_1/T_{\mathrm{ex}}} L'_{[\mathrm{CI}](^3P_1 \to {}^3P_0)} \tag{3.5.1}$$

where $Q(T_{\mathrm{ex}}) = 1 + 3e^{-T_1/T_{\mathrm{ex}}} + 5e^{-T_2/T_{\mathrm{ex}}}$ is the $[\mathrm{CI}]$ partition function and T_{ex} is defined above. Using $\mathrm{T}_{\mathrm{ex}} = 44.3 \pm 1.0\,\mathrm{K}$ and our measured luminosity of the upper

fine structure line, $[\text{CI}](^3P_1 \rightarrow \,^3P_0)$, we estimate a carbon mass of $M_{[\text{CI}]} = (9.1 \pm 0.2) \times 10^6 \, M_\odot$. Combining this with our gas mass estimated from the LVG analysis we derive a [CI] abundance of $M([\text{CI}])/6M(H_2) = (3.8 \pm 0.1) \times 10^{-5}$, which is higher than the Galactic value of 2.2×10^{-5} from Frerking et al. (1989). Similarly, the ratio of the [CI] and ^{12}CO brightness temperatures, $L'_{[\text{CI}](^3P_1 \rightarrow \,^3P_0)} / L'_{^{12}\text{CO}(1-0)} = 0.41 \pm 0.02$, falls towards the upper end of the range 0.2 ± 0.2 observed in local galaxies (Gerin & Phillips, 2000; Bayet et al., 2006). A higher abundance of [CI] relative to ^{12}CO is expected in regions with lower metallicity (Stark et al., 1997) where ^{12}CO is photodissociated, in regions with a high ionisation fraction which may drive the chemistry to equilibrium at a high $[\text{CI}]/^{12}$CO ratio, and in starburst systems with a high cosmic ray flux (Papadopoulos et al., 2004; Flower et al., 1994).

We can also attempt to model the [CI] emission within the framework of our two-phase LVG model. We find that we are only able to simultaneously fit the [CI] luminosities and ratios if the carbon abundance is allowed to vary between the two phases. To fit the observed $R_{[\text{CI}]}$ ratio and the [CI] to ^{12}CO brightness temperatures the LVG model suggests $[\text{CI}/^{12}\text{CO}] \sim 0.2$ for the warm, dense phase, which is close to the Galactic value, $[\text{CI}]/^{12}\text{CO} \sim 0.13$ (Frerking et al., 1989), while for the extended, low-density phase we require an abundance of $[\text{CI}]/^{12}\text{CO} \sim 3.0$, which suggests a deficit of oxygen, and hence possibly a very low metallicity. Using the correlation between $[\text{CI}]/^{12}$CO and metallicity $(12 + \log[\text{O/H}])$ in Bolatto et al. (2000), for the cool component we derive $12+\log(\text{O/H})=7.5$ and hence a metallicity of $\sim Z/Z_\odot = 1/25$. This is similar to that of the Sextans dwarf galaxy, to the lowest metallicity, young starbursts seen locally (Brown et al., 2008), and to the lowest metallicity galaxies found at high redshift (Yuan & Kewley, 2009). However, the high $[\text{CI}]/^{12}$CO ratio could also be due to a high cosmic ray flux in the galaxy (Papadopoulos et al., 2004; Israel & Baas, 2002). Indeed a factor of $\sim 10\times$ enhancement of cosmic ray flux will yield the high $[\text{CI}/^{12}\text{CO}]$ ratio we observe and this may not be unlikely given the high star formation rate density of the star-forming regions (Swinbank et al., 2010). Moreover, an enhanced $[\text{CI}/^{12}\text{CO}]$ ratio has also been observed in the starburst galaxy NGC 253 (Harrison et al., 1995; Bradford et al., 2003)

attributed to a high cosmic ray flux.

Finally, the [Cɪ] detections can be combined with the observations of [Cɪɪ]157.7 from Ivison et al. (2010d) to investigate the ISM cooling. We can compare the cooling in each of our lines relative to the bolometric (8–1000μm) luminosity, to assess their importance. The fraction of the bolometric luminosity in the [Cɪɪ] line is 0.24%, the rotational ^{12}CO lines (^{12}CO(1–0) to ^{12}CO(10–9)) contribute 0.09% and the [Cɪ] lines result in just 0.03%. Therefore, [Cɪɪ] dominates the cooling with the total cooling due to ^{12}CO and [Cɪ] representing ~ 50% of the cooling due to [Cɪɪ]. [Cɪɪ] is one of the brightest emission lines in galaxies and can account for 0.1–1% of the far-infrared luminosity of the nuclear regions of galaxies (Stacey et al. 1991); our source lies well within that range. This situation is in contrast to comparably luminous systems in the local Universe, e.g. Arp 220, where the [Cɪɪ] emission is just 1.3×10^{-4} of L_{FIR} (Gerin & Phillips 1998). This most likely results from saturation of [Cɪɪ] in very high-density star-forming regions (Luhman et al. 1998). The proportionally stronger [Cɪɪ] emission we see in SMM J2135 may then reflect slightly lower densities and more extended star formation (Ivison et al. 2010c), or be due to the lower metallicity of the gas compared to local ULIRGs (Israel et al. 1996; Maiolino et al. 2009).

Overall, our observations of atomic carbon suggest that it arises from a cool phase within the galaxy and that integrated over the whole galaxy the [Cɪ]/^{12}CO ratio is higher than the Galactic value. However, we also find evidence for variation in the ratio within the system, with the cool, low-density phase having significantly enhanced [Cɪ], compared to ^{12}CO, suggesting lower metallicity in this phase or a higher cosmic ray flux in the overall system.

HCN(3–2)

Our spectra also cover emission lines from a number of species other than ^{12}CO; notably, we detect HCN(3–2) emission (Table 3.2). HCN is an effective tracer of dense gas due to its high dipole moment, requiring $\sim 100\times$ higher densities for collisional excitation than ^{12}CO(1–0). Indeed, HCN is one of the most abundant

molecules at densities $n \gtrsim 3 \times 10^4 \, \mathrm{cm}^{-3}$ (compared to critical densities of $\gtrsim 500 \, \mathrm{cm}^{-3}$ for low-J_{upper} levels of ^{12}CO). We note that the velocity centroid of the HCN emission is redshifted by approximately $+230 \pm 100 \, \mathrm{km \, s}^{-1}$, relative to the nominal systemic redshift of the system derived from ^{12}CO. As we discuss below, this hints that the HCN emission may arise predominantly from only one of the kinematic components within the galaxy.

It has been shown that the HCN line luminosity is tightly correlated with far-infrared luminosity in local spirals and ULIRGs, with a linear relation holding over at least three decades in luminosity, and a similar relation may hold at high redshift (Fig. 3.3; Gao & Solomon 2004; Gao et al. 2007). This suggests that HCN is a good tracer of the dense gas which fuels the massive star formation, which in turn is responsible for the far-infrared emission. In Fig. 3.3 we show the relation between far-infrared luminosity and HCN(3–2) line luminosity for local spirals, LIRGs and ULIRGs (Gao & Solomon 2004; Juneau et al. 2009). SMM J2135 lies at the high-luminosity end of this correlation, corresponding to the highest-luminosity local ULIRGs, and is consistent with the relation. In the inset panel on Fig. 3.3 we also compare our source to local LIRGs and ULIRGs in Gao & Solomon (2004). We show the upper limit on $\mathrm{L}'_{\mathrm{HCN}(1-0)} \, / \, \mathrm{L}'_{^{12}\mathrm{CO}(1-0)}$ using our 3-σ upper limit for HCN(1–0) flux, demonstrating that this is also consistent with the increasing $\mathrm{L}'_{\mathrm{HCN}} \, / \, \mathrm{L}'_{^{12}\mathrm{CO}}$ ratio seen with increasing $\mathrm{L}_{\mathrm{FIR}}$ at low redshift.

It is also possible to estimate a total gas mass from the HCN luminosity (Gao et al., 2005). Using our 3-σ upper limit on the HCN(1–0) luminosity we derive a limit on the dense gas mass of $\mathrm{M}_{\mathrm{dense}}(\mathrm{H}_2) = \alpha_{\mathrm{HCN}(1-0)} \, \mathrm{L}'_{\mathrm{HCN}} \ll 4.5 \times 10^{10} \, \mathrm{M}_{\odot}$ with $\alpha_{\mathrm{HCN}} \ll 10 \, \mathrm{M}_{\odot} \, (\mathrm{K \, km \, s}^{-1} \, \mathrm{pc}^2)^{-1}$ (Gao & Solomon, 2004). We caution that there is at least a factor $3\times$ uncertainty arising from the uncertainty in α_{HCN}. The value of α_{HCN} we adopt is appropriate for a virialised cloud core; however, ULIRGs and LIRGs usually have a much higher HCN brightness temperature, resulting in their α_{HCN} being much lower (Gao & Solomon, 2004), and hence this is reported as an upper limit on the gas mass. Since this gas mass is consistent with the mass derived from our LVG analysis of ^{12}CO, this suggests that with better estimates of α_{HCN},
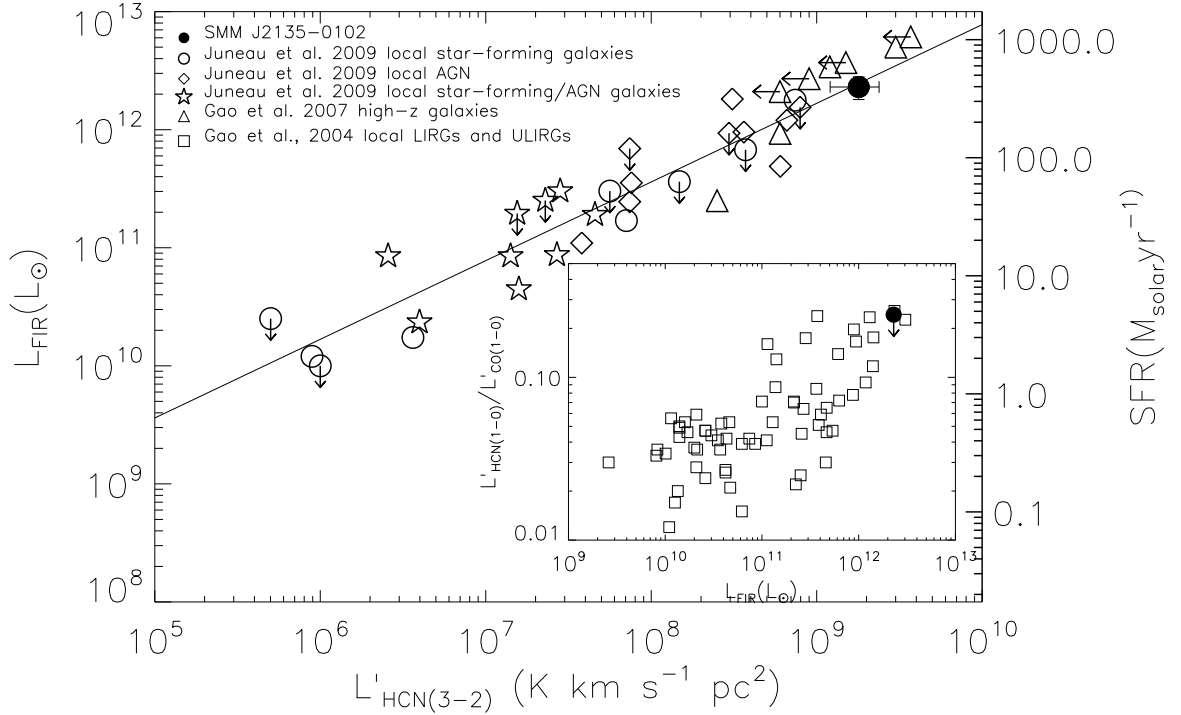
Figure 3.3: The relation between far-infrared luminosity and HCN luminosity for galaxies. We compare our observations of SMM J2135 with the correlation seen locally and find that this high-redshift galaxy follows the tight correlation seen in local galaxies (Juneau et al. 2009). In the main panel we plot observations from a sample of 34 local galaxies (star-forming galaxies, star-forming galaxies with AGN and strong AGN) taken from Juneau et al. (2009). In the inset panel we compare our upper limit on the ratio of $L'_{HCN(1-0)} / L'_{^{12}CO(1-0)}$ to the ratio in local LIRGs and ULIRGs from Gao & Solomon (2004) showing that this upper limit is consistent with the Gao & Solomon (2004) relation. Again we see that the properties of the dense gas and far-infrared emission in this galaxy are similar to those seen locally.

HCN may be a promising route to constraining the dense gas masses of high-redshift galaxies in the future. However, we note that the consistency of ^{12}CO-based and HCN-based gas mass estimates may be coincidental if these lines trace different phases. We further caution that at least two HCN lines may be required to derive the correct value of α_{HCN} due to the strong variations in HCN(4–3)/HCN(1–0) and HCN(3–2)/HCN(1–0) luminosity ratios locally (Papadopoulos, 2007).

As with [CI], we also attempted to use our two-phase LVG model from the ^{12}CO SLED to model the HCN(3–2) and HCN(1–0) emission from this system. However, we find that any models which fit the HCN SLED, in particular the bright HCN(3–2) emission, over-predict the luminosities of the ^{12}CO SLED and result in gas masses which are greater than the dynamical mass. A similar problem has been identified in local ULIRGs which exhibit enhanced HCN line emission and high ratios of $L'_{HCN} / L'_{^{12}CO}$ due to a higher proportion of dense gas in these strong starburst systems (Solomon & Vanden Bout, 2005; Gao et al., 2007).

H_2O

Finally we comment on the limits obtained for H_2O. H_2O emission arises from the warm, dense gas in the densest regions of a starburst or around an AGN. The strength of the emission is thus a probe of the radiation density and so reflects the compactness of the far-infrared source. The $H_2O\,(2_{1,1}–2_{0,2})$ (731.681 GHz) emission line has recently been detected in the local ULIRGs Mrk 231 and Arp 220 (e.g. González-Alfonso et al. 2010) revealing warm, dense material, possibly arising from an XDR associated with AGN activity (see also Spaans & Meijerink 2008 and van der Werf et al. 2010). We compare our limits on the H_2O line luminosities (as a fraction of bolometric luminosity) with Mrk 231 and Arp 220, where the luminosity ratios are $L_{H_2O}/L_{FIR} \sim 1–2 \times 10^{-6}$. We derive limits on the line luminosity ratio of $L_{H_2O}/L_{FIR} < 1–5 \times 10^{-6}$ from the $H_2O\,(5_{1,5}–4_{2,2})$ and $H_2O\,(2_{1,1}–2_{0,2})$ transitions. These suggest that if an XDR exists within SMM J2135 it is unlikely to be more luminous than those seen in these local AGN-dominated ULIRGs. This conclusion is reinforced by the relatively low luminosity of the high-J_{upper} ^{12}CO lines

in SMM J2135 compared to the substantially brighter high-J lines in Arp 220 and Mrk 231 which again require an XDR to fit their ^{12}CO SLEDs (Spaans & Meijerink, 2008; van der Werf et al., 2010).

3.5.2 Integrated properties: physical properties of the ISM

When massive stars are formed around a molecular cloud, their ultra-violet (UV) radiation changes the chemical properties of the cloud's surface layers; the far-UV flux photodissociates the outer layer and ionises the material (such as carbon). This layer then cools primarily via atomic fine structure lines of [OI], [CII], [CI], and the rotational ^{12}CO lines. Emission from these different coolants arises from different depths within the PDR (Kramer et al., 2004), such that the surface layers are dominated by emission from hydrogen, [CII] and oxygen, although further into the star-forming clouds (as the extinction, A_V, increases), hydrogen becomes molecular, whilst the ionisation of carbon declines, with [CII] becoming [CI] and then combining into CO. Moreover, with increasing density, the higher-J_{upper} ^{12}CO emission becomes stronger, as do other molecular gas tracers such as HCN, CS and CN (Kaufman et al., 1999). Deeper into the cloud, the gas is molecular, but still has a higher temperature than in the far-UV shielded core. Significant effort has been devoted to modelling (and predicting) the fine structure and molecular emission line ratios associated with these star-forming regions using PDR models. These account for variations in density, temperature, clumpiness and time-dependent chemistry (e.g. Meijerink et al. 2007; Kaufman et al. 1999) and using their predictions of the ratios of [CII], [CI] and ^{12}CO we can investigate the typical far-UV intensity and ISM density within the star-forming regions in SMM J2135.

PDR models

To model the full-range of observed line ratios from SMM J2135 we use the PDR models of Kaufman et al. (1999) and Meijerink et al. (2007) in which the emission is determined by the atomic gas density (n; the density of H nuclei) and the incident

far-UV radiation field from massive stars ($h\nu = 6\text{--}13.6\,\text{eV}$) which is expressed in terms of G_0 (where G_0 is the average far-UV radiation field in Habing units). Simple PDR models (including one of the two models we compare to; Kaufman et al. 1999) calculate the line emission generated by a cloud illuminated only on one side. However, for observations of external galaxies it is not clear that such a "single cloud" model will adequately describe the observed molecular lines. For clouds illuminated on all sides we note that an observer will detect optically thin radiation emitted from both the near and far sides of the cloud, but only see optically thick emission from the near side. Generally, low-J_{upper} ^{12}CO transitions are assumed to be optically thick for the nominal $A_V = 10$ cloud depths in the PDR models (Hailey-Dunsheath et al., 2010b), whilst [CII], [CI], ^{13}CO and L_{FIR} are assumed to be optically thin (although note our earlier estimates of the high column densities and extinction in this system). We have not applied any corrections to the emission lines to account for these differences between optically thick and optically thin emission. Instead, we also compare to more complicated models involving two or more clouds, with differing densities and incident radiation fields which have been constructed by Meijerink et al. (2007). The implementation of these models assumes all emission lines are coming from the same gas in the same region, which we know to be a vast over-simplification; however, these solutions do provide us with order of magnitude estimates of the characteristic conditions in the system.

In Figs. 3.4 and 3.5 we show the model grid of n and G_0 values for various emission line ratios for SMM J2135. The ^{12}CO $J/(J-1)$ and [CI]/^{12}CO line luminosity ratios vary over six orders of magnitude in G_0; however, the [CII]/FIR and [CII]/^{12}CO ratios appear to break this degeneracy. Indeed, in the $n \sim 10^3\text{--}10^5\,\text{cm}^{-3}$ regime, these provide a strong constraint on G_0. Using the two different PDR models we convert the allowed parameter space for each line ratio to derive the peak likelihood solution, which is shown in Fig. 3.4 and 3.5 for both models. We find that the solutions cluster around moderate densities ($n \sim 10^4\,\text{cm}^{-2}$), similar to those claimed for local ULIRGs from PDR modelling of H_2 emission (Davies et al., 2003). The peak likelihood solutions use all the line ratios available aside from the $\text{L}'_{\text{[CI]}(^3\text{P}_2 \to {}^3\text{P}_1)} / \text{L}'_{\text{[CI]}(^3\text{P}_1 \to {}^3\text{P}_0)}$
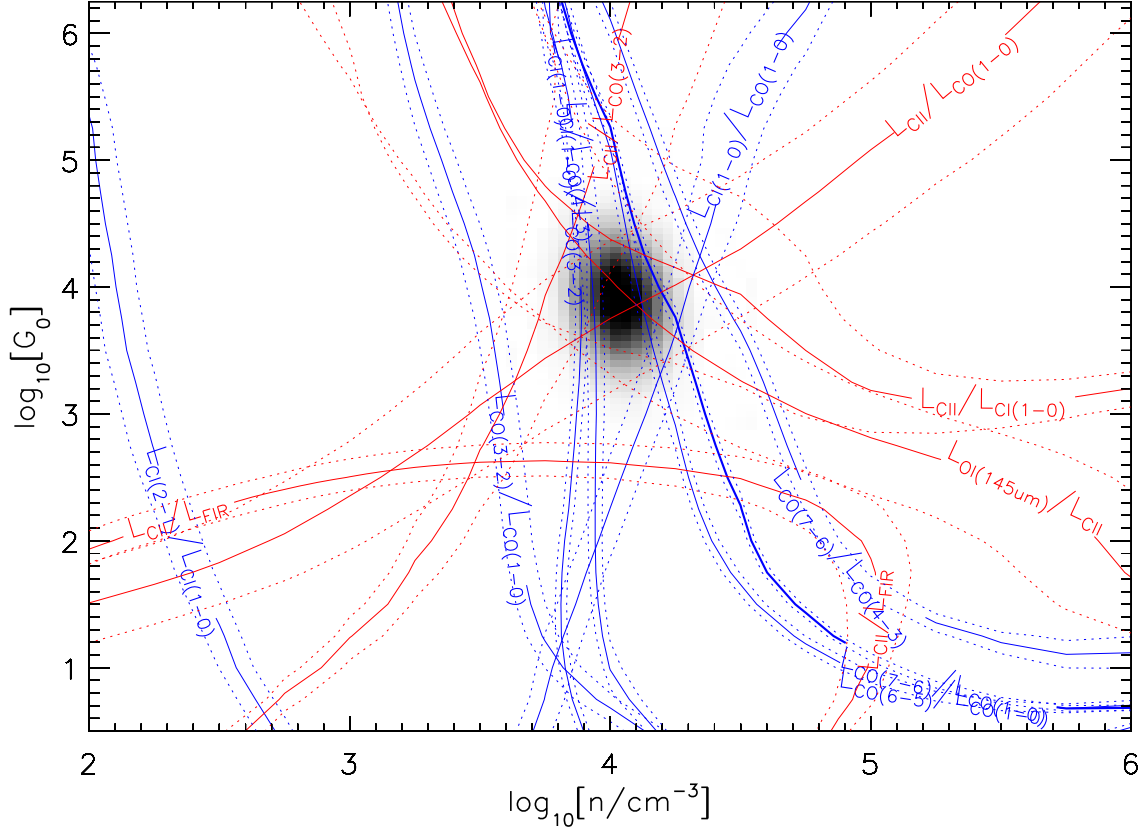
Figure 3.4: Luminosity line ratios (in units of $L_\odot$) from ^{12}CO, [C I] and [C II] as a function of density and far-UV flux (G_0 in units of Habing field), from the PDR models of Kaufman et al. (1999). Tracks are drawn for the measured ratios in solid lines with the 1-σ errors as dotted lines. The line ratios within SMM J2135 intercept at $n \sim 10^{4.1}$ cm^{-3} and $G_0 \sim 10^{3.6}$ Habing fields and $n \sim 10^{4.3}$ cm^{-3} and $G_0 \sim 10^{3.3}$ Habing fields for the Kaufman et al. (1999) and Meijerink et al. (2007) models respectively. To better display the preferred regions of parameter space we combine the probability distributions from all of these lines (excluding $L_{[\mathrm{CI}](2-1)}/L_{[\mathrm{CI}](1-0)}$ for reasons explained in Section 3.5.2) to derive a peak likelihood solution for each model.
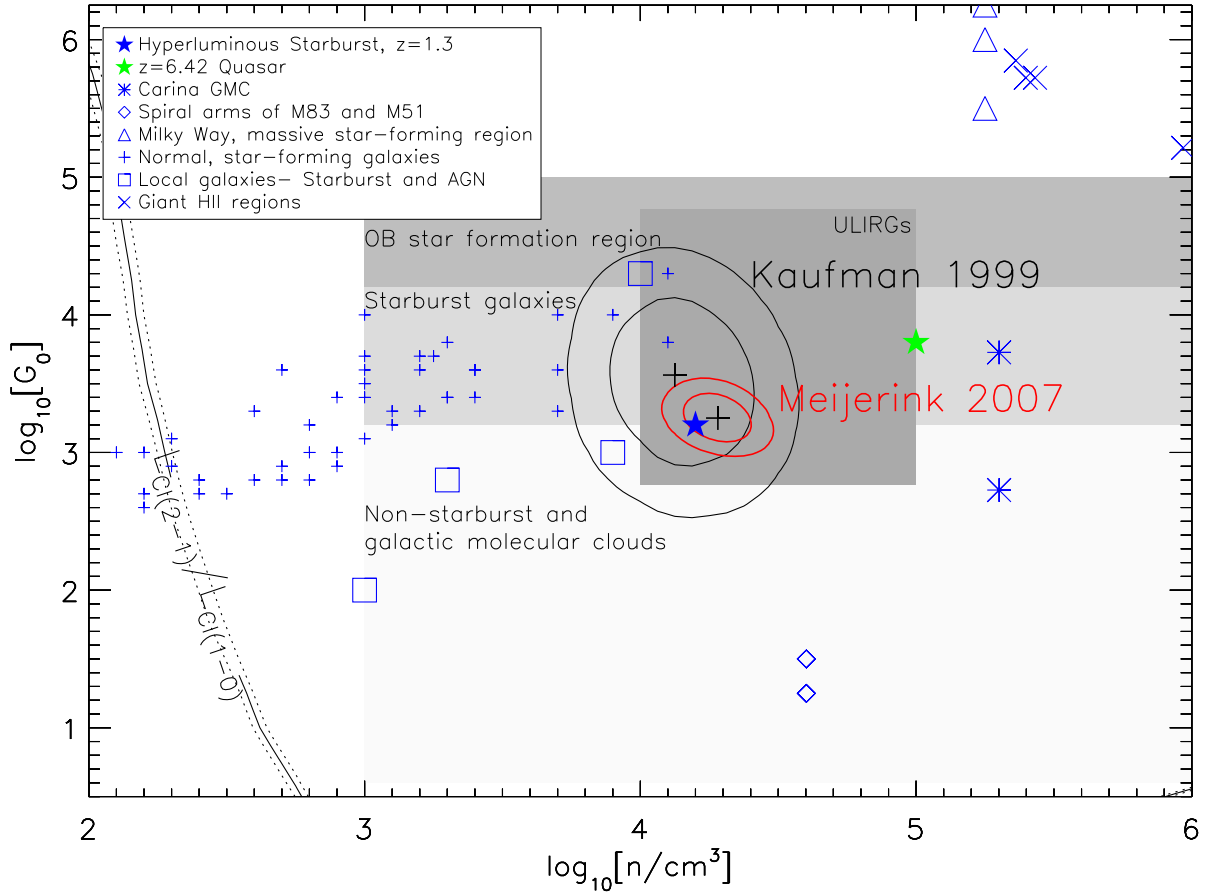
Figure 3.5: The same parameter space for the models as Fig. 3.4, now comparing the peak likelihood solutions from the model grids to the derived values of G_0 and density (n) for various low- and high-redshift galaxies and molecular clouds. We also indicate the regions of parameter space which are typically encompassed by Galactic OB star-formation regions, starburst galaxies and non-starburst and Galactic molecular clouds from Stacey et al. (1991). This shows that the line ratios for SMM J2135 are consistent with those typically found in local starbursts or ULIRGs. The local galaxy that lies within the contours of the peak likelihood for the Kaufman models is NGC 253, a spiral starburst galaxy (Negishi et al., 2001). We also show the peak likelihood solution derived from the PDR models of Meijerink et al. (2007) which provide a concomitant solution. The contours represent the 1- and 2-σ limits compared to the best-fit solution. The peak likelihood solutions are derived without including the $L_{[CI](2-1)} / L_{[CI](1-0)}$ track, which we plot on both panels to show its discrepancy from the general solution from the other lines (see Section 3.5.2).

ratio. This line's track deviates strongly from the preferred solution from the other lines. We expect this reflects the sensitivity of this line ratio to details of the PDR, such as geometry, and we discuss specific problems with the PDR model treatment of [CI] below.

The best-fit solution to our suite of line ratios is $n = 10^{4.1\pm0.3}\mathrm{cm}^{-3}$ and $G_0 = 10^{3.6\pm0.7}$ Habing fields for the PDR models from Kaufman et al. (1999) and $n \sim 10^{4.3\pm0.2}\,\mathrm{cm}^{-3}$ and $G_0 \sim 10^{3.3\pm0.2}$ Habing fields from Meijerink et al. (2007). The best-fit solutions are within 1-σ and are in agreement with earlier estimates based on just ^{12}CO(1–0), [CII] and $\mathrm{L_{FIR}}$ in Ivison et al. (2010d). As we see from Fig. 3.4 and 3.5, these physical conditions are similar to local starburst galaxies and ULIRGs (Stacey et al., 1991; Davies et al., 2003) and at the upper end of both density and G_0 for normal star-forming galaxies (Malhotra et al., 2001), for example the radiation field is $\sim 1000\times$ more intense than in the disk of the Milky Way. The characteristic density compares well to the dense star-forming cores of Galactic molecular clouds, or to the central compact nuclear gas disks of local ULIRGs such as Arp 220 (Downes & Solomon, 1998; Sakamoto et al., 1999) and is also consistent with the integrated ^{12}CO SLED (see Section 3.5.1). This characteristic density we derive is greater than the critical density for [CII], [CI] and CO(1–0), above which the intensity of the lines saturates. Similarly, the G_0 value we derive suggests the conditions in the PDRs are at the limit of the steady state solution (Kaufman et al., 1999); with radiation pressure on grains comparable to turbulence, suggesting that the PDRs may be ionising material.

Our results imply that the underlying physics of the star formation occurring in the system is similar to the dense star-forming cores of Galactic molecular clouds (characteristic of massive OB star-forming regions), even though the total energetics of the system is far more extreme than in the disk of our galaxy. Interestingly, Teyssier et al. (2010) have recently used hydrodynamic simulations of major mergers of disk galaxies to show that the density of gas at which a majority of the star formation in these systems occurs is $n\sim 10^4\,\mathrm{cm}^{-3}$, as we find here.

Of all the line ratios we analyse, the most obvious outlier in the PDR modelling

is the $[\mathrm{CI}](^3P_2 \rightarrow {}^3P_1)/[\mathrm{CI}](^3P_1 \rightarrow {}^3P_0)$ emission line ratio (Fig. 3.4 and 3.5). However, we note that this line ratio is one of the most sensitive to G_0 and n and it would only require a modest increase in the predicted $[\mathrm{CI}](^3P_1 \rightarrow {}^3P_0)$ flux in the models, $\sim 3\times$ stronger, to shift this track into agreement with the solution based on the bulk of the other ratios at $n \sim 10^4 \, \mathrm{cm}^{-3}$ and $G_0 \sim 10^{3.5}$. This problem may arise because the PDR models assume a particular geometry, which determines the ratio of diffuse to dense gas, and assume a homogeneous medium (an unrealistic assumption for our source). The resulting luminosity ratios based on $^{12}\mathrm{CO}/[\mathrm{CI}]$ and $[\mathrm{CI}]$ are sensitive to this geometry and the $[\mathrm{CI}](^3P_2 \rightarrow {}^3P_1)/[\mathrm{CI}](^3P_1 \rightarrow {}^3P_0)$ ratio is particularly sensitive to the homogeneity of the medium (Spaans, 1996), as demonstrated by the difficulty the models have in reproducing the $[\mathrm{CI}](^3P_1 \rightarrow {}^3P_0)$ or $[\mathrm{CI}](^3P_2 \rightarrow {}^3P_1)$ emission lines even in tranquil environments (e.g. Pineda & Bensch 2007; Papadopoulos & Greve 2004). Indeed, Papadopoulos & Greve (2004) argue that $[\mathrm{CI}]$ is distributed relatively ubiquitously in molecular clouds (the critical density for excitation of both $[\mathrm{CI}](^3P_1 \rightarrow {}^3P_0)$ and $[\mathrm{CI}](^3P_2 \rightarrow {}^3P_1)$ is roughly that of $^{12}\mathrm{CO}(1\text{--}0)$; Solomon & Vanden Bout 2005). This is contrary to PDR theory, which places $[\mathrm{CI}]$ in a narrow $[\mathrm{CII}]/[\mathrm{CI}]/^{12}\mathrm{CO}$ transition zone on the surface of far-UV illuminated molecular clouds, and potentially makes $[\mathrm{CI}]$ a very effective tracer of H_2 mass. Therefore our low ratio may be arising from geometrical optical depth effects in which the $[\mathrm{CI}]$ effectively follows the volume (rather than the PDR surface), which would naturally lower the $[\mathrm{CI}](^3P_2 \rightarrow {}^3P_1) /[\mathrm{CI}](^3P_1 \rightarrow {}^3P_0)$ ratio (e.g. see Kramer et al. 2008) as would happen from any process which enhances $[\mathrm{CI}]$ emission through the cloud's volume (e.g. cosmic rays). We also caution that the $[\mathrm{CI}](^3P_2 \rightarrow {}^3P_1) /[\mathrm{CI}](^3P_1 \rightarrow {}^3P_0)$ ratio has been measured in only a few local galaxies (e.g. Bayet et al. 2006) and so the fine structure excitation of neutral carbon has yet to be fully characterised and calibrated locally.

Limits on $^{13}\mathrm{CO}$, CN, HNC and HCO$^+$

Our observations have also simultaneously covered a number of dense gas tracers and from these we can place limits on the line luminosities of $^{13}\mathrm{CO}$, CN, HNC and HCO$^+$.

We can then ask if these limits are consistent with our preferred characteristic density and UV radiation field from the PDR model.

First we consider the limits on the ^{13}CO. The ^{13}C nuclei are synthesised by CNO processing of ^{12}C nuclei from earlier stellar generations (^{12}C is produced from He burning on rapid timescales in massive stars). Since ^{13}C is produced more slowly in intermediate mass stars during the red giant phase (at $\sim 1\,\mathrm{Gyr}$), the ^{12}C/^{13}C ratio has been proposed as a diagnostic of the nucleosynthesis history in galaxies. A high ratio would then be seen at high redshift as the young starbursts will have had insufficient time to form secondary nuclei of ^{13}CO. In the Milky Way and nearby star-forming galaxies, the ^{12}CO/^{13}CO line luminosity ratio ($L'_{^{12}\mathrm{CO}}/L'_{^{13}\mathrm{CO}}$) is $\sim$ 5–10. However, local ULIRGs have shown a deficiency of ^{13}CO (possibly due to gas inflow; Rupke et al. 2008), which raises the ^{12}CO/^{13}CO line ratio to $\sim$30 (Greve et al. 2009). Indeed, recently, Henkel et al. (2010) showed that the ^{12}CO/^{13}CO luminosity line ratio in the Cloverleaf quasar (z=2.6) is $L'_{^{12}\mathrm{CO}}/L'_{^{13}\mathrm{CO}}$=40±17, suggestive of a deficiency of ^{13}CO. Within SMM J2135, we estimate limits on the ratio of >5.8 and >6.5 for the $J_{\mathrm{upper}}=1$ and $J_{\mathrm{upper}}=3$ transitions respectively. These limits are consistent with the Milky Way, but more sensitive observations are required to place firm conclusions as to whether a deficiency exists similar to that observed in other local ULIRGs and high-redshift galaxies.

We can compare these limits to the predictions from the PDR models of Meijerink et al. (2007). The model predictions are $L_{^{12}\mathrm{CO}}/L_{^{13}\mathrm{CO}}$=2.13 and 2.08 for the J_{upper}=1 and J_{upper}=3 transitions respectively, indicating lower ^{13}CO abundance in SMM J2135-0102 than the model predicts. This may arise due to a number of effects. It is known that the line luminosity ratios of giant molecular clouds are lower than galaxy-integrated properties due to the lower opacity of ^{13}CO compared to ^{12}CO in the inter-cloud medium. Since we are measuring galaxy integrated properties, this would naturally lower the ratio. Clearly it would be useful to obtain a more sensitive observation of the ^{13}CO to determine the extent of this discrepancy with PDRs.

Finally, we note that the line luminosity ratio of the dense gas tracers of CS(2–1)/^{12}CO(1–0)<0.13 is lower than that predicted from the PDR model (0.43). In

contrast, the $HNC(3–2)/^{12}CO(1–0) < 1.3$ and $HCO^+(3–2)/^{12}CO(1–0) < 1.2$ are consistent with those predicted by the PDR models (1.3 and 0.15 respectively). A more detailed test of the model prediction for these dense gas tracers will again require more sensitive observations.

3.5.3 Kinematically resolved properties: decomposed ^{12}CO SLED

With the high signal-to-noise of our observations of ^{12}CO and [CI] in Fig. 3.1, it is obvious that the spectra show significant kinematic structure and that more intriguingly this structure appears to vary between the different transitions and species. We therefore attempt to fit a model to the ^{12}CO spectra and extract ^{12}CO SLEDs for each kinematic component, in order to search for excitation structure within the system.

To construct a kinematic model for the ^{12}CO emission we fit the composite spectrum (Fig. 3.1) with a series of increasingly complex models. We find that a double Gaussian profile fit provides a ~ 14-σ improvement over a single Gaussian profile, with a triple profile giving a further ~ 6-σ improvement over the double Gaussian profile. Although this model reasonably describes the line profile of the system, P. Cox et al. (in prep) use the velocity structure from high-resolution interferometry with PdBI up to $J_{\mathrm{upper}} = 7$ to derive a map of the dynamics of SMM J2135 on ~ 100-pc scales. The system can be described by two interacting disks: the lower-redshift of these displays a double-horned profile (termed Z_1 and Z_2), with a second, Y, at higher velocity which appears to connect to a further structure, X, extending to much higher velocity. Based on this interpretation we construct a model which comprises three components: two single Gaussians representing X and Y and a double-Gaussian for Z (constrained to have equal line widths and intensities for the two components). We fit this model to the composite spectrum, allowing the intensity, width and velocity of each component to vary and show the resulting best fit to the average line profile in Fig. 3.1 and report its parameters in Table 3.3.

Table 3.3: Model kinematic parameters

Component	v	σ
	(km s^{-1})	(km s^{-1})
Z_2	-167 ± 9	75 ± 8
Z_1	28 ± 9	75 ± 8
Y	165 ± 13	157 ± 17
X	396 ± 9	76 ± 9

Notes: Velocities and line widths of the three kinematic components seen in the CO and [C I] spectra. The velocities are given with respect to a heliocentric redshift of $z = 2.32591$.

This fit has a χ^2 of ~ 20 for seven degrees of freedom and provides an adequate description of the composite line profile.

Using the best-fit model parameters from the composite ^{12}CO spectrum, we apply the fit to each ^{12}CO spectrum in turn, in order to extract the SLEDs for the three components in the model. Beginning with the average model parameters, we perturb the best fit randomly by up to $\pm 20 \mathrm{km\,s}^{-1}$ and fit this new realisation to each of the ^{12}CO spectra in turn, allowing only the relative intensities of the components to vary. We then sum the χ^2 for the fit to each line for each model and determine the parameters for which the total χ^2 is a minimum. We show the best fit model's line profile on each line in Fig. 3.1 and report their parameters in Table 3.3. To calculate errors, we allow the best fit parameters of the kinematic model to randomly vary (by their 1-σ uncertainties) and run 10^5 Monte Carlo simulations, determining the 1-σ variance in the range of fluxes from those models where the total χ^2 of the model fit is within $\Delta\chi^2 = 21$ of the best fit (since we have seven emission lines and fit with three free parameters to each line). The errors on the parameters for the model fit to the average (velocity and dispersion in Table 3.3) are calculated using the standard deviation of the parameters for all models for which the total χ^2 of the model fit is within $\Delta\chi^2 = 21$ of the best fit; these are quoted in Table 3.3.

The ^{12}CO SLEDs for the three individual components are shown in Fig. 3.6. We derive the gas masses for each component using the ^{12}CO(1–0) emission line and assuming our effective conversion factor $\alpha = 2.0\,\mathrm{M}_\odot\,(\mathrm{K\,km\,s}^{-1}\,\mathrm{pc}^2)^{-1}$ and list these
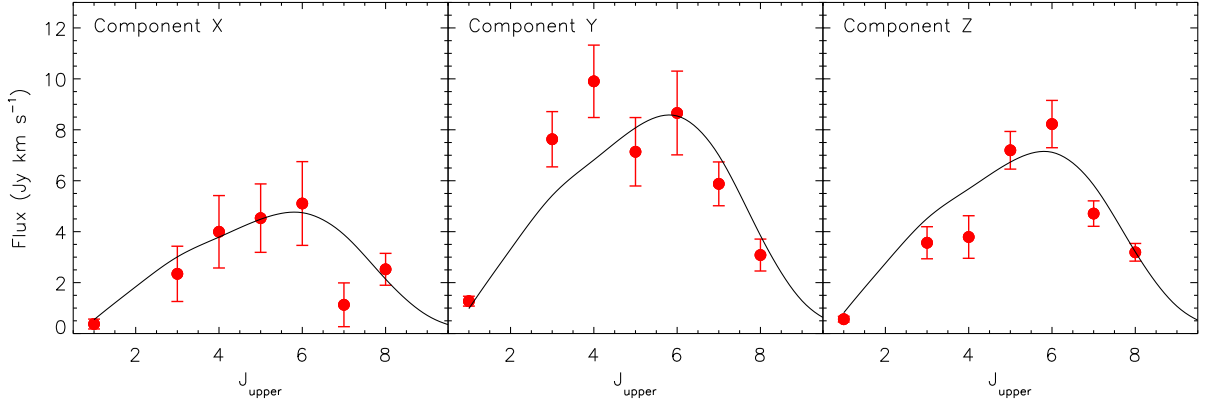
Figure 3.6: The ^{12}CO SLEDs for the three kinematic components seen within the ^{12}CO spectra (from left-to-right for the components at X, Y and Z at ~ -180, 0 and $+200\,\mathrm{km\,s^{-1}}$ respectively). We overplot on each of these a scaled version of the best-fit LVG model from the combined SLED. This shows that two components, X and Z, also peak at around $J_{\mathrm{upper}} \sim 6$, while component Y appears to peak slightly lower, $J_{\mathrm{upper}} \sim 4$, suggesting that there may also be temperature differences between the kinematic sub-components within the galaxy. Interestingly, component Y also appears to contain the bulk of the cold gas as traced by ^{12}CO(1–0) compared to either X or Z.

in Table 3.4. The most highly excited components are X and Z, peaking at $J_{\mathrm{upper}} \sim 6$, and containing $\sim 15\%$ and $\sim 25\%$ of total gas mass respectively (Table 3.4). Component Y, which we associate with the core of the second interacting system, is somewhat less excited, peaking at $J_{\mathrm{upper}} \sim 4$, and contains most of the gas in the system ($\sim 60\%$ of the total gas mass and a majority of the cold gas).

Table 3.4: Line ratios

Component	M_{H_2+He} $(10^9\,M_\odot)$	$R^a_{3,1}$	$R_{4,1}$	$R_{5,1}$	$R_{6,1}$	$R_{7,1}$	$R_{8,1}$	$\frac{L'_{CI(2-1)}}{L'_{CI(1-0)}}$	$\frac{L'_{CI(1-0)}}{L'_{CO(1-0)}}$
Total	40.0 ± 0.3	0.68 ± 0.03	0.50 ± 0.04	0.35 ± 0.02	0.28 ± 0.02	0.119 ± 0.008	0.064 ± 0.005	0.37 ± 0.02	0.41 ± 0.02
Z	10.1 ± 1.8	0.71 ± 0.19	0.42 ± 0.12	0.51 ± 0.11	0.41 ± 0.09	0.17 ± 0.04	0.09 ± 0.01	0.85 ± 0.21	0.32 ± 0.10
Y	23.1 ± 3.2	0.67 ± 0.14	0.49 ± 0.10	0.22 ± 0.05	0.19 ± 0.05	0.09 ± 0.02	0.04 ± 0.01	0.19 ± 0.05	0.43 ± 0.09
X	6.8 ± 3.2	0.70 ± 0.48	0.67 ± 0.42	0.48 ± 0.29	0.38 ± 0.23	0.06 ± 0.06	0.11 ± 0.06	0.43 ± 0.27	0.38 ± 0.28

Masses and line luminosity ratios for individual kinematic components.
[a] $R_{J,1}$ represents $L'_{CO(J+1-J)}/L'_{CO(1-0)}$

For each of the SLEDs, we perform further LVG modelling as applied to the combined spectrum. However, within the errors, we cannot measure any temperature difference between the three components although there is a hint that Y is cooler than X or Z. However, while the $[\text{CI}](^3P_2 \to {}^3P_1)$ and $[\text{CI}](^3P_1 \to {}^3P_0)$ lines have lower signal-to-noise than the ^{12}CO lines, we can also decompose them using the same method. Table 3.4 shows the ratio of $L'_{[\text{CI}](^3P_2 \to ^3P_1)} / L'_{[\text{CI}](^3P_1 \to ^3P_0)}$ for the different components, with Z having the largest ratio and Y having the smallest. The corresponding excitation temperatures are $T_{\text{ex}} > 100\,\text{K}$, $T_{\text{ex}} = 24.7 \pm 0.5\,\text{K}$ and $T_{\text{ex}} = 52.5 \pm 6.3\,\text{K}$ for Z, Y and X respectively (where the temperature calculated for the Z component may be discrepant and likely caused by a problem with the model fit to the line; see Fig. 3.1). This supports the suggestion from the ^{12}CO SLED that both X, and especially Z, are hotter than the more massive Y.

3.5.4 Physical interpretation

Swinbank et al. (2010) show that the rest-frame ~ 250-μm emission from SMM J2135 is concentrated in four bright, star-forming regions each of which has a radius of $\sim 100\,$pc spread across a more diffuse structure with a total extent of $2\,$kpc in projection. Following this we fitted the integrated dust SED of the source (see §3.5.1) assuming that $\sim 20\%$ of the 870-μm flux is coming from a relatively cool ($T_d \sim 30\,\text{K}$) extended dust component with a predicted radius of $\sim 1\,$kpc and $\sim 80\%$ emerges from the four ~ 100-pc radius, hotter ($T_d \sim 60\,\text{K}$) and optically thick, clumps. Our modelling of both the ^{12}CO SLED and the kinematically decomposed $[\text{CI}]$ line ratios supports the presence of two phases in the ISM within this galaxy with a cool, 15–25 K, phase and a hotter, 45–60 K phase (although it is likely that these actually represent a continuum of properties). We also find an enhancement in the $[\text{CI}]/^{12}$CO ratio (likely due to low metallicity and/or higher cosmic ray flux) which is associated with the cool phase in this system. Our kinematic model identifies a component Y which is relatively cool and contains the about half of the gas in the system, while the hotter material is more closely tied to component Z (and to a lesser extent X).

It is tempting to associate these kinematic components with the clumps seen in the SMA map, but as we discuss below, it is more likely that the clumps lie within these kinematic structures, rather than having a unique one-to-one relationship.

Our observations also provide other limits on the characteristic size and morphology for the emission regions. We can use the characteristic density derived from the PDR analysis, together with the total gas mass to derive an effective radius of the system. Adopting $M(H_2+He) \sim 4 \times 10^{10} M_\odot$ and a density of $\sim 10^4 \, cm^{-3}$ from the Kaufman et al. (1999) models, we derive the radius of an equivalent sphere of $\sim 300 \, pc$ (or $\sim 700 \, pc$ for a disk with a thickness of $\sim 100 \, pc$). These sizes are larger than the clump sizes in the submillimetre, which again is consistent with the interpretation from the LVG modelling that the ^{12}CO is much more wide spread than the star-forming clumps. If we similarly split the gas mass into four equal clumps, then the expected sizes of these are $\sim 200 \, pc$ in radius, which is slightly larger than the far-infrared sizes of the star-forming regions within SMM J2135.

We can also use the value of $G_0 \sim 10^{3.6}$ Habing fields, as determined from the PDR models, to estimate the characteristic size of the galaxy. Assuming a Salpeter IMF and a constant SFR in the burst then the ionising flux (6–13.6eV) is $\sim 50\%$ of the bolometric luminosity for ages of 10–100 Myrs. We can determine the size of a region where the typical ionising field, as estimated from our bolometric luminosity, equals G_0. This gives an estimate for the system's radius of $\sim 1 \, kpc$, similar to the characteristic size inferred from the LVG modelling of the dust SED and the overall extent of the system from the SMA observations.

We can use the kinematics of the components and the potential sizes and estimate the gas mass fractions in these various components. We first note that the dynamical mass of a uniform sphere with velocity dispersion of $\sigma \sim 75$–$160 \, km \, s^{-1}$ (Table 3.3) and an effective radius of $r \sim 200$–$1000 \, pc$ is ~ 0.1–$3 \times 10^{10} M_\odot$. The gas masses from Fig. 3.6 (using $\alpha = 2.0 \, M_\odot \, (K \, km \, s^{-1} \, pc^2)^{-1}$) are ~ 7–$23 \times 10^9 M_\odot$, similar to the range of dynamical masses, indicating that the gas reservoirs in these components must have effective radii comparable to the estimates above from the various size indicators. This also shows that we cannot significantly increase α, for example to

the Milky Way value of $\alpha \sim 4.6$, since this would result in a range of gas masses of $\sim (1.4\text{–}4.7) \times 10^{10}\,\mathrm{M_\odot}$, in excess of the dynamical masses unless the gas has disk-like kinematics and we are seeing these almost face on, which is unlikely given the large velocity dispersion.

Our size estimates for the gas reservoirs are larger than the size of the clumps in the SMA map and are more comparable to the extent of the whole system, which suggests that the cold gas is more widely distributed than the $\lesssim 100$-pc radius far-infrared clumps. Thus, these clumps are likely to be knots of emission lying within a colder and more extended structure. Although the clumps will trace the kinematics of the gas in which they are embedded, they may not represent the deepest parts of the potential well, and so the star formation may be free to migrate around the gas reservoir. These intense star-forming regions have crossing times of just a few Myrs and they have free-fall SFRs (Krumholz & Tan, 2007) of ~ 0.001 indicating that they are supported against collapse (most likely by internal turbulence).

Finally, with an estimate of the overall extent of the gas reservoir, we investigate where SMM J2135 lies on the Kennicutt-Schmidt relation, which links the star-formation- and gas surface density (Σ_{SFR} and Σ_{gas} respectively). This relation is approximately linear up to a threshold of $\sim 0.1\,\mathrm{M_\odot\,pc^{-2}}$, above which the density of the ISM becomes dominated by molecular gas and the star-formation law instead follows $\Sigma_{\mathrm{SFR}} \propto \Sigma_{\mathrm{gas}}^{1.4}$ (Kennicutt, 1998b). Previous work has shown broad universality of this relation with redshift, although at $z \sim 2$, both surface brightness and instrument limitations mean that a direct comparison to low-redshift galaxies has been difficult, with extrapolations from high-J CO in intrinsically luminous galaxies providing most constraints (e.g. Genzel et al. 2010). Some of this tension can be alleviated by using the CO(1–0) emission (or LVG modelling of the full CO SLED) to provide a more reliable estimate of the gas mass and spatial extent, and in Fig. 3.7 we show the Kennicutt-Schmidt relation and overlay the position of SMM J2135. We also include on the plot the high-redshift galaxies where CO(1–0) observations are available. This figure shows that SMM J2135 lies at the high star formation- and gas-density end of the correlation, although within the scatter seen for local
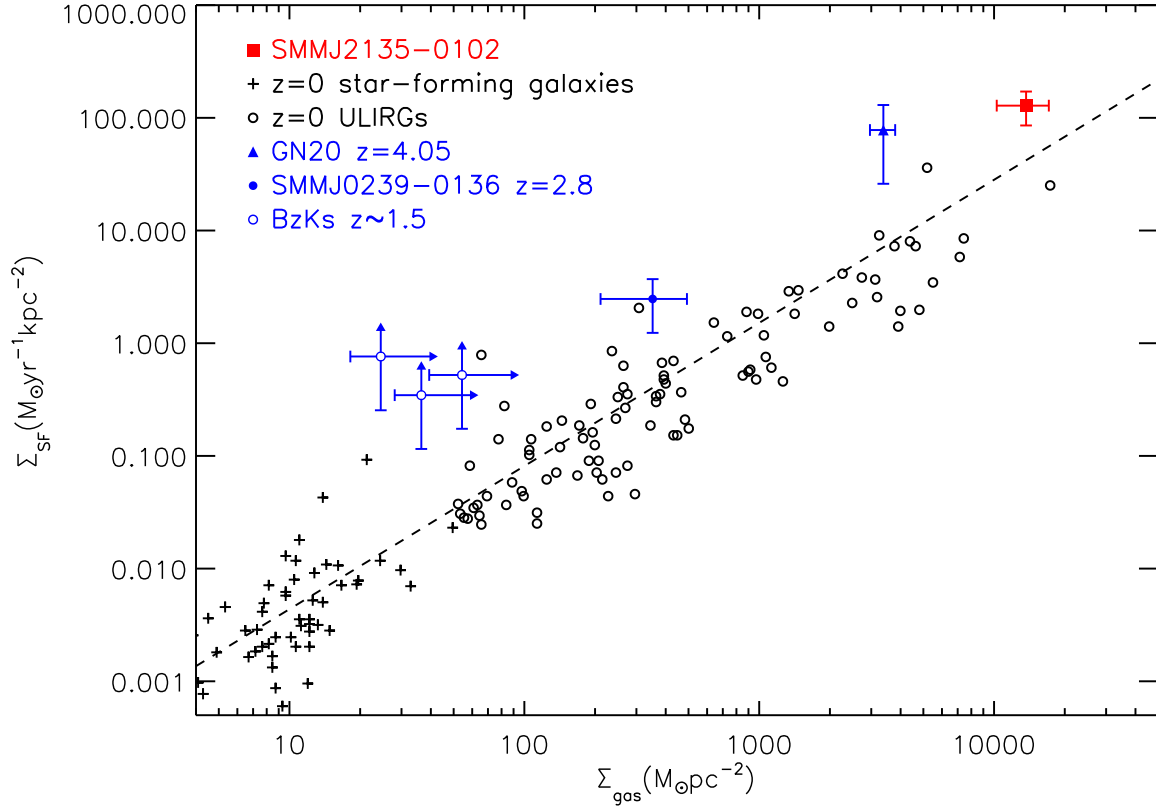
Figure 3.7: The correlation between measured gas and SFR densities for SMM J2135 compared to samples of local star-forming galaxies and ULIRGS from Kennicutt (1998b) and high-redshift, as derived from ^{12}CO(1–0). The dashed line is the best fit power law to local data with $\Sigma_{\rm SF} \propto \Sigma_{\rm gas}^{1.27}$ (Genzel et al. 2010). We see that the star formation within SMM J2135 is consistent with this relation assuming $r_{\rm gas} = r_{\rm SF} = 1\,{\rm kpc}$. SMM J02399−0136 is taken from Ivison et al. (2010), GN20 from Carilli et al. 2010 and the BzKs from Aravena et al. (2010) which are unresolved in ^{12}CO(1–0), hence the arrows representing the lower limits in measured gas density.

ULIRGs.

Although we do not have spatially resolved spectroscopy to probe the gas properties on $\sim 100\,\mathrm{pc}$ scales, we can ask where the individual star-forming regions would lie if they too followed the Kennicutt-Schmidt relation. Assuming that 80% of the bolometric luminosity arises in these clumps, and that each clump has a radius of $r_{\mathrm{SF}}=r_{\mathrm{gas}} \sim 100\,\mathrm{pc}$, then the inferred gas density would be $n \sim 3 \times 10^5\,\mathrm{cm}^{-2}$, which is substantially higher than that inferred from the PDR and LVG modelling of the dense gas tracers ($n \sim 10^{3.5-4.5}\,\mathrm{cm}^{-2}$). However, taking the remaining 20% of the bolometric luminosity with a radius of $1\,\mathrm{kpc}$ (and assuming the gas lies in an extended disk), the density is $n \sim 0.2\text{--}1 \times 10^4\,\mathrm{cm}^2$ (with the main uncertainty being the disk thickness). Thus, although this calculation should be considered crude, the results are consistent with a model in which the submillimetre emission predominantly traces the star-forming clumps on $\sim 100\,\mathrm{pc}$ scales, but these clumps are simply embedded in a much more extended structure which dominates the ^{12}CO emission. These results may also imply a break-down of the Kennicutt-Schmidt relation on scales of individual GMCs ($< 100\,\mathrm{pc}$, see also Onodera et al. 2010) although clearly high resolution millimetre observations would accurately constrain their sizes, which is a fundamental step in understanding the conditions within the ISM of high-redshift galaxies (P. Cox et al. in prep).

3.6 Conclusions

We have presented detections of a number of rest-frame, far-infrared and submillimetre molecular and atomic emission lines in the spectrum of the lensed submillimetre galaxy SMM J2135. We have used these lines to construct the ^{12}CO SLED up to $J_{\mathrm{upper}} = 10$ and analysed this and the other species, including the HCN(3–2) and [CI] fine structure lines, to investigate the physical conditions within the interstellar medium in this galaxy. Our main results are:

- The ^{12}CO SLED resembles that of local starburst galaxies. An LVG analysis

of the ^{12}CO SLED shows at least two phases with temperatures $T \sim 25$ and 60 K.

- The dust SED is best fit by a model in which the galaxy comprises an extended component with radius ~ 1–2 kpc with $T_d \sim 30$ K and four high-density, star-forming regions with sizes of order $r \sim 200$ pc and $T_d \sim 60$ K. These characteristics are roughly consistent with the rest-frame ~ 250-μm morphology of the system as seen by SMA and the two components may link to the phases identified from the ^{12}CO SLED. At $J_{\text{upper}} = 1$–0, the cooler, diffuse phase appears to comprise 50% of the molecular gas. We also derive a carbon mass of $M_{\text{CI}} = (9.1 \pm 0.2) \times 10^6 \, M_\odot$ and hence a carbon abundance of $\sim 4 \times 10^{-5}$ which is slightly above the Galactic value. LVG modelling suggests that the dense, star-forming regions have abundances similar to that seen in the Milky Way, whilst the extended diffuse gas has lower metallicity (or a higher cosmic ray flux).

- Using the ^{12}CO emission and assuming $\alpha = 0.8 \, M_\odot \, (\text{K km s}^{-1} \, \text{pc}^2)^{-1}$ we estimate the total molecular gas mass from the ^{12}CO(1–0) emission as $M(H_2) = (1.4 \pm 0.1) \times 10^{10} \, M_\odot$. Comparing this with that derived from $J_{\text{upper}} \geq 3$ transitions, assuming thermalised gas, shows that these predicted gas masses are a factor 1.5–3.6$\times$ too low, indicative of multiple gas phases, as seen in local starbursts. However, our LVG analysis indicates a higher gas mass, $M(H_2) \sim 4 \times 10^{10} \, M_\odot$, yielding an effective CO-to-H_2 conversion factor of $\alpha \sim 2.0 \, M_\odot \, (\text{K km s}^{-1} \, \text{pc}^2)^{-1}$. If these conditions are relevant in the wider SMG population then this suggests that previous, $J_{\text{upper}} \geq 3$ ^{12}CO observations of SMGs may have underestimated the molecular gas content of SMGs by at least a factor of ~ 2–5$\times$ (see also Ivison et al. 2010c; Harris et al. 2010).

- Within SMM J2135 we detect the HCN(3–2) emission at the 3-σ level, and use this to estimate a dense gas mass of $M_{\text{dense}}(H_2) = \alpha_{\text{HCN}} \, L'_{\text{HCN}} < 4.5 \times 10^{10} \, M_\odot$ assuming $\alpha_{\text{HCN}} = 10 \, M_\odot \, (\text{K km s}^{-1} \, \text{pc}^2)^{-1}$ (Gao & Solomon, 2004). Within the uncertainties in α_{HCN} this is consistent with the gas mass derived from ^{12}CO,

indicating that HCN may be a promising route to constraining the dense gas masses of high-redshift galaxies in the future (Gao et al., 2007), particularly if two or more HCN lines are measured. We also find that the HCN/FIR ratio is consistent with that of local ULIRGs and star-forming galaxies with no evidence for AGN contribution to the FIR luminosity.

- We use the atomic fine-structure and molecular line ratios to investigate the excitation conditions within the ISM, and find that they are similar to those found in local starbursts and ULIRGs. Using a grid of PDR models, we show that the molecular gas in SMM J2135 is exposed to a UV radiation field which is $\sim 1000\times$ more intense than that of the Milky Way, and has a density of $n \sim 10^4\,\mathrm{cm}^{-3}$, both characteristic of the central regions of a typical starburst galaxy. Thus, the inferred density and far-UV radiation field strength of the ISM appear similar to those seen in local ULIRGs consistent with the interpretation of SMGs as the high-redshift analogs of these merger-driven starbursts. However, the spatial extent and mass of the gas reservoir (and spatial extent of the star formation) is larger than typically found in local ULIRGs.

- We find that the ^{12}CO emission shows multiple kinematic components and we decompose the SLEDs into three kinematic components to investigate the excitation variations within the system. We find tentative evidence of temperature variation between the kinematic components, although we defer a detailed discussion of the kinematics to P. Cox et al. (in prep).

- Using a number of approaches we have derived estimates for the effective size of the gas reservoir within this system. All of our estimates are larger than the size of the clumps detected in the 870-μm map from SMA, implying that the gas traces a more extended structure. Overall, our modelling of the ^{12}CO SLED supports the presence of two phases in the ISM, with one phase associated with $\sim$solar metallicity star-forming clumps with $> 100\,\mathrm{pc}$ sizes, embedded in a low metallicity (or high cosmic ray flux), extended component

with a characteristic size of ~1 kpc. However, even the "extended" component has a much higher gas density than typically observed in local starbursts such as M 82 (although a similar density to local ULIRGs such as Arp 220), and is exposed to a UV radiation field which is ~1000× more intense than the Milky Way (Gerin & Phillips, 1998).

- Assuming that the molecular gas is evenly distributed, we show that the integrated properties of the galaxy follow the Kennicutt-Schmidt relation. We also test where the individual star-forming regions would lie if they too followed the Kennicutt-Schmidt relation, and we show that on ~100 pc scales, the gas density would be ~ 30× higher than that inferred from the LVG or PDR analysis. However, the properties of the diffuse gas disk suggest a characteristic density $n \sim 0.2\text{--}1 \times 10^4\,\text{cm}^2$, which is comparable to that inferred from the LVG and PDR models. These results are consistent with a model in which the submillimetre emission predominantly traces the dense cores of the star-forming regions, but that these clumps are simply embedded in a much more extended and diffuse structure which dominates the gas emission. These results may also imply a break-down of the Kennicutt-Schmidt relation on scales of individual GMCs (e.g. $< 100\,\text{pc}$), although clearly only high-resolution millimetre observations will accurately constrain their sizes.

These results show that it is possible to unravel the complex ISM physics within starburst galaxies at high redshift at a level of detail which, until recently has only been possible in the $z < 0.1$ Universe. Our observations provide an unique window into the physics of star-formation at $z \sim 2$ with signal-to-noise that would otherwise require the increased light grasp of the next generation facilities. Indeed this source provides insight into the science that will be routinely possible once ALMA reaches full science operations.

Chapter 4

Optically thin molecular gas tracers in SMM J2135

4.1 Motivation

To understand the rapid star formation rates in SMGs and the build-up of the massive galaxy population at the peak of its formation, it is essential to determine the molecular gas masses of the available gas reservoir. In the previous Chapter we discussed the measurement of the gas mass by applying the conversion factor $\alpha_{\mathrm{CO}} = \mathrm{M_{H_2}}/\mathrm{L'_{^{12}CO(1-0)}}\,\mathrm{M_\odot}\,(\mathrm{K\,km\,s^{-1}\,pc^2})^{-1}$, which converts the ^{12}CO line luminosity to total gas mass ($\mathrm{M_{gas}} \approx \mathrm{M_{H_2}}$). There is considerable uncertainty in this conversion factor which varies widely between different galaxy populations in the local Universe (e.g. Bolatto et al. 2013), and in fact in the previous Chapter we determine a value of $\alpha_{\mathrm{CO}} \sim 2\,\mathrm{M_\odot}\,(\mathrm{K\,km\,s^{-1}\,pc^2})^{-1}$ in the 'Cosmic Eyelash', which is significantly higher than the canonical value used for high-redshift ULIRGs of $\alpha_{\mathrm{CO}} \sim 0.8\,\mathrm{M_\odot}\,(\mathrm{K\,km\,s^{-1}\,pc^2})^{-1}$, which applies to the smoothly distributed, high-pressure, largely molecular ISM measured in local ULIRGs (Downes & Solomon 1998; Solomon & Vanden Bout 2005), thought to be the local analogues of SMGs. Often CO(1–0) observations are not available, therefore higher J_{up} lines (frequently $J_{\mathrm{up}} = 3$) are used which requires the additional constraint of understanding CO

excitation at high redshift. A value of unity is generally assumed for the ratio of ^{12}CO(3–2)/^{12}CO(1–0), however, various studies, such as Harris et al. (2010), have shown that ^{12}CO(1–0) in SMGs may be brighter than predicted, meaning that previous observations of ^{12}CO(3–2) may have underestimated the gas mass. Progress in this field can only be made through measurement of optically thin gas tracers such as ^{13}CO which provides an excellent probe of the column density and can be used to directly determine the mass with an assumption of the relative ^{13}CO-to-H$_2$ abundance ratio. However, these transitions are significantly fainter than those of the optically thick ^{12}CO, with typical [^{12}C]/[^{13}C] ratios of ≥ 40 in local starbursts (i.e. Henkel & Mauersberger 1993). The highly amplified 'Cosmic Eyelash' is therefore an ideal candidate in which to observe ^{13}CO, and combined with the extensive dataset of ^{12}CO transitions described in the previous Chapter, this provides a source capable of breaking the degeneracies of excitation analyses when constrained by ^{12}CO data alone by providing significantly better constraints on the column densities, densities, masses and temperatures of the ISM.

Although the original aim of this work was to measure ^{13}CO, this Chapter describes the simultaneous and surprisingly strong detection of C^{18}O which had further interesting implications for the conditions of the star-forming gas in this high-redshift ULIRG.

This Chapter has been published, as written here, in Danielson et al. (2013), MNRAS, 436, 2793, however, Section 4.3 has been shortened and modified from the published paper. Danielson et al. (2011) is frequently referenced within this Chapter and is the basis of Chapter 3.

4.2   Abstract

We analyse the SLEDs of ^{13}CO and C^{18}O for the $J=1{\rightarrow}0$ up to $J=7{\rightarrow}6$ transitions in the gravitationally lensed ultraluminous infrared galaxy SMM J2135-0102 at $z=2.3$. This is the first detection of ^{13}CO and C^{18}O in a high-redshift star-forming galaxy. These data comprise observations of six transitions taken with

PdBI and we combine these with $\sim 33\,\mathrm{GHz}$ JVLA data and our previous spatially resolved ^{12}CO and continuum emission information to better constrain the properties of the ISM within this system. We study both the velocity-integrated and kinematically-decomposed properties of the galaxy and coupled with a large velocity gradient model we find that the star-forming regions in the system vary in their cold gas properties, in particular in their chemical abundance ratios. We find strong $C^{18}O$ emission both in the velocity-integrated emission and in the two kinematic components at the periphery of the system, where the $C^{18}O$ line flux is equivalent to or higher than the ^{13}CO. We derive an average velocity-integrated flux ratio of ^{13}CO/$C^{18}O \sim 1$ which suggests an abundance ratio of $[^{13}CO]/[C^{18}O]$ which is at least $7\times$ lower than that in the Milky Way. This is suggestive of enhanced $C^{18}O$ abundance, perhaps indicating star formation preferentially biased to high-mass stars. We estimate the relative contribution to the ISM heating from cosmic rays and UV of $(30\text{–}3300)\times 10^{-25}\,\mathrm{erg\,s^{-1}}$ and $45 \times 10^{-25}\,\mathrm{erg\,s^{-1}}$ per H_2 molecule respectively and find them to be comparable to the total cooling rate of $(0.8\text{–}20)\times 10^{-25}\,\mathrm{erg\,s^{-1}}$ from the CO. However, our LVG models indicate high ($>100\,\mathrm{K}$) temperatures and densities ($> 10^3)\,\mathrm{cm^{-3}}$ in the ISM which may suggest that cosmic rays play a more important role than UV heating in this system. If cosmic rays dominate the heating of the ISM, the increased temperature in the star-forming regions may favour the formation of massive stars and so explain the enhanced $C^{18}O$ abundance. This is a potentially important result for a system which may evolve into a local elliptical galaxy.

4.3 Introduction

High critical density isotopologues of ^{12}CO, such as ^{13}CO and $C^{18}O$ can provide more robust measurements of the star-forming gas than the traditionally measured ^{12}CO lines, however, their low abundances mean that they are very difficult to detect at high redshift. Indeed, the only high-redshift detection of ^{13}CO and $C^{18}O$ is from the Cloverleaf quasar (Henkel et al. 2010). However, if detections can be

made in star-forming galaxies, then their strengths and line ratios with respect to other isotopologues will provide a diagnostic of the physical conditions of the ISM. For example, GMCs experiencing strong recent star formation may display elevated $C^{18}O$ and ^{12}CO abundances relative to ^{13}CO, in particular in systems preferentially forming massive stars (i.e. Henkel & Mauersberger 1993; Meier & Turner 2004). As we describe in the previous Chapter, SMM J2135 provides an ideal source in which to attempt to measure these line ratios at high redshift.

In the previous Chapter we obtain very high signal-to-noise (S/N) detections of 11 transitions from three molecular and atomic species (^{12}CO, [CI] and HCN) and limits on a further 20 transitions from nine species in the bright, lensed SMG SMM J2135. The ^{12}CO line profiles show multiple kinematic components with different excitation temperatures. Swinbank et al. (2011) probe the high-resolution kinematics of the system, identifying four dense star-forming clumps (with physical scales of $\sim$100–200 pc) which closely correspond to the kinematic components. These clumps are embedded within a rotationally supported disk, $\sim$ 5 kpc in diameter. Moreover, we show that the cold molecular gas associated with the star formation appears to be exposed to UV radiation fields $10^4\times$ more intense than in the Milky Way and suggest that photon-heating should dominate in the source. However, there have been various studies which have suggested that in galaxies with high SFR densities (and hence high supernova rates), heating due to cosmic rays may play a very significant role in the heating of the H_2 gas (e.g. Goldsmith & Langer 1978; Hailey-Dunsheath et al. 2008; Bradford et al. 2003; Bayet et al. 2011a; Bayet et al. 2011b). In particular, Papadopoulos (2010) demonstrates the importance of cosmic ray heating over photon heating in ULIRGs with high densities and high SFRs. In these systems cosmic rays are capable of penetrating the dense star-forming gas clumps and volumetrically heating the gas, resulting in kinetic temperatures $8-16\times$ higher than in UV-shielded star-forming cores in the ISM of ULIRGs, which in turn can alter the conditions for star formation and thus the characteristic mass of stars.

In this chapter we extend our previous study of SMM J2135 from the ^{12}CO SLED

analysis to include key J_{up} =1–7, ^{13}CO and C^{18}O line emission, using the Plateau de Bure Interferometer (PdBI) and the Karl. G Jansky Very Large Array[1] (JVLA). We use these data to improve the LVG modelling of this system, and hence to determine the likely physical conditions of the cold molecular gas in the ISM. We compare the ^{13}CO and C^{18}O line profiles with the optically-thick ^{12}CO to build a better understanding of the distribution, properties and kinematics of the cold molecular gas in this system. We also estimate the likely heating contributions from cosmic rays and photons in order to determine the dominant heating process.

In Section 4.4 we describe our observations of the molecular emission from SMM J2135. Our observational analysis and results are described in Section 4.5 where we first consider the velocity-integrated (hereafter 'integrated') properties of the system, followed by decomposing the source into previously identified kinematic components and deriving their individual cold molecular gas properties. In Section 4.6, we then use LVG models to further probe the properties of the cold molecular gas. We combine the observational and theoretical findings in Section 4.7 and discuss the possible physical structure and properties of SMM J2135, as well as considering the dominant heating mechanisms in the source. We give our conclusions in Section 4.8. Throughout the chapter we use a ΛCDM cosmology with $H_0 = 72 \, \mathrm{km \, s^{-1} \, Mpc^{-1}}$, $\Omega_m = 0.27$ and $\Omega_\Lambda = 1 - \Omega_m$ (Spergel et al. 2003; Spergel et al. 2007). We apply a lensing amplification correction of a factor of 37.5 ± 4.5 to any luminosities throughout (see Swinbank et al. 2011 for a summary of the gravitational lensing model).

Table 4.1: Line fluxes and flux ratios for integrated and decomposed spectra

Species or line ratio	ν_{rest} (GHz)	Integrated flux (Jy km s^{-1})	Kinematically decomposed flux[a,b,c]		
			Z	Y (Jy km s^{-1})	X
^{13}CO(1–0)	110.2014	< 0.07	< 0.03	< 0.05	< 0.03
^{13}CO(3–2)	330.5880	0.66 ± 0.08	0.11 ± 0.06	0.43 ± 0.09	0.09 ± 0.06
^{13}CO(5–4)	550.9263	0.38 ± 0.14^{e}	< 0.43	0.46 ± 0.07	< 0.21
^{13}CO(7–6)	771.1841	< 0.41	< 0.26	< 0.38	< 0.26
C^{18}O(1–0)	109.7822	< 0.07	< 0.03	< 0.05	< 0.03
C^{18}O(3–2)	329.3305	0.41 ± 0.08	0.16 ± 0.06	0.28 ± 0.09	< 0.16
C^{18}O(5–4)	548.8310	0.87 ± 0.16	0.43 ± 0.08	0.34 ± 0.13	0.21 ± 0.09
C^{18}O(7–6)	768.2514	< 0.41	< 0.26	< 0.38	< 0.26
^{12}CO(1–0)^{d}	115.2712	2.16 ± 0.11	0.56 ± 0.11	1.3 ± 0.2	0.4 ± 0.2
^{12}CO(3–2)^{d}	345.7959	13.20 ± 0.10	3.6 ± 0.6	7.6 ± 1.1	2.3 ± 1.1
^{12}CO(4–3)^{d}	461.0408	17.3 ± 1.2	3.8 ± 0.8	9.9 ± 1.4	4.0 ± 1.4
^{12}CO(5–4)^{d}	576.2679	18.7 ± 0.8	7.2 ± 0.7	7.1 ± 1.3	4.5 ± 1.3
^{12}CO(6–5)^{d}	691.4731	21.5 ± 1.1	8.2 ± 0.9	8.7 ± 1.6	5.1 ± 1.6
^{12}CO(7–6)^{d}	806.6518	12.6 ± 0.6	4.7 ± 0.5	5.9 ± 0.9	1.1 ± 0.9
^{12}CO(8–7)^{d}	921.7997	8.8 ± 0.5	3.2 ± 0.3	3.1 ± 0.6	2.5 ± 0.6
^{12}CO(1–0)/C^{18}O(1–0)	...	> 31	> 19	> 26	> 13
^{12}CO(3–2)/C^{18}O(3–2)	...	32 ± 6	23 ± 9	27 ± 10	> 15
^{12}CO(5–4)/C^{18}O(5–4)	...	21 ± 4	16 ± 4	21 ± 15	21 ± 17
^{12}CO(7–6)/C^{18}O(7–6)	...	> 31	> 18	> 16	> 4
^{12}CO(1–0)/^{13}CO(1–0)	...	> 31	> 19	> 26	> 13
^{12}CO(3–2)/^{13}CO(3–2)	...	20 ± 2	32 ± 17	18 ± 5	25 ± 21
^{12}CO(5–4)/^{13}CO(5–4)	...	49 ± 18	> 17	15 ± 10	> 21
^{12}CO(7–6)/^{13}CO(7–6)	...	> 31	> 18	> 16	> 4
^{13}CO(3–2)/C^{18}O(3–2)	...	1.6 ± 0.4	0.69 ± 0.46	1.5 ± 0.6	> 0.56
^{13}CO(5–4)/C^{18}O(5–4)	...	0.44 ± 0.18	< 1.0	1.3 ± 0.5	< 1.0

[a]We quote 3-σ limits for all lines which are not formally detected.
[b]Uncertainties on fluxes include measurement errors but do not include the flux calibration uncertainties, which we estimate as $\sim 10\%$ at 100 GHz, $\sim 15\%$ at 165 GHz and $\sim 20\%$ at 232 GHz.
[c]The fluxes in Jy km s^{-1} are observed values.

[d]Fluxes are taken from Danielson et al. (2011), shown here for comparison. Flux calibration uncertainties are estimated to contribute an additional $\sim 5\%$ for 30–200GHz and $\sim 10\%$ for 200-300GHz.

[e]The S/N of this line appears to be lower than in the line maps in Fig. 4.1 since the flux is determined by integrating over a FWZI of 900 km s^{-1} for all lines and the ^{13}CO(5–4) line is significantly narrower than the other lines.

4.4 Observations and reduction

4.4.1 Plateau de Bure interferometer observations

We used the six-element IRAM Plateau de Bure Interferometer[2] (PdBI) with the WIDEX correlator to observe the $J_{up}=3$, 5 and 7 transitions of ^{13}CO and C^{18}O, and the continuum at $\sim$100, 165 and 232 GHz respectively. WIDEX is a dual-polarisation correlator with a large bandwidth of 3.6 GHz and a fixed frequency resolution of 2 MHz. Observations were made in the lowest resolution D-configuration between March 25th 2011 and October 15th 2011. The frequency coverage was tuned to the systemic redshift determined from the ^{12}CO $J=1\rightarrow0$ (hereafter ^{12}CO(1–0)) discovery spectrum ($z=2.32591$; Swinbank et al. 2010). We integrated until we reached a noise level of ~ 0.6 mJy per 40 km s^{-1} channel in the 100 GHz and 165 GHz observations and ~ 0.8 mJy per 50 km s^{-1} in the 232 GHz data. The overall flux scale for each observing epoch was set by MWC 349 for a majority of the observations, with additional observations of 2134+004 for phase and amplitude calibrations, due to the presence of a strong radio recombination line in the emission from MWC 349 at 232 GHz. The data were calibrated, mapped and analyzed using the GILDAS[3] software package. During the mapping process natural weighting was applied. For natural weighting, beam sizes and position angles were determined to be $4\overset{''}{.}0 \times 2\overset{''}{.}5$ and P.A. $= 17.0°$, $3\overset{''}{.}4 \times 2\overset{''}{.}8$ and P.A. $= 171.0°$, and $3\overset{''}{.}4 \times 2\overset{''}{.}1$ and P.A. $= 2.3°$, for the 100 GHz, 165 GHz and 232 GHz data respectively.

We show in Fig. 4.1 the S/N maps for the ^{13}CO and C^{18}O observations. The continuum maps are produced by measuring the median over the off-line continuum in every spatial pixel and dividing it by the standard deviation of the continuum in the same frequency range. To create the line maps, we fit the continuum with a low order polynomial in every spatial pixel and subtract it from the cube, we then

---

[1]The National Radio Astronomy Observatory is a facility of the National Science Foundation operated under cooperative agreement by Associated Universities, Inc.

[2]Based on observations carried out with the IRAM Plateau de Bure Interferometer under programme u0b6. IRAM is supported by INSU/CNRS (France), MPG (Germany) and IGN (Spain).

[3]http://www.iram.fr/IRAMFR/GILDAS/

produce a collapsed image over the full width at zero intensity (FWZI) frequency range of the line (see below). We then produce S/N maps from this by dividing the signal by the product of the standard deviation of the continuum and the square root of the number of frequency channels in the line. In Fig. 4.2 we show the spectra of ^{13}CO and C^{18}O. The 1-D spectra are produced by integrating within an aperture around the full extent of the emission region in the cleaned cube. We note that the S/N maps and spectra of ^{13}CO and C^{18}O shown in Fig. 4.1 and Fig. 4.2 are continuum-subtracted.

Inspection of the velocity-integrated data cubes (Fig. 4.1) shows strong detections (S/N∼4–8) for ^{13}CO(3–2), ^{13}CO(5–4), C^{18}O(3–2) and C^{18}O(5–4), although we only detect continuum at 232 GHz (i.e. no ^{13}CO(7–6) or C^{18}O(7–6) detections). Since the spectra are clearly highly structured (see also Danielson et al. 2011) we do not fit a single Gaussian to determine the integrated flux but instead we integrate the spectra in the velocity range of -350 to $+550\,\mathrm{km\,s^{-1}}$ (the FWZI of the ^{12}CO composite line in Danielson et al. 2011; see Fig. 4.3). We note that since some of the line profiles are narrower than others, the S/N of the integrated flux value may appear low due to integrating over the same FWZI for all lines which may not be appropriate for i.e. the narrow ^{13}CO(5–4) line. For the undetected lines of ^{13}CO(7–6) and C^{18}O(7–6) we determine a $3\,\sigma$ upper limit on the fluxes by assuming a linewidth typical of the average linewidth of the detected lines for the same species ($900\,\mathrm{km\,s^{-1}}$). In Table 4.1 we provide line fluxes (with associated measurement uncertainties) or limits for the various species and we include the ^{12}CO data from Danielson et al. (2011) for completeness. We estimate additional flux calibration uncertainties of 10% at 100 GHz, 15% at 165 GHz and 20% at 232 GHz, which are taken into account in all analyses on the spectral lines but not included in the tabulated flux and error values.

4.4.2 JVLA observations

SMM J2135 was observed with the JVLA in D-configuration between September and December 2011. The Ka receiver was tuned to 33.13 GHz, covering both the ^{13}CO(1–0) and C^{18}O(1–0) lines. Standard amplitude, phase, and bandpass calibration procedures were used. While we wanted to set up our observations with a scan-averaging time of 1 second, NRAO staff instructed us to use a scan-averaging time of 3 seconds. A bug in the observing software resulted in all the integration time after the first second of every scan being discarded. Thus two thirds of the data were lost. As a result the JVLA spectrum is shallow (containing only 5 hours of integration time) and only provides upper limits on the ^{13}CO(1–0) and C^{18}O(1–0) emission. However, we still use these upper limits as constraints for the modelling in Section 4.6.
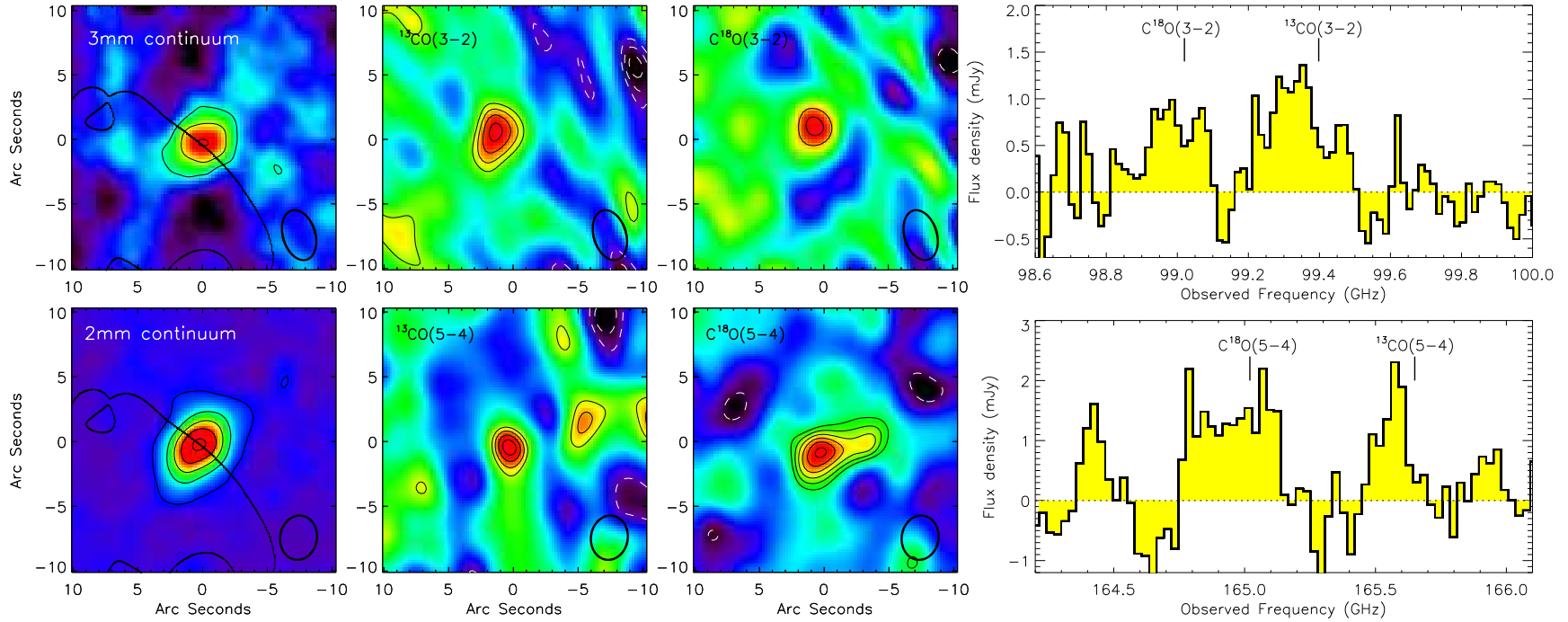
Figure 4.1: *Left and centre*: Signal-to-noise maps of the continuum and the transitions of $J_{\rm up} = 3$ and $J_{\rm up} = 5$ ^{13}CO and C^{18}O line emission, where the latter two are extracted over the frequency extent of the emission lines. The contours on the continuum maps represent 5, 10, 15σ for the 100 GHz (3 mm) data and 5, 25, 45σ for the 165 GHz (2 mm) data. The black curve through the continuum maps represents the critical curve from the gravitational lensing model (Swinbank et al., 2011). The contours on the line maps represent 3, 4, 5, 6σ etc. The line maps have been continuum-subtracted and then slightly smoothed for display purposes. These maps demonstrate that we have significant detections of the continuum and the $J_{\rm up} = 3$ and $J_{\rm up} = 5$ transitions in SMM J2135 and furthermore that the structure and extent of the emission varies between the different transitions. *Right*: The continuum-subtracted spectra (output from GILDAS) for the $J_{\rm up} = 3$ and $J_{\rm up} = 5$ transitions. The expected central frequencies of the transitions for the heliocentric redshift of $z = 2.32591$ are labelled with solid lines. The fluxes given in Table 4.1 have been determined by integrating the spectra in the velocity range of -350 to $+550$ km s^{-1} (the FWZI of the ^{12}CO lines in Danielson et al. 2011). The channel widths are 50 km s^{-1} for both spectra shown.

4.5 Analysis and results

We have observed four transitions from ^{13}CO and C^{18}O and detect both these species in their $J_{\mathrm{up}} = 3$ and $J_{\mathrm{up}} = 5$ transition and place sensitive limits on their $J_{\mathrm{up}} = 1$ and $J_{\mathrm{up}} = 7$ emission. We combine this information with the previous work of Danielson et al. (2011) to give a combined dataset with 11 detections and four limits on ^{12}CO, ^{13}CO and C^{18}O. This is a unique and unprecedented dataset for a high-redshift galaxy and allows us to probe the densities, temperatures and chemical abundances within the ISM of this starburst galaxy.

To compare the line profiles between the isotopologues of ^{12}CO and ^{13}CO, in Fig. 4.2 we overlay the corresponding ^{12}CO transition on the ^{13}CO spectra, normalised by their peak fluxes. It is clear that the different species exhibit very different line profiles and that there are multiple velocity components detected through ^{13}CO and C^{18}O. These differences are particularly prominent in $J_{\mathrm{up}} = 5$ in both ^{13}CO and C^{18}O where ^{13}CO(5–4) is significantly narrower than both the C^{18}O(5–4) and the ^{12}CO lines. Furthermore, as Fig. 4.1 shows, C^{18}O(5–4) appears to be spatially extended along the same direction as the high-resolution ^{12}CO maps (Swinbank et al. 2011) unlike the other lines which are more compact in their spatial distribution.
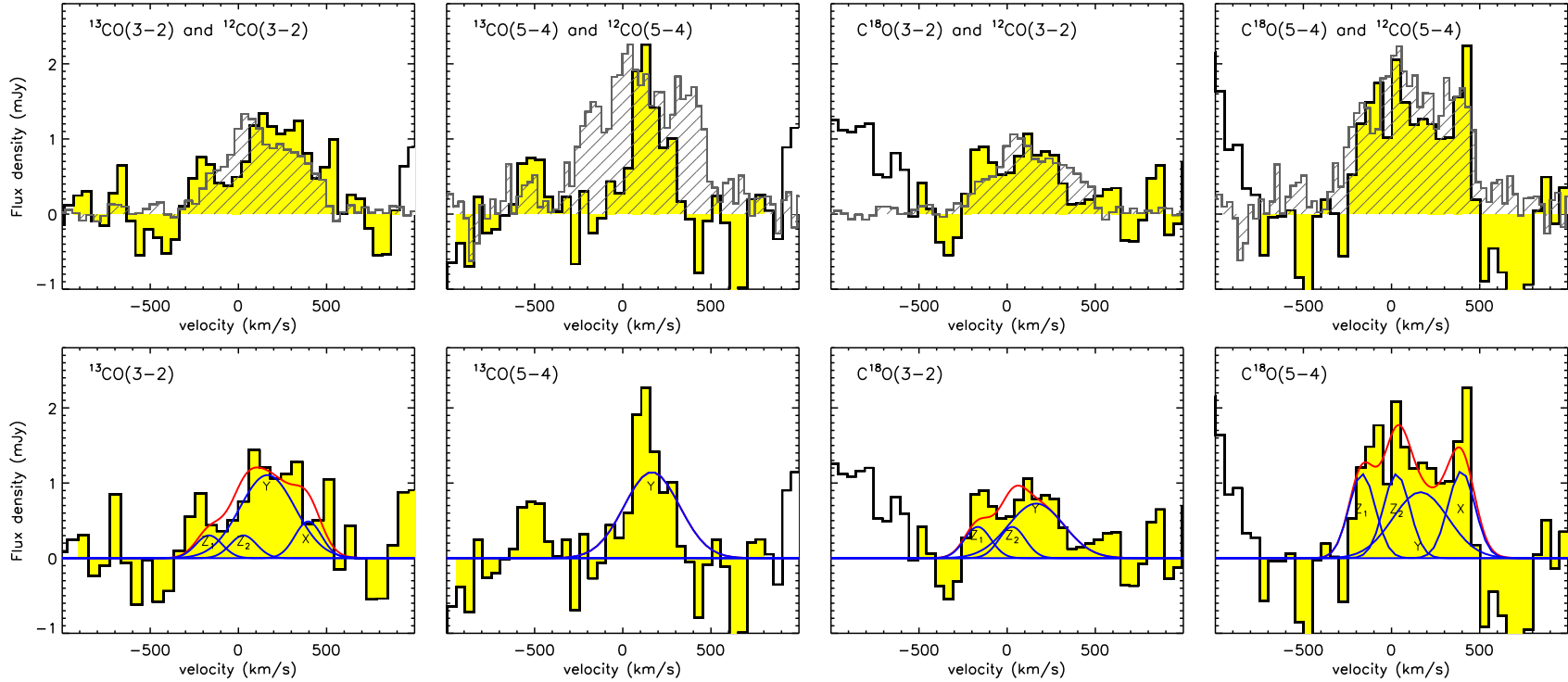
Figure 4.2: *Top row*: Continuum-subtracted spectra for the individual transitions (filled histograms) plotted to compare the line profiles of the ^{13}CO and C^{18}O. Overlaid on each is the spectrum for the respective ^{12}CO transition (normalised by peak flux) to compare the velocity structure (hatched region). *Bottom row*: The spectra for all lines, with the three-component kinematic model with components X, Y, Z, taken from the Danielson et al. (2011) fit to each line (see Section 4.5.2 and Fig. 4.3). The channel widths are $50\,\text{km}\,\text{s}^{-1}$ for the ^{13}CO and C^{18}O but $40\,\text{km}\,\text{s}^{-1}$ and $30\,\text{km}\,\text{s}^{-1}$ for the ^{12}CO(3–2) and (5–4) respectively. In each case, the continuum was fitted with a low-order polynomial and subtracted from the one-dimensional spectrum output by GILDAS. It is clear that the line profiles differ strongly between the different species. This is likely to be due to a combination of factors, potentially including differences in optical depth and abundance. The three-component kinematic fit to the spectra demonstrates that the different transitions are dominated by different kinematic components, i.e. only the Y-component is required to fit the ^{13}CO(5–4) line.

Considering the unusual profiles, large integrated flux and spatial extent of the $C^{18}O(5\text{–}4)$ we test the validity of these data by splitting the sample into two independent datasets of half the exposure time and measure the integrated flux in each half of the data. The S/N in each half of the data is obviously lower than that of the total sample but we find the $C^{18}O(5\text{–}4)$ fluxes to be 0.82 ± 0.20 and 0.83 ± 0.25 which are consistent with each other and with the total flux of 0.87 ± 0.16. Furthermore, we find that both the spatial extent and the line profile persist in both samples.

Figs. 4.2 and 4.4 clearly show the presence of multiple kinematic components with different ^{13}CO and $C^{18}O$ line strengths. In Danielson et al. (2011) we kinematically decompose the ^{12}CO emission line spectra in SMM J2135 into multiple velocity components (i.e. Fig. 4.3). In Section 4.5.2 we fit this same model to the ^{13}CO and $C^{18}O$ lines and discuss the kinematically decomposed properties of SMM J2135. However, before attempting to disentangle the internal variations of the ISM conditions within this system, we analyse the integrated properties of the galaxy and attempt to draw some broad conclusions, providing a comparison to our subsequent kinematically-resolved analysis.

4.5.1 Integrated properties

Integrated line ratios

Fig. 4.4 shows the integrated flux ratios of $^{12}CO/^{13}CO$ and $^{12}CO/C^{18}O$ for SMM J2135. These flux ratios can be used as estimates of the abundance ratios but only if the molecules have the same excitation properties and all lines are optically thin (both of which- as we see later- are unlikely to be true). We compare the integrated flux ratios in SMM J2135 with those of star-forming galaxies and ULIRGs in the nearby Universe. Given that line ratios vary with the transition observed, in order to be consistent, we must compare ratios in $J_{up} = 3$ with literature ratios in $J_{up} = 3$. Published measurements of extragalactic $C^{18}O$ ($J_{up} > 1$) emission are rare and for star-forming galaxies we only have this information for the local starburst galaxy M 82 which Petitpas & Wilson (2000) mapped in $J_{up} = 3$ for ^{12}CO, ^{13}CO and $C^{18}O$,
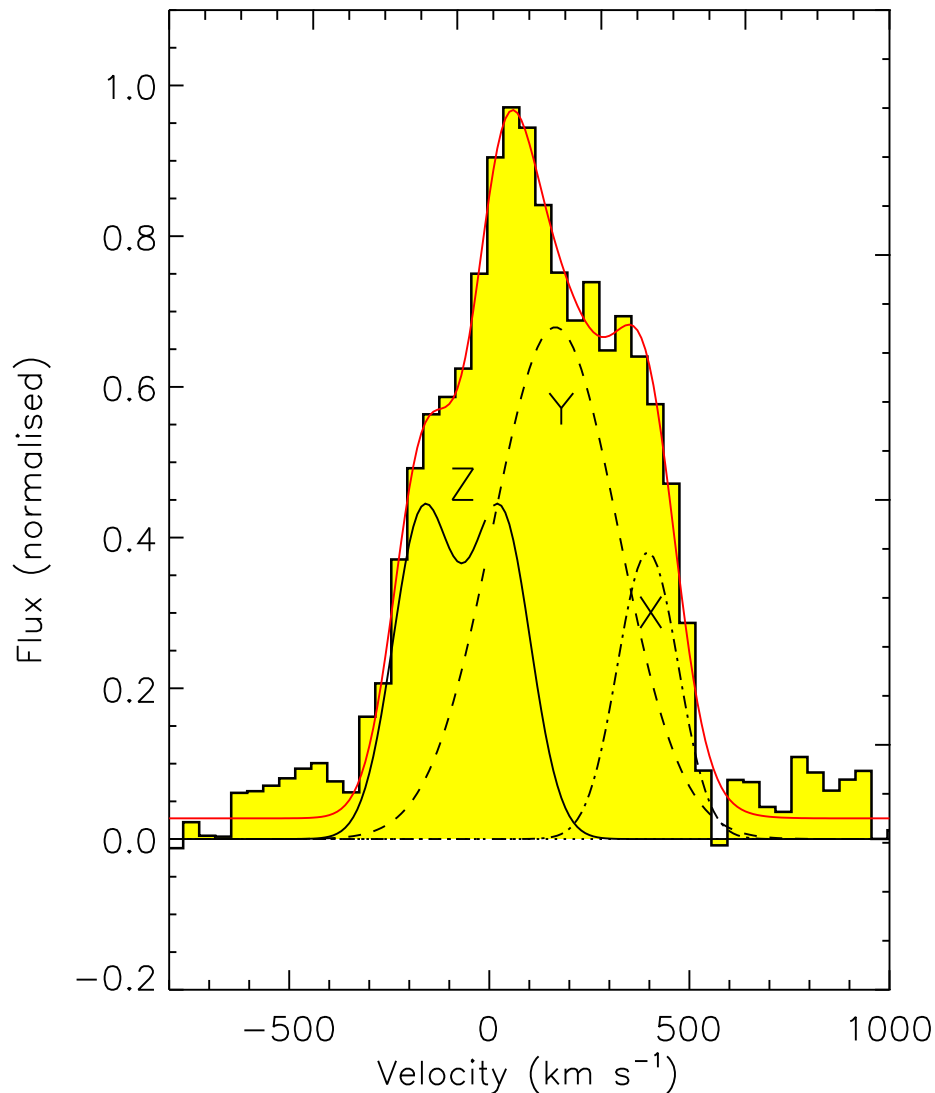
Figure 4.3: A composite spectrum of the ^{12}CO spectra of SMM J2135 from $J_{\mathrm{up}} = 1 - 8$, normalised by the peak flux, taken from Danielson et al. (2011). This composite is used to define a FWZI range over which to sum the total flux (-350 to $550\,\mathrm{km\,s^{-1}}$). Furthermore, utilising the high signal-to-noise of the ^{12}CO emission lines, this composite spectrum is used (in Danielson et al. 2011) to fit and determine the three-component (X, Y and the double-peaked Z) kinematic model plus continuum that we apply to our ^{13}CO and C^{18}O emission lines in this work.

from which we quote the line ratios from the central position in the galaxy, and for the central $23''$ of the starburst NGC 253 from Harrison et al. (1999). In Fig. 4.4 we also include the measured line ratios in $J_{up} = 5$ and $J_{up} = 7$ in SMM J2135, for completeness. There is a much more extensive galaxy sample available for ^{13}CO and C^{18}O in the $J_{up} = 1$ transition, therefore we also use our limits on $J_{up} = 1$ in order to compare our data more directly to other galaxies. For the literature line ratios of ^{12}CO(1–0)/^{13}CO(1–0) and ^{12}CO(1–0)/C^{18}O(1–0) we use Tan et al. (2011).

Our ^{12}CO/^{13}CO integrated flux ratios for SMM J2135 are $\sim 20 \pm 2$ and > 31 in $J_{up} = 3$ and $J_{up} = 1$ respectively, both of which are higher than local star-forming galaxies and ULIRGs. For example, in M 82 (Fig. 4.4) lower values of ^{12}CO(3–2)/^{13}CO(3–2) $= 12.6 \pm 1.5$ (Petitpas & Wilson 2000) and ^{12}CO(1–0)/^{13}CO(1–0) $= 19.8 \pm 8.17$ (Tan et al. 2011) are found. Furthermore, our integrated ^{12}CO(1–0)/^{13}CO(1–0) ratio lies above that for local infrared luminous sources from Tan et al. (2011). Only Arp 220 has a comparably large value of ^{12}CO(1–0)/^{13}CO(1–0) $\sim 50 \pm 30$.

There are many potential explanations for the observed elevated ^{12}CO/^{13}CO flux ratios: i) Turbulence due to mergers or winds can cause the ^{12}CO line to broaden, thus decreasing the optical depth (τ) of the line and increasing the ^{12}CO/^{13}CO intensity ratio without the need for a change in the relative abundances of the isotopologues (Aalto et al., 1995); ii) In UV radiation-dominated photodissociation regions on the surfaces of molecular clouds, ^{12}CO, with its higher optical depth, more effectively self-shields than ^{13}CO (and C^{18}O), thus ^{13}CO is more easily photodissociated than ^{12}CO, resulting in an elevated ^{12}CO/^{13}CO ratio. Similarly, C^{18}O is more easily photodissociated than ^{13}CO resulting in a higher ^{13}CO/C^{18}O ratio (Bally & Langer, 1982); iii) As ^{13}C is a secondary product from a later stage of nuclear processing than ^{12}C, age can play a role in determining the ^{12}CO/^{13}CO ratio, such that in systems with many newly forming stars ^{12}CO/^{13}CO can be much higher than in older systems where there has been enough time to synthesise ^{13}C (Henkel et al. 2010). Thus, there is a trend of increasing ^{12}CO/^{13}CO with decreasing metallicity, i.e. ULIRGs, which are characterised by lower metallicity, typically

exhibit higher ^{12}C/^{13}C ratios (Casoli et al. 1992a; Henkel et al. 1993, 1998; Meier & Turner 2004 Genzel et al. 2012); iv) Casoli et al. (1992b) find that the ^{12}CO/^{13}CO can be enhanced in regions of recent bursts of star formation, particularly of massive stars, as ^{12}C is overproduced by nucleosynthesis relative to ^{13}C leading to an overabundance of ^{12}CO; v) Similarly, infall of unprocessed gas from the disk into the nuclear region(s) of starbursts may lead to enhanced ^{12}CO/^{13}CO ratios; vi) Finally, chemical fractionation may also affect the observed ^{12}CO/^{13}CO ratio, i.e.

$$^{13}\text{C}^+ + {}^{12}\text{CO} \rightarrow {}^{12}\text{C}^+ + {}^{13}\text{CO} + \Delta\text{E}_{35\text{K}}, \qquad (4.5.1)$$
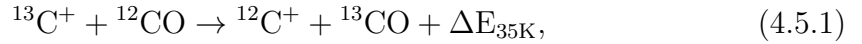
(Watson et al., 1976), which enhances ^{13}CO relative to ^{12}CO leading to a lower value for ^{12}CO/^{13}CO.

In contrast to the elevated ^{12}CO/^{13}CO flux ratio, as Fig. 4.4 shows, SMM J2135 appears to have a lower ^{12}CO/C^{18}O flux ratio than local infrared luminous galaxies. This implies either a deficiency in ^{12}CO or, more likely, enhanced C^{18}O. However, there are a few local systems which display similar characteristics. For example, Meier & Turner (2001) find very low ^{12}CO/C^{18}O integrated intensity ratios in the centre of the star-forming galaxy IC 342 (^{12}CO(1–0)/C^{18}O(1–0) = 24±7 in the central trough compared to > 110 in the off-arm regions), suggesting a very high abundance of C^{18}O relative to ^{12}CO in the star-forming regions. The mechanism for ^{18}O synthesis is not well understood, however, a high abundance of C^{18}O is thought to be due to the enrichment of C^{18}O from ^{18}O rich, massive star ejecta and winds (i.e. Henkel & Mauersberger 1993; Meier & Turner 2001). Indeed, since ^{18}O is a secondary product produced in massive stars during He-burning by ^{14}N^{18}O, an overabundance of C^{18}O in systems which are preferentially producing massive stars may be expected (e.g. due to initial mass function (IMF) variations; Henkel & Mauersberger 1993). However, it is interesting to note that initial nitrogen abundances and therefore metallicities would have to be almost solar to facilitate the production of such large quantities of ^{18}O, which would be unusual at $z = 2.3$[4].

---

[4]Using the mass-metallicity relation for $z \sim 1.5$ galaxies from Stott et al. (2013), we estimate a

It is also interesting to note that Papadopoulos et al. (1996) find a relatively low average line ratio of ^{13}CO/C^{18}O $= 3.3$ in NGC 1068 for $J_{\mathrm{up}} = 1$ and infer that this is either due to an intrinsically low [^{13}CO]/[C^{18}O] abundance ratio or optical depth effects (even though both ^{13}CO and C^{18}O are generally considered to be optically thin tracers). Similarly, in Arp 220, the line ratio ^{13}CO(1–0)/C^{18}O(1–0) is found to be only 1.0 ± 0.3 (Greve et al., 2009).

Thus, our integrated flux ratios of ^{13}CO(3–2)/C^{18}O(3–2) $= 1.6 \pm 0.4$ and ^{13}CO(5–4)/C^{18}O(5–4) $= 0.44 \pm 0.18$ in SMM J2135 are unusually low compared to those found in local starbursts and ULIRGs. This is likely to imply an enhanced abundance of C^{18}O. Fig. 4.4 demonstrates the abnormality of SMM J2135, particularly with regard to low ^{12}CO/C^{18}O ratios, further emphasising the possibility of a high abundance of C^{18}O implied by the unusually low ^{13}CO/C^{18}O line ratios.

4.5.2 Kinematically resolved properties

Kinematically resolved model

Using high-resolution mapping, Swinbank et al. (2011) demonstrated that the velocity structure in SMM J2135 coincides with the clumpy structure in the disk. Hence the ~100–200 pc star-forming clumps observed in the Smithsonian Submillimeter Array (SMA) rest-frame 260 μm map coincide with the clumps observed in the cold molecular gas and these in turn correspond with the kinematic components in the high resolution ^{12}CO spectra (Swinbank et al. 2011).

To decompose the ^{13}CO and C^{18}O lines into multiple kinematic components, we adopt the kinematic model derived from Danielson et al. (2011). This comprises three Gaussian components: X, Y and Z, where the latter is a coupled double Gaussian. This model provides a reasonable approximation of the observed line profiles (Fig. 4.3). To be consistent with the ^{12}CO analysis, we fix the central velocities and linewidths of the components X, Y and Z to the values derived using ^{12}CO but

---

metallicity for SMM J2135 of $\sim 0.3 Z_\odot$
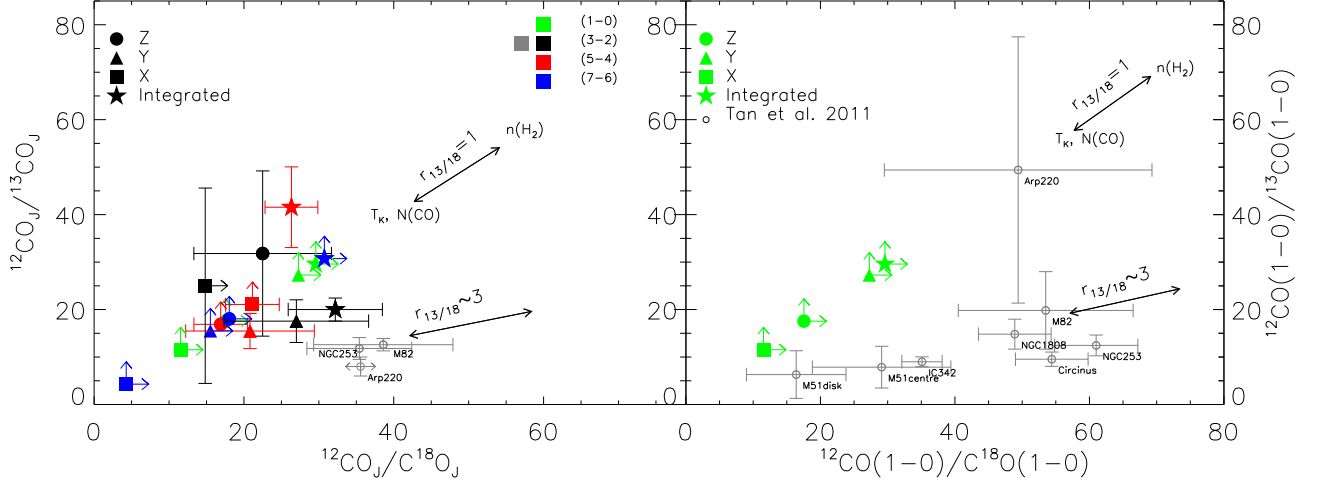
Figure 4.4: *Left:* Flux ratios of ^{12}CO/^{13}CO versus ^{12}CO/C^{18}O for the integrated emission from SMM J2135 for the different transitions available. We also plot the individual components of the three-component kinematic model. For comparison we show the flux ratios of the star-forming systems Arp 220 (Greve et al. 2009), M 82 (Petitpas & Wilson 2000) and NGC 253 (Harrison et al. 1999). The literature values are ratios using the $J_{\rm up} = 3$ transition in order to compare directly to our data, however, C^{18}O(3–2) fluxes are only published for M 82 and NGC 253, therefore for Arp 220, ^{12}CO(3–2)/C^{18}O(3–2) is determined by multiplying the known ratio in $J_{\rm up} = 1$ by the ratio of $(^{12}$CO(3–2)/C^{18}O(3–2))/$(^{12}$CO(1–0)/C^{18}O(1–0)) ~ 0.72 for M 82. Since the estimate for ^{12}CO(3–2)/C^{18}O(3–2) in Arp 220 is a derived value we do not give a horizontal error bar but note that there is large uncertainty in this estimate. Our integrated ^{12}CO/C^{18}O flux ratio is consistent with that for M 82, whereas our ^{12}CO/^{13}CO is higher than that for M 82. The vectors demonstrate the effect on the line ratios of varying the temperature ($T_{\rm K}$), density ($n(\rm H_2)$) and column density ($N(^{12}$CO)) in the LVG models described in Section 4.6 whilst fixing the other parameters in the models at their best-fit values. Increasing the temperature and column density causes a decrease in the line ratios, whereas, increasing the density causes an increase in the line ratios. $r_{13/18}$ is defined as $N(^{13}$CO)/$N(\rm C^{18}$CO) and we include a vector for a lower column density ratio to demonstrate the effect of decreasing the abundance ratio (see Section 4.6.4 for details). The different kinematic components appear to fit with different ratios of $r_{13/18} = 1 - 10$, implying that the ISM conditions may vary between the components. *Right:* We also show our 3σ lower limits from JVLA for the (1–0) emission in order to compare to a broader range of literature data (Tan et al. 2011). Our data lies at higher ^{12}CO(1–0)/^{13}CO(1–0) than local bright infrared galaxies, with the lower limits on ^{12}CO(1–0)/C^{18}O(1–0) being lower than the lower limits of the local galaxy ratios, implying potentially lower than average ^{13}CO and higher than average C^{18}O (assuming ^{12}CO is optically thick in all cases). This could be a genuine abundance effect.

Table 4.2: Kinematically decomposed model fit parameters

Component	v	σ
	$(\mathrm{km\,s}^{-1})$	$(\mathrm{km\,s}^{-1})$
Z_2	-167 ± 9	75 ± 8
Z_1	28 ± 9	75 ± 8
Y	165 ± 13	157 ± 17
X	396 ± 9	76 ± 9

Note: Velocities given with respect to the heliocentric redshift of $z = 2.32591$

allow the intensities to vary when fitting to the new observations (see Table 4.2). However, as in Danielson et al. (2011) the intensities of the double Gaussian describing component Z are tied to be equal. We show this three-component model in Fig. 4.3. The central velocities of the components are $396\,\mathrm{km\,s}^{-1}$, $165\,\mathrm{km\,s}^{-1}$, $-70\,\mathrm{km\,s}^{-1}$ for the X, Y and Z components respectively. The best fit models for ^{13}CO and C^{18}O are overlaid in Fig. 4.2 and fluxes (and associated errors) derived from the individual components are listed in Table 4.1. The ^{13}CO and C^{18}O lines are much fainter (typically $\sim 20 - 40\times$ lower) than the ^{12}CO and hence the detections have lower S/N than the previous ^{12}CO decomposition. As a result, there are degeneracies in fitting the three-component model to some of the lines, however, this approach provides a useful means of consistently comparing the data with our previous ^{12}CO decomposition. Some of the components are undetected in certain transitions and we have strong variations in the line ratios between components (see Table 4.1 and Fig. 4.4) and in Section 4.6 we attempt to model these.

There is a moderate amplification gradient across the source, causing the X-component fluxes to appear fainter than the Z-component. This is demonstrated in Swinbank et al. (2011) where the amplification increases across the source from $\sim 20 - 50$ from the X-component to Z-component. However, our kinematic decomposition is not influenced by the differential magnification as the velocities map uniquely to spatial positions in the lens plane and thus to a single magnification factor.
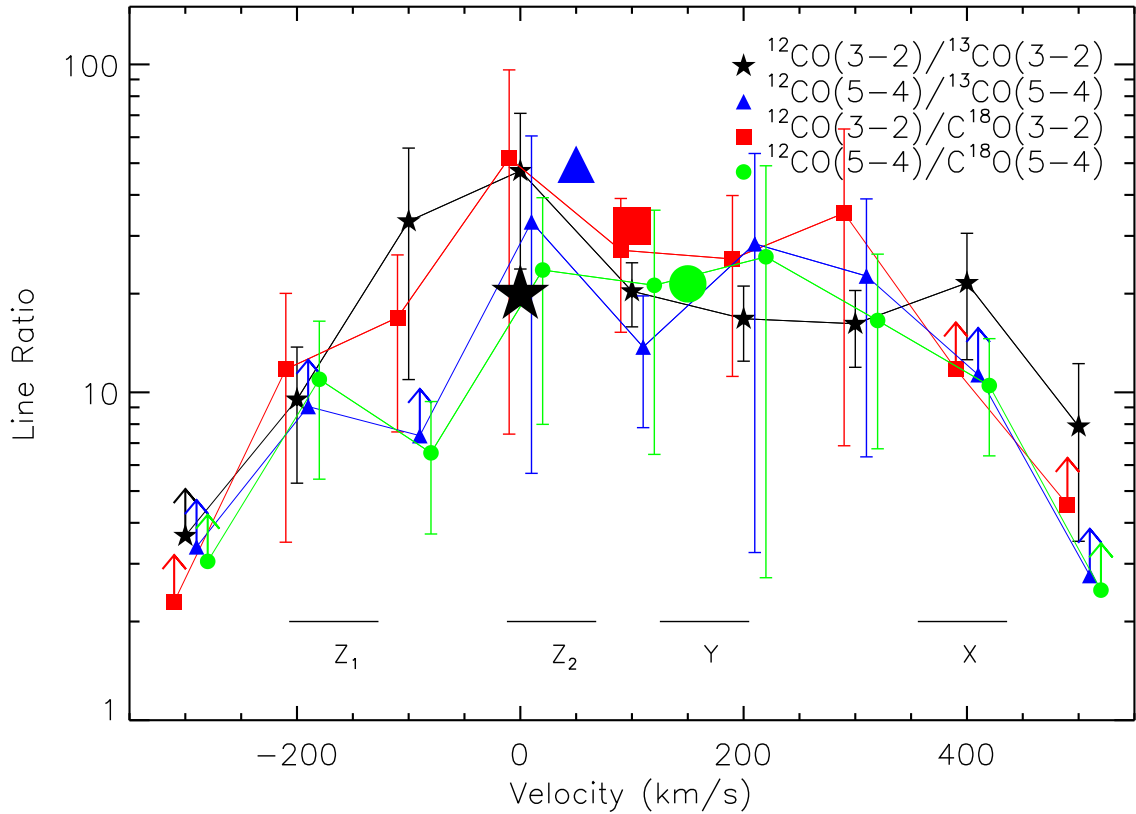
Figure 4.5: The variation of the estimated line ratios as a function of velocity across the spectral lines of ^{12}CO, ^{13}CO and C^{18}O in the $J_{\rm up} = 3$ and 5 transitions. We have re-binned the spectra into channels of $100\,\mathrm{km\,s^{-1}}$ and offset the data sets by $10\,\mathrm{km\,s^{-1}}$ from each other for clarity. The errors are determined from the standard deviation of the off-line $100\,\mathrm{km\,s^{-1}}$ channels. Lower limits at the edges are due to the ^{13}CO and C^{18}O having a narrower FWZI than the ^{12}CO. These are $3\,\sigma$ lower limits. We indicate the velocity centres of the main kinematic components. Overall there is no strong trend with velocity. The integrated line ratios over the FWZI of $900\,\mathrm{km\,s^{-1}}$ of each line are shown as larger filled symbols placed arbitrarily at 0, 50, 100 and $150\,\mathrm{km\,s^{-1}}$. They are broadly consistent with each other for all transitions.

It is clear from Fig. 4.2 that the line profiles of ^{12}CO, ^{13}CO and C^{18}O display strong variation in the ^{12}CO/^{13}CO and ^{12}CO/C^{18}O with velocity, possibly tracing variation in the optical depth of ^{13}CO and C^{18}O or abundance variations. To directly compare the lines, we re-bin the ^{12}CO, ^{13}CO and C^{18}O spectra in $J_{up} = 3$ and 5 to $100\,\text{km}\,\text{s}^{-1}$ channels and in Fig. 4.5 we plot the variation of these line ratios with velocity over the $\sim 900\,\text{km}\,\text{s}^{-1}$ FWZI of the ^{12}CO. We calculate the ratio of the flux density in each channel $(S_\nu(12)/S_\nu(i))$, where S_ν is the flux density in mJy and i refers to either ^{13}CO or C^{18}O. In Fig. 4.5 we show horizontal bars indicating the central velocity of the individual kinematic components. We see little measurable difference between the line ratios as a function of velocity however, there is an overall trend that the line ratios are higher towards the kinematic centre (Y) of the source than at the edges.

As shown by Fig. 4.4 (see also Table 4.1) the ^{12}CO/^{13}CO, ^{12}CO/C^{18}O and ^{13}CO/C^{18}O line ratios of the individual kinematic components (X, Y, Z) in $J_{up} = 3$ and 5 are all within 1σ of the galaxy-integrated values, aside from the ^{12}CO(5–4)/^{13}CO(5–4) and ^{13}CO(5–4)/C^{18}O(5–4) which are significantly different. This is mainly due to the ^{13}CO(5–4) line being significantly narrower than the other lines and hence in Fig. 4.2 only the Y-component is required to fit the line.

In Fig. 4.4, we also show vectors which demonstrate the effect of varying the abundance ratio of $N(^{13}\text{CO})/N(\text{C}^{18}\text{O})$ (r_{13}/r_{18}; see Section 4.6.4 for details). It appears that the integrated source, X- and Z-components follow the trend of the vector corresponding to $N(^{13}\text{CO})/N(\text{C}^{18}\text{O}) = 1$, whereas the different transitions of the Y component are better fit with a higher abundance closer to $N(^{13}\text{CO})/N(\text{C}^{18}\text{O}) \sim 3$ which may imply that the ISM conditions vary between the components.

In all components we find up to $\sim 10\times$ lower ^{13}CO/C^{18}O flux ratios than the typical value of $[^{13}\text{CO}]/[\text{C}^{18}\text{O}] \sim 4$ (Wang et al. 2004) found in local star-forming galaxies. This is similar to Arp 220, which exhibits low line ratios of ^{13}CO/C^{18}O ~ 1 at its centre in both $J_{up} = 1$ and 2 (Matsushita et al. 2009; Greve et al. 2009), attributed to a high abundance of C^{18}O arising from a recent starburst. As noted earlier, lower than expected abundance ratios may result from ^{18}O enriched gas

being ejected from high mass stars. Thus it may imply a bias towards high mass star formation. The ^{12}C/^{13}C abundance ratio is not affected as much since ^{13}C arises from later stages of lower-mass star formation.

4.6 LVG modelling

Whilst the comparison of line ratios of different isotopologues is useful, the degeneracies between density, temperature, optical depth and abundance mean that to better constrain the physical properties of the ISM we need to model the spectral line energy distributions (SLEDs). In this section we investigate both the galaxy-integrated properties and the kinematically-resolved component properties to better understand the ISM in this system.

4.6.1 Model description

In Danielson et al. (2011) we analysed the ^{12}CO SLED to attempt to constrain the physical conditions of the molecular gas in SMM J2135, through large velocity gradient (LVG) modelling (Weiß et al. 2005b). Here we can include in our analysis the lower abundance ^{13}CO and C^{18}O SLEDs in order to better determine the ISM conditions. We therefore use the non-LTE radiative transfer code, RADEX, developed by van der Tak et al. (2007), to model the SLEDs and determine the likely physical conditions within SMM J2135 using our complete ^{12}CO, ^{13}CO and C^{18}O SLEDs. We first apply this analysis to the integrated SLEDs, but then motivated by the strong line ratio differences seen within this source (Section 4.5.2; Figs. 4.2, 4.4 and 4.5) we apply the same approach to the kinematically decomposed SLEDs.

Briefly, RADEX solves the radiative transfer equations by assuming an isothermal and homogeneous medium without large-scale velocity fields and assuming a certain geometry to describe the photon escape probabilities. Three different geometries are available but we choose the model mimicking a uniform expanding sphere (LVG approximation), giving a corresponding escape probability formalism of $\beta_{LVG} = (1 - e^{-\tau})/\tau$ (e.g. Goldreich & Kwan 1974). In the model, the equations of statistical

equilibrium are iteratively solved, beginning by assuming low τ (optically thin) for all emission lines. To derive the physical parameters using this model, molecular collisional rates are required. We used collisional rates from the Leiden Atomic and Molecular Database (LAMDA)[5] as recommended in van der Tak et al. (2007). We assume H_2-CO collisional excitation rates from Flower (2001) and a cosmic microwave background (CMB) temperature of $\sim 9\,\mathrm{K}$ (2.73 K redshifted to $z = 2.3$).

The main input variables in the LVG model we use are: the column density $N(X)$ of the species (X) considered (^{12}CO, ^{13}CO or C^{18}O) in cm^{-2}, the line width (FWHM) ΔV for each transition in km s^{-1}, the molecular hydrogen volume gas density $n(H_2)$ in cm^{-3}, the kinetic temperature T_K in K, and the abundance ratios (i.e. ^{12}C/^{13}C). These variables must either be fixed or fitted for and are described below. In the following we describe our method for deriving the best model parameters from our LVG model.

4.6.2 Input parameter selection

In order to select a suitable velocity gradient (ΔV) we require constraints on the size and structure of the source. From previous work (Swinbank et al. 2010, 2011; Danielson et al. 2011), SMM J2135 appears to comprise at least four 100–200 pc star-forming clumps embedded in a rotating gas disk with a diameter of $\sim 5\,\mathrm{kpc}$. We initially take the average full width at half maximum (FWHM) of the disk emission ($\sim 500\,\mathrm{km\,s^{-1}}$) as an estimate of the average velocity field that the gas in the system is experiencing (ΔV). The model outputs velocity-integrated line intensities by multiplying the model-estimated radiation temperature by $1.06 \times \Delta V$ (assuming a Gaussian profile). This initial method is crude given that it assumes uniform excitation conditions throughout the entire source, which given the clear structure in the line profiles is unphysical, however, it is useful to first determine the average molecular gas properties. For each of the species ^{12}CO, ^{13}CO and C^{18}O, we carry out simulations and produce model grids with RADEX for the following

---

[5]http://www.strw.leidenuniv.nl/~moldata/

parameter ranges: kinetic temperature ranging between $T_K = 10 - 200\,\mathrm{K}$ in $10\,\mathrm{K}$ steps; gas density ranging between $n(\mathrm{H_2}) = 10^3 - 10^7 \mathrm{cm}^{-3}$ in $0.5\,\mathrm{dex}$ steps and molecular line column densities $N(^{12}\mathrm{CO},\,^{13}\mathrm{CO},\,\mathrm{C^{18}O}) = 10^{10} - 10^{20} \mathrm{cm}^{-2}$ in intervals of $0.5\,\mathrm{dex}$. See Bayet et al. (2013) for the choice of input parameters and ranges and for a more complete description of the RADEX model we implement.

4.6.3 Model outputs

In an ideal situation, where all lines are optically thin, we could make the assumption that the integrated line intensity ratio of $^{12}\mathrm{CO}/^{13}\mathrm{CO}$ is equivalent to the ratio of the column densities, $N(^{12}\mathrm{CO})/N(^{13}\mathrm{CO})$, which is equivalent to the atomic abundance ratio $[^{12}\mathrm{C}]/[^{13}\mathrm{C}]$. We make this assumption in our analysis but we note that since $^{12}\mathrm{CO}$ has a higher optical depth than $^{13}\mathrm{CO}$, the measured $^{12}\mathrm{CO}/^{13}\mathrm{CO}$ line intensity ratio provides only a lower limit on the actual $[^{12}\mathrm{CO}]/[^{13}\mathrm{CO}]$ abundance ratio. We do not fix $N(^{12}\mathrm{CO})/N(^{13}\mathrm{CO})$ when searching for the best-fitting model but instead we allow it to vary, making it an output of the models in order to determine the best-fit abundance ratio. For each unique set of parameters T_K, $n(\mathrm{H_2})$ and $N(^{12}\mathrm{CO},\,^{13}\mathrm{CO},\,\mathrm{C^{18}O})$ the model outputs are fluxes in cgs units (which we convert to $\mathrm{Jy\,km\,s^{-1}}$ in order to compare directly to our measured fluxes), excitation temperature T_{ex}, brightness temperature T_b and optical depths for $^{12}\mathrm{CO}$, $^{13}\mathrm{CO}$ and $\mathrm{C^{18}O}$ from $J_{up} = 1-18$. In order to also search for the optimal abundance ratios we construct a grid of models for all combinations of T, $n(\mathrm{H_2})$, $N(^{12}\mathrm{CO})$, $N(^{12}\mathrm{CO})/N(^{13}\mathrm{CO})$ and $N(^{13}\mathrm{CO}/N(\mathrm{C^{18}O})$. We use $N(^{13}\mathrm{CO})/N(\mathrm{C^{18}O})$ as a proxy for the $[^{13}\mathrm{CO}]/[\mathrm{C^{18}O}]$ abundance ratio. To reduce the number of possible models when searching for the best-fit model we allow only five different discrete values of $N(^{13}\mathrm{CO})/N(\mathrm{C^{18}O})$, ranging between $0.1-10$ (e.g. Penzias 1983; Zhu et al. 2007) and similarly only six discrete values of $N(^{12}\mathrm{CO})/N(^{13}\mathrm{CO})$, ranging between $\sim 1-300$ in steps of $0.5\,\mathrm{dex}$. Furthermore, we restrict the allowed parameter space such that the implied source size (Ω_S) of the emitting region has a radius of $<5\,\mathrm{kpc}$ (the diameter of the galaxy is $\sim 5\,\mathrm{kpc}$ as derived from high-resolution $^{12}\mathrm{CO}$ observations

from PdBI and JVLA; Swinbank et al. 2011). We therefore set an upper limit of 5 kpc for the radius of SMM J2135:

$$\Omega_{\mathrm{S}} = L'_{\mathrm{CO}}/(T_{\mathrm{b}}\Delta V D_{\mathrm{A}}^2) \tag{4.6.2}$$

This most noticeably restricts the minimum allowed column density of the models to $N(^{13}\mathrm{CO}) > 10^{15}\mathrm{cm}^{-2}$.

4.6.4 Integrated spectral line energy distribution

The LVG analysis from Danielson et al. (2011) showed that the $^{12}\mathrm{CO}$ galaxy-integrated SLED is best-fit by a two-phase model: a 'hot', dense phase ($T_k \sim 60\,\mathrm{K}$, $n(\mathrm{H_2}) \sim 10^{3.6}\mathrm{cm}^{-3}$) likely associated with the four dense star-forming clumps and contributing 60% of the total luminosity over all the $^{12}\mathrm{CO}$ lines, and a 'cold', diffuse ($T_k \sim 25\,\mathrm{K}$, $n(\mathrm{H_2}) \sim 10^{2.7}\mathrm{cm}^{-3}$) phase probably corresponding to an extended gas phase in which the clumps are embedded. We therefore begin by attempting a two-phase fit to the new data to test the effect of the additional constraints of $^{13}\mathrm{CO}$ and $\mathrm{C^{18}O}$ SLEDs on the results of the LVG modelling.

For this two-phase fit we first split the large model grid into 'cold' and 'hot' models with a divide at $50\,\mathrm{K}$ and search the grid for the optimum combination of 'cold' models and 'hot' models using a χ^2 calculation. We identify the best two-phase model with the minimum χ^2 value then find those two-phase models for which the predicted $^{12}\mathrm{CO}$, $^{13}\mathrm{CO}$ and $\mathrm{C^{18}O}$ SLEDs are within $\Delta\chi^2 = 1\sigma$ of the best-fit. In fitting the SLEDs with two phases simultaneously we have a total of six degrees of freedom per ISM phase: $n(\mathrm{H_2})$, T_{K}, $N(^{12}\mathrm{CO})$, $N(^{12}\mathrm{CO})/N(^{13}\mathrm{CO})$, $N(^{13}\mathrm{CO})/N(\mathrm{C^{18}O})$ and a normalisation factor. For 12 degrees of freedom we therefore have a 1σ confidence limit of $\Delta\chi^2 = 13.7$. Our general formula for calculating χ^2 is:

$$\chi^2 = \sum_{n=1-7} (^{i}\mathrm{CO_{J=n}} - ^{i}\mathrm{CO_{model,J=n}})^2/(\alpha_{^{i}\mathrm{CO_{J=n}}})^2, \tag{4.6.3}$$

where $^{i}\mathrm{CO}$ represents either $^{12}\mathrm{CO}$, $^{13}\mathrm{CO}$ or $\mathrm{C^{18}O}$, $J_{\mathrm{up}} = 1, 3, 5, 7$ for $^{13}\mathrm{CO}$ and $\mathrm{C^{18}O}$

and $J_{\rm up} = 1, 3, 4, 5, 6, 7, 8$ for ^{12}CO. We include our upper limits on $J_{\rm up} = 1$ and 7 as constraints in the χ^2 fitting, setting the value to $(2 \pm 1)\sigma$ (in Figs. 4.6 and 4.8 we show these data as 2σ upper limits). In this equation $\alpha_{i_{\rm CO_{J=n}}}$ represents the error on the line flux constraints.

The measured SLEDs for the three species are shown in Fig. 4.6 and we show the best-fit combination of 'hot' and 'cold' models. Table 4.3 gives the best-fit parameters and range of allowed parameters for models that lie within $\Delta\chi^2 = 13.7$ of the best-fit. The best-fit parameters for the 'cold' and 'hot' phases respectively are: $\chi^2_{min-reduced} = 4.1$, $N(^{13}{\rm CO})/N({\rm C}^{18}{\rm O}) = 10^{0.5}$ and 10^0, $n({\rm H}_2) = 10^3 {\rm cm}^{-3}$ and $10^4 {\rm cm}^{-3}$, $N(^{12}{\rm CO})/N(^{13}{\rm CO}) = 10^2$ for both phases, $N(^{12}{\rm CO}) = 10^{19.5} {\rm cm}^{-2}$ and $10^{20} {\rm cm}^{-2}$ and $T_{\rm K} = 50\,{\rm K}$ and $90\,{\rm K}$. The addition of the constraints of ^{13}CO and C^{18}O seems to require models with higher temperatures than those found in Danielson et al. (2011) (25 K and 60 K) but the densities are similar ($n({\rm H}_2) = 10^{2.7-3.6} {\rm cm}^{-3}$). It is important to note that there is degeneracy in the temperature and density such that it is possible that an optimal solution in fact lies at higher density and lower temperature or lower density and higher temperature. To demonstrate this effect we fix all the model parameters at their optimised values and determine the effect of varying each parameter in the models in turn. This is shown by the vectors in Fig. 4.4 (r_{13}/r_{18}) which show that increasing the temperature and column density causes a decrease in the line ratios of ^{12}CO/^{13}CO and ^{12}CO/C^{18}O, whereas, increasing the density causes an increase in the line ratios. The $N(^{13}{\rm CO})/N({\rm C}^{18}{\rm O})$ ratios for both the 'hot' and 'cold' phases imply that throughout the system (and particularly in the 'hot' phase) there may be an enhanced C^{18}O abundance compared to star-forming galaxies locally.

We note that although these are the best-fit values, a large range of parameters is allowed within $\Delta\chi^2 = 13.7$ of the best-fit model. This large range of parameters is demonstrated by Fig. 4.7 where we plot likelihood contours representing the models that lie within $\Delta\chi^2 = 1$ and 2σ of the best-fit. For the 'cold' phase, $n({\rm H}_2)$ is at the lower limit of the allowed parameter space and for the 'hot' phase $N(^{12}{\rm CO})$ is at the upper limit of the allowed parameter space, which means that the best-fitting
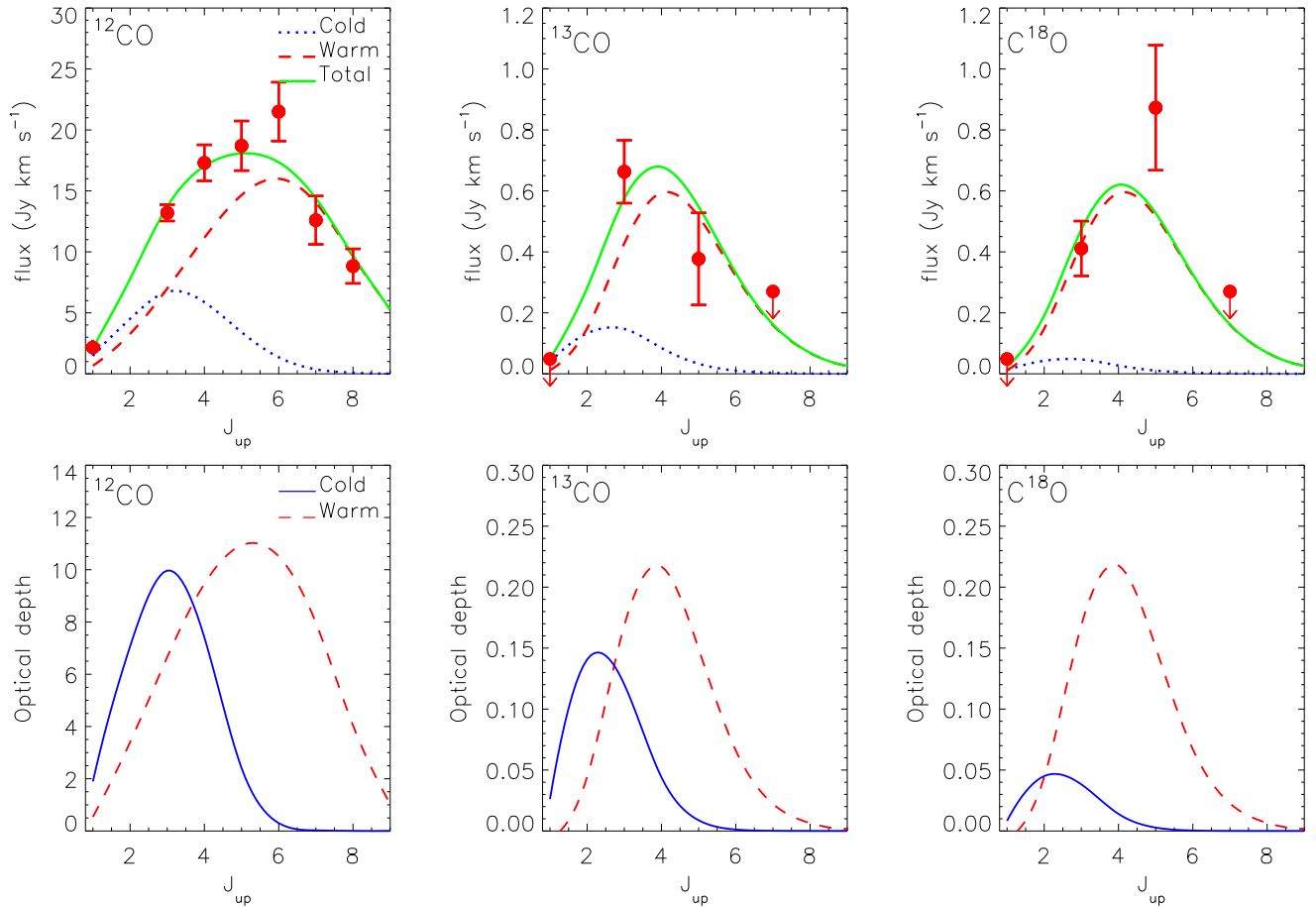
Figure 4.6: Top: SLEDs for the integrated ^{12}CO, ^{13}CO and C^{18}O emission from SMM J2135. The green solid curve is the best two-phase LVG fit to the SLEDs for all three species at once (described in Section 4.6). Also shown are the constituent 'hot' and 'cold' phases in red-dashed and blue-solid curves respectively. Upper limits shown are at a 2σ level for the undetected lines. Bottom: The distribution of the optical depth values for the best-fit 'cold' and 'hot' phases shown as blue-solid and red-dashed curves respectively.
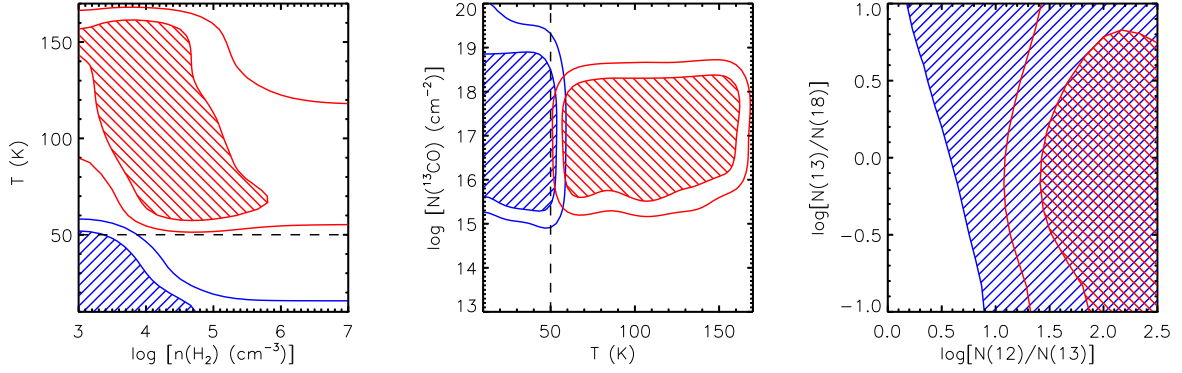
Figure 4.7: Parameter space distributions of the best-fitting 'cold' (blue) and 'hot' (red) phases for different combinations of parameters. The contours represent the models lying within $\Delta\chi^2 = 1$ and 2σ which for 12 degrees of freedom corresponds to models within $\Delta\chi^2$ of 13.7 and 21.3 respectively. The dotted lines on the left and middle plots demonstrate that for the two-phase model fits we restricted the 'cold' phase to have $T \leq 50\,\mathrm{K}$ and for the 'hot' phase we required that it have $T > 50\,\mathrm{K}$. The hashed regions show the region of parameter space occupied by all the models within $\Delta\chi^2 = 1\sigma$ of the best-fit model. Since there are a large number of degrees of freedom compared to the number of data points we have relatively poor constraints on the allowed parameter space. This provides further motivation to kinematically decompose the emission to test if we can better constrain the parameter space of the individual kinematic components.

model may in fact require even higher $N(^{12}\mathrm{CO})$ and lower $n(\mathrm{H_2})$, making it difficult to make firm conclusions. However, we note that we initially selected an upper limit of $N(^{12}\mathrm{CO}) = 10^{20}\mathrm{cm}^{-2}$ for our parameter space, as a higher column density than this would imply extreme values of $N(\mathrm{H_2})$. We also caution that since the errors on the $^{12}\mathrm{CO}$ fluxes are smaller and there are more measured fluxes for $^{12}\mathrm{CO}$ than for the less abundant species, we are slightly weighted towards the $^{12}\mathrm{CO}$ data when searching for an optimum model. Since in Danielson et al. (2011) we derived lower temperature and densities for the two phases than we derive here, this may imply that giving the $^{12}\mathrm{CO}$ SLEDs more weighting may bias the temperature and density towards lower values.

Since the models we employ also contain optical depth as part of the output, in Fig. 4.6 we also show the optical depth for each transition of $^{12}\mathrm{CO}$, $^{13}\mathrm{CO}$ and $\mathrm{C^{18}O}$ for the best-fit 'hot' and 'cold' phases. This demonstrates that $^{12}\mathrm{CO}$ is substantially optically thicker ($\sim 50\times$) than the $^{13}\mathrm{CO}$ and $\mathrm{C^{18}O}$, as expected. Furthermore, they demonstrate that the 'hot' phases are all optically thicker than the 'cold' phase. This is particularly prominent for the $\mathrm{C^{18}O}$ for which the 'hot' phase has a >4 times

higher optical depth than the 'cold' phase, however, they would both still be classed as optically thin as $\tau \ll 1$.

With the species abundance ratios and temperatures derived from RADEX we can now estimate the gas mass of SMM J2135 using the optically thin ^{13}CO emission and compare this to previous estimates based on ^{12}CO in Danielson et al. (2011).

Gas mass

In Danielson et al. (2011) we used the ^{12}CO(1–0) line luminosity and the ^{12}CO SLED to constrain a large velocity gradient model which predicted a total cold molecular gas mass of $M_{\mathrm{gas}} \sim (1.4 - 4.0) \times 10^{10} M_{\odot}$ for SMM J2135. This suggested that the empirical conversion factor between CO luminosity and gas mass ($\alpha_{\mathrm{CO}} = M_{\mathrm{H_2}}/L'_{^{12}\mathrm{CO}(1-0)}$) is likely to be $\alpha_{\mathrm{CO}} \sim 2\,\mathrm{M_{\odot}\,(K\,km\,s^{-1}\,pc^2)^{-1}}$ for this system, which is higher than the canonical $\alpha_{\mathrm{CO}} \sim 0.8\,\mathrm{M_{\odot}\,(K\,km\,s^{-1}\,pc^2)^{-1}}$ normally assumed for high-redshift ULIRGs. Swinbank et al. (2011) use high-resolution mapping of the ^{12}CO(6–5) emission to develop a kinematic model for SMM J2135 and estimate a dynamical mass of $M_{\mathrm{dyn}} = (6.0 \pm 0.5) \times 10^{10} M_{\odot}$ within $\sim 5\,\mathrm{kpc}$. Together with an estimated stellar mass of $M_* = (3 \pm 1) \times 10^{10} M_{\odot}$ (Swinbank et al. 2010) this suggests a cold molecular gas mass of $M_{\mathrm{gas}} \lesssim 4.5 \times 10^{10} M_{\odot}$, which is consistent with our predictions from the LVG analysis in Danielson et al. (2011).

However, constraints on the total mass of the H_2 reservoir can be derived using measurements of ^{13}CO and C^{18}O, with the advantage that these lower abundance species are expected to be optically thin and so able to trace the bulk of the cold molecular gas including the denser gas typically not probed by ^{12}CO emission. Of course, it is still necessary to assume an abundance ratio between these less abundant isotopologues and H_2 in order to use our measured fluxes to determine the cold gas masses.

To estimate the masses we must first determine the intrinsic source brightness temperature. The integrated line intensity is $I_{\mathrm{CO}} = \int T_{\mathrm{mb}} dV$ $(\mathrm{K\,km\,s^{-1}})$, and is obtained from the beam-diluted brightness temperature. This must be corrected for the redshift in order to get the velocity-integrated source brightness temperature.

Following Solomon et al. (1997) where the line luminosity is $L'_{CO} = T_b \Delta V \Omega_S D_A^2$, we derive a velocity-integrated source brightness temperature of $T_b \Delta V = L'_{CO}/\Omega_S D_A^2$, where Ω_S is the solid angle subtended by the source (in steradians) and D_A is the angular size distance (in parsecs). The line luminosity can be calculated from our observed quantities via:

$$L'_{CO} = 3.25 \times 10^7 S_{CO} \Delta V \nu_{obs}^{-2} D_L^2 (1+z)^{-3} / \mu (\mathrm{Kkms^{-1}pc^2}), \qquad (4.6.4)$$

where $S_{CO} \Delta V$ is the velocity-integrated flux density in $\mathrm{Jy\,km\,s^{-1}}$, ν_{obs} is the observed frequency of the transition considered in GHz, D_L is the luminosity distance in Mpc and μ is the amplification factor due to gravitational lensing of $\mu = 37.5 \pm 4.5$.

To derive the mass we use:

$$M_{H_2} = N_{H_2} \mu_G m_{H_2} \Omega_S D_A^2, \qquad (4.6.5)$$

where m_{H_2} is the molecular mass of Hydrogen (3.346×10^{-27}kg), μ_G is the mean atomic weight of the gas (1.36; including the contribution from Helium assuming a 24% Helium mass abundance; Scoville et al. 1986) and N_{H_2} is the column density in $\mathrm{cm^{-2}}$. We calculate N_{H_2} following Meier & Turner (2004):

$$N(H_2)_{iCO} = A \times \frac{[H_2]}{[^{12}CO]} \frac{[^{12}CO]}{[^iCO]} \frac{e^{iE_u/T_{ex}}}{e^{iE_u/T_{ex}} - 1} I_{iCO}, \qquad (4.6.6)$$

assuming these species to be optically thin and assuming local thermal equilibrium (LTE) for all levels. Here I_{iCO} is the velocity-integrated source brightness temperature of the chosen transition in the chosen species i (in $\mathrm{K\,km\,s^{-1}}$); ^iE_u is the rotational energy ($h\nu/k = 5.5\,\mathrm{K}$ for $J_{up} = 1$); we adopt an average abundance ratio of $[^{12}CO]/[H_2] = 8.5 \times 10^{-5}$ (Galactic value; Frerking et al. 1982) and A is a constant determined following Scoville et al. (1986):

$$A = \frac{3k}{8\pi^3 B \mu^2} \frac{e^{hBJ_1(J_1+1)/kT_{ex}}}{(J_1+1)}, \qquad (4.6.7)$$

where B is the rotational constant $(5.5101 \times 10^{10}\,\mathrm{s}^{-1})$ and μ is the permanent dipole moment ($\mu = 0.1098$ Debyes for ^{13}CO where 1 Debye $= 10^{-18}\,\mathrm{g}^{1/2}\,\mathrm{cm}^{5/2}\,\mathrm{s}^{-1}$). Since $I_{i\mathrm{CO}} = T_\mathrm{b}\Delta V = L'_\mathrm{CO}/\Omega_\mathrm{S}D_\mathrm{A}^2$ the mass equation therefore simplifies to:

$$M_{\mathrm{H}_2} = A \times \mu_\mathrm{G} m_{\mathrm{H}_2} \frac{[\mathrm{H}_2]}{[^{12}\mathrm{CO}]} \frac{[^{12}\mathrm{CO}]}{[^i\mathrm{CO}]} \frac{e^{iE_\mathrm{u}/T_\mathrm{ex}}}{e^{iE_\mathrm{u}/T_\mathrm{ex}} - 1} L'_\mathrm{CO}, \qquad (4.6.8)$$

where L'_CO must be converted into $\mathrm{K\,km\,s^{-1}\,cm^2}$.

From the LVG modelling we predict best-fit values of the excitation temperature of ^{13}CO(3–2) of $T_\mathrm{ex} = 11.3\,\mathrm{K}$ (with a 1σ range of 9.1–16.8 K) for the cold component and $T_\mathrm{ex} = 35.4\,\mathrm{K}$ (with a 1σ range of 18.9-155.3 K) for the warm component. Our best-fit value of the abundance ratio of $[^{12}\mathrm{CO}/^{13}\mathrm{CO}]$ is ~ 100 for both the cold and warm components. This is significantly higher than the values typically assumed for starburst galaxies of $[^{12}\mathrm{CO}]/[^{13}\mathrm{CO}] = 40$ (Henkel & Mauersberger 1993; Wilson & Rood 1994). However, we note that there is considerable uncertainty in the abundance ratio within the models on which the derived mass depends strongly. Furthermore, there are strong variations even within galaxies. For example, within the Milky Way the ^{12}C/^{13}C atomic abundance ratio varies from $\sim$20 in the Galactic centre to $>$100 in the outer parts of the Galaxy (Wilson & Rood 1994; Wouterloot & Brand 1996). Generally, starburst galaxies and ULIRGs exhibit a ^{12}C/^{13}C > 30 (e.g. Henkel & Mauersberger 1993; Henkel et al. 2010). However, in the starburst galaxy, M 82, ^{12}C/^{13}C $\gtrsim 140$ (Martín et al. 2010).

If we calculate a mass for the warm and cold components separately, using our best-fit value for $[^{12}\mathrm{CO}]/[^{13}\mathrm{CO}]$, we find $M_{\mathrm{H}_2}^{warm} = (5.4$–$7.2)\times 10^9 \mathrm{M}_\odot$ and $M_{\mathrm{H}_2}^{cold} = (2.1$–$7.8)\times 10^9 \mathrm{M}_\odot$ giving a range in total mass of $M_{\mathrm{H}_2} = (0.8$–$1.5)\times 10^{10}\mathrm{M}_\odot$ with the hot and cold components contributing approximately equally to the total mass. However, clearly there is uncertainty in the abundance ratio used. Indeed, if we take the maximum abundance ratio within 1σ of the best fit ($[^{12}\mathrm{CO}]/[^{13}\mathrm{CO}]\sim 300$) we derive an upper limit on the best-fit total mass of $\mathrm{M}_{\mathrm{H}_2} \sim 2.5 \times 10^{10}\mathrm{M}_\odot$. The upper limits of this estimate of H$_2$ mass (derived from ^{13}CO(3–2)) are consistent with the dynamical limits on M_{gas} derived by $M_{dyn} = M_* + M_{gas}$, with $M_* = (3\pm 1)\times 10^{10}\mathrm{M}_\odot$

and $M_{dyn} = (6.0 \pm 0.5) \times 10^{10} M_\odot$ (Swinbank et al. 2011; neglecting the contributions of dark matter which is not expected to be dynamically dominant on these scales in a high-redshift galaxy).

Finally we caution that the magnification factor that we apply is a luminosity-weighted galaxy-integrated factor, however, due to the critical curve passing through SMM J2135, there is a moderate amplification gradient across the source. This is demonstrated in Swinbank et al. (2011) where the amplification increases across the source from $\sim 20 - 50$. However, the ^{13}CO line that we are using to estimate the gas mass covers the full velocity range of the source and therefore the integrated magnification we use is probably appropriate.

4.6.5 Kinematically resolved SLEDs

It can be seen from Fig. 4.6 that in both the ^{12}CO and C^{18}O SLEDs the best-fit model does not peak as high in J_{up} as the data. In Danielson et al. (2011) the model fit peaked at $J_{up} = 6$ whereas adding in the constraints of ^{13}CO and C^{18}O results in a poorer fit to the high-excitation end of the ^{12}CO SLED. Fundamentally, the problem is that if the ^{13}CO and C^{18}O emission are both optically thin, then the difference in their SLED profiles implies that they are not tracing the same gas and therefore, even two-phase LVG models will struggle to fit both species simultaneously. Furthermore, while it is possible to find suitable fits to the data using a two-phase fit, it is difficult to constrain the allowed parameter space due to the large number of degrees of freedom. The velocity structure in the lines suggests multiple components (Figs. 4.2 and 4.4) and high-resolution mapping of SMM J2135 demonstrates that the velocity structure in SMM J2135 coincides with the clumpy structure observed in the disk (Swinbank et al. 2011). This therefore motivates us to carry out LVG modelling using the SLEDs derived from our kinematic decomposition. However, since we are now considering subcomponents within our system, we must employ a ΔV according to the physical scale of the clumps. The gas clumps identified by Swinbank et al. (2011) are $\sim 100 - 200$ pc across and have an average FWHM of

$\sim 200\,\mathrm{km\,s^{-1}}$. However, given that these clumps are likely to be comprised of much smaller structures, the average velocity that the gas in the clumps is experiencing is likely to be much lower than their overall FWHM. We therefore search for models with a $\Delta V = 50\,\mathrm{km\,s^{-1}}$. We include the same constraints as before in the χ^2 fitting but since we do not have the S/N or enough datapoints to do a two-phase fit to each kinematic component we use a single-phase fit to each velocity component with a total of six degrees of freedom: $n(\mathrm{H_2})$, T_K, $N(^{12}\mathrm{CO})$, $N(^{12}\mathrm{CO})/N(^{13}\mathrm{CO})$, $N(^{13}\mathrm{CO})/N(\mathrm{C^{18}O})$ and normalisation factor. The six degrees of freedom give a 1σ confidence limit of $\Delta\chi^2 = 7.0$. Again, if we do not detect a component in a particular transition, we include upper limits as constraints, setting the value to $(2\pm1)\sigma$.

In Fig. 4.8 we show the best LVG model fits to the individual kinematic components in SMM J2135. The corresponding best-fit parameters and possible ranges of values within $\Delta\chi^2 = 1\sigma$ of the best-fit are listed in Table 4.3. In Fig. 4.9 we show the parameter space of our five model parameters with likelihood contours that represent the models that lie within $\Delta\chi^2 = 1$, 2 and 3σ of the best-fit. We can better constrain the physical parameters when we fit to each kinematic component individually. The different components occupy different regions of parameter space in temperature, density and column densities. We now discuss the properties of the individual kinematic components:

Table 4.3: LVG model parameters

Component	Method	$\log \frac{N(^{13}\text{CO})}{N(\text{C}^{18}\text{O})}$	T_{K} (K)	$n(\text{H}_2)$ (cm^{-3})	$N(^{12}\text{CO})$ (cm^{-2})	$\log \frac{N(^{12}\text{CO})}{N(^{13}\text{CO})}$	χ^2(reduced)
Search ranges:	...	0.1–1	10–200	10^{3-7}	10^{15-20}	$10^{0-2.5}$	...
Cold	2-phase	0.5 (-1–1)	50 (10–50)	10^3 (10^{3-7})	$10^{19.5}$ (10^{18-20})	2 (0.5–2.5)	4.1
Warm	2-phase	0 (-1–1)	90 (60–160)	10^4 ($10^{3.5-7}$)	10^{20} ($10^{18.5-20}$)	2 (1.5–2.5)	4.1
X	3-component	0 (-0.5–0.5)	200 (30–200)	10^3 (10^{3-7})	10^{19} (10^{15-20})	2 (1.5–2.5)	1.8
Y	3-component	0.5 (0–0.5)	140 (110–200)	$10^{3.5}$ ($10^{3-3.5}$)	$10^{18.5}$ ($10^{18-18.5}$)	1.5 (1.5)	2.5
Z	3 component	0 (-0.5-1)	140 (30-200)	$10^{3.5}$ (10^{3-7})	10^{19} ($10^{18-19.5}$)	2 (1.5–2.5)	3.4

Note: For kinetic temperature (T_{K}), H$_2$ density ($n(\text{H}_2)$) and column density ($N(^{12}\text{CO})$) we give the parameter values associated with the minimum χ^2 and the range in these parameters (within $\Delta\chi^2 = 1\sigma$) is given in brackets. The χ^2 of the two-phase fit is based on 15 data points and 12 free parameters therefore to calculate the reduced χ^2 we divide by 3 degrees of freedom. Similarly for the kinematically decomposed models the reduced χ^2 is calculated by dividing by 9 degrees of freedom (15 data points – 6 free parameters).

X-component: This component has a velocity offset from the dynamical centre of the system by $+400 \, \mathrm{km \, s^{-1}}$. Unfortunately, as a result of it only being detected in $^{13}\mathrm{CO}(3\text{–}2)$ and $\mathrm{C}^{18}\mathrm{O}(5\text{–}4)$ the ISM properties we derive for this component are very poorly constrained. Broadly, it has a temperature which is only constrained to lie between 30–200 K, a density range of $n(\mathrm{H_2}) = 10^{3-7} \, \mathrm{cm^{-3}}$ and the same high abundance ratio of $N(^{13}\mathrm{CO})/N(\mathrm{C}^{18}\mathrm{O}) = 1$ as for the Z-component.

Y-component: This component is the centre of mass of the system, lying at $+165 \, \mathrm{km \, s^{-1}}$. It is present in all the observed emission lines in our dataset but it is marginally stronger in the $^{13}\mathrm{CO}$ than in the $\mathrm{C}^{18}\mathrm{O}$ emission lines. The LVG models suggest that the Y-component exhibits the lowest abundance ratio of all three components for $N(^{12}\mathrm{CO})/N(^{13}\mathrm{CO}) \sim 30$ and the highest for $N(^{13}\mathrm{CO})/N(\mathrm{C}^{18}\mathrm{O}) \sim 1 - 3$, possibly suggesting a relatively high abundance for $^{13}\mathrm{CO}$. It is reasonably well constrained to have a warmer best-fit solution than the X and Z components $(T = 110 - 200 \, \mathrm{K})$. The low abundance could be indicating that component Y is in a later stage of star formation, since $^{13}\mathrm{C}$ are secondary nuclei produced in longer lived low-to-intermediate mass stars. In such a scenario this component may be the oldest of the three components. This is demonstrated by the different abundance ratio vectors in Fig. 4.4. We note that the Y-component SLED fits tend to overpredict the $^{13}\mathrm{CO}$ and underpredict the $\mathrm{C}^{18}\mathrm{O}$ SLEDs and the best-fit does not peak at a high enough excitation in $\mathrm{C}^{18}\mathrm{O}$.

Z-component: The Z-component is at the opposite edge of the gas disk from the X-component at a velocity of $\sim -70 \, \mathrm{km \, s^{-1}}$. It is very similar to the X-component in terms of T, $n(\mathrm{H_2})$ and abundance ratios. We observe it to be very weak in $^{13}\mathrm{CO}$ but strong in $\mathrm{C}^{18}\mathrm{O}$, in particular the highest rotational energy, $\mathrm{C}^{18}\mathrm{O}(5\text{–}4)$. It also exhibits a high abundance ratio of $N(^{12}\mathrm{CO})/N(^{13}\mathrm{CO}) \sim 100$ and a low abundance ratio of $N(^{13}\mathrm{CO})/N(\mathrm{C}^{18}\mathrm{O}) \sim 1$. The low $N(^{13}\mathrm{CO})/N(\mathrm{C}^{18}\mathrm{O})$ ratio appears to be due to a genuinely high abundance of $\mathrm{C}^{18}\mathrm{O}$. A similarly high abundance is found in the X-component. We note that for the Z-component, the best-fit model peaks at $\mathrm{J_{up}} \sim 4$ whereas the data peaks closer to $\mathrm{J_{up}} = 5$ and the fit to the $\mathrm{C}^{18}\mathrm{O}(5\text{–}4)$ is underpredicted by $\sim 3\sigma$, so the temperature is potentially even higher. The properties
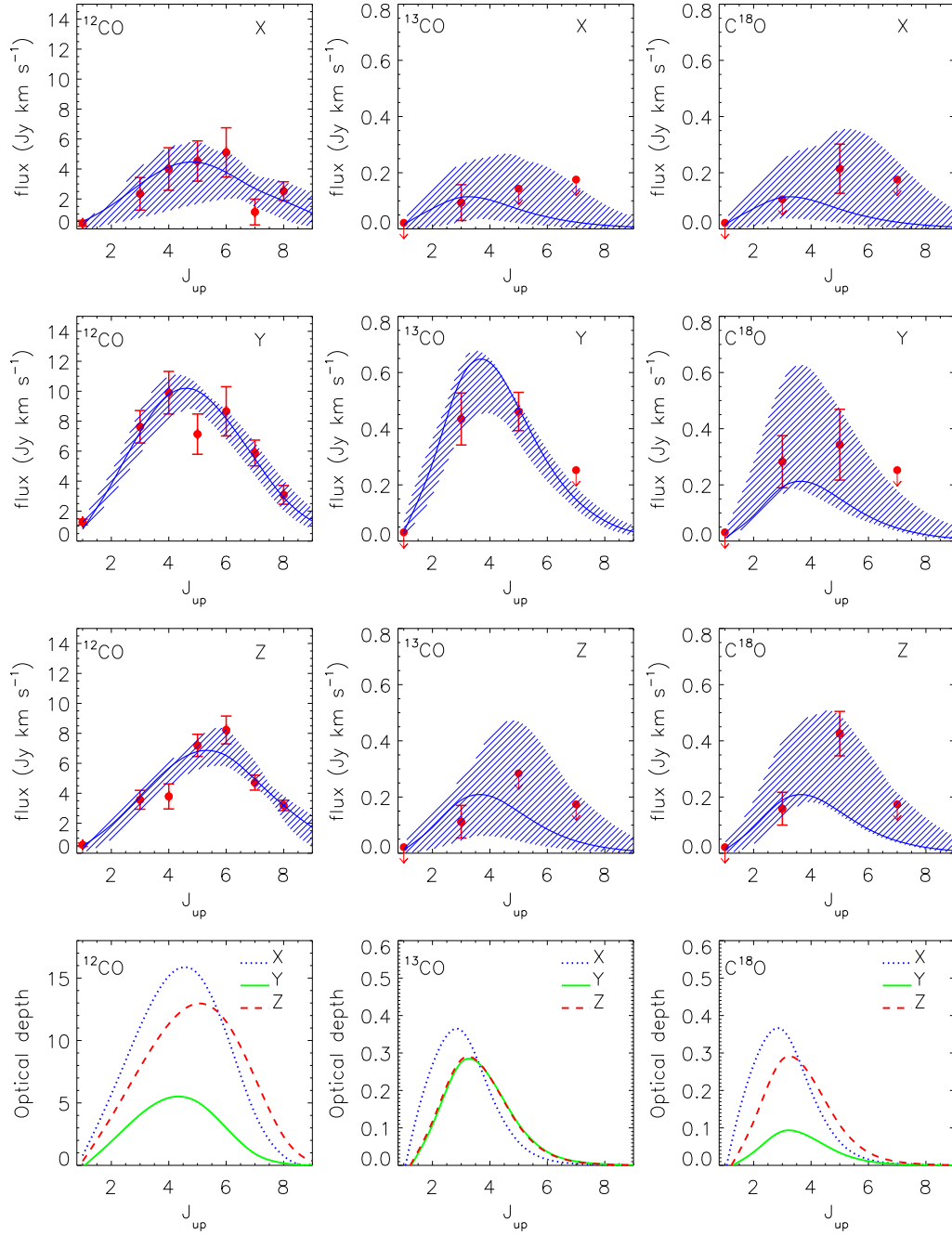
Figure 4.8: SLEDs for the individual kinematic components X, Y and Z in ^{12}CO, ^{13}CO and C^{18}O. Overlaid in hashed blue is the range in LVG model fits that are within $\Delta\chi^2 \leq 1\sigma$ of the best-fit to the ^{13}CO, C^{18}O and ^{12}CO data (all models that lie within $\Delta\chi^2 \leq 7.0$). The solid curve represents the model with the minimum total χ^2 value for the fit to all the SLEDs for that component. Upper limits are plotted at the 2σ level. The ^{13}CO and C^{18}O SLEDs clearly peak at different J$_{\rm up}$ but this is not well-described by the models. *Bottom:* The distribution of the optical depth values for the best-fit models to the individual components, demonstrating that the optical depth of ^{12}CO is$\sim 40\times$ higher than that of ^{13}CO and C^{18}O.
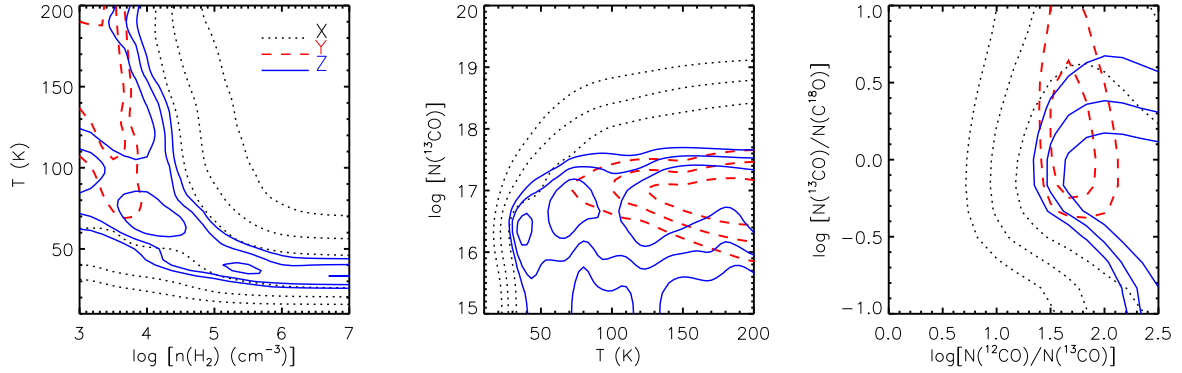
Figure 4.9: Parameter space distributions of the best-fitting models in X, Y and Z components for different combinations of parameters. The contours represent the models lying within $\Delta\chi^2 = 1$, 2 and 3σ, which for six degrees of freedom corresponds to models within $\Delta\chi^2$ of 7.0, 12.8 and 20.0 respectively. These fits to the kinematically decomposed spectral line fluxes provide better constraints on the parameter space than those using the integrated emission. The different components are represented with different colours and linestyles and it can be seen that the different components occupy different regions of parameter space, although there is overlap between all of them. The X component is clearly the least constrained as we have fewer line detections in this component.

of the Z-component are consistent with a warm, dense medium undergoing preferentially massive star formation. The similar X- and Z-components thus appear to be chemically younger than the Y-component and they may be similar structures.

The X and Z-components require a lower abundance ratio of $\left[^{13}\mathrm{CO}\right]/\left[\mathrm{C}^{18}\mathrm{O}\right]$ than the Y-component and this abundance ratio is surprisingly low (< 1), implying enhanced $\mathrm{C}^{18}\mathrm{O}$ abundance in the outer regions of the galaxy. Whereas the Y-component exhibits the lowest ratio of $N(^{12}\mathrm{CO})/N(^{13}\mathrm{CO})$ out of the three components, potentially implying an enhanced $^{13}\mathrm{CO}$ abundance in the dynamical centre of the galaxy.

4.7 Discussion

Our measurements of optically thin $^{13}\mathrm{CO}$ and $\mathrm{C}^{18}\mathrm{O}$ in the ISM of SMM J2135 suggest a molecular gas mass of $M_{\mathrm{gas}} \sim (0.8 - 1.5) \times 10^{10} \, \mathrm{M}_\odot$ (see Section 4.6.4). When combined with the stellar mass, $M_* = (3.0 \pm 1) \times 10^{10} \mathrm{M}_\odot$, the implied dynamical mass ($M_{\mathrm{dyn}} = M_{\mathrm{gas}} + M_\star$) is within $2\,\sigma$ of that derived from the galaxy dynamics $M_{\mathrm{dyn}} = (6.0 \pm 0.5) \times 10^{10} \mathrm{M}_\odot$ (Swinbank et al., 2011), if we take the upper limit

on our derived gas mass. We therefore derive a ratio of $M_{\mathrm{gas}} / M_{\mathrm{dyn}} \sim 0.25$ which is comparable to the average molecular gas fractions found for high-redshift star-forming galaxies of $M_{\mathrm{gas}} / M_{\mathrm{dyn}} \sim 0.3$–$0.5$ at $z \sim 1$–2 (Tacconi et al. 2013; Bothwell et al. 2013). Using $M_{\mathrm{gas}} \sim 1.5 \times 10^{10}\,\mathrm{M_\odot}$ we derive $\alpha_{\mathrm{CO}} \sim 0.9\,\mathrm{M_\odot}\,(\mathrm{K\,km\,s^{-1}\,pc^2})^{-1}$ which is close to the canonical value for ULIRGs (i.e. Downes & Solomon 1998) but lower than our previous estimate of $\alpha_{\mathrm{CO}} = 2\,\mathrm{M_\odot}\,(\mathrm{K\,km\,s^{-1}\,pc^2})^{-1}$ in Danielson et al. (2011).

Modelling the ^{12}CO, ^{13}CO and C^{18}O SLEDs, we find that the ISM is best described by a two-phase ISM comprising a 'cold'-phase ($T_{\mathrm{K}} \sim 50\,\mathrm{K}$) tracing the extended gas disk, and a 'hot'-phase ($T_{\mathrm{K}} \sim 90\,\mathrm{K}$), with an average density of $\sim 10^{3-4}\,\mathrm{cm^{-3}}$ (presumably tracing the denser star forming regions). However, due to the strong differences in J_{peak} for the ^{13}CO and C^{18}O SLEDs we find that a two-phase fit to the integrated emission is unable to adequately describe both simultaneously.

However, SMM J2135 exhibits highly-structured molecular emission spectra, and previous work has demonstrated that the source can be kinematically decomposed into three main components which are coincident with the bright star-forming clumps visible in the high-resolution observed 870μm SMA and JVLA ^{12}CO(1–0) maps (Swinbank et al. 2011). Thus, deriving the properties of such a complex system via the integrated flux, although illustrative for comparison to both local and high-redshift observational studies, is not probing the true conditions in the star-forming regions themselves. Furthermore, using optically thick gas tracers gives a biased view of the properties of the cold molecular gas and does not probe the densest regions in which the stars are forming. Thus, we fit a three-component kinematic model (X, Y, Z) to the spectra of the two lower abundance (and thus typically optically thinner) gas tracers: ^{13}CO and C^{18}O, in order to provide a more detailed understanding of the ISM conditions within this high-redshift star-forming galaxy. By kinematically decomposing the SLEDs into their constituent components (X, Y and Z) we show that there are no strong differences in the excitation of the ^{13}CO and C^{18}O in any of the components, although we do find abundance gradients between the components.

Danielson et al. (2011) proposed that the highly structured ^{12}CO emission line morphology of SMM J2135 arises from a merging system in which components Y and Z correspond to two different interacting galaxies with the X-component being a diffuse tidal feature. However, high-resolution ($\sim 0.2''$) dynamical maps of the ^{12}CO(6–5) and ^{12}CO(1–0) emission showed that the bulk of the gas in fact lies in a 5 kpc diameter, rotationally supported, clumpy disk (Swinbank et al., 2011). In this model the highly-structured ^{12}CO emission arises from a number of bright clumps within the disk.

Our new ^{13}CO and crucially, C^{18}O observations are consistent with the latter interpretation: the enhanced C^{18}O is found in the outer regions of the disk (the high C^{18}O is typically associated with young, high mass star-formation), and the enhanced ^{13}CO (generally associated with older, lower mass stars), is located in the central regions. However, we note that the gas disk has a very low Toomre Q, ($Q = 0.50 \pm 0.15$; Swinbank et al. 2011), suggesting that a significant, major accretion event must have recently occurred and the star formation has yet to stabilise the disk back to $Q = 1$ (e.g. Hopkins et al. 2012). One possible local analogue of SMM J2135 is the luminous galaxy NGC 6240 (e.g. Tacconi et al. 1999; Iono et al. 2007). This system has been found to comprise a thick, highly turbulent disk, centred between the two nuclei of the merging progenitors. In this system, the tidally stripped gas from the two progenitors has settled into a rotationally supported disk in the potential well of the remnant. The variations in abundance across SMM J2135 may imply that it is in a similar regime, since such chemical variations and low Toomre Q are unlikely to arise through the gravitational collapse of a single disk.

4.7.1 Cosmic rays as a heating source

There is evidence that in some star-forming galaxies, heating from cosmic rays may play a more important role than photons, due to their ability to penetrate and volumetrically heat dense gas (e.g. Goldsmith & Langer 1978; Hailey-Dunsheath et al. 2008; Bradford et al. 2003; Bayet et al. 2011a; Bayet et al. 2011b; Papadopoulos

et al. 2012b). Given the high star formation rate of this galaxy (SFR $\sim 400\,\mathrm{M_\odot\,yr^{-1}}$), particularly in the clumps, we now look at the energetics of the heating and cooling of the cold dense gas in this system, comparing the potential contributions from cosmic ray and UV heating to the total cooling we expect from our CO lines (one of the main coolants in the cold ISM).

Cosmic ray heating rate

Following Suchkov et al. (1993) and Bradford et al. (2003), assuming that cosmic rays are produced at a rate proportional to the supernova rate, and hence the current star formation rate, and are removed from star-forming regions by high-velocity galactic winds, we derive the cosmic ray heating rate, χ_{H_2}, per H_2 molecule:

$$\chi_{H_2} = \zeta_p \Delta Q (\mathrm{erg\,s^{-1}\,per\,H_2}), \tag{4.7.9}$$

where, ζ_p is the ionisation rate per H_2 molecule and ΔQ is the thermal energy deposited per ionisation (17–20 eV; Goldsmith & Langer 1978). By scaling from the Milky Way we determine the ionisation rate to be:

$$\zeta_{p,SMMJ2135} = \zeta_{p,MW} \times \frac{\psi_{SMMJ2135}}{\psi_{MW}} \times \frac{v_{MW}}{v_{w,SMMJ2135}}, \tag{4.7.10}$$

where $\zeta_{p,MW}$ is the local Galactic ionisation rate (2–$7\times10^{-17}\mathrm{s^{-1}}$ for dense gas; e.g. Goldsmith & Langer 1978; van Dishoeck & Black 1986); $\psi_{SMMJ2135}$ is the supernova rate per unit area in SMM J2135; ψ_{MW} is the supernova rate per unit area (over the entire disk) of the Milky Way; v_w is the cosmic ray diffusion velocity from the Galactic disk and $v_{w,SMMJ2135}$ is the wind velocity of SMM J2135. We assume a Galactic star formation rate of 0.68–1.45 $\mathrm{M_\odot\,yr^{-1}}$ across the whole disk (the upper limit taken from Robitaille & Whitney 2010), resulting in a SFR surface density of $\sum_{SFR,MW} = (9.6-20.1)\times10^{-4}\,\mathrm{M_\odot\,yr^{-1}\,kpc^{-2}}$ and we assume the cosmic ray diffusion velocity from the Galactic disk to be $v_w = 10\,\mathrm{km\,s^{-1}}$ (Suchkov et al., 1993).

Previous observations have suggested that $> 50\%$ of the star formation in SMM J2135

may be occurring in the clumps, which appear to be closely associated with the kinematic components X, Y and Z (Swinbank et al. 2011). To search for cosmic ray heating we therefore concentrate on these regions. We assume the supernova rate per unit area ψ_{SMMJ2135} to be proportional to the SFR surface density in the clumps of $\mathrm{SFR} = 30 - 90\,\mathrm{M}_\odot\,\mathrm{yr}^{-1}$ (assuming a Salpeter initial mass function; Swinbank et al. 2011). We also assume clump radii of $100 - 200\,\mathrm{pc}$, and that the stars do not migrate far from the clumps before they become supernovae. We adopt a wind velocity in SMM J2135 of $v_{\mathrm{w,SMMJ2135}} = 200\,\mathrm{km\,s}^{-1}$, approximately the FWHM of the individual components. Typical values for wind velocity in local starbursts and high-redshift submillimetre galaxies are $v_{\mathrm{w}} = (1 - 3) \times 10^3\,\mathrm{km\,s}^{-1}$ (Banerji et al. 2011) so $v_{\mathrm{w,SMMJ2135}} = 200\,\mathrm{km\,s}^{-1}$ is likely to be a lower limit (thus an upper limit on the cosmic ray heating rate). This suggests an ionisation rate of $\zeta_{\mathrm{p,SMMJ2135}} \sim (1 - 100) \times 10^{-13}\mathrm{s}^{-1}$. Assuming $\Delta Q = 20\,\mathrm{eV}$ per ionisation, the power deposited per H_2 molecule is $\chi_{H_2} \sim (30 - 3300) \times 10^{-25}\,\mathrm{erg\,s}^{-1}$. This is higher than the cosmic ray heating rate of $\chi_{H_2} = (5 - 18) \times 10^{-25}\,\mathrm{erg\,s}^{-1}$ in the local starburst galaxy NGC 253 (Bradford et al., 2003). However, given that the average star formation rate is significantly higher in SMM J2135 than in NGC 253 ($\mathrm{SFR} \sim 2 - 3\,\mathrm{M}_\odot\,\mathrm{yr}^{-1}$; Ott et al. 2005), it would be expected that the ionisation rate from cosmic rays should be significantly higher.

Papadopoulos (2010) predicts high temperatures of >80–$240\,\mathrm{K}$ in compact starbursts with cosmic ray ionisation rates of $(5 - 20) \times 10^{-14}\mathrm{s}^{-1}$. In SMM J2135 we derive a significantly higher ionisation rate (up to $50\times$ higher) and furthermore, the best-fit temperatures we derive using LVG modelling for the individual components X, Y and Z range between $140 - 200\,\mathrm{K}$. Thus these high temperatures could also hint that the clumps may be dominated by cosmic ray heating.

UV heating rate

For comparison to the cosmic ray heating we also estimate the likely UV photon heating per H_2 molecule from massive star formation assuming that the far-infrared luminosity is dominated by OB stars. The typical efficiency of photoelectric heating

in PDRs is $\sim 0.3\%$ (i.e. Weingartner et al. 2006), therefore the UV heating input per H_2 molecule can be estimated using, $\chi_{H_2} = 0.003 L_{IR}/(M_{H_2}/m_{H_2})$. Given an intrinsic infrared luminosity (8–1000μm) of $L_{IR} = 2.3 \times 10^{12} L_\odot$ (Ivison et al. 2010d), we derive a heating rate per H_2 molecule of $\chi_{H_2} \sim 15 \times 10^{-25} \mathrm{erg\,s^{-1}}$ over the whole system. Again, it is likely that the heating rate in the clumps is higher than the heating rate integrated over the whole system.

To estimate the UV heating per clump we assume an average clump mass of $\sim 1.3 \times 10^9 M_\odot$ (Danielson et al. 2011) and that each clump contributes $\sim 1/8$th of the observed L_{IR} ($\sim 3 \times 10^{11} L_\odot$), which is the typical clump fraction from the total $260\,\mu$m restframe emission (Swinbank et al. 2010). The heating rate per H_2 molecule can then be estimated to be $\chi_{H_2} \sim 45 \times 10^{-25} \mathrm{erg\,s^{-1}}$. This is similar to the minimum heating per clump that could be provided by cosmic rays, hence we conclude that both UV and cosmic rays are energetically capable of heating the gas.

However, we can take this estimate one stage further and ask what is the necessary distribution of gas needed for PDRs to heat the whole reservoir of warm gas? If the warm gas in the system is being heated by PDRs, then all that gas has be to in the vicinity of a hot star to reach a far-UV radiation field of $G_0 \sim 1 \times 10^{3-3.6}$ Habing fields (Ivison et al. 2010d; Danielson et al. 2011). Again, using the far-infrared luminosity of $2.3 \times 10^{12} L_\odot$ and making the approximation that the UV radiation field is dominated by O5 stars (luminosity $\sim 8 \times 10^5\,L_\odot$ per star), results in $\sim 3 \times 10^6$ O5 stars in SMM J2135. Using the SED of an O5 star, in order to have $G_0 \geq 1 \times 10^3$, the gas has to be within $3\,$pc of the star. So, using spheres of radius $\sim 3\,$pc, assuming $\sim 3 \times 10^6$ O5 stars, and using the derived gas density, we can calculate the gas mass exposed to $G_0 \geq 1 \times 10^3$. For our minimum density of $n(H_2) \sim \times 10^3 \mathrm{cm^{-3}}$ (Section 4.6.4), this becomes $M \sim 1.6 \times 10^{10}\,M_\odot$ which is in reasonable agreement with our estimated gas mass from ^{13}CO (Section 4.6.4). However, the gas can only be heated by UV up to $A_V \sim 5$ mag from the star (e.g., Tielens & Hollenbach 1985, Fig. 7). For densities up to $2 \times 10^3\,\mathrm{cm^{-3}}$, the whole $\sim 3\,$pc radius sphere is in the $A_V < 5$ mag region. Thus, for gas densities between $(1-2) \times 10^3\,\mathrm{cm^{-3}}$, the amount of PDR-heated gas will be between $M = (1.5 - 3.0) \times 10^{10}\,M_\odot$. If much of the gas is

at significantly higher density then PDRs will not be able to provide enough heating, since only the surface layer is heated. For example, for $n(H_2) \sim 1 \times 10^5 \, cm^{-3}$, $A_V = 5$ is reached at only $\sim 0.3 \, pc$ from the star and the amount of gas that can be heated is only $M \sim 1.6 \times 10^8 \, M_\odot$. Therefore, we can conclude that if the bulk gas density is significantly higher than $n(H_2) \sim 2 \times 10^3 \, cm^{-3}$ (which indeed we may be observing in some of the star-forming regions), then PDRs will not be able to provide the heating, and we need a mechanism that is capable of volumetrically heating the gas, such as cosmic rays.

Cooling rate

To estimate the cooling rate per H_2 molecule, we calculate the total CO luminosity in all species following Solomon & Vanden Bout (2005) and Hailey-Dunsheath et al. (2008):

$$\Sigma L_{CO} = \Sigma 1.04 \times 10^{-3} S_{CO,i} \Delta V \nu_{rest,i} D_L^2 (1+z)^{-1}/\mu, \qquad (4.7.11)$$

where μ is the magnification factor of 37.5 ± 4.5 and D_L is the luminosity distance in Mpc. We estimate a total intrinsic CO luminosity of $L_{CO} \approx 1.8 \times 10^8 \, L_\odot$. Using our cold gas mass estimated from $^{13}CO(3–2)$ of $M_{gas} = 1.5 \times 10^{10} \, M_\odot$, our cooling rate per H_2 molecule is $L_{CO}/(M_{H_2}/m_{H_2}) \sim 0.8 \times 10^{-25} \, erg \, s^{-1}$. In this calculation we have not included the [CII] $157.8 \, \mu m$ emission which is the dominant coolant in the outer envelopes of molecular clouds. Including the [CII] $157.8 \, \mu m$ in our calculation our cooling per H_2 becomes $\chi_{H_2} \sim 20 \times 10^{-25} \, erg \, s^{-1}$. However, at high A_V ($A_V > 5$) the [CII] $157.8 \, \mu m$ abundance significantly decreases and so has a minimal contribution to the cooling in these regions.

Balancing the temperature

We have derived heating rates from cosmic rays and UV photons of $(30–3300) \times 10^{-25} \, erg \, s^{-1}$ and $\sim 45 \times 10^{-25} \, erg \, s^{-1}$ respectively and we derive cooling rates from the atomic and molecular line emission of $\sim (0.8 - 20) \times 10^{-25} \, erg \, s^{-1}$. Although crude, overall this shows that both the cosmic ray and UV heating rates are comparable to the cooling

rate. However, we also demonstrate that for densities of $n(\text{H}_2) > 2 \times 10^5 \, \text{cm}^{-3}$, UV heating (from O5 stars) would not provide enough heating, due to extinction.

Moreover, Papadopoulos et al. (2012b) have suggested that in regions of enhanced cosmic ray density, the cosmic rays are able to penetrate to the core of the dense gas and volumetrically raise the temperature of the star-forming cores, which sets new initial conditions for star-formation and increases the characteristic mass of young stars.

Therefore, although we estimate that both the UV and cosmic rays are capable of balancing the cooling rate in SMM J2135, the high gas densities and the high ($> 100 \, \text{K}$) temperatures we derive for the star-forming clumps may provide indirect evidence that cosmic ray heating is particularly important in the individual kinematic components of SMM J2135. It is therefore possible that we are seeing evidence of this where we see an enhancement of C^{18}O, which is also indicative of preferentially massive star formation, possibly due to a raised initial temperature for star formation in these regions.

Finally, it is important to note that as well as cosmic ray heating and photon heating discussed here, X-ray heating, shocks and turbulent heating have been found to play an important role in the heating of interstellar gas both in the Milky Way and in other systems. Swinbank et al. (2011) finds a highly turbulent ISM in SMM J2135 and turbulence can have a similar effect to cosmic rays of volumetrically heating the gas (i.e. Meijerink et al. 2011; Papadopoulos et al. 2012b; Ao et al. 2013; Meijerink et al. 2013).

4.8 Conclusions

We analyse observations of ^{13}CO and C^{18}O emission from the lensed, $z = 2.3$ ULIRG, SMM J2135. We have combined these observations with our previous ^{12}CO measurements to better constrain the conditions in the ISM of this system by analysing the galaxy-integrated fluxes and the kinematically decomposed emission. Using these lower abundance tracers of H_2 we have been able to remove some of the degeneracies

in modelling the ISM. We summarise our conclusions as:

- We demonstrate that the ^{13}CO emission is likely to be optically thin ($\tau \ll 1$) and we use this to estimate the total cold gas mass of $M_{\mathrm{gas}} \sim 1.5 \times 10^{10} \, \mathrm{M}_\odot$ which is consistent with the dynamical and stellar limits on the total mass of the system but lower than the estimate based on ^{12}CO in the previous chapter. This implies $\alpha_{\mathrm{CO}} \sim 0.9 \, \mathrm{M}_\odot \, (\mathrm{K \, km \, s^{-1} \, pc^2})^{-1}$ for this high-redshift ULIRG.

- We detect $C^{18}O$ and measure a surprisingly high flux resulting in a ^{13}CO/C^{18}O flux ratio $\sim$4–15$\times$ lower than that measured in the Milky Way. Since ^{18}O is associated with the winds from massive stars, it is possible that this enrichment of C^{18}O may be due to the presence of preferentially massive star formation.

- As in the previous chapter, we find the ISM is best described by a two-phase model; a 'cold' phase at $\sim$50 K with a density of $n(\mathrm{H_2}) \sim 10^3 \, \mathrm{cm^{-3}}$, and a 'hot' phase at $\sim$90 K and $n(\mathrm{H_2}) \sim 10^4 \, \mathrm{cm^{-3}}$ respectively, both of which are hotter than the temperatures determined in the previous chapter. However, the SLEDs of ^{13}CO and C^{18}O peak at different $\mathrm{J_{up}}$ despite both appearing to be optically thin. We attribute this to variations of $[^{13}\mathrm{CO}]/[C^{18}O]$ within the galaxy and therefore kinematically decompose the line emission from the system into three main components, X, Y and Z. We find that the Y-component, which appears to be coincident with the centre of mass of the system, is warm ($T_{\mathrm{K}} \sim 140 \, \mathrm{K}$) and dense ($n(\mathrm{H_2}) \sim 10^{3.5} \, \mathrm{cm^{-3}}$) potentially with a higher abundance of ^{13}CO ($[^{12}\mathrm{CO}]/[^{13}\mathrm{CO}] \sim 30$) implying older star formation from intermediate mass stars. In contrast, the Z- and X-components are similar to each other. Both these regions display low $[^{13}\mathrm{CO}]/[C^{18}O]$ ratios, possibly implying enhanced massive star formation leading to a higher abundance of C^{18}O in these regions.

- We have derived an average cooling rate from all the observed CO lines of $\sim (0.8 - 20) \times 10^{-25} \, \mathrm{erg \, s^{-1}}$ per $\mathrm{H_2}$ molecule. We determine the possible contribution to the heating from cosmic rays (originating largely in supernovae) and

from UV photon heating of $(30–3300) \times 10^{-25} \, \mathrm{erg \, s^{-1}}$ and $\sim 45 \times 10^{-25} \, \mathrm{erg \, s^{-1}}$ respectively. Although crude, both cosmic ray heating and UV heating can plausibly balance the cooling occurring in the system. However, the high temperatures ($T_{\mathrm{K}} = 140 - 200 \, \mathrm{K}$) derived in the highest density components may suggest that cosmic rays may play a more important role than UV heating in this system.

Since SMM J2135 is a representative high-redshift ULIRG, this study paves the way for future detailed studies of this population. With ALMA in full science operations we will be able to resolve sub-kpc structure in these faint lines and derive resolved ISM properties. Furthermore, ALMA will enable the important observations of high density chemical tracers such as CS and HCN, giving insight into the origin of the intense star formation activity in this galaxy and potentially testing for systematic variation in the relative abundances of $^{12}\mathrm{CO}$, $^{13}\mathrm{CO}$ and $\mathrm{C}^{18}\mathrm{O}$ which may reflect variation in the IMF.

Chapter 5

The cosmic history of hot gas cooling and radio AGN activity in massive early-type galaxies

5.1 Motivation

There is evidence that an evolutionary link exists between high-redshift ULIRGs, QSOs and passive early-type galaxies, which was first suggested by Sanders et al. (1988). The most commonly accepted evolutionary scenario for highly luminous galaxies is that mergers drive gas towards the core of a merging system igniting an intense burst of star formation forming vast quantities of dust, and as the cores coalesce, the supermassive black holes merge producing an active galactic nucleus (AGN). In the dust-enshrouded phase the star-formation will dominate both the luminosity and any feedback processes (ULIRG phase), however, the large gas supply will also cause the SMBH to rapidly grow and move from an obscured phase to dominating both the luminosity and the feedback processes as it expels gas and dust from the system through radiation pressure, and winds generated by the AGN (e.g. Page et al. 2011; Tremonti et al. 2007). As the gas and dust are removed from the system, the star formation rate falls (e.g. Page et al. 2004) and the galaxy enters

a QSO phase in which the host galaxy is typically difficult to observe (e.g. Croom et al. 2004). The QSO fades rapidly (over timescales of ~ 100Myr; Di Matteo et al. 2005) as the cold gas supply is used up, leaving a hot gas halo from feedback, a massive SMBH embedded in a spheroid of passively evolving stars with little or no further star-formation occurring, thus the galaxy quickly reddens (Hopkins et al. 2008). The galaxy may then be classed as an elliptical or early-type galaxy. Many theoretical galaxy evolutionary models successfully invoke feedback from SMBHs to regulate and ultimately halt star formation in massive galaxies (i.e. Croton et al. 2006; Bower et al. 2006).

The cosmic star formation density has decreased almost exponentially from its peak at $z \sim 2$ to the present day. At this peak of star formation, the volume density of ULIRGs was $\sim 1000\times$ higher than it is today. It is still unclear what causes galaxies to evolve from the dust-enshrouded, rapidly star-forming systems observed at $z = 2$ to the massive, passive elliptical galaxies we observe locally, however, there is strong observational evidence that SMGs are the progenitors of the local massive early-type galaxies. In part this comes from a similarity between the redshift distributions of SMGs and QSOs (e.g. Chapman et al. 2005) suggesting an intimate link between high-redshift ULIRGs such as those sources discussed in the previous chapters, and AGN activity (Coppin et al. 2008). Similarly, Hickox et al. (2012) measure the clustering of optical QSOs and the LESS SMGs and demonstrate that they are consistent, which supports the evolutionary scenario in which powerful starbursts and QSOs occur in the same systems at high-redshift. It is therefore possible that feedback from SMBHs may be responsible for the rapid decline in the ULIRG population below $z = 2$. However, the feedback mechanisms by which AGN are able to heat and physically remove the gas from galaxies are still relatively poorly understood.

In this chapter we study the X-ray and radio emission from a large sample of massive early-type galaxies in the *Chandra* Deep Fields, to constrain the mechanical heating from AGN versus X-ray cooling mechanisms within passive galaxies in order to determine whether the AGN feedback in these systems is sufficient to prevent the

gas from cooling, thus preventing stars from forming and causing a decline in the cosmic star formation rate density towards the present day.

The content of this Chapter is published, as written here, in Danielson et al. (2012), MNRAS, 422, 494, however, Section 5.3 has been adapted and shortened from the published paper.

5.2   Abstract

We study the X-ray properties of 393 optically selected early-type galaxies (ETGs) over the redshift range of $z \approx 0.0$–1.2 in the *Chandra* Deep Fields. To measure the average X-ray properties of the ETG population, we use X-ray stacking analyses with a subset of 158 passive ETGs (148 of which were individually undetected in X-ray). This ETG subset was constructed to span the redshift ranges of $z = 0.1$–1.2 in the $\sim$4 Ms CDF-S and $\sim$2 Ms CDF-N and $z = 0.1$–0.6 in the $\sim$250 ks E-CDF-S, where the contribution from individually undetected AGNs is expected to be negligible in our stacking. We find that 55 of the ETGs are individually X-ray detected and 12 of these galaxies have properties consistent with being passive hot-gas dominated systems (i.e., systems not dominated by an X-ray bright AGN). On the basis of our analyses, we find little evolution in the mean 0.5–2 keV to B-band luminosity ratio ($L_{\mathrm{X}}/L_{\mathrm{B}} \propto [1 + z]^{1.2}$) since $z \approx 1.2$, implying that some heating mechanism prevents the gas from cooling in these systems. We consider that feedback from radio-mode AGN activity could be responsible for heating the gas. We select radio AGNs in the ETG population using their far-infrared/radio flux ratio. Our radio observations allow us to constrain the duty cycle history of radio AGN activity in our ETG sample. We estimate that if scaling relations between radio and mechanical power hold out to $z \approx 1.2$ for the ETG population being studied here, the average mechanical power from AGN activity is a factor of $\sim$1.4–2.6 times larger than the average radiative cooling power from hot gas over the redshift range $z \approx 0$–1.2. The excess of inferred AGN mechanical power from these ETGs is consistent with that found in the local Universe for similar types of galaxies.

5.3 Introduction

AGN are thought to play an important role in heating and in some cases removing gas in galaxies, making AGN feedback essential in the evolution of galaxies. A more complete understanding of the history of gas cooling and feedback heating in the massive ETG population requires direct X-ray and radio observations respectively, of distant ETG populations, covering a significant fraction of cosmic history. At present, such studies are difficult due to the very deep X-ray observations required to detect the hot X-ray emitting gas in such distant populations (however, see, e.g., Ptak et al. 2007 and Tzanavaris & Georgantopoulos 2008 for some early work). Notably, Lehmer et al. (2007) utilised X-ray stacking techniques and the $\sim$250 ks E-CDF-S and $\sim$1 Ms *Chandra* Deep Field-South (CDF-S) to constrain the evolution of hot gas cooling (via soft X-ray emission) in optically luminous ($L_{\rm B} \gtrsim 10^{10}\ L_{B,\odot}$) ETGs over the redshift range of $z \approx 0$–0.7. This study showed that the mean X-ray power output from optically luminous ETGs at $z \approx 0.7$ is $\sim$1–2 times that of similar ETGs in the local universe, suggesting the evolution of the hot gas cooling rate over the last $\sim$6.3 Gyr is modest at best. Considering the relatively short gas cooling timescales for such ETGs ($\sim$$10^8$ yr), this study provided indirect evidence for the presence of a heating source. Lehmer et al. (2007) found rapid redshift evolution for X-ray luminous AGNs in the optically luminous ETG population, which given the very modest evolution of the hot gas cooling, suggests that AGN feedback from the radiatively-efficient accreting SMBH population is unlikely to be the mechanism providing significant feedback to keep the gas hot over the last $\sim$6.3 Gyr. However, the mechanical feedback from radio AGNs, which is thought to be an important AGN feedback component, was not measured.

In this chapter, we improve upon the Lehmer et al. (2007) results in the following key ways: (1) we utilise significantly improved spectroscopic and multiwavelength photometric data sets to select hot gas dominated optically luminous ETGs (via

rest-frame colours, morphologies, and spectroscopic/photometric redshifts) and sensitively identify AGN and star-formation activity in the population (see Section 5.4 and 5.5); (2) we make use of a larger collection of *Chandra* survey data (totalling a factor of $\sim$4 times the *Chandra* investment used by Lehmer et al. 2007) from the $\sim$2 Ms *Chandra* Deep Field-North (CDF-N; Alexander et al. 2003), the $\sim$4 Ms CDF-S (Xue et al. 2011), and the $\sim$250 ks E-CDF-S (Lehmer et al. 2005) (collectively the CDFs), which allows us to study the properties of hot gas (e.g., luminosity and temperature) in optically luminous ETGs to $z \approx 1.2$; and (3) we make use of new radio data from the VLA to measure the radio luminous AGN activity and the evolution of its duty cycle in the ETG population and provide direct constraints on the radio jet power available for feedback. The chapter is organised as follows. In Section 5.4, we define our initial working sample and discuss the ancillary multiwavelength data used to identify non-passive ETG populations. In Section 5.5, we use various selection criteria to identify passive ETGs and ETGs hosting radio AGNs. In Section 5.6, we constrain the evolution of the X-ray emission from hot gas in our passive ETG sample using X-ray stacking techniques. In Section 5.7, we discuss the level by which radio AGN can provide heating to the hot gas in the ETG population. Finally, in Section 5.8, we summarise our results. Throughout this chapter, we make use of Galactic column densities of $N_{\rm H}$= 1.6×10^{20} cm^{-2} for the CDF-N (Lockman 2004) and $N_{\rm H}$= 8.8×10^{19} cm^{-2} for the E-CDF-S region (which also includes the CDF-S; Stark et al. 1992). In our X-ray analyses, we make use of photometry from five bands: the full band (FB; 0.5-8 keV), soft band (SB; 0.5-2 keV), soft sub-band 1 (SB1; 0.5-1 keV), soft sub-band 2 (SB2; 1-2 keV) and hard band (HB; 2-8 keV). The following constants have been assumed, $\Omega_{\rm M} = 0.3$, $\Omega_{\Lambda} = 0.7$ and $H_0 = 70$ km s^{-1}Mpc^{-1} implying a lookback time of 8.4 Gyr at $z = 1.2$. Throughout the chapter, optical luminosity in the B-Band ($L_{\rm B}$) is quoted in units of B-band solar luminosity ($L_{\rm B,\odot} = 5.2 \times 10^{32}$ erg s^{-1}).

Figure 5.1: (a): Histogram of the entire sample of sources after imposing the selection criteria (1) to (3) in Section 5.4, showing the bimodal distribution of late-type and early-type galaxies. The dashed line shows the Bell et al. (2004) colour-cut, whereas the solid line shows the cut that we apply, slightly offset due to our different selection methods, using the redshift dependency taken from Bell et al. (2004) but varying the constant. The dotted and solid curves correspond to fitting a double gaussian to the sample in order to separate out the late and early-type populations, where the solid curve is the combination of the two gaussians. (b): Rest frame $U-V$ colour versus absolute (Vega) V-band magnitude. The small filled grey circles represent the whole original sample of sources, again after imposing the selection criteria (1) to (3) in Section 5.4 (including both ETGs and LTGs). The open symbols represent the 393 sources in our final sample of ETGs and the dotted lines represent the colour cut applied using the minimum source redshift and maximum source redshift in our sample, with the line for the median redshift shown as a solid line (this cut was then applied to our model data later in Fig. 5.4).

5.4 Early-type galaxy sample selection

The primary goals of this study are to constrain the potential heating from AGN activity and the cooling of the hot gas in the optically luminous (massive) ETG population over the redshift range $z = 0.0$–1.2 (i.e., over the last 8.4 Gyr). To achieve these goals optimally, we constructed samples of optically luminous ETGs in the most sensitive regions of the CDFs.

We began our galaxy selection using master optical source catalogues in the CDF-N and E-CDF-S, which contain a collection of IR–to–optical photometric data and good redshift estimates (either spectroscopic redshifts or photometric redshifts). The CDF-N master source catalogue consists of 48,858 optical sources detected across the entire CDF-N region (see Rafferty et al. 2011). This catalogue is based on optical sources detected in the Hawaii HDF-N optical and near-IR catalogue from Capak et al. (2004), and includes cross-matched photometry from GOODS-N through *HST* ACS and *Spitzer* IRAC catalogues (e.g., Giavalisco et al. 2004), *GALEX* photometry,[1] and deep K_s-band imaging (Barger et al., 2008). In the E-CDF-S, we made use of a master catalogue of 100,318 sources (see Rafferty et al. 2011). This catalogue is based on the MUSYC (Gawiser et al. 2006), COMBO-17 (Wolf et al. 2004), and the GOODS-S (Grazian et al. 2006) optical surveys, and includes cross-matched photometry from MUSYC near-IR (Taylor et al. 2009), SIMPLE *Spitzer* IRAC (Damen et al. 2011), *GALEX* (see footnote 1), and GOODS-S deep U-band photometry (Nonino et al. 2009). Our master catalogs are estimated to be complete to R≤ 26 (see section 2.1 of Xue et al. 2010).

Whenever possible, we utilised secure spectroscopic redshifts, which were collected from a variety of sources in the literature and incorporated into the master source catalogues discussed above.[2] When spectroscopic redshifts were not available, we made use of high-quality photometric redshifts, which were calculated by Rafferty et al. (2011) using an extensive library of spectral templates (appropriate for

---

[1] see http://galex.stsci.edu/GR4/.

[2] For a comprehensive list of spectroscopic references, see Rafferty et al. (2011).

galaxies, AGNs, hybrid galaxy and AGN sources, and stars), the optical–to–near-IR photometry discussed above, and the Zurich Extragalactic Bayesian Redshift Analyzer (ZEBRA; Feldmann et al. 2006). We compared these redshifts to the photometric redshift catalogue of Cardamone et al. (2010) finding a median difference of 0.01±0.16 between $z = 0.0 - 0.8$ and 0.01±0.32 between $z = 0.8 - 1.2$ in the two catalogues, thus providing additional evidence for the validity of these redshifts.

Starting with the master catalogues of 149,176 collective CDF sources, we imposed a series of selection criteria that led to the creation of our optically luminous ETG catalogue that we use throughout this chapter; the imposed selection criteria are summarised below:

1. We restricted ETG catalogue inclusion to sources with HST optical magnitudes of $z_{850} < 23$ that were measured to be cosmologically distant (i.e., $z > 0.05$). The requirement of $z_{850} < 23$ ensures that the photometric redshifts of the remaining sources are of high quality [3] and provides a highly optically complete (see Fig. 5.1) sample of relatively bright optically luminous ETGs out to $z \approx 1.2$. Note that these photometric redshifts were computed using a redshift training procedure that implements spectroscopic redshifts. The true accuracy of the photometric redshifts is expected to be < 6-7 times worse than those available for sources with spectroscopic redshifts (see Luo et al. 2010 for details). This requirement further restricts our study to sources where HST imaging is available, thus allowing for further visual inspection of the optical morphologies to reasonably good precision (see criterion 5 below). This criterion restricted our working sample to 9732 CDF sources.

2. We required that the sources are located within $6'$ of at least one of the six independent *Chandra* aimpoints in the CDFs (i.e., the $\sim$4 Ms CDF-S, four $\sim$250 ks E-CDF-S pointings, and $\sim$2 Ms CDF-N). This criterion ensures that

---

[3]CDFN: median $| z_{spec} - z_{phot} | / (1 + z_{spec}) \approx 0.015$, mean$\approx$0.032 and dispersion$\approx$0.090; E-CDF-S: median $| z_{spec} - z_{phot} | / (1 + z_{spec}) \approx 0.007$, mean$\approx$0.016 and dispersion$\approx$0.046, for $z_{850} < 23$ sources.

the galaxies are located in regions where the *Chandra* imaging is most sensitive and of highest quality (e.g., in these regions the *Chandra* point-spread function is small and relatively symmetric). Applying this additional restriction led to a working sample consisting of 6446 CDF sources.

3. Using the redshift information available, we restricted our galaxy sample to include only sources with $z = 0.05 - 1.2$. The upper redshift limit corresponds to the maximum distances to which we could obtain a complete sample of optically luminous ETGs that were relatively bright ($z_{850} < 23$) and contain useful morphological information from *HST* imaging (see also, e.g., Häussler et al. 2007). Furthermore, this redshift upper limit for our survey allows us to detect the majority of X-ray luminous AGNs with $L_{2-8 \text{ keV}} \geq 10^{42}$ erg s^{-1} located in the $\sim$2 Ms CDF-N and $\sim$4 Ms CDF-S surveys. This therefore defines the redshift baseline over which we can reliably measure hot gas emission through X-ray stacking without significant impact from undetected AGNs (see Section 5.6). As we will discuss below, when performing X-ray stacking analyses, we further exclude galaxies with $z \leq 0.6$ in the more shallow $\sim$250 ks E-CDF-S based on the same logic. For the moment, however, our galaxy sample includes E-CDF-S sources with $z \sim 0.6$–1.2, since we will later use these galaxies to constrain the radio AGN duty cycle in the ETG populations (see Section 5.7.1). The imposed redshift limits led to the inclusion of 5734 galaxies with $z = 0.05 - 1.2$.

4. Since we are ultimately interested in measuring the hot gas X-ray emission from massive ETGs, we required that the galaxies that make up our sample have rest-frame B-band luminosities in the range of $L_{\rm B} = 3$–30 $\times 10^{10} L_{\rm B,\odot}$. As noted by O'Sullivan et al. 2001 (see also Ellis & O'Sullivan 2006 and Boroson et al. 2011), such optically luminous ETGs in the local Universe have relatively massive dark matter halos, and are therefore observed to have 0.5–2 keV emission dominated by hot interstellar gas ($kT \gtrsim 0.3$–1 keV) with minimal contributions from other unrelated X-ray emitting sources (e.g., low-mass X-

ray binaries; see Fig. 5.3b). This further restriction on including only optically luminous galaxies led to 2431 galaxies.

5. To identify passive ETGs in our sample, we made use of the multiwavelength photometry and redshift information discussed above to measure rest-frame $U - V$ colours, and we further used HST imaging to provide morphological information about our galaxies. As noted by Bell et al. (2004), the rest-frame $U - V$ colour straddles the 4000 Å break and provides a sensitive indication of mean stellar age. For our sample, we first required that all galaxies have rest-frame $U - V$ colours redder than

$$(U - V)_{\rm rest} = 1.15 - 0.31z - 0.08(M_V + 22.4), \qquad (5.4.1)$$

where M_V is the absolute V-band magnitude. Equation 5.4.1 (established to be valid out to $z \sim 1$) is based on Bell et al. (2004; see Section 5.7); however we have used a different constant term based on our analysis in Fig. 5.1a where we determine the red/blue galaxy bimodal division by fitting a double gaussian to the distribution of $U - V + 0.31z + 0.08M_V$ for our sample of galaxies after imposing the selection criteria (1) to (3). In this exercise, we applied the redshift dependency from Bell et al. (2004) but shifted the constant (by ~ -0.13) to fit to our sample, which is consistent with a typical colour scatter of < 0.2 mag for the red sequence colour-magnitude relation (see Section 5.6 in Bell et al. 2004). We classified galaxies lying below this divide as 'blue cloud' galaxies and those above as 'red sequence' galaxies. We (A.L.R.D. and B.D.L.) then visually inspected all red-sequence galaxies using grayscale HST images from the z_{850} band, and for the subset of sources located in the GOODS-N and GOODS-S footprints, we also inspected HST false-colour images based on B_{435}, V_{606}, and z_{850} observations. We strictly required the galaxies to have bulge dominant optical morphologies for ETG catalogue inclusion, and we rejected ETG candidates that appeared to be possible edge-on spirals, which may simply be reddened by intrinsic galactic

dust. Furthermore, we removed five sources which were very near the edges of the *HST* images, where morphological classification was not possible. Applying these morphological criteria led to our *final sample of 393 optically luminous ETGs.* The basic properties of our parent sample are shown in Table 5.1.

Table 5.1: Master catalogue

RA (J2000) (1)	Dec (J2000) (2)	z (3)	spec/phot? (4)	z_{850} (5)	M_U (6)	M_B (7)	M_V (8)	L_B $\log(L_{B,\odot})$ (9)	M_* $\log(M_\odot)$ (10)	X-ray? (11)	1.4GHz? (12)	$24\mu m$? (13)
52.8483000	-27.9371400	0.816	p	21.52	-21.79	-22.06	-22.83	11.01	11.16	0	0	0
52.8506205	-27.9442900	1.056	p	21.79	-21.41	-21.78	-22.36	10.91	11.00	0	0	0
52.8527205	-27.7069500	0.526	p	20.62	-20.49	-20.83	-21.65	10.52	10.84	0	0	0
52.8637605	-27.6886300	0.908	p	21.32	-21.22	-21.79	-22.53	10.91	11.29	0	0	0
52.8672000	-28.0023100	0.727	p	21.78	-20.64	-20.96	-21.55	10.57	10.73	0	0	0
52.8714105	-28.0047900	0.727	p	20.82	-21.33	-21.56	-22.24	10.81	11.04	0	0	0
52.8717405	-27.9800800	0.771	p	21.81	-21.25	-21.55	-22.15	10.81	10.88	0	0	0
52.8731805	-28.0159400	0.685	p	20.95	-20.95	-21.33	-22.23	10.72	11.10	0	1	0
52.8741105	-28.0181600	0.727	p	21.64	-20.81	-20.99	-21.67	10.59	10.80	0	0	0
52.8809595	-27.7222000	1.005	p	22.21	-21.27	-21.40	-21.98	10.75	11.02	0	0	0

NOTES: Columns (1)–(2): Optical J2000 coordinates. Column (3): Source redshift. Column (4): s=spectroscopic redshift, p=photometric redshift. Column (5): z_{850} magnitude. Column (6): U-band magnitude. Column (7): B-band magnitude. Column (8): V-band magnitude. Column (9): Logarithmic B-band optical luminosity ($\log(L_{B,\odot})$). Column (10): Logarithmic stellar mass derived from K-band magnitude ($\log(M_\odot)$). Column (11): Indicates whether the source was X-ray detected or not (0=not detected, 1=detected). Column (12): Indicates whether the source was 1.4GHz radio detected or not (0=not detected, 1=detected). Column (13): Indicates whether the source was $24\mu m$ detected or not (0=not detected, 1=detected). Table 5.1 is presented in its entirety (393 sources) in Section 1 of the Appendices of this thesis. Only a portion (first 10 sources) is shown here for guidance.

We note that out of the 393 optically luminous ETGs that make up our sample, 190 of these galaxies lie in the CDF-S or CDF-N at $z = 0.05$–1.2, or in the E-CDF-S at $z = 0.05$–0.6, which could potentially be used in X-ray stacking. The remaining 203 sources lie in the E-CDF-S at $z = 0.6$–1.2. Of the 393 galaxies in our sample, 163 have spectroscopic redshifts, and the remaining 230 sources have high-quality photometric redshifts from the Rafferty et al. (2011) catalogue. Furthermore, 128 out of 190 sources potentially to be used in X-ray stacking have spectroscopic redshifts.

Using both the photometric and spectroscopic redshifts we carry out a basic test of the environment of our sources by searching for neighbouring galaxies with an angular separation of <500kpc from each of our 393 ETGs and within a redshift difference of 0.09 and 0.046 in the CDF-N and E-CDF-S respectively (the dispersion in the photometric redshifts; see footnote 3). We first apply the cut in z_{850} optical magnitude of $z_{850} < 23$ in order to ensure we are only using high quality photometric redshifts and apply a further cut in absolute magnitude of $M_{z850} < -21$. This results in a total galaxy sample of ~ 3500 galaxies in the CDF-N and ~ 1000 in the E-CDF-S. We find a median of 10 ± 1 and 4 ± 2 companions per ETG in the CDF-N and E-CDF-S respectively. We then check the number of neighbours we find for a random galaxy by searching within the comparison galaxy catalogues, and find a slightly lower median number of companions within 500kpc of 7 ± 2 and 3 ± 1 for the CDF-N and E-CDF-S respectively. Therefore, we find tentative evidence that the massive ETGs are in richer than average environments (likely small groups). Since we are using the photometric redshifts there is quite a large uncertainty, however, when using only the spectroscopic redshifts (giving us a much smaller and likely incomplete sample) we do still find evidence for clustered environments. This is not unexpected since we are selecting massive ETGs.

Figure 5.2: The optical B-band luminosity of the ETG sample versus the redshift. The entire sample of 5734 sources after imposing the selection criteria (1) to (3) in Section 5.4 is represented by filled grey circles with the final ETG sample of 393 galaxies as open circles. The boxed areas show the bins from which sources were selected for X-ray stacking analysis, described in Section 5.6.1. The bins were selected to be evenly separated in co-moving volume.

Figure 5.3: (a): The ratio of count-rates in the SB2 and SB1 X-ray bands against redshift. The solid line at $\Gamma_{\mathrm{eff}} = 2.3$ shows our adopted divide between hot-gas dominated sources and possible low mass X-ray binary (LMXB) and/or AGN dominated sources. The SED for a 1.5 keV Raymond-Smith plasma (Raymond & Smith 1977) is shown as a dashed curve. Our stacked results (open triangles) are consistent with this SED. The errors on the band ratio were determined following the 'numerical method' described in § 1.7.3 of Lyons (1991). Band ratios are corrected for differential vignetting between the different bands using the appropriate exposure maps. (b): The rest-frame k-corrected SB (0.5–2 keV) X-ray luminosity (derived from the 0.5–1 keV flux to minimise contribution from LMXBs, and converted to 0.5–2keV luminosity using a 1.5 keV Raymond-Smith plasma SED) versus the faded, rest-frame B-band luminosity (where the evolution of L_{B} is removed, using Faber et al. (2007) to parameterise the effect: $L_{\mathrm{B},z=0} = L_{\mathrm{B}} \times 10^{-0.4 \times 1.23 \times z}$). The solid line and the 1σ dispersion (shaded) show the contribution to X-ray emission from hot gas (O'Sullivan et al. 2001; converted from bolometric to soft-band X-ray luminosity). The dashed line represents the expected contribution to X-ray emission from LMXBs (O'Sullivan et al. 2001); arrows represent the 3σ upper limit X-ray luminosities. Those sources identified as hot-gas dominated from their band ratios are represented here as filled circles, and they lie well within 3σ of the hot gas relation from O'Sullivan et al. (2001). The results from the stacking procedure in six redshift bins are shown as open triangles and these results are based on the SB1 (0.5–1 keV) emission, convolved with the SED of a 1.5 keV Raymond-Smith plasma (Raymond & Smith 1977) to determine the corresponding SB (0.5–2 keV) emission.

Table 5.2: Hot gas dominated X-ray detected galaxies.

RA (J2000) (1)	Dec (J2000) (2)	z (3)	SB1 counts (0.5–1keV) (4)	SB2 counts (1–2keV) (5)	SB2/SB1 (6)	$L_{X,SB}$ 10^{41}erg s^{-1} (7)	$L_{1.4GHz}$ $10^{22}\mu$Jy (8)	$\log(L_{B,z=0})$ $\log(L_{B,\odot})$ (9)	stack(y/n) (10)
03:32:09.706	−27:42:48.110	0.727	$74.36^{+12.16}_{-10.98}$	$125.44^{+15.84}_{-14.67}$	$1.44^{+0.31}_{-0.26}$	$185.79^{+30.38}_{-27.43}$	56.54 ± 2.79	10.90	N
03:32:28.734	−27:46:20.298	0.737	$61.89^{+9.56}_{-8.37}$	$95.67^{+11.59}_{-10.41}$	$1.52^{+0.30}_{-0.26}$	$10.17^{+1.57}_{-1.38}$	59.63 ± 2.81	10.62	Y
03:32:34.342	−27:43:50.092	0.668	$40.22^{+8.36}_{-7.14}$	$52.90^{+9.85}_{-8.64}$	$1.22^{+0.35}_{-0.29}$	$5.19^{+1.08}_{-0.92}$	<5.39	10.50	Y
03:32:38.786	−27:44:48.923	0.736	$8.96^{+5.14}_{-3.85}$	<15.31	<1.61	$1.51^{+0.87}_{-0.65}$	13.10 ± 1.42	10.34	Y
03:32:41.406	−27:47:17.185	0.685	$7.97^{+4.82}_{-3.51}$	$8.41^{+4.99}_{-3.69}$	$1.02^{+1.00}_{-0.59}$	$1.06^{+0.64}_{-0.47}$	<5.72	10.65	Y
03:32:44.088	−27:45:41.461	0.488	$8.70^{+5.15}_{-3.86}$	$11.10^{+5.88}_{-4.62}$	$1.20^{+1.14}_{-0.67}$	$0.49^{+0.29}_{-0.22}$	<2.56	10.67	Y
03:32:46.536	−27:57:13.104	0.770	$25.31^{+9.69}_{-8.50}$	$37.30^{+11.75}_{-10.58}$	$1.12^{+0.67}_{-0.44}$	$68.68^{+26.29}_{-23.08}$	<7.55	10.95	N
03:32:46.949	−27:39:02.916	0.152	$24.77^{+8.11}_{-6.90}$	<25.36	<0.73	$1.32^{+0.43}_{-0.37}$	0.65 ± 0.04	10.64	Y
03:32:52.066	−27:44:25.044	0.534	$17.67^{+7.97}_{-6.76}$	$23.03^{+9.58}_{-8.39}$	$1.13^{+0.84}_{-0.54}$	$17.88^{+8.07}_{-6.84}$	15.66 ± 1.29	10.87	Y
12:36:39.760	62:15:47.832	0.848	$14.42^{+5.37}_{-4.21}$	<11.56	<0.86	$8.41^{+3.13}_{-2.45}$	<6.34	10.49	Y
12:36:44.414	62:11:33.347	1.013	$12.11^{+5.16}_{-3.89}$	$14.00^{+5.37}_{-4.21}$	$1.22^{+0.75}_{-0.52}$	$9.27^{+3.95}_{-2.98}$	876.37 ± 28.74	10.76	Y
12:36:52.895	62:14:44.152	0.321	$35.05^{+7.37}_{-6.21}$	$44.53^{+8.11}_{-6.95}$	$1.35^{+0.38}_{-0.32}$	$1.34^{+0.28}_{-0.24}$	6.41 ± 0.31	10.35	Y

NOTES: Columns (1)–(2): Optical J2000 coordinates. Column (3): Source redshift. Column (4): (0.5–1 keV) net counts. Column (5): (1–2 keV) net counts. Column (6): (1–2 keV)/(0.5–1 keV) count-rate ratio (SB2/SB1). Column (7): Rest-frame 0.5–2 keV luminosity (ergs s^{-1}) derived from SB1 counts and Raymond-Smith plasma SED. Column (8): Radio luminosity ($L_{1.4\ GHz}$). Column (9): Logarithm of the B-band optical luminosity ($\log L_{B,\odot}$), Column (10): Indicates whether the source was included in our stacking analyses (Y/N).

5.5 Multiwavelength characterisations of ETGs using ancillary data

In this section, we make use of the extensive multiwavelength data available in the CDFs to identify both passive and non-passive (e.g., star-forming and AGN) ETGs. In the next section (Section 5.6), we will perform X-ray stacking analyses of the passive ETG population to measure directly the evolution of the mean hot gas emission. In the analyses below, we match our 393 optically luminous ETG optical source positions to those provided in multiwavelength catalogues using closest-counterpart matching, which is a reasonable method provided that the optimum matching radius is carefully selected. We selected the optimum matching radius for each multiwavelength catalogue by first performing matching using a $30''$ matching radius and then observing the distribution of closest-counterpart matching offsets. For all catalogues discussed below (i.e. optical-x-ray, optical-radio, optical-infrared matching), we found the distribution of offsets to peak close to $\sim 0''$, reach a minimum at $\sim 1''\!.5$, and subsequently rise toward larger offsets due to spurious matches. A matching radius of $1''\!.5$ was therefore adopted as the optimum matching radius for all but the radio catalogues, for which the positional errors are very small, therefore $1''$ was more appropriate. Matches were visually inspected to further ensure they were sensible. The number of spurious matches was determined for each data set analytically by calculating the ratio between the total area covered by the parent sample sources, each with $1''\!.5$ or $1''$ matching radius ($\pi(1.5)^2 \times 393 \approx 2778$sq. arcsec or $\pi(1.0)^2 \times 393 \approx 1234$sq. arcsec respectively) and the total area of the CDFs (within $6'$ of each pointing; 0.188 sq. degrees or 2436480 sq. arcsec). This ratio was then multiplied by the total number of sources in the multiwavelength catalogues that lie within $6'$ of one of the *Chandra* aimpoints.

Figure 5.4: Selecting passive galaxies to use in the X-ray stacking analysis based on their IRAC 5.8 μm/8 μm colours. The solid curve shows the median 5.8 μm/8 μm colours of the 5000 model passive galaxy SEDs generated by *hyperz* with the 2σ dispersion shown as dotted curves. In this figure, the most active galaxies (e.g. star-forming galaxies) have redder colours than those expected for passive ETGs. The error bars shown at $z = 0.05$ are representative error bars, plotted at the median 5.8μm/8μm colour for the following three cases: sources lying within $\pm 2\sigma$ of the passive line; outliers with lower signal to noise with bluer colours ($> 2\sigma$ above the passive line); redder AGN and active star-forming galaxies ($> 2\sigma$ below the passive line). In our stacking analysis in Section 5.6.1 we test the effect of including/not including the sources lying in regions which are $> 2\sigma$ away from the passive line but which have not otherwise been classified as active, however, there is very little difference in the final result aside from signal-to-noise. In our final stacking analysis presented in Fig. 7 these sources have therefore been included.

5.5.1 X-ray properties of ETGs

The ultradeep *Chandra* data in the CDFs provide a direct means for classifying X-ray detected ETGs as either hot gas dominated or likely AGNs. We used the published main catalogues for each of the CDFs, which consist of 503 sources in CDF-N ($\sim$2 Ms; $\sim$0.12 deg^2 survey, Alexander et al. 2003), 740 sources in the CDF-S ($\sim$4 Ms; $\sim$0.13 deg^2 survey, Xue et al. 2011), and 762 sources in the E-CDF-S (four contiguous $\sim$250 ks *Chandra* observations that flank the CDF-S proper; $\sim$0.31 deg^2, Lehmer et al. 2005). Using our sample of 393 ETGs, the optical coordinates of the galaxies were matched to the CDF X-ray catalogue positions using our adopted matching radius of $1\rlap{.}''5$. When an ETG matched to a source in both the E-CDF-S and the CDF-S simultaneously (due to overlap between the E-CDF-S and CDF-S) we chose to use the data for the CDF-S, since these X-ray data are significantly deeper with smaller positional errors. In total, 55 X-ray matches were found once repetitions had been removed, including 11 in the CDF-N and 44 in the E-CDF-S region. The fraction of spurious matches in all the CDFs together was estimated to be $\sim$2.8% (or $\sim$2 expected spurious matches).

In Fig. 5.3a, we show the SB2/SB1 count-rate ratio versus redshift for the X-ray detected ETGs in our sample. The SB2/SB1 ratio provides an effective discriminator of the X-ray spectral shape in the SB, the energy regime where hot gas is expected to dominate. Typically, $z \sim$ 0-2 AGNs have $\Gamma_{\mathrm{eff}} \sim$ 1.8-2.3 (e.g., Alexander et al. 2005, Vignali et al. 2002, Reeves & Turner 2000). Therefore we took the upper limit of this range and conservatively classified sources with SB2/SB1 $\leq$ 1.7 (corresponding to $\Gamma_{\mathrm{eff}} \geq$ 2.3) as sources having SB emission dominated by a hot gas component. Sources detected only in SB2 (i.e., having only a lower-limit on SB2/SB1), that had SB2/SB1 limits below our adopted cut were not classed as hot gas dominated sources. Sources with SB2/SB1 hardness ratio greater than this cut (i.e., SB2/SB1 > 1.7), have X-ray emission likely dominated by low mass X-ray binaries (LMXBs) or X-ray AGNs. However, by construction, our choice to study optically luminous ETGs will inherently minimise contributions from LMXB-dominated sys-

tems and therefore AGNs are expected to dominate the SB2/SB1 > 1.7 population (see below). Our SB2/SB1 criterion indicated 12 hot-gas dominated sources and 25 likely AGNs (Fig. 5.3a). The SB2/SB1 ratios imply that a Raymond-Smith plasma (Raymond & Smith 1977) of kT~1.5keV is a good spectral model from which to convert count-rates to flux. In Table 5.2, we tabulate the properties of these X-ray detected ETGs.

In Fig. 5.3b, we show the 0.5–2 keV luminosity (hereafter, L_X) versus $L_{B,0}$ (see Section 5.6 for details) for the ETGs in our sample. In order to minimise the contribution from LMXBs we calculated the rest-frame 0.5–2 keV luminosities $L_{X,SB}$ based on the 0.5–1 keV SB1 fluxes provided in the *Chandra* catalogues and convert them to 0.5–2 keV SB fluxes, applying a k-correction:

$$L_X = 4\pi d_L^2 f_X k \quad (\text{erg s}^{-1}), \tag{5.5.2}$$

where d_L is the luminosity distance in cm, f_X is the 0.5–2 keV flux in units of erg cm^{-2} s^{-1}. The quantity k is the redshift-dependent k-correction. For sources that were characterised as hot gas dominated we used the observed 0.5–1 keV flux and a Raymond-Smith plasma SED (with $kT_X = 1.5$ keV; Raymond & Smith 1977; see Fig. 5.3a) to compute L_X. For sources that were identified as AGN dominant, we used a power-law SED (with $\Gamma = 1.8$) and the observed 0.5–2 keV flux to compute L_X. The solid line and shaded region shows the best-fit local relation and 1σ dispersion for hot gas dominated ETGs, and the dashed line shows the expected contribution from LMXBs (based on O'Sullivan et al. 2001 and typically a factor of ~10 below the hot gas contribution). We note that nearly all ETGs without X-ray detections (plotted as upper limits) and the 12 ETGs with SB2/SB1 band ratios consistent with being hot gas dominated (highlighted with filled circles) also have L_X/L_B values similar to those observed for local hot gas dominated ETGs. The majority of the remaining X-ray detected sources with SB2/SB1 > 1.7 are expected to be AGNs. As Fig. 5.3b shows, these sources typically have large values of L_X/L_B, again consistent with that expected from AGNs (see O'Sullivan et al. 2001; Ellis & O'Sullivan 2006). To

Figure 5.5: Radio images of the three extended radio matches discovered by visual inspection of the radio images. The axes give the distance to the centre of the image in arcseconds. All of these extended sources have significantly higher 1.4GHz fluxes (1.2–4.8mJy) than the other 16 radio-bright AGN in our ETG sample.

further check for AGNs in our sample we cross-matched our optical catalogue with spectroscopic data from Szokoly et al. (2004), Mignoli et al. (2005), Ravikumar et al. (2007), Boutsia et al. (2009) and Silverman et al. (2010) using a $1\rlap{.}''5$ radius in order to identify any sources with spectral features indicative of AGN, such as broad emission lines. We identified two potential broad line AGN in the E-CDF-S, both of which were X-ray detected and had already been flagged as likely AGN using our band ratio analysis (Fig. 5.3).

5.5.2 5.8–24 μm properties of ETGs

In order to explore further whether the ETGs contained more subtle signatures of AGN or star-formation activity than provided by their X-ray and optical spectro-scopic properties, we utilised *Spitzer* photometry over the 5.8–24 μm range. We began by using *Spitzer* IRAC 5.8 μm/8 μm colours. Since AGN tend to be redder than galaxies in the mid-infrared, the 5.8 μm/8 μm colour can be used to identify AGNs when the continuum is dominated by a rising power law component rather than a dropping stellar component (e.g., Stern et al. 2005). Similarly, the SEDs of powerful star-forming galaxies, containing a large hot dust component, may exhibit this rise towards redder wavelengths and may also be identified by their 5.8 μm/8 μm colour.

In the E-CDF-S, we take the photometry in these channels from Damen et al. (2011) and in the CDF-N, we take photometry from GOODS-N, cutting both catalogues at a signal-to-noise level of S/N< 5. [4]

We matched the positions from our sample of 393 ETGs to the *Spitzer* IRAC catalogues using a matching radius of 1″.5 and found 384 matches. We estimated a spurious matching fraction of ∼3.1% (∼12 matches). In Fig. 5.4, we show the 5.8 μm/8 μm colour versus redshift for the 384 ETGs in our main sample. To determine the expected 5.8 μm/8 μm colours for passive galaxies, we used the code `hyperz` (Bolzonella et al., 2000) with the SED library of Bruzual A. & Charlot (1993) to generate 5000 model galaxy SEDs based on a wide range of star formation histories and redshifts. For each galaxy, we adopted a formation redshift randomly selected to lie between the galaxy redshift (i.e., $t_{\mathrm{age}} = 0$) and $z \approx 5$. In Fig. 5.4, we plot the running median of the 5.8 μm/8 μm colours for the `hyperz` sample, after imposing the rest-frame $U - V$ color criterion in equation 5.4.1 (the solid line in Fig. 5.4), and calculate the 2σ dispersion either side of the median (the dashed lines on Fig. 5.4). This curve was calculated by binning the data into bins of $\Delta z = 0.05$ and computing the median and dispersion for each bin. Sources with very red IRAC colours lying below the passive line are likely AGN or star forming galaxies, and it can be seen that X-ray, radio and 24 μm detected galaxies tend to lie below the solid line. In our stacking analyses (see Section 5.6.1), we experimented with removing the sources that lie outside of the 2σ dispersion boundaries of our hyper-z normal galaxy envelope. However, we found no difference in the general results since most of the sources exhibiting non-passive activity (either due to star formation or AGNs) had already been identified by other indicators, and we therefore decided to include all of our galaxies in our subsequent stacking analyses (unless otherwise flagged as non-passive). As an additional test we experimented with the IRAC colour-colour diagnostic as in Stern et al. (2005), Fig. 1, however, we find that only three of our sources lie in their region of active sources, all three of which we have already flagged

---

[4]http://data.spitzer.caltech.edu/popular/goods/

as active sources through our other diagnostics.

To identify additional ETGs in our sample that have signatures of star formation or AGN activity from dust emission, we cross-matched our ETG sample with *Spitzer* MIPS 24 μm catalogues. The E-CDF-S was observed with *Spitzer*/MIPS as part of the FIDEL legacy program [5] (PI: Mark Dickinson; see § 2.1.2–2.1.3 of Magnelli et al. 2009). We have used a catalogue of 20329 sources produced by the DAOPHOT package in IRAF (see § 2.3 of Biggs et al. 2011). The MIPS 24 μm sensitivity over the E-CDF-S varies significantly across the $30' \times 30'$ field, with exposure times ranging from 11,000–36,000 s. We make use of sources having signal-to-noise of at least 5σ ($\sim$30–70 μJy limits; see Magnelli et al. 2009). For the CDF-N, we made use of the publicly available GOODS *Spitzer* Legacy survey catalogues of 1198 sources (PI: M. Dickinson). We utilised the 5σ sample (flux limits of 70 μJy in the E-CDF-S and 30 μJy in the CDF-N; Magnelli et al. 2009). Using a $1''\!.5$ matching radius we found a total of 20 matches to the 393 ETGs in our sample; three in the CDF-N and 17 in the E-CDF-S, with $\sim$1.7 spurious matches expected. 24 μm provides a robust diagnostic of the presence of cold dust emission from the circumstellar envelopes of young embedded UV-luminous stars, characterised by a rising SED through the mid-infrared Muzerolle et al. (2004). Such systems are expected to contain significant X-ray contributions from populations that are unrelated to hot gas, and we therefore classify these 20 sources to be star-formation active systems.

5.5.3 Radio properties of ETGs

To measure powerful radio emission produced by either radio-loud AGNs or star-formation activity, we cross-matched the optical coordinates of the parent sample with 1.4 GHz VLA catalogues in the CDFs (using a $1''$ matching radius). We utilised the catalogue from Miller et al. (2008), but included additional sources at S/N>5 (Miller et al. 2013) for the E-CDF-S region, which contains 940 radio sources with S/N> 5 and reaches a 5σ limiting flux density of 30 μJy with a synthesised

---

[5]http://irsa.ipac.caltech.edu/data/SPITZER/FIDEL/

beam of $2.8'' \times 1.6''$. For the CDF-N, we utilised the catalogue from the Morrison et al. (2010) GOODS-N observations, which provides entries for 1227 discrete radio sources with S/N> 5 and 5σ flux density limit of 20 μJy at the field centre, with a $1.7''$ beam. In total, 24 radio detected counterparts to the 393 ETGs were found (six in the CDF-N and 18 in the E-CDF-S) and 15 of these radio detected ETGs were also X-ray detected. The spurious matching fraction was estimated to be $\sim$0.5% ($\sim$0.1 matches) and therefore negligible. Since the radio emission from radio luminous AGNs can be extended (e.g., Fanaroff & Riley 1974), the radio maps were carefully inspected by eye against the $1''$ radius matching circles (overlaid at the locations of the parent sample positions) to verify the accuracy of the matches and isolate extended sources. We identified three bright extended sources that were all identified using closest-counterpart matching; radio images of these sources have been provided in Fig. 5.5. We note that some of these individual sources have been well studied in the literature (e.g. J123644.4; Richards et al. 1998, J033238.8 and J033210.1; Kellermann et al. 2008).

We calculated rest-frame 1.4 GHz monochromatic luminosities for all radio detected sources following,

$$L_{1.4\ \mathrm{GHz}} = 4\pi d_{\mathrm{L}}^2 f_{1.4\mathrm{GHz}} 10^{-36} (1+z)^{\alpha-1} \mathrm{W\ Hz^{-1}}, \qquad (5.5.3)$$

where $f_{1.4\ \mathrm{GHz}}$ is the 1.4 GHz flux density (μJy) and α is the radio spectral index for a power-law radio SED (i.e., $F_\nu \propto \nu^{-\alpha}$). We adopted a power-law spectral index of $\alpha = 0.85$ (see Richards 2000 for motivation). For normal galaxies without active radio AGNs, radio emission originates from HII regions and Type II and Ib supernovae, which produce synchrotron radiation from relativistic electrons and free-free emission (Condon 1992). In passive ETGs, the contribution from these processes is unlikely to exceed $10^{18-19}\,\mathrm{W\,Hz^{-1}}$ (Ledlow 1997). The radio luminosity for all radio detected sources in our sample was greater than 10^{20} W Hz^{-1}, which is expected given the flux limits of our survey. Therefore, detecting them at all suggests an excess of non-passive activity from either star-formation (SFR $\gtrsim 0.1\ M_\odot$ yr^{-1})

or AGN activity.

To discriminate between star-formation and AGN activity in the radio-detected population, we use the well-known strong correlation between radio and far-infrared emission, which extends to cosmologically significant redshifts (at least $z \approx 1$; Appleton et al. 2004, and $z > 2$ using total infrared luminosity; Mao et al. 2011). For all our ETGs that are detected at both 24 μm and 1.4 GHz we measured the quantity $q_{24} \equiv \log(f_{24\mu m}/f_{1.4\text{GHz}})$ (Appleton et al., 2004) (where $f_{24\mu m}$ and $f_{1.4\text{GHz}}$ are observed fluxes). Radio-excess AGN can be identified by comparing their infrared emission to their radio emission, as their radio emission is significantly brighter than their infrared emission when compared to star-forming galaxies, which fit tightly along the far-infrared/radio correlation. Following Del Moro et al. (2013) demonstrating the typical q_{24} of radio-excess AGN based on starburst SEDs, we apply a selection of $q_{24} < 0.5$ to be indicative of radio AGN. This results in 19 of the 24 radio-detected galaxies being classified as radio AGN, with the remaining five radio-detected galaxies being classified as star-forming galaxies (as indicated in Table 5.4). In this exercise 10 ETGs with 24 μm detections but not radio detections were excluded from the final sample. We note that 16 of the 24 radio AGN were also X-ray detected. Table 5.4 shows the matched radio sources that are classified as radio AGN from the q$_{24}$ analysis, and which are used to estimate the AGN heating in Section 5.7. We note that this approach identified all the sources with extended radio emission in Fig. 5.5 as radio AGN.

In Table 5.3, we summarise the various source classifications described in Section 5.5 for clarity. Of the original 393 galaxies in the ETG sample 190 of them can potentially be used in the X-ray stacking (see Section 5.4). However, through various classification schemes we find that 32 of these are non-passive (potential X-ray AGN or star-forming galaxies) and are therefore excluded from the main stacking sample, thus leaving a sample of 158 passive galaxies which are suitable for X-ray stacking analyses. Of the 393 ETGs, 24 are radio detected and 20 of these are likely radio AGN while the other five have radio emission dominated by star formation. We classify a further 10 sources as likely star-forming galaxies, which have detections

Table 5.3: Summary of source classifications.

Classification	No. of galaxies
ETG sample	393
X-ray detected	55
Passive X-ray detected	12
Potential LMXB/X-ray AGN	43
Radio detected	24
Radio AGN	19
24μm detected	20
Star-forming galaxies	15
X-ray stacked galaxies (main)	158
X-ray stacked galaxies (faded)	60

only in 24 μm and not radio, and lower limits of $q_{24} > 0.5$.
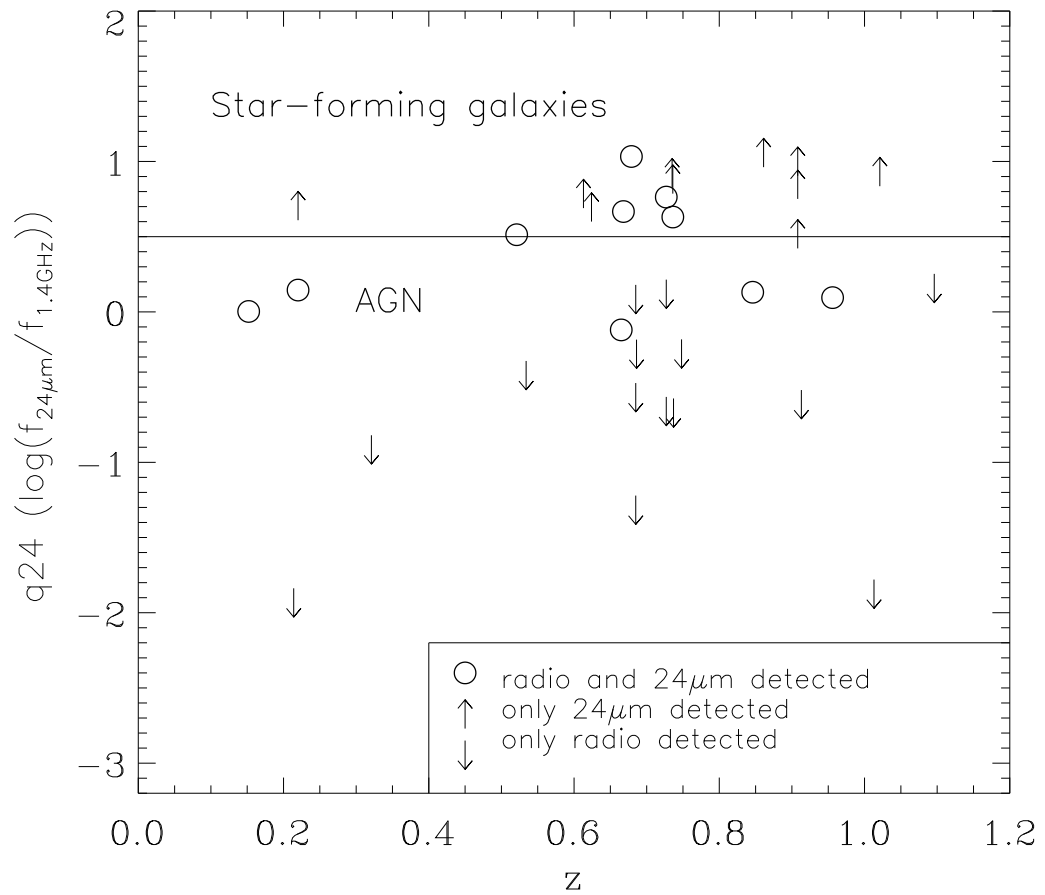
Figure 5.6: Ratio of observed flux in 24 μm and radio (1.4GHz) versus redshift. Sources which lie below the solid line (Del Moro et al., 2013) are taken to be radio AGN.

Table 5.4: Radio-bright ETGs.

RA (J2000) (1)	Dec (J2000) (2)	z (3)	$f_{1.4\text{GHz}}$ (μJy) (4)	$\log(\text{L}_{1.4GHz})$ (10^{23}WHz^{-1}) (5)	$f_{24\mu m}$ (μJy) (6)	q_{24} (7)	$\text{L}_{X,SB}$ (10^{42}erg s^{-1}cm^{-2}) (8)	$\log(\text{L}_B)$ ($\log(\text{L}_{B,\odot})$) (9)	Extended (Y/N) (10)	Note (AGN/SF) (11)
03:31:29.563	-28:00:57.384	0.685	46.3±8.8	0.9±0.2	<70	<0.18	...	10.7	N	A
03:31:32.210	-27:43:08.076	0.956	68.7±7.3	2.9±0.3	85.5±6.2	0.09	<5.1	10.9	N	A
03:31:39.041	-27:53:00.096	0.220	61.2±7.0	0.08±0.01	85.5±5.3	0.15	...	10.6	N	A
03:31:40.044	-27:36:47.628	0.685	208.1±15.4	4.0±0.3	<70	<-0.47	...	11.2	N	A
03:31:45.895	-27:45:38.772	0.727	42.7±6.8	0.9±0.2	<70	<0.22	...	11.3	N	A
03:31:57.782	-27:42:08.676	0.665	97.2±6.5	1.7±0.1	73.7±3.1	-0.12	8.4	10.8	N	A
03:32:09.706	-27:42:48.110	0.727	257.2±12.7	5.6±0.3	<70	<-0.57	18.6	11.3	N	A
03:32:10.137	-27:59:38.220	0.685	1165.0±36.0	22.2±0.7	<70	<-1.22	...	11.2	Y	A
03:32:19.305	-27:52:19.330	1.096	39.1±6.2	2.3±0.4	<70	<0.25	...	11.3	N	A
03:32:28.734	-27:46:20.298	0.737	263.3±12.4	6.0±0.3	<70	<-0.58	1.0	11.0	N	A
03:32:28.817	-27:43:55.646	0.214	4814.0±103.0	6.3±0.1	<70	<-1.84	0.04	10.6	Y	A
03:32:38.786	-27:44:48.923	0.736	58.0±6.3	1.3±0.1	247.8±2.4	0.63	0.2	10.7	N	S
03:32:39.485	-27:53:01.648	0.686	107.0±6.2	2.04±0.12	<70	<-0.18	<0.2	11.0	N	A
03:32:46.949	-27:39:02.916	0.152	105.5±7.0	0.060±0.004	106.2±2.7	0.003	0.1	10.7	N	A
03:32:48.177	-27:52:56.608	0.668	32.8±6.2	0.6±0.1	152.4±2.3	0.67	4.9	11.2	N	S
03:32:52.066	-27:44:25.044	0.534	148.3±12.2	1.6±0.1	<70	<-0.326	1.79	11.1	N	A
03:33:05.671	-27:52:14.268	0.521	55.7±6.8	0.6±0.1	181.5±7.6	0.51	<2.4	11.3	N	S
03:33:15.427	-27:45:24.012	0.727	63.5±6.9	1.4±0.2	368.3±2.7	0.76	...	10.6	N	S
12:36:01.813	62:11:26.659	0.913	99.2±5.5	3.8±0.2	<30	<-0.52	...	10.9	N	A
12:36:08.137	62:10:36.136	0.679	213.1±7.9	4.0±0.2	2300.0±12.9	1.03	0.2	10.7	N	S
12:36:17.098	62:10:11.554	0.846	65.3±8.3	2.1±0.3	88.2±6.4	0.13	7.95	10.7	N	A
12:36:22.705	62:09:46.313	0.748	45.7±5.1	1.1±0.1	<30	<-0.18	...	10.6	N	A
12:36:44.414	62:11:33.347	1.013	1805.1±59.2	87.6±2.9	<30	<-1.78	0.9	11.3	Y	A
12:36:52.895	62:14:44.152	0.321	198.3±9.6	0.64±0.03	<30	<-0.82	0.1	10.5	N	A

NOTES: Columns (1)–(2): Optical J2000 coordinates. Column (3): Redshift. Column (4): Radio (1.4GHz) flux density (μJy). Column (5): Radio (1.4 GHz) luminosity ($\log 10^{23}$W Hz^{-1}). Column (6): 24 μm flux density (μJy). Column (7): q_{24} ratio, ($\log f_{24\mu m}/f_{1.4GHz}$). Column (8): 0.5–2 keV flux (10^{42} ergs s^{-1} cm^{-2}) derived from SB1 (0.5–1 keV) counts and converted using the 1.5 keV Raymond-Smith plasma. Column (9): B-band luminosity ($\log L_{B,\odot}$). Column (10): Indicates whether there is extended emission (Y=yes, N=no). Column (11): Note on classification: S = radio detected ETGs for which the radio emission is likely dominated by star formation (as implied by their q_{24} value), A = radio emission dominated by an AGN.

5.6 Cosmic history of X-ray emission from massive ETGs

Approximately 90% of the ETGs in our passive sample are undetected in the X-ray (338 galaxies). Therefore to measure the hot gas emission from the whole population it is necessary to implement X-ray stacking techniques. This investigation focuses on measuring the cooling of the hot gas in ETGs, which dominates emission at soft X-ray energies (0.5–2 keV), as opposed to LMXBs, which dominate emission in the hard band (2–8 keV). Stacking analyses were therefore carried out in the soft bands (i.e., SB1 and SB2), which we expect to be dominated by hot-gas emission and to have minimal contributions from LMXBs. In Fig. 5.2, we plot six redshift intervals of galaxies with $L_B = (3 - 30) \times 10^{10} L_{B,\odot}$ where we performed stacking analyses for each subsample (solid boundaries). The redshift divisions were chosen to encompass roughly equal intervals of comoving volume, and the larger redshift interval spacing beyond $z \approx 0.6$ is the result of excluding from our stacking analyses sources that were within the ~250 ks exposure of the E-CDF-S (see Section 5.4 for details).

We note that previous studies (e.g., Bell et al. 2004; Faber et al. 2007) have shown that, from $z = 1 - 0$, the B-band luminosity of typical massive ETGs fades by ~1 mag. To estimate the mean X-ray luminosity evolution for an ETG population with similar $z = 0$ B-band luminosities ($L_{B,z=0}$), we thus constructed six "faded" redshift-divided subsamples of ETGs with $L_{B,z=0} = (3 - 30) \times 10^{10} L_{B,\odot}$. We calculated $L_{B,z=0}$ following the Faber et al. (2007) prescription: $L_{B,z=0} = L_B \times 10^{-0.4 \times 1.23 \times z}$. With these faded luminosities only 60 of the 158 stacking sources lay within the allowed range of optical luminosities. In total, we stacked 12 subsamples of ETGs (six main and six faded) with both the main and faded samples having the same divides in redshift but with 158 sources in the total main sample and only 60 in the total faded sample.

5.6.1   X-ray stacking technique

Our stacking procedure, summarised below, makes use of images, background maps, and exposure maps that were constructed by Alexander et al. (2003) for the $\sim$2 Ms CDF-N, Lehmer et al. (2005) for the $\sim$250 ks E-CDF-S, and Xue et al. (2011) for the $\sim$4 Ms CDF-S.

We chose to use circular apertures of constant radii to extract on-source counts. We chose to extract X-ray counts (source plus background) from a $1''\!.5$ radius circular aperture centered on the locations of sources that were within $6'$ of any of the six *Chandra* aimpoints (the $\sim$2 Ms CDF-N, the $\sim$4 Ms CDF-S, and the four $\sim$250 ks pointings in the E-CDF-S). These choices of source inclusion radius and extraction aperture radius were previously found to optimise the stacked signal (see, e.g., Lehmer et al. 2005b, 2007) and are therefore implemented here. For each source, we used our source extraction aperture to extract source plus background counts s_i from images and exposure times t_i from exposure maps. For each stacked sample, total source plus background counts were computed as $S = \sum_i s_i$ and exposure times were computed as $T = 0.03 \sum_i t_i$ (the 0.03 factor comes from the fact that t_i is the sum of exposure map values over $\sim$30 pixels).

Background and exposure maps were then used to measure the background counts and exposures for each source. For this exercise, we used a $15''$ radius circular aperture centred on the location of each source to extract local background counts $b_{i,\text{local}}$ and exposure times $t_{i,\text{local}}$. The on-source background counts b_i, were estimated following $b_i = b_{i,\text{local}} \times t_i/t_{i,\text{local}}$. Total stacked background counts were then obtained through the summation $B = \sum_i b_i$.

For each stacked sample, any galaxy that was classified as a normal ETG (see Section 5.5) was stacked. The stacking procedure was carried out with three different samples: (a) a sample including all radio AGN, passive X-ray detected sources (10 galaxies) and passive X-ray undetected sources; (b) a sample including only X-ray undetected galaxies and (c) a sample including passive X-ray undetected galaxies and radio AGN but excluding passive X-ray detected galaxies. However, we found

that the inclusion of both X-ray detected normal galaxies and radio AGN in the stacking did not significantly change our results, implying that most X-ray luminous AGN had been successfully excluded from the sample via direct X-ray detection and classification. Therefore all radio AGN and X-ray detected normal galaxies (thus all passive galaxies) were included in all of the stacks resulting in a final sample of 158 and 60 passive ETGs to be stacked in the main and faded samples, respectively.

For each stacked sample, we measured the signal-to-noise ratio ($S/N = (S - B)/\sqrt{B}$). For a significant detection, we required that $S/N > 3$, and for such stacks, we measured net counts as $N = S - B$. When a stacked sample was not detected, we placed 3σ upper limits on the net counts i.e. $N < 3\sqrt{\alpha_S^2 + \alpha_B^2}$, where α_S and α_B are the bootstrapped errors on the total and background counts respectively. The error on the net counts was determined by applying a bootstrapping method. For each stacked sample containing n galaxies, we randomly drew n sources from the sample (allowing for multiple draws of the same source) and restacked the scrambled sample to measure net counts. This exercise was performed 1000 times for each stacked sample, thus giving a sense of the variance of the population. The count-rates Φ for each stacked sample were determined as $\Phi = \xi N/T$, where ξ is a mean aperture correction. Since many of the sources with relatively large PSFs (at $\approx$3–6$'$ off axis) had aperture radii that did not encompass the whole PSF, it was necessary to factor in a correction (ξ_i) for each of the stacked sources. The average correction factor used was computed as $\xi \equiv \sum_i \xi_i t_i / \sum_i t_i$ where ξ_i and t_i are the correction factors and exposure times measured for each individual source. The stacked count-rates Φ were then converted to fluxes using the SED for a 1.5 keV Raymond-Smith plasma (Raymond & Smith 1977; see Fig. 5.3a for motivation and see Table 5.5 for kT_X values used in each stack sample). Errors on the count-rate to flux conversion were calculated by propagating errors on the mean SB2/SB1 ratio, which can be used as a proxy for temperature in our Raymond-Smith SED. The errors on the luminosity were determined by propagating the bootstrapped errors on the source counts and the errors on the countrate-to-flux conversion factor based on the errors in the SED temperature described above. When calculating luminosities,

the luminosity distance is calculated using the mean redshift in each bin (since as Fig. 5.2 demonstrates, the redshifts are quite evenly distributed in each stacking bin).

Table 5.5: X-ray stacking properties.

z_{mean}	N_{tot}	Net counts (S-B)		Exposure time		S/N		f_{SB1}	kT_X	$L_{X,SB}$	$L_{B,mean}$	$L_{X,SB}/L_B$
		SB1	SB2	SB1 (Ms)	SB2 (Ms)	SB1	SB2	$\log(\mathrm{erg\ s^{-1}cm^{-2}})$	(keV)	$\log(\mathrm{erg\ s^{-1}})$	$\log(\mathrm{L}_{B,\odot})$	$\log(\mathrm{erg\ s^{-1}L_{B,\odot}^{-1}})$
(1)	(2)	(3)	(4)	(5)	(6)	(7)	(8)	(9)	(10)	(11)	(12)	(13)
							General Sample					
0.278	19	80.7±42.2	125.3±66.3	12.2	12.3	29.3	36.4	-16.1	$1.3^{+0.2}_{-0.1}$	40.7±0.2	10.7	29.9±0.2
0.519	19	38.8±20.3	55.0±28.1	25.7	26.3	9.9	11.1	-16.8	$1.3^{+0.6}_{-0.1}$	40.6±0.2	10.8	29.8±0.2
0.630	33	58.2±40.5	97.3±50.2	85.2	85.5	7.7	10.2	-17.0	$1.6^{+0.5}_{-0.4}$	40.5±0.3	10.7	29.8±0.2
0.790	43	112.6±59.0	178.8±93.5	111.6	111.6	12.7	16.5	-16.9	$1.5^{+0.3}_{-0.3}$	40.9±0.2	10.8	30.2±0.2
0.973	32	35.4±12.9	43.5±17.8	71.7	71.6	5.0	5.1	-17.1	$1.2^{+1.2}_{-0.1}$	40.9±0.2	10.8	30.1±0.1
1.124	12	6.1±4.8	9.4±6.8	34.7	34.7	1.3	1.5	<-17.2	...	<40.9	10.9	<30.1
							Faded Sample					
0.284	13	29.3±23.2	32.0±24.3	6.2	6.4	15.8	13.3	-16.5	$1.0^{+0.2}_{-0.1}$	40.3±0.3	10.7	29.7±0.3
0.518	11	35.1±17.6	51.9±24.5	17.6	18.2	10.9	13.0	-16.8	$1.33^{+0.03}_{-0.45}$	40.5±0.2	10.7	$29.9^{+0.3}_{-0.2}$
0.632	13	49.4±34.9	79.4±48.4	37.3	37.7	9.8	12.6	-17.1	$1.5^{+0.2}_{-0.6}$	40.4±0.3	10.6	29.8±0.2
0.767	15	105.8±54.9	151.0±85.2	41.7	41.7	19.4	22.3	-16.9	$1.3^{+0.1}_{-0.4}$	40.8±0.2	10.6	30.2±0.3
0.980	5	16.5±8.5	18.4±9.6	13.4	13.3	5.4	4.8	-17.4	$1.2^{+0.5}_{-0.4}$	40.6±0.2	10.7	30.0±0.3
1.119	3	2.6±3.1	2.8±1.4	9.6	9.6	1.0	0.8	<-17.5	...	<40.7	10.6	<30.0

NOTES: Column (1): Mean redshift of bin. Column (2): Number of sources in stacking bin. Columns (3)–(4): Net counts for SB1 and SB2. Columns (5)–(6): Exposure times in Ms for SB1 and SB2. Columns (7)–(8): Stacked signal-to-noise ratio for SB1 and SB2. Column (9): Logarithm of the stacked SB1 flux (ergs s^{-1} cm^{-2}). Column (10): X-ray temperature (keV). Column (11): Logarithm of the stacked 0.5–2 keV luminosity L_X (ergs s^{-1}) measured using the SB1 flux and an assumed Raymond-Smith plasma SED with 1.5 keV temperature. Column (12): Logarithm of the B-band luminosity (for the faded sample, we list $L_{B,z=0}$). Column (13) Logarithm of the 0.5–2 keV to B-band luminosity ratio (for the faded sample, we list $L_X/L_{B,z=0}$).

5.6.2   X-ray stacking results

The results of stacking the X-ray data of the sample, are summarised in Table 5.5. In Figs. 5.3a and 5.3b, we have overlaid our stacking results, demonstrating that our galaxies have SB2/SB1 count-rate ratios consistent with our adopted 1.5 keV Raymond-Smith plasma SED (which we use to convert count-rates to fluxes and luminosities) and L_X versus $L_{B,z=0}$ values consistent with local hot gas dominated ETGs. In Figs. 5.7a, b, we display the rest-frame 0.5–2 keV luminosity (computed following equation 5.5.2) per B-band luminosity L_X/L_B versus redshift for our main and faded samples, respectively (*circles*). The 10 individually X-ray detected, hot gas dominated ETGs are shown as triangles in Figs. 5.7a and b (only eight are shown on Fig. 5.7b as only eight fulfilled the constraints of the stacking for the faded sample). Only 10 out of the 12 galaxies shown in Table 5.2 are included in the stacking as, for stacking, we add the limitation that all galaxies in the E-CDF-S must have $z < 0.6$. As would be expected from an X-ray selected subset, these sources generally have higher values of L_X/L_B. For comparison, we have also plotted the mean L_X/L_B values obtained by Lehmer et al. (2007) for ETGs with $L_B > 10^{10}$ $L_{B,\odot}$ (*squares*).

To constrain evolution to $z = 0$, we take the Boroson et al. (2011) sample of 30 nearby ETGs and select only those 14 with $L_B = (3$–$30) \times 10^{10} L_{B,\odot}$. We convert their 0.3–8 keV luminosities to 0.5–2 keV luminosities using our adopted 1.5 keV Raymond-Smith plasma SED and find a mean value of $\log L_X/L_B = 29.7 \pm 0.2$ (*crosses* in Figs. 5.7a, b). The combination of the Boroson et al. (2011) mean L_X/L_B and our stacking results indicates that there is little apparent evolution in L_X/L_B for these optically luminous ETGs. However, a Spearman's ρ test reveals that the quantity L_X/L_B is correlated with z at the 92% and 96% probability level for the main and faded samples respectively. To constrain the allowable redshift evolution of L_X/L_B, we fit a simple two parameter model to the data $\log L_X/L_B = A + B \log(1+z)$ and find best-fit values of $[A,B] = [29.73 \pm 0.14, \ 1.19 \pm 0.68]$ and $[29.71 \pm 0.14, \ 1.07\pm0.68]$ for the main and faded samples, respectively. These values indicate mild
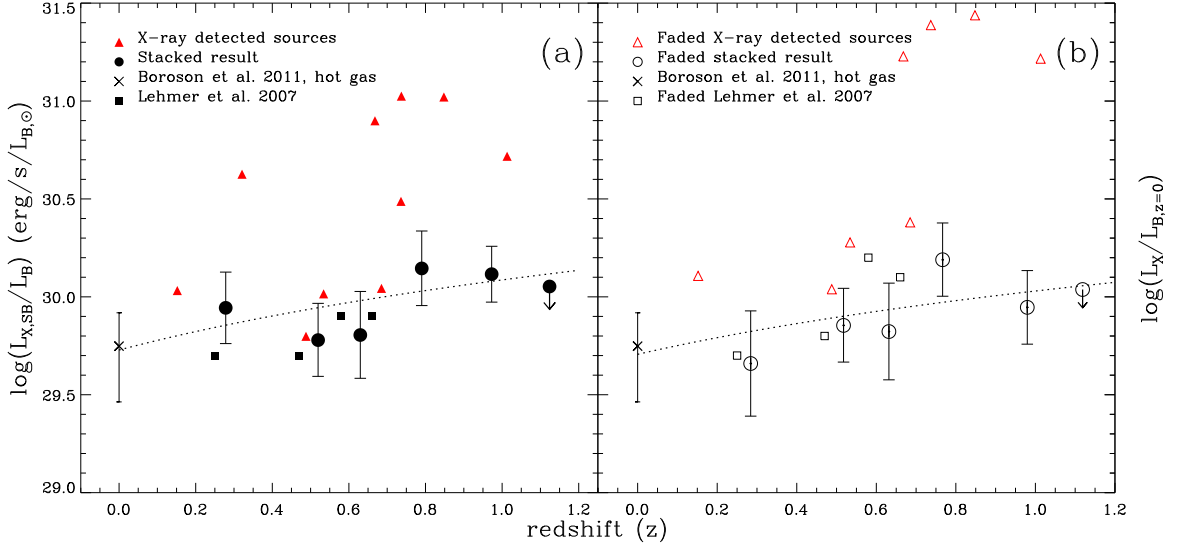
Figure 5.7: (a): The evolution of the soft X-ray properties of hot-gas dominated ETGs in terms of B-band optical luminosity, including passive X-ray detected galaxies, passive X-ray undetected galaxies and radio AGN. All galaxies with individual detections in the SB band are plotted as triangles. The circles represent the stacked results in six redshift bins with only an upper limit in the highest redshift bin. *There is very little evolution of $L_{X,SB1}/L_B$ in these hot gas dominated galaxies, in particular given the very short expected cooling time of hot gas.* To minimise the contribution from LMXBs we stack in SB1 (0.5-1keV) but we use the SED of a 1.5keV plasma to convert this to SB (0.5-2keV) in order to more easily compare the data to previous studies. $z = 0$ points are shown for the hot gas contribution as determined from a subset of the ETG sample of Boroson et al. (2011). The simple two-parameter fit for $\log L_X/L_B = A + B \log(1 + z)$ is shown as a dotted curve on both panels (a) and (b), with best-fit values of $[A,B] = [29.73 \pm 0.14, 1.19 \pm 0.68]$ and $[29.71 \pm 0.14, 1.07 \pm 0.68]$ for the main and faded samples, respectively. (b): Represents the faded sample, showing that the fading of L_B with cosmic time is a fundamental effect and acts to slightly decrease the observed $L_{X,SB}/L_B$ ratio with increasing redshift. The errors on the luminosity are derived from propagating the bootstrapped errors on the net counts and systematic errors on the conversion between count-rate and flux using the 1.5keV Raymond-Smith plasma SED.

evolution in the X-ray activity of luminous ETGs and are consistent with those of Lehmer et al. (2007). Using this model, we find that at z=1.2, ETGs are $\sim 2.4 \pm 0.9$ times or $\sim 2.2 \pm 0.9$ times (for the main and faded sample respectively) more X-ray luminous (per unit L_B) than at z=0, which suggests only modest evolution. Our best-fit relations have been highlighted in Figs. 5.7a, b as dashed curves.

Since the stacked X-ray properties (i.e., SB2/SB1 band ratio and L_X versus L_B) are consistent with those expected from hot gas dominated ETGs, with little expected contributions from LMXBs, we can use the X-ray luminosity versus redshift diagram for our stacked samples as a direct tracer of the hot gas cooling history for massive ETGs with $L_B = (3 - 30) \times 10^{10} L_{B,\odot}$. The observed mild decline in X-ray luminosity per unit B-band luminosity and roughly constant X-ray gas temperature for massive ETGs over the last $\sim$8.4 Gyr of cosmic history suggest that, on average, the gas is being kept hot. We expect that many complex processes are contributing to the evolution of the gas including radiative cooling, periodic AGN heating and outflows, replenishment from stellar winds and supernovae, interactions and sloshing, and intergalactic medium and poor group inflow (e.g. Tabor & Binney 1993, Best et al. 2006, Faber & Jackson 1976 and Brighenti & Mathews 1999). The detailed influences that each of these processes has on the gas are difficult to quantify, particularly without a strong idea of the environment in which each galaxy resides. However, we know that most of our sources reside within small groups and clusters, therefore, processes such as intergalactic medium and poor group infall may be important. One of the goals of this chapter is to test whether AGN feedback from mechanical feedback can provide enough energy to keep the gas hot and counter the observed cooling over the long baseline of cosmic time spanned by our observations.

In the next section, we discuss the viability of AGN feedback heating of the gas by directly measuring the history of radio AGN events in our galaxy population and computing the mechanical energy available from these events.

5.7 Discussion

5.7.1 The hot gas cooling and mechanical heating energy budgets

The above X-ray stacking results indicate that the X-ray power output from hot gas in the massive ETG population remains well regulated across a large fraction of cosmic history (since $z \sim 1$). To determine whether the heating from AGNs is sufficient to keep the gas hot, we estimated the mechanical power input from AGNs and the radiative cooling power from the hot gas. As discussed in Section 5.6.2, the history of gas cooling power can be directly inferred from our X-ray stacking results; the gas cooling power, can be expressed as

$$L_{\mathrm{cool}} = C_{\mathrm{bol}} L_{\mathrm{X}} \approx C_{\mathrm{bol}} L_B 10^A (1+z)^B, \tag{5.7.4}$$

where $A = 29.73 \pm 0.14$ and $B = 1.19 \pm 0.68$ were computed in Section 5.6.2, $L_B \approx 6.3 \times 10^{10}$ $L_{\mathrm{B},\odot}$ is the mean value of L_{B}, and $C_{\mathrm{bol}} \approx 1.8$ is the bolometric correction for a hot gas SED with 1.5 keV temperature (see Section 5.6.2). In Fig. 5.9, we plot the mean cooling history (*filled circles* and *dashed curve* for stacked values and best-fit model, respectively), since $z \approx 1.2$.

To estimate the energy input from radio AGNs over the last $\sim$8.4 Gyr of cosmic history, we began by measuring the radio AGN fraction as a function of radio luminosity (a proxy for mechanical heating) and redshift. By making the assumption that all galaxies will go through multiple AGN active phases, we can use the radio-luminosity and redshift dependent AGN fraction as a proxy for the typical AGN duty cycle history for galaxies in our sample.

To establish a baseline local ($z \approx 0$) measurement of the ETG radio AGN fraction, we used the Best et al. (2005) (hereafter B05) sample of radio-loud AGN from the SDSS survey, which included both early-type and late-type galaxies. For the sake of comparing these data with our ETG sample, we selected galaxies in the B05 sample with elliptical-like concentration indices $C > 2.6$ (Strateva et al., 2001). The

concentration index is defined as $C = r_{90}/r_{50}$, where r_{90} and r_{50} are radii containing 90% and 50% of the optical light respectively. By applying the flux density limit of 5 mJy, we limit the B05 sample to a lower radio luminosity limit of $\sim 10^{23}$ W Hz^{-1}, which corresponds to a maximum redshift of $z = 0.1$. To measure the AGN fraction for galaxies in the distant Universe, we used the sample of distant ETGs presented in this chapter. Using $L_{1.4\ \mathrm{GHz}} = 10^{23}$ W Hz^{-1}, the luminosity limit used for the B05 data, we determined that the corresponding CDF-N and E-CDF-S radio flux limits (see Section 5.5.3) allow us to study similar AGNs out to $z \approx 1$ and 0.85, respectively. We calculated the AGN fraction for both the local B05 local galaxies and our distant galaxies in three bins of radio luminosity (in even logarithmic luminosity intervals) in the range of $L_{1.4\ \mathrm{GHz}} \sim (1-100) \times 10^{23}$ W Hz^{-1}, each bin with a different allowed redshift range due to the flux limits. These bins in luminosity and redshift then result in a total of 2642 elliptical galaxies containing a radio AGN from the B05 sample and 13 radio AGN from our sample. The AGN fraction was computed in each bin, for both the B05 sample and our sample, by taking the total number of radio AGN in a particular luminosity range and dividing it by the total number of galaxies in which an AGN with a luminosity lying within that range could have been detected if present. We estimate 1σ errors on the AGN fractions following Gehrels (1986). By comparing the radio AGN fraction at the mean redshift $z = z_{\mathrm{mean}}$ of our distant galaxy sample with that of the B05 $z \approx 0$ sample, we can estimate the evolution of the duty cycle of the AGN outbursts in each radio luminosity bin. The time-dependent radio AGN fraction for each bin of radio-luminosity was computed following

$$f_{AGN}(t, L_{1.4\ \mathrm{GHz},i}) = \frac{f_{\mathrm{AGN},z=z_{\mathrm{zmean},i}} - f_{\mathrm{AGN},z\approx0,i}}{\Delta t_i} t + f_{\mathrm{AGN},z\approx0,i}, \qquad (5.7.5)$$

where Δt_i is the difference in the mean lookback time between $z = z_{\mathrm{mean},i}$ and $z = 0$ (i.e., our AGN fraction and that of B05) in a particular bin of mean radio luminosity $L_{1.4\ \mathrm{GHz},i}$.

Several studies have now shown that the radio power output $L_{1.4\ \mathrm{GHz}}$ from AGNs

within nearby giant elliptical (gE) and cluster central galaxies correlates with the inferred mechanical power L_{mech} that is needed to inflate the cavities within hot X-ray halos (e.g., Bîrzan et al. 2004; Bîrzan et al. 2008; Cavagnolo et al. 2010; O'Sullivan et al. 2011). Until recently, these relations have been calibrated using the cores of cooling clusters, and may not be appropriate for the massive early-type galaxies studied here. Cavagnolo et al. (2010) have added a sample of 21 gE galaxies and have shown that, as long as the radio structures are confined to the hot X-ray emitting gas region, gE galaxies provide a natural extension to the L_{mech}–$L_{1.4\ \mathrm{GHz}}$ correlation at low L_{mech}. However, as noted by Cavagnolo et al. (2010), gE galaxies and FRI sources in group environments (e.g., Croston et al. 2008) tend to have $L_{\mathrm{mech}}/L_{1.4\ \mathrm{GHz}}$ ratios much lower than the correlation derived including clusters. Since our galaxies are expected to be gE and group central galaxies, we made use of L_{mech} and $L_{1.4\ \mathrm{GHz}}$ values for the sample of 21 gEs from Cavagnolo et al. (2010) to derive the L_{mech}–$L_{1.4\ \mathrm{GHz}}$ correlation for these sources. Fig. 5.8 shows the 21 gEs from Cavagnolo et al. (2010). We find that the best-fit relation from Cavagnolo et al. (2010) (*dashed line* in Fig. 5.8), which includes radio galaxies at the centers of galaxies, overpredicts the $L_{\mathrm{mech}}/L_{1.4\ \mathrm{GHz}}$ ratios for AGNs with $L_{1.4\ \mathrm{GHz}} \gtrsim 10^{22}$ W Hz^{-1}. Using these data, we derived the following relation, which is applicable to gE galaxies:

$$L_{\mathrm{mech}} \approx 3.36 \times 10^{35} \left(\frac{L_{1.4\ \mathrm{GHz}}}{10^{24}\mathrm{W\ Hz}^{-1}} \right)^{0.11} \mathrm{W}. \tag{5.7.6}$$

Our best-fit relation is plotted in Fig. 5.8 as a solid line.

Using equations 5.7.5 and 5.7.6, we then estimate the average mechanical feedback power per galaxy over the last $\sim$8.4 Gyr of cosmic history considering all radio AGNs in the range of $L_{1.4\ \mathrm{GHz}} \sim (1$–$100) \times 10^{23}$ W Hz^{-1} via the following summation:

$$L_{\mathrm{heating}} = \sum_i f_{AGN}(t, L_{1.4\ \mathrm{GHz},i})\, L_{\mathrm{mech,i}} \tag{5.7.7}$$

In Fig. 5.9, we show the mean heating luminosity and 1σ errors (*solid curve* with
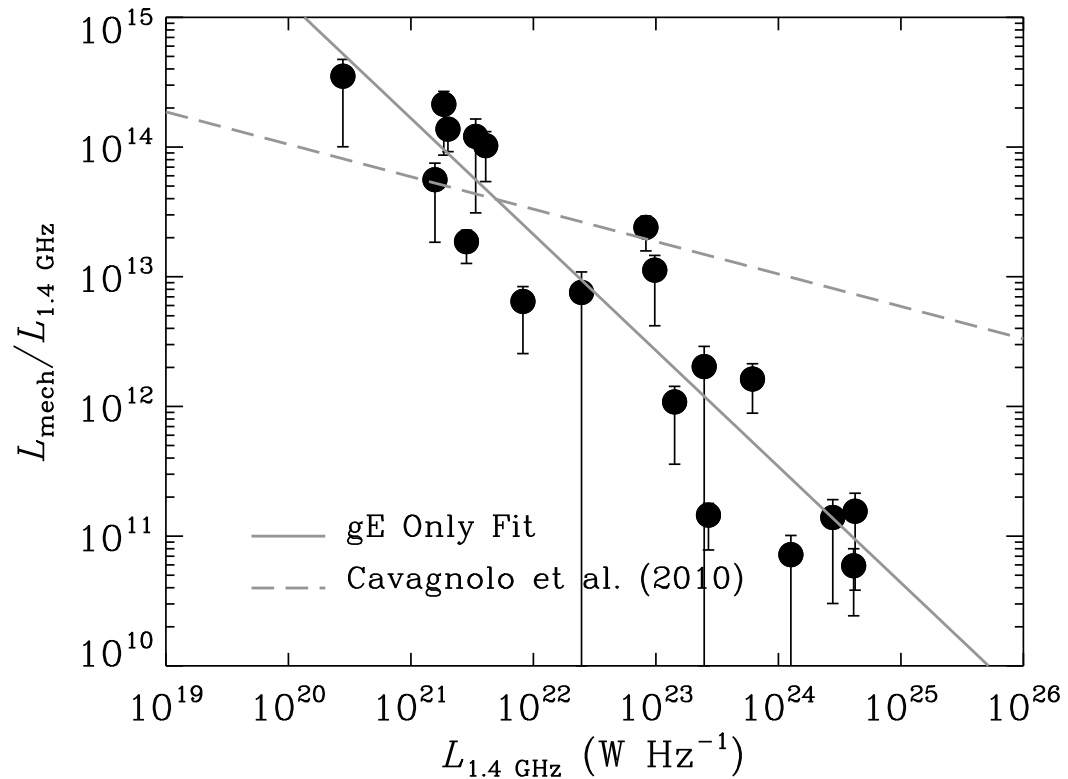
Figure 5.8: Ratio of mechanical power to 1.4 GHz radio luminosity ($L_{\mathrm{mech}}/L_{1.4\ \mathrm{GHz}}$) versus $L_{1.4\ \mathrm{GHz}}$ for the 21 giant elliptical (gE) galaxies studied by Cavagnolo et al. (2010; *filled circles*). The Cavagnolo et al. (2010) relation, which includes gE galaxies and radio galaxies at the centers of cooling clusters (from Bîrzan et al. 2008), has been shown as a dashed line. Our best-fit relation for gE only galaxies, presented in equation 5.7.6, is shown as a solid line.

shaded envelope) derived following equation 5.7.7. From Fig. 5.9, we see that on average there appears to be more than sufficient input mechanical energy from radio AGN events to balance the hot gas radiative cooling. From the five stacked bins where we obtain X-ray detections, we estimate on average $L_{\text{heating}}/L_{\text{cool}} \approx$ $2.4^{+0.9}_{-0.5}$. This result is broadly in agreement with that found for local elliptical galaxies of comparable mass where the mechanical power has been measured using X-ray cavities (e.g., Nulsen et al. 2007). Nulsen et al. (2007) estimate that the total cavity heating can be anywhere between 0.25 and 3 times the total gas cooling if 1 pV of heating is assumed per cavity; however, the enthalpy of the cavity and therefore the total heating may be much higher. Stott et al. (2012) find a trend in groups and clusters indicating the ratio of intra-cluster medium (ICM) AGN heating (from the brightest cluster galaxy) to ICM cooling increases with decreasing halo mass. For halo masses $< 5 \times 10^{12} \text{M}_\odot$ the heating can exceed the cooling. We have found that most of our galaxies are likely to live in small group environments. Therefore extrapolating this relation to the expected halo masses of the galaxies in our sample ($\sim[1\text{–}10] \times 10^{12} M_\odot$ for $L_\text{B} \sim [3\text{–}30] \times 10^{10} \ L_{\text{B},\odot}$; Vale & Ostriker 2004) would similarly imply that the mechanical heating would likely exceed the radiative cooling.

We note that our heating calculation is based on duty cycle histories derived primarily from the <20 distant radio AGNs in our sample and is based on the assumption that each galaxy will have many radio outbursts that span the full range of radio luminosities studied here. We therefore expect these calculations will have significant uncertainties that we cannot determine. In the next section, we estimate the global ETG hot gas cooling and radio AGN heating power as a function of redshift.

5.7.2   Cosmic evolution of global heating and cooling density

Using a large sample of radio-loud AGNs in the local Universe, Best et al. (2006) computed the radio-luminosity and black-hole mass dependent AGN fraction of

nearby galaxies. Their data show that the population-averaged mechanical power (probed by 1.4 GHz power) produced by these AGN events increases with black-hole mass (and also B-band luminosity) and balances well the radiative power output from X-ray cooling of the hot gas (see their Fig. 2). Their analyses further revealed that relatively low luminosity radio AGN ($\log L_{1.4\ \mathrm{GHz}}/(\mathrm{W\ Hz}^{-1}) \approx 22$–$25$) are likely to provide the majority of the mechanical feedback power for the population as a whole. They estimated that in the local universe, the mean mechanical power output density from mechanical heating from radio AGNs with $L_{1.4\ \mathrm{GHz}} > 10^{22}\mathrm{W\ Hz}^{-1}$ is $\sim 4 \times 10^{31}\ \mathrm{W\ Mpc}^{-3}$.

Due to the relatively small number of radio AGNs found in our survey, it is not feasible to calculate the evolution of the radio and mechanical luminosity density of the Universe. However, the evolution of the radio AGN luminosity function has recently been measured out to $z \approx 1.3$ using the VLA-COSMOS survey (Schinnerer et al., 2007) to relatively faint luminosity levels ($L_{1.4\ \mathrm{GHz}} \gtrsim 10^{21}$–$10^{23}$ W Hz^{-1}; Smolčić et al. 2009). By converting radio luminosity into mechanical luminosity, Smolčić et al. (2009) integrated their luminosity functions to determine the estimated mechanical power density of the Universe out to $z \approx 1.3$. In Fig. 5.10, we show the expected mechanical feedback power density evolution, based on the Smolčić et al. (2009) radio luminosity function and equation 5.7.6 for both pure-luminosity density evolution ($L_* \propto [1+z]^{0.8}$) and pure-density evolution ($\Phi_* \propto [1+z]^{1.1}$), the best-fit parameterisations for the evolution of the 1.4 GHz luminosity function.

As shown in Section 5.6, our X-ray stacking measurements can be described on average as $L_{\mathrm{cool,mod}} \approx C_{\mathrm{bol}}10^A(1+z)^B L_B$ (with $C_{\mathrm{bol}} = 1.8$, $A = 29.73 \pm 0.14$, $B = 1.19 \pm 0.68$, and $L_B \approx 6.3 \times 10^{10}\ L_{B,\odot}$) for the ETG population. Using this scaling relation and the observed evolution of the ETG B-band luminosity function φ_B from Faber et al. (2007; see their Table 4), we can compute the expected volume-averaged cooling luminosity density. In this exercise, we assumed a constant intrinsic scatter of $\sigma \approx 1$ dex for the L_X/L_B ratio (Boroson et al. 2011) and transformed the B-band luminosity function into a X-ray gas cooling luminosity function using the
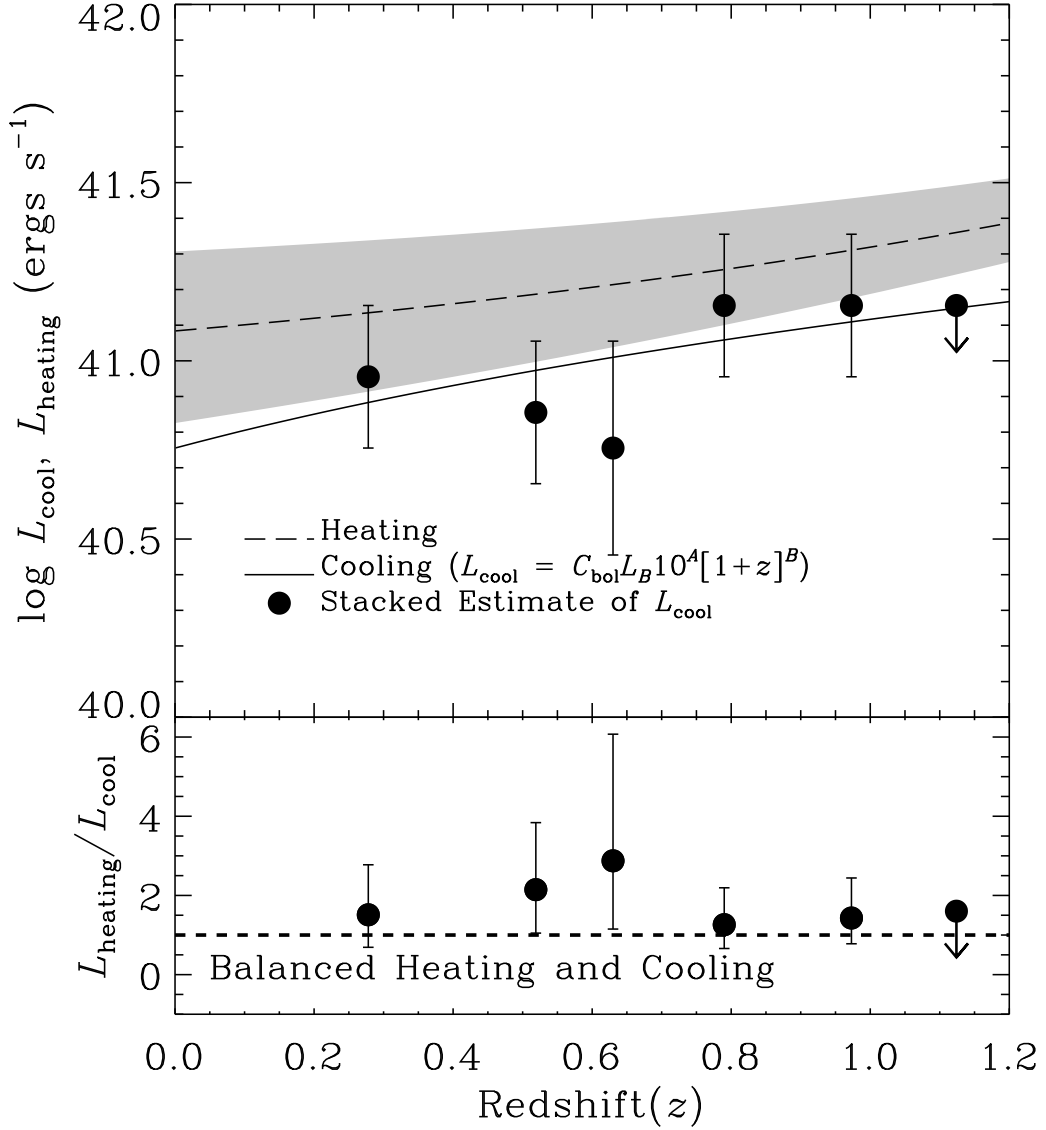
Figure 5.9: (*Top panel*) Mean radiative cooling power L_{cool} and mean mechanical heating power $L_{heating}$ versus redshift. The filled circles and 1σ error bars show the bolometrically corrected estimates of L_{cool} (see Table 5.5) and the solid curve shows our best-fit model. The *long-dashed curve* with shaded region represents our best estimate of the mean heating luminosity as presented in equation 5.7.7. These measurements show that for the early-type galaxies in our sample, there is more than enough energy available from radio AGN heating to keep the gas from cooling. (*Bottom panel*) Ratio of mean heating to radiative cooling luminosity versus redshift. We find that the average heating power is $\sim$1.4–2.6 times larger than the radiative hot gas cooling power.
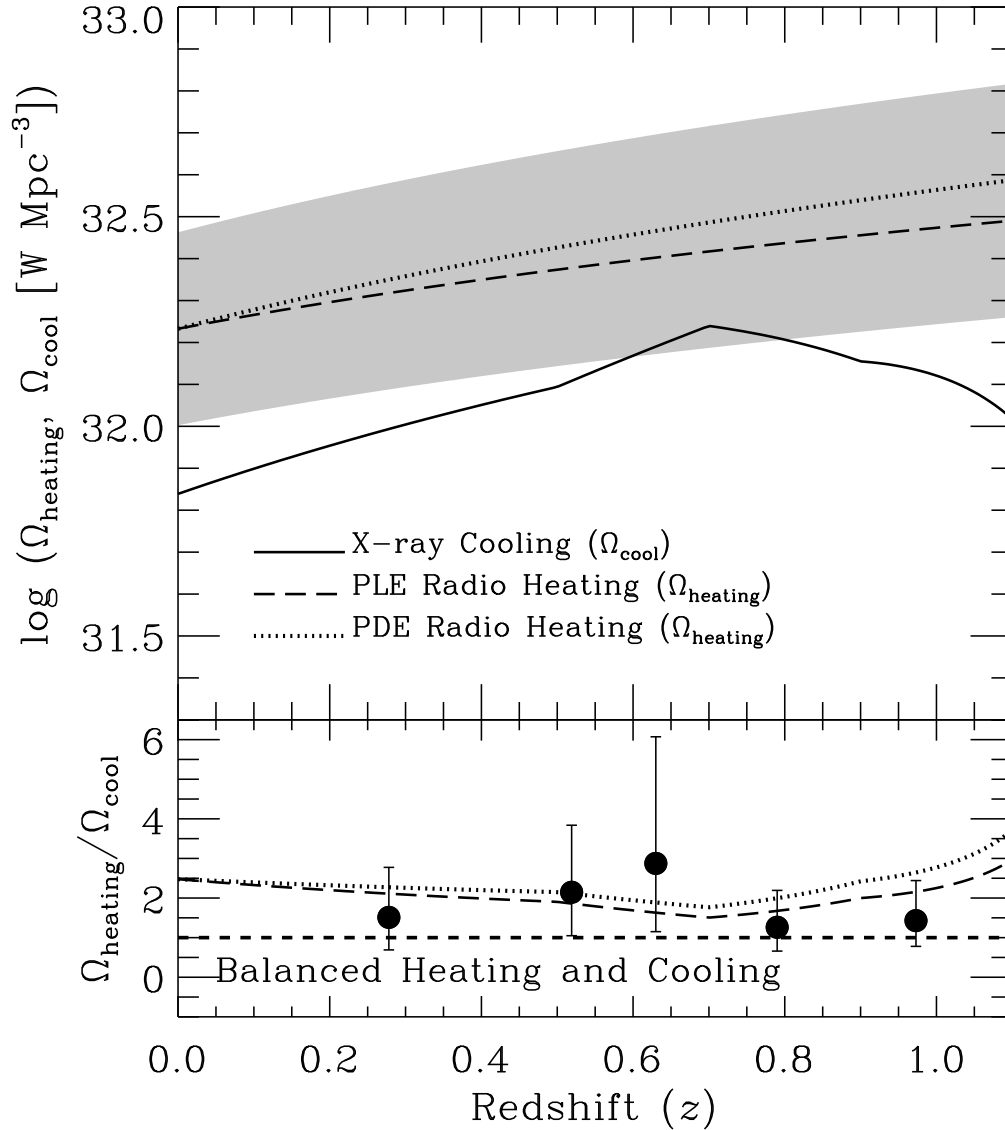
Figure 5.10: Top panel: Cosmic history of mechanical heating $\Omega_{\mathrm{heating}}$ and radiative cooling Ω_{cool} of hot gas since $z \approx 1.1$. The mechanical luminosity density versus redshift for radio AGNs, as computed by Smolčić et al. (2009), for pure-luminosity evolution and pure density evolution are indicated as dashed and dotted curves, respectively. The shaded envelope provides the estimated uncertainties between the $L_{1.4 \mathrm{~GHz}}$ and L_{mech} correlation. The cooling history of hot gas in ETGs is indicated as a solid curve (see Section 5.7.2 for details). Bottom panel: Ratio of mechanical heating to radiative cooling versus redshift. For comparison, we have plotted our estimates of the mean heating-to-cooling luminosity ratios ($L_{\mathrm{heating}}/L_{\mathrm{cool}}$ as provided in the bottom panel of Fig. 5.9 (*filled circles*). This relation shows that there is plenty of mechanical energy potential available to keep the gas hot over the last ∼8.4 Gyr.

following transformation:

$$\varphi_{\mathrm{X}}(\log L_{\mathrm{X}}, z) = \int_{-\infty}^{\infty} \varphi_B(\log L_{\mathrm{B}}, z) P(\log L_{\mathrm{X}} | \log L_{\mathrm{B}}) \, d \log L_{\mathrm{B}}$$

$$P(\log L_{\mathrm{X}} | \log L_{\mathrm{B}}) = \frac{1}{\sqrt{2\pi}\sigma} \exp\left[-\frac{(\log L_{\mathrm{cool,mod}} - \log L_{\mathrm{X}})^2}{2\sigma^2} \right]. \tag{5.7.8}$$

The total redshift-dependent cooling density $\Omega_{\mathrm{cool}}(z)$ of the Universe can therefore be computed following

$$\Omega_{\mathrm{cool}}(z) = \int_0^{\infty} \varphi_{\mathrm{X}}(\log L_{\mathrm{X}}, z) \, L_{\mathrm{X}} \, d \log L_X. \tag{5.7.9}$$

In Fig. 5.10, we show the resulting $\Omega_{\mathrm{cool}}(z)$ versus redshift (*solid curve*). Our analyses show that the estimated mechanical power provided by radio AGN activity is a factor of $\sim$1.5–3.5 times larger than the radiative cooling power (see bottom panel of Fig. 5.10), and the shape of the heating and cooling histories appear to be in good overall agreement. For comparison, we plot the mean values of $L_{\mathrm{heating}}/L_{\mathrm{cool}}$ as measured in Section 5.7.1 and Fig. 5.9 (*filled circles*), which are in agreement with the global heating-to-cooling estimates obtained here.

The combination of the approaches for estimating global and mean galaxy heating and cooling taken here and in Section 5.7.1, respectively, indicate that mechanical heating exceeds that of the radiative gas cooling for early-type galaxies with $L_{\mathrm{B}} \approx (3\text{--}30) \times 10^{10} \, L_{\mathrm{B},\odot}$. These computations are based on the assumption that the radio luminosity provides a direct proxy for mechanical power, which scales for our early-type galaxies in the same way as that measured for local gEs (i.e., based on data from Cavagnolo et al. 2010). Indeed, some studies have suggested that AGN heating in less massive systems, like those studied here, may have different heating cycles and mechanical efficiencies (Gaspari et al. 2011). Future studies that characterise how the radio and mechanical power are related in galaxies like those studied here would be needed to exclude the possibility that the excess of mechanical power compared with cooling power (as observed here) is due to the calibration.

5.8 Summary and future work

The X-ray and multiwavelength properties of a sample of 393 massive ETGs in the *Chandra* Deep Field surveys have been studied, in order to constrain the radiative cooling and mechanical feedback heating history of hot gas in these galaxies. We detected 55 of the galaxies in our sample in the X-ray bandpass, and using the X-ray and multiwavelength properties of these sources, we find that 12 of these systems are likely to be dominated by X-ray emission from hot gas. To measure the evolution of the average ETG X-ray power output, and thus hot gas cooling, we stacked the 0.5–1 keV emission of the X-ray undetected and detected "normal" galaxy population in redshift bins.

We find that the average rest-frame 0.5–2 keV luminosity per unit B-band luminosity (L_X/L_B) has changed very little since $z \approx 1.2$ and is consistent with $\propto (1 + z)^{1.1 \pm 0.7}$ evolution. This suggests that the population averaged hot gas power output is well regulated over timescales of $\sim$8 Gyr; much longer than the typical cooling timescale of the hot gas ($\sim$0.1–1 Gyr). We hypothesise that mechanical heating from radio luminous AGNs in these galaxies is likely to play a significant role in keeping the gas hot, and we compare the implied gas cooling from our stacking analyses with radio-AGN based estimates of the heating.

We find that if local relations between radio luminosity and mechanical power hold at high redshifts, then the observed radio-luminosity dependent AGN duty cycle suggests that there would be more than sufficient (factor 1.4–2.6 times) mechanical energy needed to counter the inferred cooling energy loss. Similarly, we find that the evolution of the mechanical power density of the Universe from radio AGNs increases only mildly with redshift and remains a factor of $\sim$1.5–3.5 times higher than the radiative hot gas cooling power density of ETGs in the Universe. These results are concordant with previous lower redshift studies (e.g Best et al. 2005 and Lehmer et al. 2007) and with theoretical feedback models such as Churazov et al. (2005), Croton et al. (2006) Bower et al. (2008) and Bower et al. (2006) where feedback from radio AGN maintains the balance between heating and cooling

rates of hot interstellar gas in massive ETGs.

Understanding the evolution of both the X-ray and radio properties of optically luminous ETGs could be improved in future work by: (1) gaining a better understanding of the environments of these sources in order to better constrain the likely contribution of e.g. gas infall to the evolution of the X-ray properties and probe the influence of environment on the balance between gas cooling and heating in galaxies. This could be achieved by measuring spectroscopic redshifts for the whole sample, as there is currently significant uncertainty in photometric redshifts. (2) Conducting deeper X-ray observations could provide stronger constraints on the evolution of the hot gas. We focus our observations in the soft band in which the background is lowest, therefore doubling the *Chandra* exposure time to 8Ms could provide a factor of 1.4–1.6 improvement in the sensitivity resulting in the faintest detectable sources having soft band fluxes of 6.0×10^{-18}erg cm^{-2} s^{-1} (Xue et al., 2011) and improved statistics on the average X-ray emission from the ETG population.

Chapter 6

Conclusions and future work

This thesis investigates the properties of some of the most rapidly star-forming galaxies throughout the history of the Universe. In Chapter 2 we measure the spectroscopic redshift distribution of SMGs, investigate their environments, determine their average properties and attempt to understand the processes which drive the high infrared luminosities within these systems. In Chapters 3 and 4, we undertake a detailed analysis of the observations of the gravitationally lensed SMG, SMM J2135, which gives insight into the conditions within the ISM of a representative SMG at the peak of cosmic star formation history. This advances our understanding of the composition and properties of the gas available for star formation within the dense and rapidly evolving ISM of a high-redshift galaxy and provides a benchmark for future high-resolution observations of high-redshift galaxies. Such massive star-forming galaxies at $z \sim 2$ are believed to evolve into massive, passive elliptical galaxies with little or no star formation by $z = 0$. In Chapter 5, the potential influence of AGN on the suppression of star formation within ETGs is discussed. Here the conclusions from each chapter are summarised followed by a discussion of the future directions of this work.

6.1 Summary

6.1.1 The redshift distribution of ALMA-identified SMGs

We have undertaken a redshift survey of 131 ALMA-identified SMGs in the ECDFS. ALMA detections have the significant advantage over previous sub-mm surveys as ALMA provides $< 1''$ resolution at 870μm, thus allowing the sub-mm emission to be directly pinpointed. ALMA provides precise sub-mm flux measurements, as well as allowing multi-wavelength counterparts to be unambiguously identified for spectroscopic follow-up. A median redshift of $z = 2.4 \pm 0.1$ is measured for the ALESS SMGs, similar to previous studies of radio-identified SMGs. However, a high redshift tail is observed out to $z = 4.95$ and the interquartile range is found to be $z = 2.1 - 3.0$ with 23% of the ALESS SMGs lying at $z > 3$, contrary to previous SMG redshift surveys which were limited to lower redshifts due to the prerequisite of radio detections. The ALESS SMGs are found to be typically young, heavily dust-obscured starbursts with an average stellar mass of $M_* = (6 \pm 1) \times 10^{10}\,M_\odot$ but a broad mass range of $M_* \sim 10^{9-12}\,M_\odot$. The population demonstrates a diverse range in spectral classifications and properties.

There is strong evidence of galaxy-scale outflows in many of the SMGs, with velocities of up to $\sim 3000\,\mathrm{km\,s^{-1}}$. These outflows appear to be predominantly driven by intense star-formation, although there may be contributions from AGN, which can be very difficult to spectroscopically disentangle from star-formation driven winds.

Despite various studies finding very strong clustering of SMGs, there is little evidence for the ALESS SMGs residing within overdense environments. However, our spectroscopic incompleteness due to the faintness of some of the multiples within the ALMA maps means that deeper spectroscopic observations would be required to test this further.

Finally, an analysis of the reddening of the SMGs compared to the dust attenuation provides tentative evidence of an increasingly blue UV slope at higher redshift, possibly implying complex morphologies where the UV and FIR emitting compo-

nents are decoupled. This may be expected if the SMGs are indeed predominantly merger-driven which results in disturbed morphologies.

Furthermore, the newly acquired spectroscopic redshifts provide the information required for high-resolution follow-up with i.e. SINFONI, *HST*, ALMA and PdBI. Combining *HST* imaging of the ALESS SMGs (Chen et al. in prep) and high-resolution ALMA follow-up (Hodge et al. in prep) will provide excellent constraints on the sub-mm versus optical morphologies and help to discern the dominant star formation trigger mechanisms within SMGs.

6.1.2 The ISM within a star-forming galaxy at z=2.3

In Chapters 3 and 4, follow-up observations of the gravitationally lensed SMG, SMM J2135 are presented. The strong magnification of $37.5\times$, provided by the foreground galaxy cluster, facilitates a uniquely detailed analysis of the ISM of a star-forming galaxy at $z = 2.3$. Crucially, the unlensed flux of SMM J2135 is $\sim 3\,\mathrm{mJy}$ which is representative of the sub-mm background, thus although this analysis focuses on one galaxy, it gives an important insight into the typical properties of the SMG population. A wealth of high signal-to-noise molecular and atomic emission lines have been measured within this work, from 11 species, including ^{12}CO transitions from $J_{\mathrm{up}} = 1 - 10$, HCN, [CI] and the first detections in a high-redshift star-forming galaxy of ^{13}CO and C^{18}O.

^{13}CO and C^{18}O are less abundant than ^{12}CO but are typically optically thin and can provide improved constraints on the gas masses, and in combination with the ^{12}CO information can improve estimates of the optical depth, densities, temperatures and column densities in the interstellar gas. LVG modelling of the ^{12}CO transitions indicates a gas mass for SMM J2135 of $\sim 4 \times 10^{10}\,\mathrm{M_\odot}$ which is higher than the gas mass derived from ^{13}CO of $\mathrm{M_{gas}} = 1.5 \times 10^{10}\,\mathrm{M_\odot}$ (implying $\alpha_{\mathrm{CO}} \sim 0.9\,\mathrm{M_\odot\,(K\,km\,s^{-1}pc^2)^{-1}}$). This gas mass is significantly lower than the average mass of the ALESS SMGs ($\sim 6 \times 10^{10}\,\mathrm{M_\odot}$).

Through analysis of the line ratios, abundances and excitation, the ISM within

SMM J2135 is best described by two main phases: four high density, hot star-forming clumps which dominate the sub-mm emission, embedded in a cooler, more diffuse, extended structure which dominates the gas emission. The addition of the constraints of ^{13}CO and C^{18}O in the LVG modelling (in Chapter 4) seems to require models with higher temperatures (50 K and 90 K for the cold and hot phases respectively) than those found in the ^{12}CO modelling in Chapter 3 (25 K and 60 K), but with similar densities ($n(\mathrm{H}_2) = 10^{2.7-3.6}$ cm^{-3}). PDR modelling of the excitation conditions within SMM J2135, using various line ratios, implies similar conditions to local ULIRGs and starburst galaxies. The molecular gas appears to be exposed to a UV radiation field 1000× more intense than that of the Milky Way but with a gas density typical of a starburst galaxy. However, both the spatial extent and the star formation rate appear to be significantly higher than local galaxies. The integrated properties of the galaxy are in agreement with the Kennicutt-Schmidt relation, linking the star formation and the gas surface density, however, on the scale of the star-forming clumps (< 100 pc), the relation appears to break down. This may imply that star-formation at high-redshift is governed by different physical processes to those in local star-forming galaxies. This will be investigated further via high-resolution ALMA follow-up of selected ALESS SMGs, measuring the spatially-resolved Kennicutt-Schmidt relation on ∼kpc scales.

A kinematic decomposition of SMM J2135 reveals it to comprise multiple kinematic components with different gas properties, including a factor of ∼ 4 temperature range between the components, and strongly varying chemical abundance ratios. Kinematic decomposition of the emission lines reveals an enhancement in C^{18}O in the outer regions of SMM J2135, implying preferentially massive star formation in these regions, compared to typically older, intermediate mass stars in the central regions, with a higher abundance of ^{13}CO. The enhancement of C^{18}O is a surprising result and may be indicative of a high cosmic ray flux within SMM J2135.

High cosmic ray fluxes have recently been inferred within local star-forming galaxies to explain the high gas temperatures found within the densest regions of GMCs (Papadopoulos et al. 2012a). Cosmic rays can penetrate even the densest

regions of the ISM where UV photons are impeded, and are thus capable of volu-metrically heating gas. This could dramatically alter the initial conditions for star formation within the star-forming cores, raising the temperature and potentially in-creasing the mass scale required for the cloud to collapse, resulting in the formation of preferentially massive stars. The high SFRs within SMGs will result in a very high supernovae rate causing an increase in the cosmic ray rate, thus it is likely that cosmic ray heating plays a very important role in high-redshift star formation. There are various indications of a high cosmic ray flux within SMM J2135. In Chapter 3 high ratios of $[CI]/^{12}CO$ are found which can be indicative of either low metallicity, or high cosmic ray flux. Similarly, the LVG modelling and energetics modelling in Chapter 4 demonstrate that cosmic rays play a more important role than UV heating in this system. If cosmic rays dominate the heating of the ISM, this could explain the increased temperature in the star forming regions. High temperatures in the star-forming cores would favour the formation of massive stars which could explain the enhanced $C^{18}O$ abundance found in the integrated emission and in the outer regions in the kinematically decomposed analysis. Further measurements of ^{12}CO, ^{13}CO and importantly $C^{18}O$ with ALMA and PdBI, in high-redshift galaxies across a range of masses and SFRs will provide crucial information on the relative importance of UV and cosmic ray heating and the potential differences between low and high-redshift star formation.

These observations have provided a fascinating and detailed view of the condi-tions within the ISM of a relatively normal SMG at $z \sim 2$, and give an insight into the possibilities with ALMA in full operations, where such detail could be achieved without the need for gravitational lensing.

6.1.3   Hot gas cooling and radio AGN heating in ETGs

SMGs exhibit similar properties to local ULIRGs but are $1000\times$ more common at $z \sim 2$ than they are locally. The star formation rate density has rapidly declined since its peak at $z \sim 2$. It is therefore evident that there has been a dramatic

shut-off of star formation and also that various processes are capable of heating gas within galaxies and preventing the formation of further stars. Various studies have suggested that SMGs evolve into massive elliptical galaxies in the local Universe. In Chapter 5 the potential role of radio-mode AGN activity in the heating of interstellar gas and thus the suppression of star formation is investigated.

In a large sample of ETGs in the ECDFS and CDFN over the redshift range $z = 0.0 - 1.2$, X-ray, optical and radio emission are studied in order to understand the temperature balance within these systems and the evolution in the heating and cooling contributions. Very little evolution in the ratio of X-ray to optical luminosity (L_X/L_B) is observed since $z \sim 1.2$, implying that the hot gas in these ETGs is not cooling as rapidly as expected. It is suggested that mechanical heating from radio-luminous AGN may be maintaining the high temperatures in the gas. The gas cooling is calculated via X-ray stacking analyses and compared to estimates of the heating from radio-AGN. Assuming locally-calibrated relations between radio luminosity and mechanical power, the radio AGN duty cycle suggests that there should be more than sufficient mechanical energy to counter the cooling of the hot gas since $z \sim 1.2$. Furthermore, the mechanical power density of the Universe increases only slightly with redshift but remains $1.5 - 3.5 \times$ higher than the radiative hot gas cooling power density of ETGs. This mode of AGN feedback may not be responsible for the sharp cut-off in star-formation after the SMG phase but could certainly be responsible for keeping the interstellar gas hot and preventing further star-formation within ETGs.

If ETGs are indeed the descendants of SMGs, there are still large uncertainties in the processes causing the sudden halting of star-formation in these systems resulting in their passive evolution to local massive ETGs and further investigation is required to understand whether SMGs lie in sufficiently large dark matter haloes to support this evolutionary scenario.

6.2 Ongoing and future work

Although spectroscopic surveys and SED modelling give us a good indication of the general properties of the SMG population, detailed follow-up of individual sources remains essential to understand the energetics, dynamics and chemistry of SMGs. Even locally there are still relatively few examples of ULIRGs with detailed follow-up. I have been allocated time on various instruments for follow-up observations based on the work presented in Chapter 2, 3 and 4, to probe the resolved dynamics within SMGs and the spatial distribution of star formation and stellar mass, in order to address some of the most pressing issues concerning SMGs.

6.2.1 Resolved dynamics within SMGs

One of the main questions still remaining regarding SMGs is: what is the dominant triggering mechanism of the intense star formation within these systems? If they are considered to be high-redshift analogues to local ULIRGs then it may be expected that major mergers are the main driver, however, SMGs are $1000\times$ more common at $z = 2$ than locally and theoretical models have shown that there would be insufficient mergers at high redshift to account for the SMG population (Davé et al. 2010). Thus secular bursts within isolated disks may also play a role (i.e. Hayward et al. 2011). High-resolution follow-up of the internal dynamics of a large sample of SMGs are required to investigate this. In Chapter 2 we determine the redshifts for 52 ALMA-identified SMGs in the ECDFS. From this sample, 21 lie between $z = 1 - 3.5$ where Hα is redshifted into the near-IR and thus accessible to SINFONI IFU for detailed dynamical studies. We have been granted time on SINFONI to pre-image the whole sample and observe the seven brightest targets with deeper observations. With this data we will attempt to: i) measure the dynamics, searching for disks, tidal interactions and mergers; ii) derive metallicity gradients- used to test the merger hypothesis, since merging can drive less-enriched gas from the outskirts of the galaxies inwards, thus flattening the metallicity gradients; iii) measure the spatial distribution of star-formation, searching for resolved star-forming clumps at
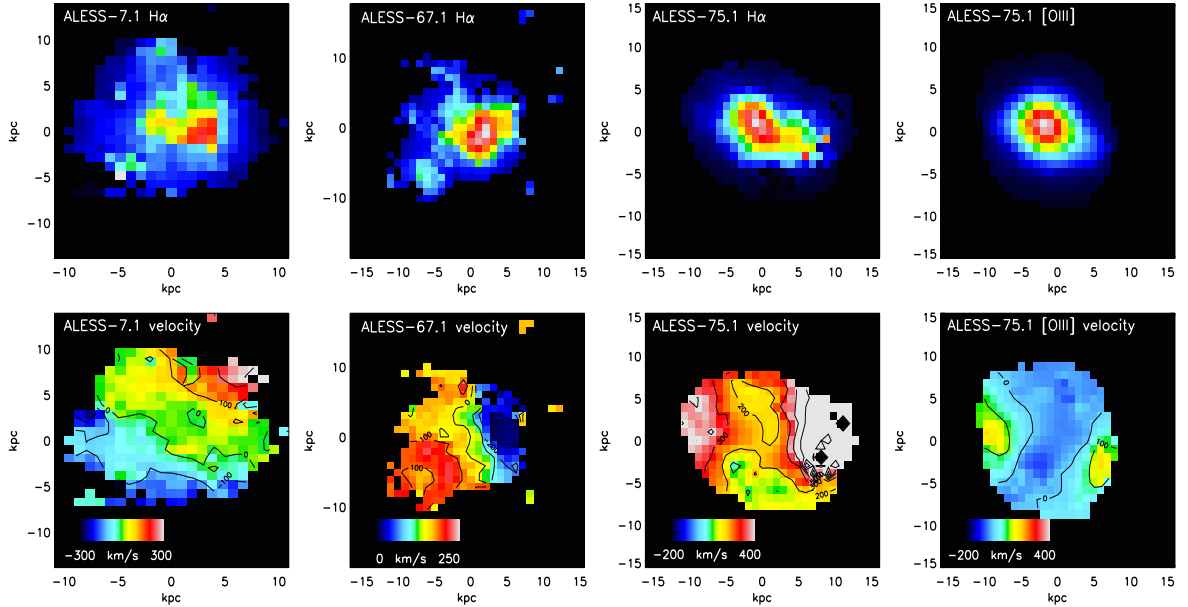
Figure 6.1: Velocity distributions and Hα (and [OIII]) maps for three ALMA-identified SMGs observed with SINFONI. ALESS007.1 was observed using natural guide star adaptive optics to improve the resolution. ALESS067.1 and ALESS007.1 appear to have disk-like velocity structure whereas ALESS075.1 appears to be more disturbed.

a comparable resolution to the *HST* data we have obtained for many of these targets (see Chen et al. in prep) ; iv) search for AGN and/or star-formation driven outflows and measure their energetics.

The first seven targets were observed in the programme 091.B-0920(E) with detailed follow-up of ALESS007.1, ALESS067.1 and ALESS075.1, for which the velocity distributions of Hα (and [OIII] for ALESS075.1) are shown in Fig. 6.1. The remaining 14 targets have been allocated time in the programme 094.B-0798(A) with follow-up of the brightest four targets. The completed programme will provide high-resolution dynamical information for seven SMGs in the ECDFS which will significantly improve our knowledge of the triggering mechanisms of SMGs. In the data analysed so far, shown in Fig. 6.1, two of the SMGs appear to have velocity-structure consistent with a disk whereas ALESS 075.1 has a more disturbed morphology, in particular in the Hα map.

6.2.2 Measuring the spatial distribution of the stellar mass distribution within SMM J2135

The high magnification of SMM J2135 by a foreground cluster results in an increase in the linear resolution of $16\times$. This has allowed us to study this SMG in unprecedented detail, since a $0.15''$ point spread function (PSF) corresponds to an effective resolution of $\sim 0.01''$ on source, or only $\sim 80\,$pc. SMM J2135 has undergone extensive high-resolution follow-up observations. The cool dust has been mapped to scales of $\sim 0.2''$ via SMA 870μm (rest-frame 260μm) observations, revealing the clumpy internal structure of the obscured star formation (Swinbank et al. 2010). The cold molecular gas has been mapped in CO(1–0) and CO(6–5) to scales of $0.19''$ with PdBI to determine the kinematics of the gas and search for evidence of various starburst triggering mechanisms through the dynamics of the central regions (Swinbank et al. 2011). Furthermore, SINFONI observations utilising adaptive optics have provided maps of the [OIII] in SMM J2135, allowing us to investigate the potential influence of an AGN in the system. However, we still require detailed observations to trace the stellar mass in this SMG at an equivalent resolution to that of the cool gas and dust maps (i.e. $\sim 0.2''$).

We have been allocated 11 hours of time on the Nasmyth Adaptive Optics System (NAOS) Near-Infrared Imager and Spectrograph (CONICA), or NACO, to observe SMM J2135 in the programme 088.A-0977(B) (PI: Danielson). Our proposal was to observe SMM J2135 in L$'$ and K_S-band in order to measure the distribution of the stellar mass on scales of $100-200\,$pc. At the redshift of SMM J2135 ($z = 2.32591$) the L$'$-band corresponds to rest-frame $\sim 1.14\mu$m ($\sim J$-band) which is relatively close to the '1.6μm stellar bump' and therefore a good tracer of the stellar emission. K_S-band corresponds to rest-frame $\sim 0.66\mu$m which is approximately equivalent to the R-band. The aim of this work is to robustly isolate individual structures in the stellar mass distribution and to correlate them with the structure of the brightest star-forming regions and the peaks in the gas distribution.

This work will improve our understanding of the correlation between stellar mass,

star formation and cold molecular gas on scales only marginally larger than the scale of GMCs in the local Universe. Via L$'$-band observations, we will measure the morphology, sizes and intensity of the stellar regions and constrain the mass-to-light ratios in the 'clumps'. With our complementary K_S band observations we will then be able to measure the rest-frame $R - J$ colours which can provide a measure of the reddening and a strong indicator of the ages of the stellar populations, providing an insight into the evolution of the star formation within this relatively 'normal' high-redshift ULIRG.

6.2.3 50-pc resolution mapping of SMM J2135

Obtaining a detailed understanding of the star formation within SMM J2135 and its relation to the gas dynamics, requires high-resolution far-infrared continuum mapping. As described previously, we have mapped SMM J2135 with SMA down to scales of ~ 90 pc at 870μm, corresponding to rest-frame $\sim 260\mu$m and thus tracing the dust-obscured star formation. However, the SMA map of SMM J2135 has low fidelity due to a limited number of baselines and low signal-to-noise in the resolved clumps. Furthermore, the $\sim 100 - 200$ pc sizes estimated for the clumps are upper limits dictated by the instrumental resolution. It is essential to determine reliable measurements of the physical sizes and distribution of the star-forming regions to combine with our PdBI spatially-resolved cold gas measurements and NACO stellar mass distribution data.

ALMA in full operations is an ideal instrument with which to not only test the fidelity of the original SMA data but also to resolve down to even smaller scales within SMM J2135. We have been granted ALMA time (2012.1.01029.Sl; PI: Danielson) to carry out Band 7 (870μm) and Band 9 (450μm) observations in both C32-1 (compact) and C32-6 (extended) configurations, to map the rest-frame 260μm and 140μm continuum morphology of SMM J2135. This is likely to be observed in Cycle 2. The extended configuration observations will probe to resolutions of $0.08''$ and $0.16''$ for Band 7 and Band 9 respectively, which is equivalent to a spatial resolution

of $\sim 50\,\mathrm{pc}$ for the Band 7 $450\mu\mathrm{m}$ observations. This is a significant improvement on the previous SMA observations, allowing us to accurately probe the relationship between cold molecular gas and star formation on the scale of GMCs. Furthermore, the complementary compact configuration observations will ensure that all the flux is recovered and a large range of angular scales are explored within the source. This will also allow us to determine what fraction of the total star formation is occurring within the 'clumps'. When combined with existing maps of SMM J2135, of comparable resolution, we will be able to measure the morphology of the sub-mm emission (and thus the star-formation), the star formation efficiencies of the 'clumps' and using recently-acquired radio data on JVLA $(4-8\,\mathrm{GHz})$, we will investigate the spatially-resolved far-infrared - radio correlation.

6.3   Concluding remarks

Since their discovery nearly 20 years ago, SMGs have been found to be a crucial stage in the evolution of galaxies, hosting a large proportion of the total star formation in the Universe and forming stars at rates of up to $1000\,\mathrm{M_\odot yr^{-1}}$. Significant advancements in sub-mm telescopes have allowed us to define sub-mm selected SMG samples with unambiguous multiwavelength counterparts from which to measure their redshift distribution. We find SMGs to be most common at $z \sim 2.4$, with a diverse range of properties, due in part to the wide redshift range they cover (ALESS SMGs range between $z = 0.683 - 4.954$). High-resolution follow-up observations of a large sample of SMGs across a wide range of redshifts, masses and SFRs will better our understanding of the internal properties of the ISM within high-redshift star-forming galaxies, and enable us to determine the main processes responsible for the rapid evolution of these systems. High-resolution observations with instruments such as SINFONI/VLT and KMOS/VLT could provide spatially-resolved dynamical information including well-constrained dynamical masses for large samples of high-redshift star-forming galaxies. Detailed mapping of Hα could potentially provide a means of measuring the contribution of AGN within star-forming galaxies,

by measuring the resolved dynamics in the central regions of the galaxies. PdBI, ALMA and JVLA can provide high-resolution maps of the dust continuum and the molecular gas within SMGs, allowing the Kennicutt-Schmidt law to be tested on the scale of individual star-forming regions to determine whether the laws that govern star formation locally hold true at high-redshift. They can also be used to determine the composition of the molecular gas and the temperatures and densities within the star-forming regions. *HST* and eventually *JWST* will be essential for determining the typical morphologies thus the predominant triggering mechanisms of the immense luminosity of these galaxies.

In order to understand the role SMGs play in the evolution of galaxies it is vital to determine how they relate to other high-redshift galaxy populations. Since various theoretical models predict that they evolve from SMGs, through a QSO phase which halts the star formation, to passive galaxies and eventually massive ETGs, it is essential to better understand the role that AGN can have on the evolution of galaxies, in particular what caused the rapid decline in the average star formation rate density of the Universe since $z \sim 2$. If SMGs do indeed evolve into QSOs, the populations would be expected to display similar large-scale clustering, redshift distributions and mass distributions. Deeper spectroscopic redshift surveys are required to provide strong constraints on the clustering measurements and to provide an adequate comparison sample of QSOs at a similar epoch to SMGs. If the QSO mode halted the star formation within the galaxy one would expect to find quiescent systems at relatively high redshift. Indeed Whitaker et al. (2012) find a large population of massive ($M_* > 5 \times 10^{10} \, M_\odot$), young, 'post-starburst' galaxies at $z > 1$ with typical ages of $\sim 1 \, \mathrm{Gyr}$. Such galaxies could then evolve into massive elliptical galaxies at $z = 0$ through a series of minor mergers and through accretion of smaller galaxies. One of the big uncertainties in this scenario is how SMGs, which have been found to have complex, clumpy morphologies can evolve very rapidly into compact, quiescent spheroids. If there is indeed a QSO phase, it must be capable of both quenching the star formation and strongly influencing the physical structure of the galaxy. Probing the co-evolution of supermassive black holes and their host

galaxies will enable a better understanding of the influence of both processes on gas depletion, expulsion and heating. Developments in theoretical models to determine the importance of these feedback mechanisms are essential to provide comparisons to the observations.

Although the field of SMG research has developed hugely since its advent ~ 20 years ago, many fundamental questions remain unanswered. However, the many powerful new instruments both commissioned and in development will be capable of rapidly detecting large samples of even the faintest SMGs, probing to the resolution of single GMCs within SMGs and disentangling the contributions of AGN and star-formation within this important galaxy population.

Appendix A

Data

The following table is the full master table of the basic properties of our parent sample of early type galaxies shown in part in Chapter 5 (Table 5.1).

RA	Dec	z	spec/ phot?	z_{850}	M_U	M_B	M_V	L_B	M_*	X-ray?	1.4GHz?	24μm?
(J2000)	(J2000)							$\log(L_{B,\odot})$	$\log(M_{\odot})$			
(1)	(2)	(3)	(4)	(5)	(6)	(7)	(8)	(9)	(10)	(11)	(12)	(13)
52.8483000	-27.9371400	0.816	p	21.52	-21.79	-22.06	-22.83	11.01	11.16	0	0	0
52.8506205	-27.9442900	1.056	p	21.79	-21.41	-21.78	-22.36	10.91	11.00	0	0	0
52.8527205	-27.7069500	0.526	p	20.62	-20.49	-20.83	-21.65	10.52	10.84	0	0	0
52.8637605	-27.6886300	0.908	p	21.32	-21.22	-21.79	-22.53	10.91	11.29	0	0	0
52.8672000	-28.0023100	0.727	p	21.78	-20.64	-20.96	-21.55	10.57	10.73	0	0	0
52.8714105	-28.0047900	0.727	p	20.82	-21.33	-21.56	-22.24	10.81	11.04	0	0	0
52.8717405	-27.9800800	0.771	p	21.81	-21.25	-21.55	-22.15	10.81	10.88	0	0	0
52.8731805	-28.0159400	0.685	p	20.95	-20.95	-21.33	-22.23	10.72	11.10	0	1	0
52.8741105	-28.0181600	0.727	p	21.64	-20.81	-20.99	-21.67	10.59	10.80	0	0	0
52.8809595	-27.7222000	1.005	p	22.21	-21.27	-21.40	-21.98	10.75	11.02	0	0	0
52.8842100	-27.7189100	0.956	p	21.62	-21.41	-21.82	-22.55	10.92	11.27	1	1	1
52.8868305	-27.7150100	1.005	p	21.86	-21.77	-21.92	-22.50	10.96	11.01	0	0	0
52.8892905	-27.7307100	0.190	p	17.65	-20.32	-20.78	-21.59	10.50	10.77	0	0	0
52.8925005	-27.7140600	0.564	p	20.95	-20.30	-20.76	-21.60	10.49	10.85	0	0	0
52.8945405	-27.9403400	0.678	s	20.70	-21.20	-21.55	-22.29	10.81	11.03	0	0	0
52.8950700	-27.9791700	0.644	p	20.52	-21.38	-21.81	-22.59	10.92	11.13	0	0	0
52.8956400	-28.0106900	0.526	p	19.77	-20.96	-21.43	-22.26	10.76	11.07	0	0	0
52.8991005	-27.9706200	0.685	p	20.72	-21.25	-21.67	-22.43	10.86	11.11	0	0	0
52.9000095	-27.8732900	1.005	p	21.41	-22.57	-23.05	-23.79	11.41	11.79	0	0	0
52.9015200	-27.7532300	1.056	p	22.82	-20.70	-21.05	-21.68	10.61	10.73	0	0	0
52.9051800	-27.9616800	0.644	p	20.26	-21.24	-21.73	-22.59	10.88	11.18	0	0	0
52.9064205	-27.7669100	0.727	p	21.25	-21.47	-21.87	-22.70	10.94	10.98	0	0	0
52.9066695	-27.9691700	0.644	p	20.44	-21.13	-21.57	-22.34	10.82	11.04	0	0	0
52.9089300	-27.6413100	1.005	p	22.60	-21.20	-21.72	-22.07	10.88	10.84	0	0	0
52.9093005	-27.9172800	0.685	p	20.75	-21.34	-21.71	-22.43	10.87	11.10	0	0	0
52.9095105	-27.9632300	0.685	p	20.56	-21.22	-21.54	-22.25	10.81	11.00	0	0	0
52.9118205	-27.7770200	0.674	s	21.07	-21.03	-21.20	-21.84	10.67	10.72	0	0	0
52.9126695	-27.8833600	0.220	p	17.40	-20.60	-21.10	-22.01	10.63	11.02	0	1	1
52.9143405	-27.7573400	1.107	p	22.78	-21.00	-21.28	-21.79	10.70	10.68	0	0	0
52.9168500	-27.6132300	0.685	p	20.15	-22.04	-22.52	-23.30	11.20	11.40	0	1	0
52.9179705	-27.6111500	0.727	p	21.24	-21.14	-21.35	-22.00	10.73	10.92	0	0	0
52.9188600	-27.6690200	0.603	p	19.93	-21.47	-21.91	-22.79	10.96	11.24	0	0	0
52.9215405	-27.9477500	1.160	p	22.97	-21.42	-21.51	-21.98	10.80	10.97	0	0	0
52.9240395	-27.9756700	0.861	p	20.93	-21.91	-22.24	-22.86	11.09	11.24	0	0	0
52.9268205	-27.7452100	0.685	p	19.87	-22.16	-22.43	-23.00	11.16	11.23	0	0	0
52.9300800	-27.6410800	0.979	s	22.34	-21.20	-21.42	-22.00	10.76	10.88	0	0	0
52.9363005	-27.9324600	1.005	p	22.55	-21.08	-21.25	-21.76	10.69	10.69	0	0	0
52.9365795	-27.7905700	0.220	p	17.94	-20.30	-20.84	-21.70	10.53	10.87	0	0	0
52.9367595	-27.9621900	0.644	p	20.89	-21.26	-21.45	-22.17	10.77	10.91	0	0	0
52.9369200	-27.7395900	0.956	p	21.99	-20.92	-21.49	-22.18	10.79	11.06	0	0	0
52.9373400	-27.9446400	0.719	s	20.83	-21.36	-21.76	-22.48	10.90	11.16	0	0	0
52.9375500	-27.6998900	0.669	s	20.18	-21.64	-22.04	-22.84	11.01	11.34	0	0	0
52.9399395	-27.7709300	0.247	s	18.27	-20.20	-20.74	-21.58	10.49	10.83	0	0	0
52.9406400	-27.7435400	0.771	p	22.01	-20.69	-21.08	-21.87	10.63	10.91	0	0	0
52.9412295	-27.7607700	0.727	p	20.25	-22.45	-22.74	-23.42	11.29	11.45	0	1	0
52.9461705	-27.6428300	1.005	p	21.43	-22.01	-22.27	-22.88	11.10	11.24	0	0	0
52.9516095	-27.6101000	0.771	p	21.27	-21.33	-21.57	-22.30	10.82	11.14	0	0	0
52.9526805	-27.7762900	0.956	p	22.24	-20.83	-21.36	-22.11	10.74	11.09	0	0	0
52.9529595	-27.9827800	0.644	p	19.80	-21.67	-22.14	-22.95	11.05	11.35	0	0	0
52.9555395	-27.6626900	0.956	p	22.19	-20.77	-21.64	-22.20	10.85	11.00	0	0	0
52.9562205	-27.6856500	1.005	p	21.08	-22.36	-22.85	-23.37	11.33	11.48	0	0	0
52.9564605	-27.6631800	1.005	p	22.62	-21.19	-21.45	-22.04	10.77	11.04	0	0	0
52.9574205	-27.9006200	1.160	p	22.95	-21.24	-21.58	-22.47	10.82	11.24	0	0	0
52.9577505	-27.6053800	0.956	p	21.83	-21.35	-21.69	-22.24	10.87	11.02	0	0	0
52.9579995	-27.7236500	1.056	p	21.24	-22.73	-22.97	-23.46	11.38	11.41	0	0	0
52.9596105	-27.8805300	0.696	s	21.29	-20.67	-21.00	-21.68	10.59	10.84	0	0	0
52.9601295	-27.9077800	0.564	p	20.48	-20.82	-21.14	-21.90	10.65	10.87	0	0	0

RA	Dec	z	spec/ phot?	z$_{850}$	M$_U$	M$_B$	M$_V$	L$_B$	M$_*$	X-ray?	1.4GHz?	24μm?
(J2000)	(J2000)							log(L$_{B,\odot}$)	log(M$_\odot$)			
(1)	(2)	(3)	(4)	(5)	(6)	(7)	(8)	(9)	(10)	(11)	(12)	(13)
52.9615305	-27.6544300	0.613	s	19.59	-22.21	-22.45	-23.23	11.17	11.43	0	0	1
52.9669800	-27.6086300	0.816	p	22.33	-20.46	-20.78	-21.59	10.50	10.62	0	0	0
52.9672500	-27.9672000	1.005	p	21.86	-21.45	-21.96	-22.59	10.98	11.35	0	0	0
52.9686300	-27.7077600	0.734	s	20.71	-21.78	-21.98	-22.64	10.98	11.08	0	0	0
52.9687995	-27.6983700	0.685	p	21.03	-20.99	-21.29	-21.96	10.71	10.92	0	0	0
52.9697505	-27.6987500	1.005	p	22.67	-21.14	-21.42	-22.04	10.76	10.82	0	0	0
52.9736505	-27.9828200	1.107	p	22.02	-21.89	-22.18	-22.61	11.07	11.13	0	0	0
52.9744800	-27.8732200	0.908	p	21.67	-21.58	-21.82	-22.41	10.92	11.14	0	0	0
52.9750005	-27.6282400	0.956	p	20.95	-22.32	-22.82	-23.57	11.32	11.58	0	0	0
52.9756605	-27.9966600	0.740	s	21.52	-20.71	-20.99	-21.63	10.59	10.77	1	0	0
52.9768605	-27.9119300	0.536	s	19.98	-21.03	-21.28	-22.09	10.70	10.95	0	0	0
52.9776600	-27.7281200	0.771	p	19.80	-22.54	-22.93	-23.60	11.36	11.55	0	0	0
52.9805400	-27.7204200	0.861	s	21.68	-21.28	-21.44	-22.09	10.77	10.87	1	0	0
52.9833300	-27.6618500	0.548	s	19.46	-21.44	-21.98	-22.90	10.98	11.29	1	0	0
52.9848195	-27.6954600	1.107	p	22.98	-20.83	-21.20	-21.79	10.67	10.91	0	0	0
52.9859805	-27.7748000	1.160	p	22.96	-21.05	-21.16	-21.70	10.65	10.69	0	0	0
52.9862400	-27.6240900	0.956	p	22.56	-20.74	-20.95	-21.45	10.57	10.74	0	0	0
52.9866195	-27.9888600	0.908	p	21.78	-21.46	-21.72	-22.56	10.88	11.19	0	0	0
52.9872105	-27.6562400	0.861	p	22.74	-20.44	-21.11	-21.80	10.64	10.53	0	0	0
52.9907595	-27.7024100	0.665	s	20.97	-21.05	-21.41	-22.24	10.76	11.20	1	1	1
52.9910100	-27.7125400	0.644	p	19.60	-21.89	-22.33	-23.23	11.12	11.37	0	0	0
52.9922595	-27.7498200	0.575	s	20.12	-21.17	-21.55	-22.42	10.81	11.08	1	0	0
52.9940895	-27.8991500	0.644	p	20.45	-21.05	-21.44	-22.20	10.77	11.01	0	0	0
52.9971000	-27.6923300	0.908	p	21.76	-21.36	-21.68	-22.33	10.87	11.04	0	0	0
52.9984305	-27.9032400	0.685	p	21.20	-20.91	-21.19	-22.03	10.67	11.00	0	0	0
52.9996305	-27.9243400	0.691	s	21.26	-21.04	-21.39	-22.13	10.75	11.01	0	0	0
53.0010900	-27.9668200	0.649	s	20.34	-21.38	-21.81	-22.56	10.92	11.10	0	0	0
53.0017095	-27.8745900	0.631	s	20.80	-20.87	-21.18	-21.94	10.66	10.95	1	0	0
53.0048505	-27.6504100	0.908	p	21.45	-21.39	-21.92	-22.49	10.96	11.11	0	0	0
53.0077305	-27.6593200	0.908	p	22.77	-20.67	-20.90	-21.63	10.55	10.71	0	0	0
53.0078205	-27.8231100	1.056	p	21.62	-22.02	-22.41	-23.04	11.16	11.45	0	0	0
53.0080395	-27.8888700	0.381	p	18.46	-21.20	-21.73	-22.55	10.88	11.22	0	0	0
53.0103705	-28.0355900	0.381	p	18.58	-21.31	-21.82	-22.59	10.92	11.21	0	0	0
53.0112405	-27.8717400	0.685	p	21.34	-20.81	-21.16	-21.83	10.66	10.87	0	0	0
53.0114205	-27.8405600	0.564	p	20.70	-20.59	-21.00	-21.88	10.59	10.85	0	0	0
53.0115405	-27.8429000	0.644	p	20.05	-21.43	-21.81	-22.55	10.91	11.08	0	0	0
53.0143695	-27.9186000	0.679	s	21.28	-20.60	-20.92	-21.69	10.56	10.91	0	0	0
53.0163795	-27.9629400	0.816	p	22.15	-20.58	-20.86	-21.27	10.54	10.58	0	0	0
53.0164095	-27.8765900	0.861	p	21.56	-21.05	-21.44	-22.07	10.77	10.95	0	0	0
53.0165400	-27.9504100	0.416	p	19.02	-22.21	-22.46	-23.11	11.17	11.11	0	0	0
53.0168700	-27.6237400	0.975	s	22.50	-21.15	-21.21	-22.12	10.68	10.92	1	0	0
53.0176090	-27.7544840	0.288	s	18.22	-20.89	-21.48	-22.32	10.79	11.11	0	0	0
53.0203095	-27.6161500	0.956	p	22.35	-20.65	-21.35	-21.97	10.73	10.87	0	0	0
53.0210295	-27.8866900	1.160	p	22.02	-21.81	-22.01	-23.00	11.00	11.43	0	0	0
53.0212905	-27.6170800	0.956	p	22.01	-21.54	-21.96	-22.67	10.98	11.29	0	0	0
53.0230695	-27.9677100	1.107	p	22.54	-21.63	-21.86	-22.43	10.94	11.13	0	0	0
53.0243505	-27.9503400	1.005	p	20.94	-22.47	-22.83	-23.42	11.32	11.53	0	0	0
53.0245605	-27.9137400	0.685	s	19.81	-22.24	-22.64	-23.41	11.25	11.47	1	0	0
53.0249505	-27.6458300	0.803	s	20.89	-21.63	-21.99	-22.53	10.99	11.17	0	0	0
53.0264595	-27.6261800	0.908	p	21.76	-21.01	-21.38	-22.04	10.74	10.97	0	0	0
53.0270120	-27.7343390	0.958	s	22.17	-21.17	-21.64	-22.29	10.85	11.13	0	0	0
53.0290305	-27.8997300	0.687	s	21.01	-21.07	-21.34	-22.09	10.73	10.97	0	0	0
53.0293995	-28.0275100	0.956	p	21.10	-21.91	-22.31	-23.03	11.11	11.50	0	0	0
53.0332305	-27.6575400	0.908	p	22.12	-20.88	-21.15	-21.84	10.65	11.15	0	0	1
53.0349120	-27.7808910	0.861	p	22.60	-20.28	-20.74	-21.50	10.49	10.76	0	0	0
53.0350605	-27.9152300	0.689	s	20.66	-21.27	-21.67	-22.43	10.86	11.19	0	0	0
53.0351910	-27.6960810	0.736	s	21.51	-21.20	-21.46	-22.27	10.78	10.99	0	0	0

RA	Dec	z	spec/ phot?	z$_{850}$	M$_U$	M$_B$	M$_V$	L$_B$	M$_*$	X-ray?	1.4GHz?	24μm?
(J2000)	(J2000)							log(L$_{B,\odot}$)	log(M$_\odot$)			
(1)	(2)	(3)	(4)	(5)	(6)	(7)	(8)	(9)	(10)	(11)	(12)	(13)
53.0355570	-27.7049270	0.771	p	20.98	-22.36	-22.48	-23.50	11.18	11.36	0	0	0
53.0360530	-27.7505050	0.873	s	21.01	-22.08	-22.38	-22.99	11.14	11.28	0	0	0
53.0366210	-27.8495240	0.736	s	21.71	-21.06	-21.02	-21.73	10.60	10.66	1	0	1
53.0372295	-27.9333600	0.816	p	20.35	-22.45	-22.67	-23.22	11.26	11.46	0	0	0
53.0379705	-27.9198700	0.771	p	21.47	-20.79	-21.03	-21.48	10.60	10.73	0	0	0
53.0380395	-27.9281300	0.727	p	19.95	-22.53	-22.77	-23.48	11.30	11.51	0	0	0
53.0383070	-27.7071130	0.727	p	21.67	-20.72	-20.95	-21.77	10.57	10.91	1	0	0
53.0387295	-27.9360900	0.727	p	20.84	-21.49	-21.75	-22.51	10.89	11.18	0	0	0
53.0399895	-27.6206900	0.908	p	21.06	-22.03	-22.31	-22.95	11.12	11.34	0	0	0
53.0404400	-27.7133640	0.727	p	20.28	-22.43	-22.67	-23.71	11.26	11.55	1	1	0
53.0418280	-27.7258680	1.056	p	21.38	-22.52	-22.90	-23.48	11.35	11.61	0	0	0
53.0421710	-27.7259270	1.023	s	22.40	-21.33	-21.75	-22.38	10.89	11.10	0	0	0
53.0422395	-27.9939500	0.685	p	19.84	-22.09	-22.58	-23.36	11.23	11.51	0	1	0
53.0423280	-27.7262080	1.020	s	22.05	-21.70	-22.09	-22.68	11.03	11.23	0	0	0
53.0432740	-27.7168940	0.771	p	19.87	-22.69	-23.05	-23.81	11.41	11.74	0	0	0
53.0469705	-27.9878700	0.526	p	19.63	-20.68	-21.26	-22.29	10.70	10.89	0	0	0
53.0475350	-27.7805460	0.575	s	21.31	-20.51	-20.73	-21.50	10.49	10.64	1	0	0
53.0495700	-27.9980300	1.160	p	22.72	-21.85	-22.01	-22.78	11.00	11.43	0	0	0
53.0499730	-27.7724880	1.032	s	22.81	-21.19	-21.40	-21.92	10.75	10.85	0	0	0
53.0508190	-27.7583520	0.677	s	20.74	-21.51	-21.81	-22.50	10.91	11.09	1	0	0
53.0512890	-27.7576240	0.680	s	21.85	-20.54	-20.73	-21.50	10.48	10.65	0	0	0
53.0515800	-27.9240700	0.251	p	18.50	-20.64	-21.10	-21.90	10.63	10.74	0	0	0
53.0516595	-27.6552900	1.107	p	21.20	-22.64	-22.92	-23.67	11.36	11.79	0	0	0
53.0519290	-27.7914470	1.018	s	22.06	-21.81	-22.09	-22.69	11.03	11.19	0	0	0
53.0535795	-28.0026800	1.107	p	22.93	-21.03	-21.07	-21.81	10.62	11.03	0	0	0
53.0537505	-27.9909200	0.603	p	20.69	-20.90	-21.21	-21.99	10.68	10.89	0	0	0
53.0542260	-27.8294960	0.644	p	20.13	-21.82	-22.27	-23.12	11.10	11.37	0	0	0
53.0546070	-27.8921240	0.685	p	21.83	-20.45	-20.73	-21.40	10.49	10.64	0	0	0
53.0547405	-27.9146800	0.251	p	18.04	-20.39	-20.97	-21.86	10.58	10.90	0	0	0
53.0547495	-27.6658200	0.861	p	22.14	-20.84	-21.08	-21.69	10.62	10.82	0	0	0
53.0551695	-27.9645000	0.624	s	21.53	-20.59	-20.73	-21.43	10.48	10.72	1	0	1
53.0582400	-27.9746400	0.771	p	21.74	-20.77	-20.99	-21.60	10.59	10.85	0	0	0
53.0601620	-27.7734680	0.735	s	21.73	-20.82	-21.05	-21.69	10.61	10.79	0	0	0
53.0618130	-27.7939820	0.735	s	21.84	-20.62	-20.95	-21.58	10.57	10.77	1	0	0
53.0624200	-27.8575150	0.676	s	20.47	-21.57	-21.90	-22.64	10.95	11.23	1	0	0
53.0640450	-27.8458310	0.251	p	18.54	-20.30	-20.80	-21.68	10.51	10.82	1	0	0
53.0658720	-27.7871110	0.738	s	20.47	-22.02	-22.28	-22.95	11.10	11.35	0	0	0
53.0673900	-27.8781380	1.107	p	22.69	-21.64	-21.82	-22.45	10.92	11.16	0	0	0
53.0688780	-27.7908990	0.729	s	21.19	-21.21	-21.48	-22.12	10.78	11.02	0	0	0
53.0695300	-27.8775010	1.045	s	22.58	-21.29	-21.62	-22.28	10.84	11.01	0	0	0
53.0698780	-27.8354890	0.729	s	22.53	-20.79	-21.02	-21.63	10.60	10.42	0	0	0
53.0714570	-27.8755610	1.160	p	22.58	-21.85	-22.11	-22.76	11.04	11.42	0	0	0
53.0720480	-27.8020860	0.735	s	21.95	-20.58	-20.86	-21.52	10.54	10.70	0	0	0
53.0726700	-27.8014980	0.733	s	21.55	-21.07	-21.33	-21.98	10.72	10.90	0	0	0
53.0727650	-27.8763200	1.100	s	21.90	-22.13	-22.36	-23.10	11.14	11.46	0	0	0
53.0728610	-27.7435340	0.734	s	21.49	-21.56	-21.65	-22.31	10.85	10.86	0	0	0
53.0740240	-27.7874640	0.730	s	21.51	-21.69	-21.85	-22.66	10.93	11.01	0	0	0
53.0746310	-27.6896320	1.041	s	22.13	-21.62	-21.91	-22.63	10.96	11.31	0	0	0
53.0747600	-27.7892990	0.732	s	20.30	-22.59	-22.80	-23.55	11.31	11.49	0	0	0
53.0768200	-27.7601720	0.523	s	20.00	-21.24	-21.67	-22.47	10.86	11.04	0	0	0
53.0768740	-27.7655260	0.735	s	20.77	-21.61	-21.92	-22.65	10.96	11.25	1	0	1
53.0771600	-27.8327470	0.644	p	20.74	-21.10	-21.48	-22.26	10.79	11.09	0	0	0
53.0777240	-27.8692780	0.760	s	21.72	-21.02	-21.22	-21.95	10.68	10.87	0	0	0
53.0785140	-27.7581180	0.296	s	18.68	-21.24	-21.42	-22.25	10.76	10.87	1	0	0
53.0801730	-27.7756040	0.738	s	20.88	-21.51	-21.82	-22.50	10.92	11.22	1	0	0
53.0804370	-27.8720360	1.096	s	22.00	-22.34	-22.79	-23.22	11.31	11.44	0	1	0
53.0816310	-27.7177180	0.603	p	21.14	-20.61	-21.15	-21.90	10.65	10.85	0	0	0

RA	Dec	z	spec/ phot?	z$_{850}$	M$_U$	M$_B$	M$_V$	L$_B$ log(L$_{B,\odot}$)	M$_*$ log(M$_\odot$)	X-ray?	1.4GHz?	24μm?
(J2000) (1)	(J2000) (2)	(3)	(4)	(5)	(6)	(7)	(8)	(9)	(10)	(11)	(12)	(13)
53.0843320	-27.8050960	0.733	s	20.89	-21.97	-22.19	-22.91	11.07	11.20	0	0	0
53.0854640	-27.8907360	1.056	p	22.69	-21.16	-21.56	-22.16	10.82	11.01	0	0	0
53.0861050	-27.7462330	0.726	s	21.53	-21.02	-21.22	-21.97	10.68	11.02	0	0	0
53.0897520	-27.8592570	0.536	s	20.83	-20.34	-20.74	-21.53	10.49	10.77	0	0	0
53.0922130	-27.8505270	0.734	s	21.67	-20.75	-21.01	-21.77	10.60	10.86	0	0	0
53.0958940	-27.7254120	0.727	p	21.98	-20.69	-20.94	-21.61	10.57	10.75	0	0	0
53.0969050	-27.8505130	0.964	s	21.89	-21.43	-21.80	-22.47	10.91	11.13	0	0	0
53.1016200	-27.7734170	0.895	s	21.93	-21.22	-21.50	-22.20	10.79	11.13	0	0	0
53.1044540	-27.8803560	1.107	p	22.40	-21.51	-21.93	-22.83	10.96	11.45	0	0	0
53.1049960	-27.8359390	1.107	p	22.89	-21.33	-21.45	-22.07	10.77	10.93	0	0	0
53.1061170	-27.7243190	0.668	s	20.10	-21.81	-22.29	-23.11	11.11	11.49	0	0	0
53.1119580	-27.9064730	0.619	s	21.03	-21.17	-21.38	-22.10	10.74	10.87	0	0	0
53.1132700	-27.7379090	0.419	s	19.38	-21.09	-21.50	-22.31	10.79	11.04	1	0	0
53.1161650	-27.8612170	0.521	s	20.25	-20.91	-21.28	-22.07	10.70	10.97	0	0	0
53.1170350	-27.8673250	0.560	s	20.29	-21.10	-21.48	-22.25	10.79	11.05	0	0	0
53.1197240	-27.7723050	0.737	s	21.15	-21.76	-21.99	-22.75	10.99	11.25	1	1	0
53.1200710	-27.7321240	0.214	s	17.87	-20.56	-21.06	-21.98	10.62	10.90	1	1	0
53.1217310	-27.7854390	0.669	s	20.64	-21.34	-21.75	-22.54	10.89	11.36	1	0	0
53.1253090	-27.8612900	0.532	s	19.83	-21.58	-22.03	-22.82	11.00	11.16	0	0	0
53.1253395	-27.8499300	0.727	p	20.46	-21.87	-22.05	-22.75	11.01	11.24	0	0	0
53.1253740	-27.8500770	0.733	s	20.81	-21.53	-21.89	-22.69	10.95	11.24	0	0	0
53.1300890	-27.7590850	1.097	s	22.98	-21.17	-21.55	-22.18	10.81	10.99	0	0	0
53.1307070	-27.8886530	0.908	p	21.07	-22.08	-22.56	-23.27	11.22	11.58	0	0	0
53.1323780	-27.8142380	0.948	s	22.59	-21.11	-21.24	-21.83	10.69	10.78	0	0	0
53.1363870	-27.8507060	0.735	s	20.73	-21.55	-21.96	-22.77	10.97	11.29	0	0	0
53.1373520	-27.7626880	0.366	s	19.93	-20.35	-20.75	-21.53	10.49	10.68	0	0	0
53.1375890	-27.7435050	0.605	s	20.37	-21.37	-21.65	-22.41	10.85	11.06	0	0	0
53.1411210	-27.7326550	0.979	s	22.67	-20.72	-21.00	-21.54	10.59	10.94	0	0	0
53.1430930	-27.7305810	0.668	s	21.07	-21.32	-21.60	-22.33	10.83	10.92	1	0	0
53.1459350	-27.9014510	0.688	s	21.36	-20.95	-21.24	-21.99	10.69	10.93	0	0	0
53.1477200	-27.7391970	0.894	s	22.41	-21.22	-21.31	-21.88	10.71	10.72	0	0	0
53.1489600	-27.7996830	0.664	s	20.39	-21.56	-21.97	-22.76	10.98	11.26	0	0	0
53.1554410	-27.7914850	0.667	s	19.87	-22.07	-22.54	-23.41	11.21	11.52	1	0	0
53.1594770	-27.8984570	0.688	s	21.75	-20.69	-20.93	-21.64	10.56	10.75	0	0	0
53.1601600	-27.7755280	0.727	p	21.78	-20.72	-20.94	-21.69	10.57	10.84	0	0	0
53.1606670	-27.8971120	0.564	p	20.11	-21.34	-21.77	-22.57	10.90	11.18	1	0	0
53.1616100	-27.7469230	0.736	s	21.53	-21.14	-21.29	-21.92	10.71	11.06	1	1	1
53.1616290	-27.7802470	0.619	s	21.35	-20.42	-20.79	-21.64	10.51	10.85	0	0	0
53.1634180	-27.7995470	0.665	s	20.67	-21.24	-21.69	-22.45	10.87	11.21	0	0	0
53.1644550	-27.8834690	0.644	p	20.66	-21.12	-21.48	-22.43	10.78	11.20	1	1	0
53.1645200	-27.8837910	0.686	s	20.51	-21.55	-21.91	-22.82	10.96	11.36	1	1	0
53.1646880	-27.6881770	1.056	p	22.16	-21.68	-21.97	-22.72	10.98	11.28	0	0	0
53.1647490	-27.8245470	0.669	s	21.04	-21.10	-21.41	-22.10	10.76	10.95	0	0	0
53.1661905	-27.9722000	1.056	p	22.77	-21.72	-21.90	-22.57	10.95	11.25	0	0	0
53.1694720	-27.7919410	0.644	p	21.29	-20.75	-21.07	-21.91	10.62	10.94	0	0	0
53.1697695	-27.6601700	0.678	s	20.90	-21.04	-21.44	-22.19	10.77	11.05	0	0	0
53.1725230	-27.7881070	0.685	p	20.70	-21.68	-21.99	-22.74	10.99	11.23	1	0	0
53.1734390	-27.8659760	0.771	p	20.20	-22.71	-23.03	-23.74	11.40	11.63	0	0	0
53.1784800	-27.6574800	0.727	p	20.79	-21.44	-21.71	-22.45	10.88	11.18	0	0	0
53.1785700	-27.8902150	0.644	p	20.66	-21.19	-21.59	-22.34	10.83	11.07	0	0	0
53.1793305	-28.0040600	1.160	p	21.94	-22.47	-22.59	-23.24	11.23	11.42	0	0	0
53.1836205	-27.6279200	0.685	p	21.21	-20.81	-21.12	-21.79	10.64	10.89	0	0	0
53.1837010	-27.7615170	0.488	p	19.57	-21.46	-21.80	-22.55	10.91	11.09	1	0	0
53.1844440	-27.8574300	1.160	p	22.84	-21.90	-22.17	-22.74	11.06	11.20	0	0	0
53.1845590	-27.8360310	1.038	s	22.61	-21.35	-21.65	-22.37	10.85	11.01	0	0	0
53.1852300	-27.8278350	1.017	s	22.32	-21.85	-21.80	-22.50	10.91	11.18	1	0	0
53.1873105	-27.6543000	0.816	p	22.63	-20.32	-20.72	-21.35	10.48	10.66	0	0	0

RA	Dec	z	spec/ phot?	z$_{850}$	M$_U$	M$_B$	M$_V$	L$_B$	M$_*$	X-ray?	1.4GHz?	24μm?
(J2000)	(J2000)							log(L$_{B,\odot}$)	log(M$_\odot$)			
(1)	(2)	(3)	(4)	(5)	(6)	(7)	(8)	(9)	(10)	(11)	(12)	(13)
53.1881595	-27.6450300	0.727	p	21.16	-21.06	-21.34	-21.99	10.73	10.95	0	0	0
53.1895905	-27.6813500	0.685	p	20.01	-21.76	-22.09	-22.83	11.03	11.31	0	0	0
53.1917895	-27.6803400	0.861	p	22.31	-20.84	-20.94	-21.48	10.57	10.60	0	0	0
53.1918790	-27.9124280	0.733	s	21.51	-21.11	-21.34	-22.12	10.73	10.94	0	0	0
53.1929400	-27.7143150	0.727	p	21.62	-20.84	-21.14	-22.02	10.65	11.05	1	0	0
53.1939000	-27.9536400	0.770	s	19.68	-22.53	-22.84	-23.38	11.33	11.47	1	0	0
53.1948795	-28.0041500	0.488	p	20.02	-20.53	-20.99	-21.85	10.59	10.90	0	0	0
53.1956205	-27.6508100	0.152	s	16.58	-20.75	-21.30	-22.25	10.71	10.97	1	1	1
53.1986205	-27.6827700	0.727	p	21.60	-20.86	-21.10	-21.79	10.63	10.85	0	0	0
53.2005540	-27.8124850	0.685	p	21.45	-20.61	-20.99	-21.76	10.59	10.88	0	0	0
53.2007370	-27.8823910	0.668	s	19.86	-22.28	-22.57	-23.27	11.22	11.46	1	1	1
53.2013700	-28.0123500	0.603	p	21.30	-20.62	-20.73	-21.47	10.48	10.63	0	0	0
53.2021200	-27.9424200	0.685	p	20.96	-21.32	-21.61	-22.32	10.84	10.95	0	0	0
53.2024095	-28.0154400	0.956	p	20.47	-22.81	-23.21	-23.74	11.48	11.63	0	0	0
53.2032590	-27.9049360	0.600	s	20.74	-20.86	-21.24	-22.00	10.69	11.00	0	0	0
53.2053495	-27.9503500	0.816	p	21.88	-20.80	-21.13	-21.73	10.64	10.84	0	0	0
53.2058295	-28.0286700	0.908	p	21.06	-22.07	-22.49	-23.12	11.19	11.42	0	0	0
53.2087605	-28.0397200	0.220	p	17.37	-20.66	-21.27	-22.21	10.70	11.05	0	0	0
53.2090070	-27.9273590	0.564	p	20.49	-20.95	-21.29	-22.06	10.71	10.95	0	0	0
53.2169400	-27.7402900	0.534	s	19.49	-21.85	-22.36	-23.20	11.13	11.27	1	1	0
53.2207995	-27.9940500	0.220	p	17.34	-20.77	-21.34	-22.24	10.73	11.04	0	0	0
53.2211595	-27.7551900	0.251	p	18.15	-20.41	-21.04	-21.95	10.61	10.92	0	0	0
53.2230795	-28.0276900	0.644	p	21.20	-20.35	-20.80	-21.58	10.51	10.75	0	0	0
53.2250630	-27.9005970	0.908	p	22.40	-20.97	-21.24	-21.89	10.69	10.80	1	0	0
53.2250710	-27.8018400	1.160	p	22.88	-21.43	-21.40	-22.16	10.75	11.15	0	0	0
53.2267200	-27.6486900	0.956	p	22.18	-21.09	-21.48	-22.23	10.78	11.08	0	0	0
53.2315395	-27.7149700	0.771	p	21.27	-21.18	-21.48	-22.19	10.78	11.06	0	0	0
53.2363005	-27.6117600	0.251	p	17.65	-20.82	-21.46	-22.36	10.78	11.12	0	0	0
53.2415295	-28.0094000	0.956	p	21.30	-21.88	-22.27	-22.80	11.10	11.26	0	0	0
53.2439505	-27.9480900	0.771	p	21.66	-20.81	-21.05	-21.56	10.61	10.81	0	0	0
53.2445895	-27.7101600	0.282	p	17.78	-20.83	-21.51	-22.41	10.80	11.19	0	0	0
53.2446600	-28.0332600	0.771	p	21.15	-21.19	-21.42	-22.00	10.76	10.96	0	0	0
53.2496295	-28.0179100	0.727	p	21.13	-21.16	-21.39	-22.13	10.75	10.96	0	0	0
53.2508295	-27.9830000	0.732	s	20.92	-21.46	-21.76	-22.50	10.90	11.16	0	0	0
53.2544100	-27.7682000	0.727	p	21.57	-20.74	-20.93	-21.62	10.56	10.68	0	0	0
53.2550390	-27.8914700	0.685	p	21.41	-20.80	-21.09	-21.82	10.63	10.88	0	0	0
53.2561905	-27.6950400	0.908	p	21.86	-21.13	-21.57	-22.30	10.82	11.09	1	0	1
53.2571910	-27.8621560	0.519	s	20.41	-20.57	-21.00	-21.83	10.59	10.99	0	0	0
53.2587705	-28.0377300	0.644	p	20.43	-20.98	-21.46	-22.33	10.78	11.15	0	0	0
53.2590195	-27.7276200	0.956	p	22.39	-21.10	-21.43	-22.15	10.77	11.00	0	0	0
53.2629195	-27.9640600	0.644	p	20.07	-21.22	-21.76	-22.75	10.90	11.32	0	0	0
53.2637295	-27.9743800	0.685	p	21.47	-20.70	-21.00	-21.53	10.59	10.69	0	0	0
53.2642200	-27.6466000	1.107	p	21.29	-22.38	-22.59	-23.22	11.23	11.49	0	0	0
53.2658100	-28.0399000	0.727	p	20.57	-21.79	-22.23	-23.04	11.08	11.41	0	0	0
53.2675995	-28.0399000	0.771	p	21.00	-21.41	-21.71	-22.43	10.88	11.15	0	0	0
53.2687200	-27.8995800	0.526	p	18.50	-22.38	-22.83	-23.70	11.33	11.59	0	0	0
53.2724295	-27.8706200	0.381	p	19.95	-21.27	-21.78	-22.86	10.90	10.88	0	0	0
53.2732005	-27.6816000	1.107	p	21.57	-22.38	-22.46	-23.07	11.18	11.48	0	0	0
53.2736295	-27.8706300	0.521	s	18.70	-22.37	-22.83	-23.71	11.32	11.65	1	1	1
53.2739295	-27.9103100	0.771	p	22.75	-20.55	-20.85	-21.60	10.53	10.38	0	0	0
53.2759305	-27.9938000	0.644	p	20.34	-21.37	-21.69	-22.50	10.87	11.03	0	0	0
53.2760295	-27.8767300	0.644	p	20.06	-21.59	-21.86	-22.55	10.94	11.15	0	0	0
53.2763505	-27.9247600	0.771	p	21.76	-21.00	-21.78	-22.54	10.90	10.91	0	0	0
53.2766805	-28.0303900	0.908	p	21.64	-21.32	-21.72	-22.31	10.88	11.04	0	0	0
53.2796100	-27.7776300	0.220	p	17.73	-20.60	-21.11	-21.96	10.63	10.97	0	0	1
53.2820700	-27.8589000	0.727	p	21.38	-20.98	-21.19	-21.92	10.67	10.89	0	0	0
53.2881795	-27.6642100	1.160	p	21.82	-22.09	-22.22	-23.05	11.08	11.51	0	0	0

RA	Dec	z	spec/phot?	z_{850}	M_U	M_B	M_V	L_B	M_*	X-ray?	1.4GHz?	24μm?
(J2000)	(J2000)							$\log(L_{B,\odot})$	$\log(M_\odot)$			
(1)	(2)	(3)	(4)	(5)	(6)	(7)	(8)	(9)	(10)	(11)	(12)	(13)
53.2896495	-27.9023200	0.861	p	22.06	-21.01	-21.27	-21.92	10.70	10.88	0	0	0
53.2900095	-27.6811600	0.956	p	21.31	-21.94	-22.34	-22.98	11.13	11.42	0	0	0
53.2906605	-27.9010800	0.644	p	21.40	-20.62	-20.86	-21.59	10.54	10.70	0	0	0
53.2943400	-27.9894000	0.771	p	20.50	-21.79	-22.17	-22.80	11.06	11.27	0	0	0
53.2952595	-27.7455000	0.861	p	21.72	-21.15	-21.55	-22.22	10.81	11.09	0	0	0
53.2966695	-27.9799600	0.564	p	20.75	-20.78	-21.29	-22.14	10.71	11.04	0	0	0
53.2986300	-27.9339700	0.603	p	19.70	-21.77	-22.20	-23.00	11.07	11.29	0	0	0
53.3000205	-27.8779300	0.861	p	20.87	-22.19	-22.45	-23.01	11.17	11.48	0	0	1
53.3014005	-27.9626400	0.908	p	22.45	-20.89	-21.20	-21.82	10.67	10.87	0	0	0
53.3036895	-27.7054600	0.683	s	20.99	-21.32	-21.55	-22.36	10.81	10.92	1	0	0
53.3044500	-27.6421000	0.956	p	22.29	-20.88	-21.23	-21.85	10.69	10.91	0	0	0
53.3044800	-27.7746800	0.526	p	19.44	-21.63	-22.05	-22.94	11.01	11.22	0	0	0
53.3047305	-27.8791800	1.107	p	22.51	-21.23	-21.78	-22.55	10.91	11.29	0	0	0
53.3066595	-27.9598300	0.685	p	20.19	-22.63	-23.04	-23.72	11.41	11.37	0	0	0
53.3140200	-27.7195600	0.816	p	21.51	-21.12	-21.49	-22.19	10.79	11.02	0	0	0
53.3142795	-27.7566700	0.727	p	21.79	-21.00	-21.08	-21.72	10.63	10.79	0	1	1
53.3160495	-28.0369200	0.771	p	20.98	-21.69	-21.99	-22.69	10.99	11.22	0	0	0
53.3184900	-27.6920400	0.685	p	19.49	-22.38	-22.79	-23.58	11.31	11.58	0	0	0
53.3185995	-27.9770400	1.056	p	21.73	-21.97	-22.14	-22.77	11.05	11.40	0	0	0
53.3199195	-27.7594600	0.644	p	19.55	-22.20	-22.53	-23.30	11.20	11.37	0	0	0
53.3202195	-27.9802600	1.056	p	21.59	-22.24	-22.49	-23.07	11.19	11.40	0	0	0
53.3219700	-27.9824900	0.956	p	21.80	-21.34	-21.81	-22.43	10.92	11.11	0	0	0
53.3247600	-27.7659700	0.908	p	21.74	-20.87	-21.45	-22.14	10.77	11.08	0	0	0
53.3249700	-27.6754300	0.685	p	21.40	-20.68	-21.02	-21.68	10.60	10.70	0	0	0
53.3263500	-27.9385600	0.816	p	21.70	-21.27	-21.44	-22.03	10.77	11.01	0	0	0
53.3275200	-27.7321400	0.526	p	19.59	-21.25	-21.64	-22.49	10.85	11.04	0	0	0
53.3314500	-27.7265200	0.526	p	19.95	-21.28	-21.61	-22.35	10.84	11.03	0	0	0
53.3323695	-27.6920600	1.107	p	21.45	-22.31	-22.50	-23.21	11.19	11.49	0	0	0
53.3381205	-27.6809500	1.107	p	22.26	-21.67	-22.04	-22.79	11.01	11.25	0	0	0
53.3396700	-27.9051300	1.107	p	21.07	-22.87	-23.08	-23.63	11.42	11.65	0	0	0
53.3397495	-27.7649900	1.056	p	21.17	-22.29	-22.57	-22.96	11.22	11.39	0	0	0
53.3403300	-28.0033100	0.603	p	21.33	-20.43	-20.76	-21.52	10.50	10.68	0	0	0
53.3414805	-27.9997900	0.956	p	20.88	-22.01	-22.48	-22.93	11.18	11.29	0	0	0
53.3433000	-27.9757600	0.816	p	21.09	-21.36	-21.78	-22.48	10.91	11.15	0	0	0
53.3446500	-27.7014500	1.107	p	22.90	-21.19	-21.34	-21.86	10.73	10.81	0	0	0
53.3467695	-27.7209500	0.526	p	20.18	-20.75	-21.11	-21.95	10.64	10.92	0	0	0
53.3474400	-27.7554700	0.908	p	22.58	-20.59	-20.94	-21.60	10.57	10.50	0	0	0
53.3478195	-27.6469500	1.107	p	21.00	-22.87	-23.14	-23.73	11.45	11.72	0	0	0
53.3500095	-27.7195700	0.908	p	20.88	-22.06	-22.47	-23.08	11.18	11.33	0	0	1
53.3536200	-27.9525800	0.908	p	22.61	-20.66	-20.89	-21.40	10.55	10.64	0	0	0
53.3545095	-27.9830100	1.160	p	22.63	-21.61	-21.77	-22.33	10.90	11.05	0	0	0
53.3621595	-27.9399000	0.564	p	19.34	-21.61	-22.18	-23.10	11.06	11.38	0	0	0
53.3629200	-27.7398300	0.771	p	21.09	-21.10	-21.58	-22.25	10.82	11.12	0	0	0
53.3658705	-27.7386500	0.968	s	21.31	-21.97	-22.31	-22.89	11.12	11.36	1	0	0
189.0022430	62.1988258	0.562	s	19.55	-21.37	-21.67	-22.49	10.86	11.14	0	0	0
189.0026550	62.1965370	0.947	s	21.84	-20.79	-21.10	-21.66	10.63	10.84	0	0	0
189.0045776	62.2567673	0.599	p	20.52	-20.89	-21.05	-21.80	10.61	10.80	0	0	0
189.0075531	62.1907387	0.913	s	21.21	-21.32	-21.69	-22.36	10.87	11.19	0	1	0
189.0178833	62.1805649	0.851	s	21.18	-21.24	-21.45	-21.98	10.77	10.89	0	0	0
189.0339050	62.1767044	0.679	s	20.53	-21.21	-21.36	-21.94	10.74	10.86	1	1	1
189.0632629	62.2486839	1.140	s	22.75	-20.80	-20.76	-21.32	10.50	10.81	0	0	0
189.0712433	62.1698761	0.846	s	21.77	-21.04	-21.14	-22.02	10.65	11.01	1	1	1
189.0730896	62.1627922	0.845	s	21.77	-20.44	-20.76	-21.37	10.50	10.76	0	0	0
189.0779724	62.1887474	1.021	s	22.62	-20.72	-20.80	-21.39	10.51	10.76	0	0	1
189.0781860	62.2785606	1.147	p	22.78	-21.07	-21.26	-21.86	10.69	10.98	0	0	0
189.0862579	62.1518631	1.012	s	21.42	-21.47	-21.77	-22.35	10.90	11.21	0	0	0
189.0877075	62.2937546	0.767	p	21.17	-20.76	-21.09	-21.73	10.63	10.83	0	0	0

RA	Dec	z	spec/ phot?	z$_{850}$	M$_U$	M$_B$	M$_V$	L$_B$	M$_*$	X-ray?	1.4GHz?	24μm?
(J2000)	(J2000)							log(L$_{B,\odot}$)	log(M$_\odot$)			
(1)	(2)	(3)	(4)	(5)	(6)	(7)	(8)	(9)	(10)	(11)	(12)	(13)
189.0919037	62.1474380	1.016	s	21.87	-21.05	-21.32	-21.85	10.72	10.96	0	0	0
189.0946045	62.1628647	0.748	s	21.08	-20.75	-21.07	-21.78	10.62	10.90	0	1	0
189.0984344	62.2963753	0.785	p	21.16	-21.14	-21.28	-21.91	10.70	10.89	0	0	0
189.1016846	62.2483978	0.639	s	19.84	-21.48	-21.79	-22.63	10.91	11.25	0	0	0
189.1023865	62.1865540	0.748	s	21.34	-20.54	-20.81	-21.45	10.52	10.77	1	0	0
189.1127625	62.2526245	0.794	s	20.53	-21.39	-21.80	-22.49	10.91	11.18	0	0	0
189.1219788	62.2720070	0.846	s	21.82	-20.49	-20.80	-21.47	10.51	10.75	0	0	0
189.1278839	62.1580887	1.016	s	21.88	-21.09	-21.32	-21.85	10.72	10.94	0	0	0
189.1326141	62.1518898	0.845	s	20.28	-22.39	-22.54	-23.38	11.21	11.56	1	0	0
189.1348114	62.1373749	0.850	s	21.12	-21.43	-21.74	-22.61	10.89	11.20	0	0	0
189.1550751	62.2794609	0.852	s	21.04	-21.23	-21.55	-22.13	10.81	10.98	0	0	0
189.1556244	62.2799492	0.943	s	21.21	-21.54	-21.74	-22.27	10.89	11.01	0	0	0
189.1620941	62.1510773	0.843	s	21.34	-20.82	-21.21	-21.88	10.68	11.01	0	0	0
189.1627655	62.3058701	0.557	s	20.08	-20.75	-21.08	-21.96	10.63	11.00	0	0	0
189.1637115	62.2730064	0.849	s	21.89	-20.44	-20.74	-21.38	10.49	10.74	0	0	0
189.1656647	62.2632866	0.848	s	20.81	-21.40	-21.79	-22.45	10.91	11.12	1	0	0
189.1673126	62.2821503	0.943	s	21.50	-21.24	-21.46	-21.93	10.77	10.81	1	0	0
189.1799011	62.2117615	0.846	s	21.17	-21.08	-21.40	-22.00	10.75	10.97	0	0	0
189.1799774	62.2736435	0.851	s	20.80	-21.39	-21.73	-22.29	10.88	11.12	0	0	0
189.1826477	62.1952934	0.768	s	20.44	-21.53	-21.84	-22.49	10.93	11.15	0	0	0
189.1850586	62.1925964	1.013	s	20.57	-22.31	-22.68	-23.28	11.26	11.59	1	1	0
189.1869202	62.1457214	0.971	s	22.12	-20.78	-20.96	-21.48	10.57	10.73	0	0	0
189.1917267	62.1837120	0.936	s	21.81	-20.97	-21.37	-22.09	10.74	11.07	0	0	0
189.1922913	62.2129517	0.905	s	21.90	-20.76	-20.95	-21.45	10.57	10.61	0	0	0
189.1972656	62.2745285	0.871	s	20.85	-21.76	-21.95	-22.61	10.97	11.17	0	0	0
189.2025757	62.2646370	0.852	s	21.06	-21.32	-21.57	-22.11	10.82	10.98	0	0	0
189.2095642	62.2127304	0.681	s	21.08	-20.60	-20.79	-21.54	10.51	10.79	0	0	0
189.2160645	62.1500053	0.971	s	22.29	-20.63	-20.84	-21.42	10.53	10.76	0	0	0
189.2176971	62.1502876	0.973	s	21.92	-20.90	-21.15	-21.71	10.65	10.87	0	0	0
189.2180328	62.2603302	0.938	s	21.42	-21.16	-21.53	-22.13	10.81	11.05	0	0	0
189.2190094	62.1555176	0.954	s	21.59	-21.13	-21.42	-21.96	10.76	10.92	0	0	0
189.2203979	62.2455978	0.321	s	18.83	-20.70	-20.80	-21.65	10.51	10.89	1	1	0
189.2209473	62.2524452	0.938	s	21.56	-21.07	-21.39	-22.00	10.75	11.04	0	0	0
189.2262573	62.2819939	0.942	s	21.57	-21.02	-21.41	-22.03	10.75	11.05	0	0	0
189.2310638	62.2198143	0.955	s	21.62	-21.06	-21.39	-21.99	10.75	11.02	1	0	0
189.2360840	62.2056046	0.954	s	21.89	-20.84	-21.08	-21.62	10.62	10.84	0	0	0
189.2477112	62.2829704	1.105	p	22.71	-20.65	-20.74	-21.20	10.49	10.57	0	0	0
189.2792358	62.2744942	0.943	s	22.14	-20.56	-20.85	-21.46	10.53	10.85	0	0	0
189.3103943	62.2582932	0.857	s	21.64	-20.63	-21.00	-21.66	10.59	10.90	0	0	0
189.3144836	62.2033272	1.021	s	22.24	-20.71	-20.99	-21.61	10.59	11.01	0	0	0
189.3236542	62.1872864	0.903	s	20.75	-21.75	-22.08	-22.71	11.02	11.30	0	0	0
189.3349152	62.2557983	0.937	s	21.46	-20.98	-21.32	-21.81	10.72	10.97	0	0	0
189.3349152	62.2565498	0.937	s	21.57	-21.07	-21.46	-22.15	10.77	11.17	1	0	0
189.3396454	62.2262917	0.475	s	19.43	-21.02	-21.33	-22.14	10.72	11.10	0	0	0
189.3432465	62.2620621	0.938	s	21.62	-21.03	-21.32	-21.89	10.72	10.96	0	0	0
189.3514404	62.2117615	0.800	s	21.35	-21.24	-21.22	-22.00	10.68	10.97	1	0	0
189.3706970	62.1909637	0.936	s	21.70	-20.99	-21.26	-21.84	10.69	10.95	0	0	0
189.3746643	62.2169266	0.512	s	19.67	-21.24	-21.41	-22.17	10.76	11.08	0	0	0
189.3831329	62.2676468	0.850	s	21.80	-20.53	-20.80	-21.42	10.51	10.77	0	0	0
189.3929291	62.2114487	0.850	s	20.61	-21.58	-21.96	-22.63	10.98	11.35	0	0	0
189.4035645	62.2379150	0.688	s	20.99	-20.64	-20.90	-21.67	10.55	10.94	0	0	0

NOTES: (1)–(2): Optical J2000 coordinates. (3): Source redshift. (4): s=spectroscopic redshift, p=photometric redshift. (5): z$_{850}$ magnitude. (6): U-band magnitude. (7): B-band magnitude. (8): V-band magnitude. (9): Logarithmic B-band optical luminosity (log($L_{B,\odot}$)). (10):

Logarithmic stellar mass derived from K-band magnitude ($\log(M_\odot)$). (11): Indicates whether the source was X-ray detected or not (0=not detected, 1=detected). (12): Indicates whether the source was 1.4GHz radio detected or not (0=not detected, 1=detected). (13): Indicates whether the source was 24μm detected or not (0=not detected, 1=detected).

Appendix B

GLOSSARY

B.1 Acronyms

AGB	Asymptotic giant branch
AGN	Active galactic nucleus
ALESS	ALMA LABOCA ECDFS Submillimetre Survey
ALMA	Atacama Large Millmeter Array
APEX	Atacama Pathfinder EXperiment
CDF-N	*Chandra* Deep Field- North
CIB	Cosmic infrared background
CMB	Cosmic Microwave Background
COBE	Cosmic Background Explorer
CRDR	Cosmic ray dominated region
DDT	Directors discretionary time
DEIMOS	DEep Imaging Multi-Object Spectrograph
DIRBE	Diffuse Infrared Background Experiment
ECDFS	Extended *Chandra* Deep Field-South
EMIR	Eight MIxer Receiver
ESO	European Southern Observatory
ETG	Early-type galaxy

EVLA	Extended Very Large Array
FIDEL	Far-Infrared Deep Extragalactic Legacy Survey
FIR	Far-infrared
FIRAS	Far infrared Absolute Spectrophotometer
FORS2	FOcal Reducer and low dispersion Spectrograph 2
FWHM	Full-width half-maximum
FWZI	Full-width zero-intensity
GALEX	Galaxy Evolution Explorer
GBT	Green Bank Telescope
GMC	Giant molecular cloud
GNIRS	Gemini Near-Infrared Spectrograph
GOODS	The Great Observatories Origins Deep Survey
HerMES	*Herschel* Multi-tiered Extragalactic Survey
HDF	*Hubble* Deep Field
HST	*Hubble* Space Telescope
IMF	Initial mass function
IRAC	Infrared Array Camera
IRAM	Institut de Radioastronomie Millimétrique
IRAS	Infrared Astronomical Satellite
ISM	Interstellar medium
JCMT	James Clerk Maxwell Telescope
JVLA	Karl. G Jansky Very Large Array
JWST	James Webb Space Telescope
KMOS	K-band Multi-Object Spectrograph
ΛCDM	Cold dark matter
LABOCA	Large Apex BOlometer CAmera
LBG	Lyman break galaxy
LESS	LABOCA ECDFS Submillimetre Survey
LIRG	Luminous infrared galaxy
LRIS	Low-resolution Imaging Spectrograph

LTE	Local thermodynamic equilibrium
LTG	Late-type galaxy
LVG	Large velocity gradient
MAMBO	Max-Planck Millimetre Bolomoter Array
MIPS	Multiband Imaging Photometer for SIRTF
MOS	Multi-object spectroscopy
MOSFIRE	Multi-Object Spectrometer for Infra-Red Exploration
MUSYC	Multiwavelength Survey by Yale-Chile
NIR	Near-infrared
PdBI	IRAM Plateau de Bure Interferometer
PDR	Photodissociation region
RMS	Root mean square
SCUBA	Sub-millimetre Common-User Bolometer Array
SD	Standard deviation
SED	Spectral energy distribution
SFR	Star formation rate
SHADES	SCUBA Half Degree Extragalactic Survey
SHFI	Swedish Hetrodyne Facility Instrument
SIMPLE	*Spitzer* IRAC/MUSYC Public Legacy Survey in the Extended Chandra Deep Field South
SIRTF	Space Infrared Telescope Facility
SLED	Spectral line energy distribution
SMA	Submillimeter Array
SMBH	Supermassive black hole
SMG	Submillimetre galaxy
TENIS	Taiwan ECDFS Near-Infrared Survey
UV	Ultraviolet
ULIRG	Ultraluminous infrared galaxy
VIMOS	VIsible MultiObject Spectrograph
VLA	Very Large Array

VLT	Very Large Telescope
WIDEX	Wideband Express
WILMA	Wide-band line multiple autocorrelator
XDR	X-ray dominated region

Bibliography

Aalto S., Booth R. S., Black J. H., Johansson L. E. B., 1995, A&A, 300, 369

Adelberger K. L., 2005, ApJ, 621, 574

Alexander D. M. et al., 2003, AJ, 125, 383

Alexander D. M., Hickox R. C., 2012, New Astronomy Reviews, 56, 93

Alexander D. M., Smail I., Bauer F. E., Chapman S. C., Blain A. W., Brandt W. N., Ivison R. J., 2005, Nature, 434, 738

Allen S. W., Dunn R. J. H., Fabian A. C., Taylor G. B., Reynolds C. S., 2006, MNRAS, 372, 21

Antonucci R., 1993, ARA&A, 31, 473

Ao Y. et al., 2013, A&A, 550, A135

Appleton P. N. et al., 2004, ApJS, 154, 147

Aravena M. et al., 2010, ApJ, 718, 177

Aretxaga I. et al., 2007, MNRAS, 379, 1571

Baker A. J., Tacconi L. J., Genzel R., Lehnert M. D., Lutz D., 2004, ApJ, 604, 125

Baldwin J. A., Phillips M. M., Terlevich R., 1981, PASP, 93, 5

Balestra I. et al., 2010, A&A, 512, A12

Bally J., Langer W. D., 1982, ApJ, 255, 143

Banerji M., Chapman S. C., Smail I., Alaghband-Zadeh S., Swinbank A. M., Dunlop J. S., Ivison R. J., Blain A. W., 2011, MNRAS, 418, 1071

Barger A. J., Cowie L. L., Sanders D. B., Fulton E., Taniguchi Y., Sato Y., Kawara K., Okuda H., 1998, Nature, 394, 248

Barger A. J., Cowie L. L., Smail I., Ivison R. J., Blain A. W., Kneib J.-P., 1999, AJ, 117, 2656

Barger A. J., Cowie L. L., Wang W.-H., 2008, ApJ, 689, 687

Baugh C. M., Lacey C. G., Frenk C. S., Granato G. L., Silva L., Bressan A., Benson A. J., Cole S., 2005, MNRAS, 356, 1191

Bayet E. et al., 2013, MNRAS, 432, 1742

Bayet E., Gerin M., Phillips T. G., Contursi A., 2004, A&A, 427, 45

Bayet E., Gerin M., Phillips T. G., Contursi A., 2006, A&A, 460, 467

Bayet E., Viti S., Hartquist T. W., Williams D. A., 2011a, MNRAS, 417, 627

Bayet E., Williams D. A., Hartquist T. W., Viti S., 2011b, MNRAS, 414, 1583

Bell E. F., 2003, ApJ, 586, 794

Bell E. F. et al., 2004, ApJ, 608, 752

Bennett C. L. et al., 1994, ApJ, 434, 587

Bergin E. A., Tafalla M., 2007, ARA&A, 45, 339

Best P. N., Kaiser C. R., Heckman T. M., Kauffmann G., 2006, MNRAS, 368, L67

Best P. N., Kauffmann G., Heckman T. M., Brinchmann J., Charlot S., Ivezić Ž., White S. D. M., 2005, MNRAS, 362, 25

Biggs A. D. et al., 2011, MNRAS, 413, 2314

Bîrzan L., McNamara B. R., Nulsen P. E. J., Carilli C. L., Wise M. W., 2008, ApJ, 686, 859

Bîrzan L., Rafferty D. A., McNamara B. R., Wise M. W., Nulsen P. E. J., 2004, ApJ, 607, 800

Blain A. W., Chapman S. C., Smail I., Ivison R., 2004, ApJ, 611, 725

Blain A. W., Smail I., Ivison R. J., Kneib J.-P., Frayer D. T., 2002, PhR, 369, 111

Blandford R. D., Netzer H., Woltjer L., Courvoisier T. J.-L., Mayor M., eds., 1990, Active Galactic Nuclei

Boehringer H., Voges W., Fabian A. C., Edge A. C., Neumann D. M., 1993, MNRAS, 264, L25

Bolatto A. D., Jackson J. M., Kraemer K. E., Zhang X., 2000, ApJ, 541, L17

Bolatto A. D., Leroy A. K., Rosolowsky E., Walter F., Blitz L., 2008, ApJ, 686, 948

Bolatto A. D., Wolfire M., Leroy A. K., 2013, ARA&A, 51, 207

Bolzonella M., Miralles J.-M., Pelló R., 2000, A&A, 363, 476

Bonzini M. et al., 2012, ApJS, 203, 15

Boroson B., Kim D.-W., Fabbiano G., 2011, ApJ, 729, 12

Bothwell M. S. et al., 2013, MNRAS, 429, 3047

Boutsia K., Leibundgut B., Trevese D., Vagnetti F., 2009, A&A, 497, 81

Bower R. G., Benson A. J., Malbon R., Helly J. C., Frenk C. S., Baugh C. M., Cole S., Lacey C. G., 2006, MNRAS, 370, 645

Bower R. G., McCarthy I. G., Benson A. J., 2008, MNRAS, 390, 1399

Bradford C. M., Nikola T., Stacey G. J., Bolatto A. D., Jackson J. M., Savage M. L., Davidson J. A., Higdon S. J., 2003, ApJ, 586, 891

Bregman J. N., Parriott J. R., 2009, ApJ, 699, 923

Brighenti F., Mathews W. G., 1999, ApJ, 512, 65

Brown W. R., Kewley L. J., Geller M. J., 2008, AJ, 135, 92

Bruzual G., Charlot S., 2003, MNRAS, 344, 1000

Bruzual A. G., Charlot S., 1993, ApJ, 405, 538

Bryant P. M., Scoville N. Z., 1996, ApJ, 457, 678

Bunker A. J., Stanway E. R., Ellis R. S., McMahon R. G., McCarthy P. J., 2003, MNRAS, 342, L47

Calzetti D., Armus L., Bohlin R. C., Kinney A. L., Koornneef J., Storchi-Bergmann T., 2000, ApJ, 533, 682

Calzetti D., Kinney A. L., Storchi-Bergmann T., 1994, ApJ, 429, 582

Capak P. et al., 2008, ApJ, 681, L53

Capak P. et al., 2004, AJ, 127, 180

Cardamone C. N. et al., 2010, ApJS, 189, 270

Carilli C. L. et al., 2010, ApJ, 714, 1407

Casey C. M. et al., 2012, ApJ, 761, 140

Casey C. M., Chapman S. C., Smail I., Alaghband-Zadeh S., Bothwell M. S., Swinbank A. M., 2011, MNRAS, 411, 2739

Casey C. M., Narayanan D., Cooray A., 2014, ArXiv e-prints

Casoli F., Dupraz C., Combes F., 1992a, A&A, 264, 49

Casoli F., Dupraz C., Combes F., 1992b, A&A, 264, 55

Cavagnolo K. W., McNamara B. R., Nulsen P. E. J., Carilli C. L., Jones C., Bîrzan L., 2010, ApJ, 720, 1066

Chapman S. C., Blain A., Ibata R., Ivison R. J., Smail I., Morrison G., 2009, ApJ, 691, 560

Chapman S. C., Blain A. W., Smail I., Ivison R. J., 2005, ApJ, 622, 772

Charlot S., Fall S. M., 2000, ApJ, 539, 718

Churazov E., Sazonov S., Sunyaev R., Forman W., Jones C., Böhringer H., 2005, MNRAS, 363, L91

Clements D. L. et al., 2008, MNRAS, 387, 247

Combes F. et al., 2012, A&A, 538, L4

Condon J. J., 1992, ARA&A, 30, 575

Condon J. J., Anderson M. L., Helou G., 1991, ApJ, 376, 95

Cooper M. C. et al., 2012, MNRAS, 425, 2116

Copernicus N., 1543, D revolutionibus orbium coelestium

Coppin K. E. K. et al., 2012, MNRAS, 427, 520

Coppin K. E. K. et al., 2009, MNRAS, 395, 1905

Coppin K. E. K. et al., 2008, MNRAS, 389, 45

Coppin K. E. K. et al., 2007, ApJ, 665, 936

Cox P. et al., 2011, ApJ, 740, 63

Cristiani S. et al., 2000, A&A, 359, 489

Croom S. M., Schade D., Boyle B. J., Shanks T., Miller L., Smith R. J., 2004, ApJ, 606, 126

Croom S. M., Smith R. J., Boyle B. J., Shanks T., Loaring N. S., Miller L., Lewis I. J., 2001, MNRAS, 322, L29

Croston J. H., Hardcastle M. J., Birkinshaw M., Worrall D. M., Laing R. A., 2008, MNRAS, 386, 1709

Croton D. J. et al., 2006, MNRAS, 365, 11

da Cunha E., Charlot S., Elbaz D., 2008, MNRAS, 388, 1595

Daddi E. et al., 2009, ApJ, 694, 1517

Daddi E. et al., 2005, ApJ, 631, L13

Damen M. et al., 2011, ApJ, 727, 1

Danielson A. L. R., Lehmer B. D., Alexander D. M., Brandt W. N., Luo B., Miller N., Xue Y. Q., Stott J. P., 2012, MNRAS, 422, 494

Danielson A. L. R. et al., 2013, MNRAS, 436, 2793

Danielson A. L. R. et al., 2011, MNRAS, 410, 1687

Davé R., Finlator K., Oppenheimer B. D., Fardal M., Katz N., Kereš D., Weinberg D. H., 2010, MNRAS, 404, 1355

Davies R. I., Sternberg A., Lehnert M., Tacconi-Garman L. E., 2003, ApJ, 597, 907

De Breuck C. et al., 2014, A&A, 565, A59

de Jong T., Klein U., Wielebinski R., Wunderlich E., 1985, A&A, 147, L6

Del Moro A. et al., 2013, A&A, 549, A59

Devereux N., Taniguchi Y., Sanders D. B., Nakai N., Young J. S., 1994, AJ, 107, 2006

Di Matteo T., Springel V., Hernquist L., 2005, Nature, 433, 604

Dickinson M. et al., 2004, ApJ, 600, L99

Dickman R. L., Snell R. L., Schloerb F. P., 1986, ApJ, 309, 326

Doherty M., Bunker A. J., Ellis R. S., McCarthy P. J., 2005, MNRAS, 361, 525

Downes D., Solomon P. M., 1998, ApJ, 507, 615

Draine B. T. et al., 2007, ApJ, 663, 866

Dunne L., Eales S. A., 2001, MNRAS, 327, 697

Eales S. et al., 2010, PASP, 122, 499

Eisenstein D. J. et al., 2003, ApJ, 585, 694

Elbaz D. et al., 2011, A&A, 533, A119

Ellis S. C., O'Sullivan E., 2006, MNRAS, 367, 627

Erb D. K., Shapley A. E., Steidel C. C., Pettini M., Adelberger K. L., Hunt M. P.,
    Moorwood A. F. M., Cuby J., 2003, ApJ, 591, 101

Faber S. M., Jackson R. E., 1976, ApJ, 204, 668

Fanaroff B. L., Riley J. M., 1974, MNRAS, 167, 31P

Feldmann R. et al., 2006, MNRAS, 372, 565

Ferland G. J., Korista K. T., Verner D. A., Ferguson J. W., Kingdon J. B., Verner
    E. M., 1998, PASP, 110, 761

Flower D. R., 2001, MNRAS, 328, 147

Flower D. R., Le Bourlot J., Pineau Des Forets G., Roueff E., 1994, A&A, 282, 225

Forman W. et al., 2005, ApJ, 635, 894

Frayer D. T. et al., 1999, ApJ, 514, L13

Frayer D. T., Ivison R. J., Scoville N. Z., Yun M., Evans A. S., Smail I., Blain A. W., Kneib J., 1998, ApJ, 506, L7

Frerking M. A., Keene J., Blake G. A., Phillips T. G., 1989, ApJ, 344, 311

Frerking M. A., Langer W. D., Wilson R. W., 1982, ApJ, 262, 590

Gao L., Springel V., White S. D. M., 2005, MNRAS, 363, L66

Gao Y., Carilli C. L., Solomon P. M., Vanden Bout P. A., 2007, ApJ, 660, L93

Gao Y., Solomon P. M., 2004, ApJ, 606, 271

Gaspari M., Brighenti F., D'Ercole A., Melioli C., 2011, MNRAS, 415, 1549

Gawiser E. et al., 2006, ApJS, 162, 1

Gehrels N., 1986, ApJ, 303, 336

Genzel R. et al., 2012, ApJ, 746, 69

Genzel R. et al., 2010, MNRAS, 407, 2091

Georgantopoulos I. et al., 2013, A&A, 555, A43

Gerin M., Phillips T. G., 1998, ApJ, 509, L17

Gerin M., Phillips T. G., 2000, ApJ, 537, 644

Giavalisco M., Ferguson H. C., Dickinson M., Alexander D. M., Bauer F. E., Bergeron J., Biagetti C., Brandt, W. et al., 2004, ApJ, 600, L93

Giodini S. et al., 2010, ApJ, 714, 218

Goldader J. D., Meurer G., Heckman T. M., Seibert M., Sanders D. B., Calzetti D., Steidel C. C., 2002, ApJ, 568, 651

Goldreich P., Kwan J., 1974, ApJ, 189, 441

Goldsmith P. F., Langer W. D., 1978, ApJ, 222, 881

González-Alfonso E. et al., 2010, A&A, 518, L43

González Delgado R. M., Leitherer C., 1999, ApJS, 125, 479

González Delgado R. M., Leitherer C., Heckman T. M., 1999, ApJS, 125, 489

Grazian A. et al., 2006, A&A, 449, 951

Greif T. H., Johnson J. L., Klessen R. S., Bromm V., 2008, MNRAS, 387, 1021

Greve T. R. et al., 2005, MNRAS, 359, 1165

Greve T. R., Ivison R. J., Papadopoulos P. P., 2003, ApJ, 599, 839

Greve T. R., Papadopoulos P. P., Gao Y., Radford S. J. E., 2009, ApJ, 692, 1432

Groenewegen M. A. T., Lamers H. J. G. L. M., Pauldrach A. W. A., 1989, A&A, 221, 78

Guesten R., Serabyn E., Kasemann C., Schinckel A., Schneider G., Schulz A., Young K., 1993, ApJ, 402, 537

Hailey-Dunsheath S., Nikola T., Stacey G. J., Oberst T. E., Parshley S. C., Benford D. J., Staguhn J. G., Tucker C. E., 2010a, ApJ, 714, L162

Hailey-Dunsheath S., Nikola T., Stacey G. J., Oberst T. E., Parshley S. C., Benford D. J., Staguhn J. G., Tucker C. E., 2010b, ApJ, 714, L162

Hailey-Dunsheath S., Nikola T., Stacey G. J., Oberst T. E., Parshley S. C., Bradford C. M., Ade P. A. R., Tucker C. E., 2008, ApJ, 689, L109

Hainline L. J., Blain A. W., Smail I., Alexander D. M., Armus L., Chapman S. C., Ivison R. J., 2011, ApJ, 740, 96

Hainline L. J., Blain A. W., Smail I., Frayer D. T., Chapman S. C., Ivison R. J., Alexander D. M., 2009, ApJ, 699, 1610

Harris A. I., Baker A. J., Jewell P. R., Rauch K. P., Zonak S. G., O'Neil K., Shelton A. L., Norrod, R. et al.,, 2007, in Astronomical Society of the Pacific Conference Series, Vol. 375, From Z-Machines to ALMA: (Sub)Millimeter Spectroscopy of Galaxies, A. J. Baker, J. Glenn, A. I. Harris, J. G. Mangum, & M. S. Yun , ed., pp. 82–+

Harris A. I., Baker A. J., Zonak S. G., Sharon C. E., Genzel R., Rauch K., Watts G., Creager R., 2010, ApJ, 723, 1139

Harrison A., Henkel C., Russell A., 1999, MNRAS, 303, 157

Harrison A., Puxley P., Russell A., Brand P., 1995, MNRAS, 277, 413

Harrison C. M. et al., 2012, MNRAS, 426, 1073

Hauser M. G., Dwek E., 2001, ARA&A, 39, 249

Häussler B. et al., 2007, ApJS, 172, 615

Hayward C. C., Jonsson P., Kereš D., Magnelli B., Hernquist L., Cox T. J., 2012, MNRAS, 424, 951

Hayward C. C., Kereš D., Jonsson P., Narayanan D., Cox T. J., Hernquist L., 2011, ApJ, 743, 159

Heavens A., Panter B., Jimenez R., Dunlop J., 2004, Nature, 428, 625

Heckman T., Best P., 2014, ArXiv e-prints

Helou G., Soifer B. T., Rowan-Robinson M., 1985, ApJ, 298, L7

Henkel C., Chin Y.-N., Mauersberger R., Whiteoak J. B., 1998, A&A, 329, 443

Henkel C., Downes D., Weiß A., Riechers D., Walter F., 2010, A&A, 516, A111

Henkel C., Mauersberger R., 1993, A&A, 274, 730

Henkel C., Mauersberger R., Wiklind T., Huettemeister S., Lemme C., Millar T. J., 1993, A&A, 268, L17

Herbert P. D., Jarvis M. J., Willott C. J., McLure R. J., Mitchell E., Rawlings S., Hill G. J., Dunlop J. S., 2010, MNRAS, 406, 1841

Hickox R. C. et al., 2012, MNRAS, 421, 284

Hlavacek-Larrondo J., Fabian A. C., Edge A. C., Ebeling H., Allen S. W., Sanders J. S., Taylor G. B., 2013, MNRAS, 431, 1638

Hocuk S., Spaans M., 2010, A&A, 510, A110+

Hodge J. A. et al., 2013, ApJ, 768, 91

Hollenbach D. J., Tielens A. G. G. M., 1997, ARA&A, 35, 179

Hopkins P. F., Hernquist L., Cox T. J., Kereš D., 2008, ApJS, 175, 356

Hopkins P. F., Quataert E., Murray N., 2012, MNRAS, 421, 3488

Hubble E. P., 1929, ApJ, 69, 103

Hughes D. H. et al., 1998, Nature, 394, 241

Iono D. et al., 2007, ApJ, 659, 283

Israel F. P., Baas F., 2002, A&A, 383, 82

Israel F. P., Maloney P. R., Geis N., Herrmann F., Madden S. C., Poglitsch A., Stacey G. J., 1996, ApJ, 465, 738

Israel F. P., White G. J., Baas F., 1995, A&A, 302, 343

Ivison R. J. et al., 2010a, MNRAS, 402, 245

Ivison R. J. et al., 2002, MNRAS, 337, 1

Ivison R. J. et al., 2010b, A&A, 518, L31

Ivison R. J., Papadopoulos P. P., Smail I., Greve T. R., Thomson A. P., Xilouris E. M., Chapman S. C., 2011, MNRAS, 412, 1913

Ivison R. J. et al., 2005, MNRAS, 364, 1025

Ivison R. J., Smail I., Papadopoulos P. P., Wold I., Richard J., Swinbank A. M., Kneib J., Owen F. N., 2010c, MNRAS, 404, 198

Ivison R. J. et al., 2010d, A&A, 518, L35

Iwasawa K. et al., 2012, A&A, 546, A84

Juneau S., Narayanan D. T., Moustakas J., Shirley Y. L., Bussmann R. S., Kennicutt R. C., Vanden Bout P. A., 2009, ApJ, 707, 1217

Karim A. et al., 2013, MNRAS, 432, 2

Kauffmann G. et al., 2003, MNRAS, 346, 1055

Kaufman M. J., Wolfire M. G., Hollenbach D. J., Luhman M. L., 1999, ApJ, 527, 795

Kellermann K. I., Fomalont E. B., Mainieri V., Padovani P., Rosati P., Shaver P., Tozzi P., Miller N., 2008, ApJS, 179, 71

Kennicutt, Jr. R. C., 1998a, ARA&A, 36, 189

Kennicutt, Jr. R. C., 1998b, ApJ, 498, 541

Kewley L. J., Maier C., Yabe K., Ohta K., Akiyama M., Dopita M. A., Yuan T., 2013, ApJ, 774, L10

Knudsen K. K., Neri R., Kneib J.-P., van der Werf P. P., 2009, A&A, 496, 45

Kong X., Charlot S., Brinchmann J., Fall S. M., 2004, MNRAS, 349, 769

Kormendy J., Richstone D., 1995, ARA&A, 33, 581

Kramer C. et al., 2008, A&A, 477, 547

Kramer C., Jakob H., Mookerjea B., Schneider N., Brüll M., Stutzki J., 2004, A&A, 424, 887

Kriek M. et al., 2008, ApJ, 677, 219

Krumholz M. R., Tan J. C., 2007, ApJ, 654, 304

Kurk J. et al., 2013, A&A, 549, A63

Lagache G., Puget J.-L., Dole H., 2005, ARA&A, 43, 727

Le Fèvre O. et al., 2013, A&A, 559, A14

Le Fèvre O. et al., 2005, A&A, 439, 845

Ledlow M. J., 1997, in Astronomical Society of the Pacific Conference Series, Vol. 116, The Nature of Elliptical Galaxies; 2nd Stromlo Symposium, Arnaboldi M., Da Costa G. S., Saha P., eds., pp. 421–+

Lehmer B. D. et al., 2005, ApJS, 161, 21

Lehmer B. D. et al., 2007, ApJ, 657, 681

Leitherer C., Robert C., Heckman T. M., 1995, ApJS, 99, 173

Lilly S. J., Le Fevre O., Hammer F., Crampton D., 1996, ApJ, 460, L1+

Lilly S. J., Longair M. S., 1984, MNRAS, 211, 833

Luo B. et al., 2011, ApJ, 740, 37

Lutz D. et al., 2011, A&A, 532, A90

Madau P., Dickinson M., 2014, ArXiv e-prints

Madau P., Ferguson H. C., Dickinson M. E., Giavalisco M., Steidel C. C., Fruchter A., 1996, MNRAS, 283, 1388

Magnelli B., Elbaz D., Chary R. R., Dickinson M., Le Borgne D., Frayer D. T., Willmer C. N. A., 2009, A&A, 496, 57

Magnelli B. et al., 2010, A&A, 518, L28

Magnelli B. et al., 2012, A&A, 539, A155

Magorrian J. et al., 1998, AJ, 115, 2285

Maiolino R., Caselli P., Nagao T., Walmsley M., De Breuck C., Meneghetti M., 2009, A&A, 500, L1

Malhotra S. et al., 2001, ApJ, 561, 766

Mao M. Y., Huynh M. T., Norris R. P., Dickinson M., Frayer D., Helou G., Monkiewicz J. A., 2011, ApJ, 731, 79

Mao M. Y. et al., 2012, MNRAS, 426, 3334

Mao R. Q., Henkel C., Schulz A., Zielinsky M., Mauersberger R., Störzer H., Wilson T. L., Gensheimer P., 2000, A&A, 358, 433

Marigo P., Girardi L., 2007, A&A, 469, 239

Marks M., Kroupa P., Dabringhausen J., Pawlowski M. S., 2012, MNRAS, 422, 2246

Martín S., Aladro R., Martín-Pintado J., Mauersberger R., 2010, A&A, 522, A62

Mathews W. G., Brighenti F., 2003, ARA&A, 41, 191

Matsushita S. et al., 2009, ApJ, 693, 56

McNamara B. R., Kazemzadeh F., Rafferty D. A., Bîrzan L., Nulsen P. E. J., Kirkpatrick C. C., Wise M. W., 2009, ApJ, 698, 594

McNamara B. R., Nulsen P. E. J., 2007, ARA&A, 45, 117

McNamara B. R., Nulsen P. E. J., 2012, New Journal of Physics, 14, 055023

Meier D. S., Turner J. L., 2001, ApJ, 551, 687

Meier D. S., Turner J. L., 2004, AJ, 127, 2069

Meijerink R. et al., 2013, ApJ, 762, L16

Meijerink R., Spaans M., 2005, A&A, 436, 397

Meijerink R., Spaans M., Israel F. P., 2007, A&A, 461, 793

Meijerink R., Spaans M., Loenen A. F., van der Werf P. P., 2011, A&A, 525, A119

Meurer G. R., Heckman T. M., Calzetti D., 1999, ApJ, 521, 64

Michałowski M., Hjorth J., Watson D., 2010, A&A, 514, A67

Michałowski M. J., Dunlop J. S., Cirasuolo M., Hjorth J., Hayward C. C., Watson
D., 2012, A&A, 541, A85

Mignoli M. et al., 2005, A&A, 437, 883

Miller N. A. et al., 2013, ApJS, 205, 13

Miller N. A., Fomalont E. B., Kellermann K. I., Mainieri V., Norman C., Padovani
P., Rosati P., Tozzi P., 2008, ApJS, 179, 114

Morrison G. E., Owen F. N., Dickinson M., Ivison R. J., Ibar E., 2010, ApJS, 188,
178

Mullaney J. R., Alexander D. M., Fine S., Goulding A. D., Harrison C. M., Hickox
R. C., 2013, MNRAS, 433, 622

Murphy E. J. et al., 2008, ApJ, 672, L85

Muzerolle J. et al., 2004, ApJS, 154, 379

Myers A. D., White M., Ball N. M., 2009, MNRAS, 399, 2279

Narayanan D., Krumholz M. R., 2014, MNRAS, 442, 1411

Negishi T., Onaka T., Chan K., Roellig T. L., 2001, A&A, 375, 566

Neugebauer G. et al., 1984, ApJ, 278, L1

Nonino M. et al., 2009, ApJS, 183, 244

Nulsen P. E. J., Jones C., Forman W. R., David L. P., McNamara B. R., Rafferty D. A., Bîrzan L., Wise M. W., 2007, in Heating versus Cooling in Galaxies and Clusters of Galaxies, H. Böhringer, G. W. Pratt, A. Finoguenov, & P. Schuecker , ed., p. 210

Oliver S. J. et al., 2012, MNRAS, 424, 1614

Onodera S. et al., 2010, ApJ, 722, L127

Osterbrock D. E., Ferland G. J., 2006, Astrophysics of gaseous nebulae and active galactic nuclei

O'Sullivan E., Forbes D. A., Ponman T. J., 2001, MNRAS, 328, 461

O'Sullivan E., Giacintucci S., David L. P., Gitti M., Vrtilek J. M., Raychaudhury S., Ponman T. J., 2011, ApJ, 735, 11

Ott J., Weiss A., Henkel C., Walter F., 2005, ApJ, 629, 767

Overzier R. A. et al., 2011, ApJ, 726, L7

Page M. J., Carrera F. J., Stevens J. A., Ebrero J., Blustin A. J., 2011, MNRAS, 416, 2792

Page M. J., Stevens J. A., Ivison R. J., Carrera F. J., 2004, ApJ, 611, L85

Panuzzo P. et al., 2010, A&A, 518, L37

Papadopoulos P. P., 2007, ApJ, 656, 792

Papadopoulos P. P., 2010, ApJ, 720, 226

Papadopoulos P. P., Greve T. R., 2004, ApJ, 615, L29

Papadopoulos P. P., Isaak K. G., van der Werf P. P., 2007, ApJ, 668, 815

Papadopoulos P. P., Seaquist E. R., Scoville N. Z., 1996, ApJ, 465, 173

Papadopoulos P. P., Thi W., Viti S., 2004, MNRAS, 351, 147

Papadopoulos P. P., Thi W.-F., Miniati F., Viti S., 2011, MNRAS, 414, 1705

Papadopoulos P. P., van der Werf P., Isaak K., Xilouris E. M., 2010, ApJ, 715, 775

Papadopoulos P. P., van der Werf P., Xilouris E., Isaak K. G., Gao Y., 2012a, ApJ, 751, 10

Papadopoulos P. P., van der Werf P. P., Xilouris E. M., Isaak K. G., Gao Y., Mühle S., 2012b, MNRAS, 426, 2601

Penzias A. A., 1983, ApJ, 273, 195

Petitpas G. R., Wilson C. D., 2000, ApJ, 538, L117

Pety J., 2005, in SF2A-2005: Semaine de l'Astrophysique Francaise, F. Casoli, T. Contini, J. M. Hameury, & L. Pagani, ed., pp. 721–+

Pineda J. L., Bensch F., 2007, A&A, 470, 615

Popesso P. et al., 2014, ArXiv e-prints

Popesso P. et al., 2009, A&A, 494, 443

Prantzos N., Aubert O., Audouze J., 1996, A&A, 309, 760

Ptak A., Mobasher B., Hornschemeier A., Bauer F., Norman C., 2007, ApJ, 667, 826

Rafferty D. A., Brandt W. N., Alexander D. M., Xue Y. Q., Bauer F. E., Lehmer B. D., Luo B., Papovich C., 2011, ApJ, 742, 3

Rafferty D. A., McNamara B. R., Nulsen P. E. J., Wise M. W., 2006, ApJ, 652, 216

Ravikumar C. D. et al., 2007, A&A, 465, 1099

Raymond J. C., Smith B. W., 1977, ApJS, 35, 419

Reddy N. A., Erb D. K., Pettini M., Steidel C. C., Shapley A. E., 2010, ApJ, 712, 1070

Reeves J. N., Turner M. J. L., 2000, MNRAS, 316, 234

Richards E. A., 2000, ApJ, 533, 611

Richards E. A., Kellermann K. I., Fomalont E. B., Windhorst R. A., Partridge R. B., 1998, AJ, 116, 1039

Richards G. T. et al., 2011, AJ, 141, 167

Richards G. T., Vanden Berk D. E., Reichard T. A., Hall P. B., Schneider D. P., SubbaRao M., Thakar A. R., York D. G., 2002, AJ, 124, 1

Riechers D. A. et al., 2010, ApJ, 720, L131

Robitaille T. P., Whitney B. A., 2010, ApJ, 710, L11

Röllig M. et al., 2007, A&A, 467, 187

Röllig M., Ossenkopf V., Jeyakumar S., Stutzki J., Sternberg A., 2006, A&A, 451, 917

Rousselot P., Lidman C., Cuby J.-G., Moreels G., Monnet G., 2000, A&A, 354, 1134

Rupke D. S., Veilleux S., Sanders D. B., 2005, ApJS, 160, 115

Sakamoto K., Scoville N. Z., Yun M. S., Crosas M., Genzel R., Tacconi L. J., 1999, ApJ, 514, 68

Sanders D. B., Mazzarella J. M., Kim D.-C., Surace J. A., Soifer B. T., 2003, AJ, 126, 1607

Sanders D. B., Mirabel I. F., 1996, ARA&A, 34, 749

Sanders D. B., Soifer B. T., Elias J. H., Madore B. F., Matthews K., Neugebauer G., Scoville N. Z., 1988, ApJ, 325, 74

Schinnerer E. et al., 2008, ApJ, 689, L5

Schinnerer E. et al., 2007, ApJS, 172, 46

Scoville N., 2004, in Astronomical Society of the Pacific Conference Series, Vol. 320, The Neutral ISM in Starburst Galaxies, S. Aalto, S. Huttemeister, & A. Pedlar, ed., pp. 253–+

Scoville N. Z., Sargent A. I., Sanders D. B., Claussen M. J., Masson C. R., Lo K. Y., Phillips T. G., 1986, ApJ, 303, 416

Scoville N. Z., Yun M. S., Bryant P. M., 1997, ApJ, 484, 702

Seibert M. H., 2004, PhD thesis, THE JOHNS HOPKINS UNIVERSITY

Serjeant S., Farrah D., Geach J., Takagi T., Verma A., Kaviani A., Fox M., 2003, MNRAS, 346, L51

Shapley A. E., 2011, ARA&A, 49, 525

Shapley A. E., Steidel C. C., Pettini M., Adelberger K. L., 2003, ApJ, 588, 65

Silverman J. D. et al., 2010, ApJS, 191, 124

Simpson J. M. et al., 2014, ApJ, 788, 125

Smail I., Chapman S. C., Ivison R. J., Blain A. W., Takata T., Heckman T. M., Dunlop J. S., Sekiguchi K., 2003, MNRAS, 342, 1185

Smail I., Ivison R. J., Blain A. W., 1997, ApJ, 490, L5

Smail I., Ivison R. J., Blain A. W., Kneib J.-P., 2002, MNRAS, 331, 495

Smolčić V. et al., 2011, ApJ, 731, L27

Smolčić V., Riechers D. A., 2011, ApJ, 730, 64

Smolčić V. et al., 2009, ApJ, 696, 24

Socrates A., Davis S. W., Ramirez-Ruiz E., 2008, ApJ, 687, 202

Soifer B. T., Neugebauer G., 1991, AJ, 101, 354

Solomon P. M., Downes D., Radford S. J. E., Barrett J. W., 1997, ApJ, 478, 144

Solomon P. M., Vanden Bout P. A., 2005, ARA&A, 43, 677

Spaans M., 1996, A&A, 307, 271

Spaans M., Meijerink R., 2008, ApJ, 678, L5

Spergel D. N. et al., 2007, ApJS, 170, 377

Spergel D. N. et al., 2003, ApJS, 148, 175

Stacey G. J., Geis N., Genzel R., Lugten J. B., Poglitsch A., Sternberg A., Townes
    C. H., 1991, ApJ, 373, 423

Stanway E. R., Bunker A. J., McMahon R. G., Ellis R. S., Treu T., McCarthy P. J.,
    2004a, ApJ, 607, 704

Stanway E. R. et al., 2004b, ApJ, 604, L13

Stark A. A., Bolatto A. D., Chamberlin R. A., Lane A. P., Bania T. M., Jackson
    J. M., Lo K., 1997, ApJ, 480, L59+

Stark A. A., Gammie C. F., Wilson R. W., Bally J., Linke R. A., Heiles C., Hurwitz
    M., 1992, ApJS, 79, 77

Stark D. P., Swinbank A. M., Ellis R. S., Dye S., Smail I. R., Richard J., 2008,
    Nature, 455, 775

Steidel C. C., Erb D. K., Shapley A. E., Pettini M., Reddy N., Bogosavljević M.,
    Rudie G. C., Rakic O., 2010, ApJ, 717, 289

Stern D. et al., 2005, ApJ, 631, 163

Sternberg A., 2005, in IAU Symposium, Vol. 231, Astrochemistry: Recent Successes
    and Current Challenges, Lis D. C., Blake G. A., Herbst E., eds., pp. 141–152

Stoerzer H., Stutzki J., Sternberg A., 1996, A&A, 310, 592

Storey P. J., Zeippen C. J., 2000, MNRAS, 312, 813

Stott J. P. et al., 2012, MNRAS, 422, 2213

Stott J. P. et al., 2013, MNRAS, 436, 1130

Strateva I. et al., 2001, AJ, 122, 1861

Strolger L.-G. et al., 2004, ApJ, 613, 200

Stutzki J. et al., 1997, ApJ, 477, L33+

Suchkov A., Allen R. J., Heckman T. M., 1993, ApJ, 413, 542

Swinbank A. M., Chapman S. C., Smail I., Lindner C., Borys C., Blain A. W., Ivison R. J., Lewis G. F., 2006, MNRAS, 371, 465

Swinbank A. M. et al., 2012, MNRAS, 427, 1066

Swinbank A. M. et al., 2011, ApJ, 742, 11

Swinbank A. M. et al., 2014, MNRAS, 438, 1267

Swinbank A. M., Smail I., Chapman S. C., Blain A. W., Ivison R. J., Keel W. C., 2004, ApJ, 617, 64

Swinbank A. M. et al., 2010, Nature, 464, 733

Szokoly G. P. et al., 2004, ApJS, 155, 271

Tabor G., Binney J., 1993, MNRAS, 263, 323

Tacconi L. J. et al., 2008, ApJ, 680, 246

Tacconi L. J., Genzel R., Tecza M., Gallimore J. F., Downes D., Scoville N. Z., 1999, ApJ, 524, 732

Tacconi L. J. et al., 2006, ApJ, 640, 228

Tacconi L. J. et al., 2013, ApJ, 768, 74

Takata T., Sekiguchi K., Smail I., Chapman S. C., Geach J. E., Swinbank A. M., Blain A., Ivison R. J., 2006, ApJ, 651, 713

Takeuchi T. T., Yuan F.-T., Ikeyama A., Murata K. L., Inoue A. K., 2012, ApJ, 755, 144

Tan Q.-H., Gao Y., Zhang Z.-Y., Xia X.-Y., 2011, Research in Astronomy and Astrophysics, 11, 787

Taylor E. N. et al., 2009, ApJS, 183, 295

Teyssier R., Chapon D., Bournaud F., 2010, ApJ, 720, L149

Thompson T. A., Quataert E., Murray N., 2005, ApJ, 630, 167

Tielens A. G. G. M., Hollenbach D., 1985, ApJ, 291, 722

Toft S. et al., 2014, ApJ, 782, 68

Treister E. et al., 2009, ApJ, 693, 1713

Tremonti C. A., Moustakas J., Diamond-Stanic A. M., 2007, ApJ, 663, L77

Turnshek D. A., 1988, in QSO Absorption Lines: Probing the Universe, Blades J. C., Turnshek D. A., Norman C. A., eds., p. 17

Tzanavaris P., Georgantopoulos I., 2008, A&A, 480, 663

Urry C. M., Padovani P., 1995, PASP, 107, 803

Vale A., Ostriker J. P., 2004, MNRAS, 353, 189

van der Kruit P. C., 1971, A&A, 15, 110

van der Tak F. F. S., Black J. H., Schöier F. L., Jansen D. J., van Dishoeck E. F., 2007, A&A, 468, 627

van der Wel A., Franx M., van Dokkum P. G., Rix H.-W., 2004, ApJ, 601, L5

van der Werf P. P. et al., 2010, A&A, 518, L42

van Dishoeck E. F., Black J. H., 1986, ApJS, 62, 109

Vanzella, et al. E., 2008, A&A, 478, 83

Vassilev V. et al., 2008, A&A, 490, 1157

Veilleux S., Osterbrock D. E., 1987, ApJS, 63, 295

Vignali C., Bauer F. E., Alexander D. M., Brandt W. N., Hornschemeier A. E., Schneider D. P., Garmire G. P., 2002, ApJ, 580, L105

Walter F. et al., 2012, Nature, 486, 233

Walter F., Riechers D., Cox P., Neri R., Carilli C., Bertoldi F., Weiss A., Maiolino R., 2009, Nature, 457, 699

Wang S. X. et al., 2013, ApJ, 778, 179

Wang W.-H., Cowie L. L., Barger A. J., 2004, ApJ, 613, 655

Ward J. S., Zmuidzinas J., Harris A. I., Isaak K. G., 2003, ApJ, 587, 171

Wardlow J. L. et al., 2011, MNRAS, 415, 1479

Watson W. D., Anicich V. G., Huntress, Jr. W. T., 1976, ApJ, 205, L165

Weingartner J. C., Draine B. T., Barr D. K., 2006, ApJ, 645, 1188

Weiß A., Downes D., Henkel C., Walter F., 2005a, A&A, 429, L25

Weiß A., Downes D., Neri R., Walter F., Henkel C., Wilner D. J., Wagg J., Wiklind T., 2007, A&A, 467, 955

Weiß A., Downes D., Walter F., Henkel C., 2005b, A&A, 440, L45

Weiß A. et al., 2009, ApJ, 707, 1201

Weiß A., Walter F., Scoville N. Z., 2005c, A&A, 438, 533

Whitaker K. E., Kriek M., van Dokkum P. G., Bezanson R., Brammer G., Franx M., Labbé I., 2012, ApJ, 745, 179

Whitaker K. E. et al., 2013, ApJ, 770, L39

White G. J., Ellison B., Claude S., Dent W. R. F., Matheson D. N., 1994, A&A, 284, L23

Wild W., Harris A. I., Eckart A., Genzel R., Graf U. U., Jackson J. M., Russell A. P. G., Stutzki J., 1992, A&A, 265, 447

Williams R. J., Maiolino R., Santini P., Marconi A., Cresci G., Mannucci F., Lutz D., 2014, MNRAS, 443, 3780

Wilson T. L., Rood R., 1994, ARA&A, 32, 191

Wolf C. et al., 2004, A&A, 421, 913

Wouterloot J. G. A., Brand J., 1996, A&AS, 119, 439

Wuyts S., van Dokkum P. G., Franx M., Förster Schreiber N. M., Illingworth G. D., Labbé I., Rudnick G., 2009, ApJ, 706, 885

Xia L. et al., 2011, AJ, 141, 64

Xue Y. Q. et al., 2011, ApJS, 195, 10

Young J. S., Scoville N. Z., 1984, ApJ, 287, 153

Young J. S., Scoville N. Z., 1991, ARA&A, 29, 581

Yuan T., Kewley L. J., 2009, ApJ, 699, L161

Zhu L.-B., Yang J., Wang M., 2007, ChA&A, 31, 387

Zmuidzinas J., Betz A. L., Boreiko R. T., Goldhaber D. M., 1988, ApJ, 335, 774